



Politecnico di Milano
Department of Civil and Environmental Engineering
Doctoral program in Environmental and Infrastructure Engineering

Multi-scale and multi-temporal photogrammetry for alpine glacier monitoring

THESIS OF
FRANCESCO IOLI
FOR THE DOCTORAL DEGREE IN
ENVIRONMENTAL AND INFRASTRUCTURE ENGINEERING

ADVISOR: PROF. LIVIO PINTO
Co-ADVISOR: PROF. FRANCESCO NEX
TUTOR: PROF. RICCARDO BARZAGHI
CHAIR OF THE DOCTORAL PROGRAM: MONICA RIVA

36th PhD cycle
May, 2024

THIS THESIS HAS BEEN APPROVED BY
LIVIO PINTO, ADVISOR
FRANCESCO NEX, CO-ADVISOR

EXAMINATION BOARD
PROF. MATTIA CRESPI, EXAMINER
PROF. ANETTE ELTNER, EXAMINER
PROF. RICCARDO RONCELLA, EXAMINER

POLITECNICO DI MILANO
DEPARTMENT OF CIVIL AND ENVIRONMENTAL ENGINEERING
MILANO, ITALY

©2024 – FRANCESCO IOLI
ALL RIGHTS RESERVED.



POLITECNICO
MILANO 1863

Acknowledgments

This thesis marks an important milestone in my journey at the Politecnico di Milano. In the last four years, I have gained extensive experience, studied a wide range of topics, and conducted my research. This achievement would not have been possible without the technical and personal support of many people.

First of all, I would like to thank my supervisor, Prof. Livio Pinto, who has been guiding me since my BSc thesis. He introduced me to photogrammetry, 3D reconstruction, Macugnaga and Belvedere Glacier, which has become a second home to me. I am deeply grateful for his support throughout my PhD research and the writing process of this thesis. His dedication to my academic and personal growth has been precious and will continue to shape my career for years to come.

I would also like to thank my co-supervisor, Prof. Francesco Nex, for believing in the potential of the project of a photogrammetric monitoring system with low-cost stereo cameras. Hosting me at the University of Twente allowed me to tackle challenging problems and delve into state-of-the-art topics such as deep learning feature matching and reconstruction algorithms. His ongoing encouragement and patience during the final stages of paper and thesis writing have been truly invaluable.

I would also like to thank the crew of the LabMGF (Laboratory of Geodetic and Photogrammetric Measurements) research group: Federica, Federico, and Rebecca. Our collaboration went beyond mere work and became a true friendship. Thanks for the support and for the numerous projects and fieldwork, including all the surveys of bridges, dams, and, of course, Belvedere Glacier. A special acknowledgment goes to Federica, with whom I have worked since our first year at university. Thanks for sharing countless experiences, thoughts, complaints, and suggestions for the future and for the many conference trips. Thanks also to Öykü and Chiara for their invaluable friendship, support for pushing towards the end of this thesis, and all the moments spent together in the lab.

I am grateful to Luca Morelli, with whom I have worked closely over the past year, for sharing our passion for developing Deep-Image-Matching. My thanks also go to Niccolò Dematteis and Daniele Giordan for their enthusiasm and valuable contributions to the stereo monitoring project of the Belvedere Glacier, particularly in the development of our latest paper.

To all the friends I have met at various conferences over the past four years, thank you for the valuable discussions that have helped improve our research. I am especially grateful to Vivien, whom I met at our first EGU participation and we have developed a friendship that goes beyond professional collaboration.

Finally, I thank the reviewers, Prof. Anette Eltner and Prof. Riccardo Roncella, for their suggestions that improved my thesis.

Francesco

Multi-scale and multi-temporal photogrammetry for alpine glacier monitoring

ABSTRACT

Alpine glaciers are key indicators of global climate change, experiencing rapid transformations due to the climate crisis. Understanding these changes is essential for assessing climate impacts, predicting future trends, and mitigating related hazards. This thesis comprehensively investigates multi-scale and multi-temporal photogrammetry for monitoring alpine glaciers, focusing on the debris-covered Belvedere Glacier in the Italian Alps.

This research employs various photogrammetric techniques, from historical aerial image analysis to high-resolution UAV surveys and a novel low-cost stereo camera system for daily 3D motion analysis. Archival aerial images have been used to reconstruct the evolution of Belvedere Glacier over the last 50 years. This analysis revealed a period of expansion until a surge event in the early 21st century, followed by a significant retreat in recent decades. Recent annual UAV surveys have provided 3D glacier reconstructions with sub-decimetre accuracy, allowing quantification of ice volume loss and determination of glacier flow kinematics through digital image correlation.

Recognizing the inherently non-linear nature of glacier dynamics, this thesis presents a low-cost stereoscopic system built with homemade time-lapse cameras controlled by microcontrollers for deriving daily 3D models of the glacier terminal lobe by photogrammetry. An automated workflow, powered by state-of-the-art deep learning feature matching algorithms, overcomes the challenges posed by the wide baselines of the stereo cameras and has resulted in the derivation of daily 3D displacements and glacier melt. This has allowed for correlating the glacier kinematics and ice melting with external factors such as air temperature, highlighting a strong short-term correlation between the three variables.

A commitment to open science underpins this research. Datasets, including point clouds, orthophotos, and DSMs, are publicly available to encourage collaboration and future research. The software tools developed, ICEPy4D and Deep-Image-Matching, are released as open source for wider use and are easily adaptable to other photogrammetry-based monitoring applications.

This thesis demonstrates that photogrammetry is a versatile and effective tool for monitoring alpine glaciers and deriving valuable 3D information across different spatial and temporal scales. The high-resolution data acquired and the methods developed enhance our understanding of the effects of climate change in alpine environments and can be used to monitor their evolution and refine glaciological models.

KEYWORDS: Belvedere Glacier, 3D reconstruction, UAV, historical images, Deep-Learning photogrammetry, low-cost cameras, image correlation, feature matching, climate change, open data.

Contents

1	INTRODUCTION	1
1.1	Motivation and relevance	2
1.2	Remote and close-range sensing of alpine glaciers	5
1.3	The Belvedere Glacier	7
1.4	Objectives	9
1.5	Thesis outline	10
	References	18
2	BACK TO THE PAST: RECONSTRUCTING GLACIER TOPOGRAPHY WITH ARCHIVAL AERIAL IMAGES (1977-2009)	19
2.1	Introduction	20
2.2	Datasets	21
2.2.1	Historical Aerial Datasets of 1977, 1991 and 2001	22
2.2.2	Digital aerial dataset of 2009	24
2.2.3	Digital UAV dataset of 2019	25
2.2.4	GNSS Survey for Block Georeferencing	26
2.3	Methodology	26
2.3.1	SfM-MVS	26
2.3.2	Point cloud pre-processing	30
2.3.3	Glacier evolution analysis	31
2.4	Results	32
2.4.1	SfM-MVS	32
2.4.2	Point cloud pre-processing	33
2.4.3	Glacier evolution analysis	34
2.4.4	Comparison with previous studies	38
	References	41
3	UAV PHOTOGRAMMETRY FOR ANNUAL GLACIER RECONSTRUCTION (2015-2023)	42
3.1	Introduction	43
3.2	Instruments and datasets	43
3.2.1	GNSS measurements	44

3.2.2	UAV flights	44
3.2.3	Challenges and adaptations in the 2017, 2018 and 2020 surveys	47
3.3	Methodology	48
3.3.1	SfM workflow	48
3.3.2	Glacier flow velocity	49
3.3.3	Volume variations	51
3.4	Results	54
3.4.1	SfM	54
3.4.2	Glacier flow velocity	54
3.4.3	Volume variations	60
3.5	Glacier mass variations from 1977 to 2023	63
3.6	An open-source framework for sharing monitoring results	64
	References	71
4	DEEP LEARNING LOW-COST PHOTGRAMMETRY FOR 4D SHORT-TERM GLACIER MONITORING (2022-2023)	72
4.1	Introduction	74
4.2	Image matching in challenging scenarios	75
4.3	The low-cost stereoscopic system	78
4.3.1	Power supply	79
4.3.2	Controlling circuit and acquisition scheduling	79
4.3.3	Connectivity	82
4.3.4	Case and protection	83
4.3.5	General performances	83
4.3.6	The choice of the camera	83
4.3.7	Site selection for permanent installation	84
4.3.8	Camera installation	86
4.4	Datasets	88
4.4.1	Stereoscopic image sequences	88
4.4.2	UAV surveys	88
4.4.3	Meteorological monitoring station	89
4.5	Methodology	89
4.5.1	Image selection	90
4.5.2	Camera calibration	91
4.5.3	Camera stability and GCPs	91
4.5.4	Stereoscopic image processing workflow	92
4.5.5	Volume variation estimation	96
4.5.6	Automatic extraction of ice cliff top edge	98
4.5.7	Digital Image Correlation from single cameras	99
4.5.8	Correlation between glacier dynamics and meteorological variables	100
4.6	Results	101

4.6.1	Automatic detection of GCPs	101
4.6.2	Wide-baseline feature matching and tracking	101
4.6.3	3D scene reconstruction	102
4.6.4	Volume variations and glacier retreat	103
4.6.5	Validation of the stereo models with UAV data	103
4.6.6	Glacier surface velocity and morphology	107
4.6.7	Velocity orthorectification uncertainty	109
4.6.8	Comparison between surface velocity, frontal ice loss and meteorological variables	110
4.7	Discussion	110
4.7.1	Hand-crafted vs deep learning matching	110
4.7.2	Merging stereoscopic and monoscopic processings to study the glacier dynamics	112
4.7.3	Glacier velocity, frontal ablation and temperature	112
4.7.4	Transferability of the system	113
	References	120
5	TOWARDS A LOW-COST MULTI-CAMERA MULTI-EPOCH MONITORING WITH DEEP LEARNING PHOTOGRAMMETRY	121
5.1	Introduction	122
5.2	Limitations of Deep Learning local features	123
5.3	Deep-Image-Matching	124
5.3.1	Matching strategies	125
5.3.2	Image resolution and tiling	127
5.3.3	Image rotations	128
5.3.4	Matching pipelines	129
5.4	Case studies	131
5.4.1	Low-textures scenes	131
5.4.2	Historical internet images	135
5.4.3	Combining UAV and terrestrial images	137
	References	145
6	CONCLUSION	146
6.1	Summary of the results	146
6.2	Global considerations and future perspective	149
	References	152

APPENDIX A ORTHOPHOTOS 1977-2023

APPENDIX B SURFACE VELOCITY FIELDS 2015-2023

APPENDIX C CROSS-SECTIONS

APPENDIX D CAMERA RESIDUALS

Listing of figures

1.1	Images of the Planpincieux Glacier (Mont Blanc Massif). (a) Close-up photo of the Whymper Serac. The fracture fractures in the frontal part of the serac, from where several ice break-offs are triggered, are clearly visible (photo Fondazione Montagna Sicura, 2020, Chiarle et al. (2023)); (b) illustration of the Planpincieux Glacier with overlapped the area of three sectors identified by the permanent monitoring system based on their different kinematics properties (photo Fondazione Montagna Sicura, 2023, Giordan et al. (2020)).	3
1.2	Impact of the August 27, 2023 debris flow on the Belvedere Glacier (Anscasca Valley, Italian Alps). (a) Aerial view acquired (August 30, 2023, author's photo) reveals the extent of debris accumulation within the Castelfranco gully and across the glacier's northern lobe; (b) Picture of the Belvedere Glacier northern lobe few hours after the debris flow event (August 28, 2023, 4:00 PM), captured by the fixed monitoring system. Note the muddy channels carved into the glacier's surface. These channels are remnants of the powerful flow that washed away much of the debris.	4
1.3	(a) Location of Belvedere Glacier, base map (source: Swisstopo www.geo.admin.ch); (b) Picture of the Belvedere Glacier taken from the nearby Monte Moro.	8
2.1	Historical datasets of a,b 1977, c,d 1991, e,f and 2001. A picture depicting the image acquisition geometry (left) and a sample of the scanned analog images (right) is presented for each dataset.	23
2.2	Digital datasets of a,b 2009 (aerial), c,d 2019 (UAV). For each dataset, a picture depicting the image acquisition geometry (left) and a sample image (right) is presented.	25
2.3	Workflow for image orientation of the five photogrammetric blocks. Virtual Ground Control Points (vGCPs) refer to Ground Control Points (GCPs) extracted from a previous photogrammetric model by identifying characteristic features (either natural or artificial) that have remained unchanged over time across multiple images of the previous photogrammetric block. The 3D coordinates of the Virtual Ground Control Points (vGCPs) are obtained through forward triangulation of their image coordinates in 3D space.	27

2.4	Sketches of the GCPs and CPs locations for the different photogrammetric block: (a) 2019 block; (b) 2009 block; (c) 1977, 1991 and 2001 block. For the 2009 block and the historical blocks, the points are vGCPs and vCPs.	27
2.5	Examples of points chosen as Virtual Ground Control Points (vGCPs) or Virtual Check Points (vCPs): (a) artificial features in 1977, 1991, and 2001 aerial images; (d) natural features in 1977, 1991, and 2001 aerial images.	29
2.6	Interpolated gridded point clouds: (a) 1977; (b) 1991; (c) 2001; (d) 2009; (e) 2019.	31
2.7	Steps for defining the final mask for defining the glacier boundaries: (a) binary mask defining the valid area of each survey overlapped; (b) common area between the masks; (c) high-variability area (i.e., areas for which the height difference between consecutive survey epochs was greater than 10 m); (d) filtered high-variability area; (e) buffered high-variability area, i.e., considered glacier shape.	32
2.8	Model accuracy comparison in terms of RMS error on CPs.	33
2.9	Glacier contours at different epochs: (a) 1977; (b) 1991; (c) 2001; (d) 2009; (e) 2019.	35
2.10	Binned glacier altitude variations in different periods with bin size set to 25 m: (a) 1977–1991; (b) 1991–2001; (c) 2001–2009; (d) 2009–2019.	37
3.1	(a) Location of the targets used for the photogrammetric surveys. For each year, a subset of the targets were used as GCPs, while the remaining as CPs; (b) an example of a photogrammetric target deployed over the glacier moraine.	45
3.2	Barplot of reprojection RMSE computed on CPs for each photogrammetric model. Due to the technical problems that occurred in 2020 (see Sec. 3.2.3), the 2020 RMSE refers only to the survey of the lower part of the glacier, excluding the upper accumulation sector.	52
3.3	Orthophotos obtained from the photogrammetric model for each year. (a) 2015, (b) 2016, (c) 2017, (d) 2018, (e) 2019, (f) 2020, (g) 2021, (h) 2022, (i) 2023. Orthophotos are overlapped to the SwissTopo base map (source: SwissTopo www.geo.admin.ch). Refer to the Appendix A for a better visualization of the orthophotos.	53
3.4	(a) Time series of the velocity computed from the GNSS measurements of the targets deployed across the glacier. (b) Location of the targets in the last surveying year.	54
3.5	Surface velocity fields derived by DIC on pair of consecutive DSM between 2015 and 2018 and orthophotos between 2019 and 2023. (a) 2015-2016, (b) 2016-2017, (c) 2017-2018, (d) 2018-2019. All the surface velocity fields are overlapped to the 2009 orthophoto (De Gaetani et al., 2021) as reference. Refer to the Appendix B for better visualization of the orthophotos (continue on the next page).	56
3.5	Surface velocity fields derived by DIC on pair of consecutive DSM between 2015 and 2018 and orthophotos between 2019 and 2023. (e) 2019-2020, (f) 2020-2021, (g) 2021-2022, (h) 2022-2023. All the surface velocity fields are overlapped to the 2009 orthophoto (De Gaetani et al., 2021) as reference. Refer to the Appendix B for better visualization of the orthophotos (cont.).	57

3.6	(a) Time series of median annual velocities for each cluster derived from DIC. The solid lines represent the median velocity, while the light-colored bands indicate the interquartile range, visualizing velocity variability within each cluster. Cluster colors correspond to the spatial mapping in (b). Marker positions correspond to the year of the master image used in DIC processing (i.e., the first image of each pair). The velocity value obtained from 2017-2018 was excluded from the time series; (b) Location of clusters with homogeneous movement patterns.	58
3.7	Boxplots of the differences between the displacements computed by GNSS measurements and those obtained by DIC on DSMs (from 2015 to 2018) and orthophotos (from 2018 to 2023). The differences are grouped by the image source (orthophoto – <i>ort</i> – and DSM) and divided into the East and North components and the magnitude of the displacement vectors.	59
3.8	Yearly volume variation computed as the difference between DSM of consecutive years. The error bars represent the uncertainty of each value.	60
3.9	(a) Elevation profiles obtained from the DSM computed for the years 2015-2023 along four different cross-sections. (b) Location of cross-sections. Cross-sections are viewed from south to north.	61
3.10	Longitudinal profiles of the glacier extracted each year along the centerline. The location of the profile is marked in Fig. 3.9b.	62
3.11	(a) Cumulative volumes variations Belvedere Glacier (1977-2023) with 1977 as the reference year (b) Cumulative ice mass variations (in megatonnes), assuming an ice density of $(850 \pm 60) \text{ kg m}^{-3}$, considering periods longer than 5 years (Huss, 2013).	63
3.12	(a) Web platform based on Potree (Schütz et al., 2016) for exploring the photogrammetric point clouds of the Belvedere Glacier acquired during the different surveys. (b) Example of two cross sections extracted directly from the Potree web interface from the point clouds of 2023 and 2015 to easily estimate the glacier thinning.	66
3.13	ERD diagram of the PostgreSQL database used for storing the Belvedere results.	67
3.14	Example of georeferenced layer queries from the PostgreSQL database using QGIS. The layer symbology is directly stored within the database and is automatically loaded into the QGIS project upon layer loading.	68
4.1	Timeline development of detectors, descriptors, and matches from preliminary works, hand-crafted, machine-learning, and deep-learning local features (figure adapted from Remondino et al. (2022)).	76
4.2	Scheme of a single monitoring station's proposed acquisition system configuration. Arrows indicate the direction of signal initiation. Image adapted from Greig Sheridan's repository.	78
4.3	Prototyping stripboard on which are soldered the main components of the internal circuit: capacitors (1), voltage regulators (2), real-time clock with coin-cell battery (3), Arduino Pro Mini (4), optoisolators (5), and Raspberry Pi Zero W (6).	80

4.4	Final circuit version with the components soldered on a smaller PCB. The 4G hat for internet connection is attached to the Raspberry Pi.	80
4.5	Example of some of the pages of the web-based interface to remotely control the monitoring units.	82
4.6	Battery voltage and temperature of boards with and without the solar panel during a period of tests. Starting from a fully charged condition, the system was kept without the solar panel at around 2 °C for the first six days. After nine days, the battery was fully discharged, and the system was reconnected to the panel and exposed to solar radiation.	84
4.7	(a) Map of the Belvedere Glacier, with marked the location of the two cameras C1 and C2, the Automatic Weather Station (AWS) and the Zamboni Zappa Hut; (b) The area of study: the stereoscopic reconstruction is focused on the terminal ice cliff (dashed light blue line), while the monoscopic DIC processing from camera C2 image sequence is focused on the upper area of the north lobe (dashed green line).	85
4.8	(a) Picture of the monitoring unit prototype installed for tests at the Belvedere Glacier site. (b) Picture of the final camera installation installed on the streamwise right moraine.	87
4.9	Days with images acquired by the two cameras C1 and C2. Valid shots are represented with dark colors, while discarded days due to bad weather conditions are represented with light colors.	88
4.10	(a) UAV-A block and (b) UAV-B block processed with Agisoft Metashape. The flags represent the targets used either as GCPs in the BA or as CPs to evaluate the quality of the photogrammetric block.	89
4.11	General workflow with two parallel processing chains involving stereoscopic reconstruction of terminal ice cliff from stereo-pairs of images to derive ice volume losses at the glacier terminus and glacier retreat and monoscopic digital image correlation to derive surface velocities.	90
4.12	Example of template matching used to track GCPs on a monocular image sequence. The green square represents the template on the reference image that is searched in all the other images of the sequence. The red cross marks the estimated position of the center of the template in a new image.	92
4.13	Scheme of the stereoscopic workflow performed with ICEPy4D. At a generic epoch i , new features are extracted and matched. At the same time, features from the previous epoch $i - 1$ are tracked on the current epoch images. After geometric verification, features successfully matched are used for 3D scene reconstruction. Point clouds obtained on different days are used to compute ice volume differences and glacier retreat.	93

4.14	Scheme of feature tracking in stereo-cameras sequence. At each epoch, new features are matched on the stereo pair (horizontal lines), but also tracked from previous epochs (oblique lines). At epoch 0, the matches are only the corresponding features matched between current the stereo pair (red triangles). At epoch 1, the valid matches are the new corresponding features matched (green triangles) plus the successfully tracked features from epoch 0 (red triangles). The same holds for epoch 2, where the matches are the new corresponding features (yellow pentagons), plus the features tracked from both epoch 0 and 1.	95
4.15	Scheme of Dem of Difference (DOD) approach used to compute volume variations at the glacier terminal ice cliff. Two point clouds built at epoch i and $i+dt$ (we used $dt=5$ days to increase the signal-to-noise ratio), were rasterized to a vertical Y-Z planes, with normals parallel to the glacier flow direction (X direction). Before rasterization, the point clouds are clipped with the same convex polygon in the Y-Z plane (red line). The colors of the grids represent the depth of each cell of the two rasters along the X direction (i.e., the distance along X from a reference plane). Volume variation was computed by DOD of the two rasters along X.	97
4.16	Example of features successfully matched on the stereo-pair acquired on 27/09/2022.	101
4.17	(a) Number of valid matches extracted from the stereo pair at each epoch and number of points tracked from the previous epoch. (b) Average and standard deviation of the reprojection error obtained by projecting the 3D coordinates of the tie points to the images. The average reprojection error was computed as the mean reprojection error for all the point on the two images.	102
4.18	Series of the point clouds built at the beginning of each month from 01/05/22 to 01/11/22. The basemap is derived from a previous UAV survey carried out by the authors in July 2022	103
4.19	Vertical cross-sections extracted at the location marked in Fig. 4.18. All the cross-sections are extracted in a local reference system, with the X-direction pointing in the direction of the glacier flow, the Z-direction pointing upward, and the Y-direction completing the right-hand reference system. Please note the different scales of the figures, indicated by the scale bar (in meters).	104
4.20	(a) Daily ice volume lost at the glacier terminus, estimated by DOD of pairs of point clouds spaced by 5 days. (b) Cumulative curve of the ice volume loss during the study period.	105
4.21	(a) Location of the segmented ice cliff top edge at the beginning of each month from May to November 2022; (b) Estimation of daily retreat based on the displacement of the top edge along the flow direction (X-direction). The location of the ice cliff on 01/05/2022 is considered as a baseline for the retreat. The orange marker indicates the day of the UAV-A survey.	105

4.22	Comparison of the 28/07/22 stereo point cloud with the reference UAV point cloud acquired on the same day, computed with M ₃ C ₂ algorithm (Lague et al., 2013). The stereo-point cloud is represented by a color scale indicating the distances relative to the UAV point cloud (represented by a light gray color as a reference).	106
4.23	(a) DIC displacement map between 25 and 30 July 2022. (b) Orthorectified DIC displacement map between 25 and 30 July 2022. The triangles indicate the points P ₁ and P ₂ , where we extracted the velocity time series. (c, d) Glacier domains are characterized by specific morphology and kinematics.	107
4.24	Time series of displacement extracted in the terminal part of the glacier lobe. The red curves correspond to point P ₁ , located 10 m from the terminal ice cliff (considering the location of the terminal ice cliff on 28/07/2022), and the blue curves correspond to point P ₂ , located 120 m far from the ice cliff. The location of points P ₁ and P ₂ is marked in Fig. 4.23.	108
4.25	Uncertainty analysis of velocity vector orthorectification against possible DSM variation. Blue boxes represent the difference between the velocity vectors back-projected on the true DSM of 28/07/2022 and those back-projected on a simulated DSM advanced downstream by 12m (as it was in May 2022). Red boxes represent the difference between the true velocity vectors and those obtained with a simulated DSM with the glacier front retreating 5 meters upstream (as it was in November 2022). v_E , v_N , v_z , and v are respectively the three components in the east, north, and height directions and the magnitude of the differences of the velocity vectors.	109
4.26	Time series of the daily volume loss due to the glacier terminus retreat, compared to the time series of glacier surface velocity extracted by monoscopic DIC at the location of point P ₁ (located close to the ice cliff terminus and marked with an orange triangle in Fig. 4.23) and the 5-day smoothed time series air temperature measured by the AWS at the location marked in Fig. 4.7.	111
5.1	Scheme of the DIM workflow.	124
5.2	Scheme of the main different matching strategies implemented in DIM given an unordered image set (a). (b) Brute-force strategy (i.e., <i>all-to-all</i>); (c) Sequential strategy with overlap equal to 2 (i.e., match all images with next 3 images, note that the overlap parameter is zero-based); (d) Low-resolution guided matching strategy (i.e., perform a fast brute-force on low-resolution images and match only good candidates at high resolution).	126
5.3	Scheme of the DIM's cluster-based approach to estimate the best rotation of the images before performing the image matching.	129
5.4	Images of Dataset A - Winter. Images in the first row are taken by UAV, while those in the second row are acquired by terrestrial cameras.	132

5.5	Dense reconstructions of the northwest lobe of Belvedere Glacier using (a) Agisoft Metashape and (b) RoMa. The RoMa reconstruction was computed using camera poses estimated by DIM’s SuperPoint+LightGlue pipeline. Note the number of oriented images with the two different approaches, and the greater coverage of the snow-covered surface and the streamwise right moraine achieved by RoMa despite the lower overall point density (highlighted by the yellow circles).	134
5.6	Sample images Dataset B - Nadar	135
5.7	Results for Nadar dataset. (a) SIFT matches and (b) DISK matches on an image pair; (c) camera poses and (d) 3D tie points; (e-f) semi-dense point cloud generated from RoMA tie points; (g-h) textured mesh 3D model.	137
5.8	Sample images Dataset C - Castle. Images in the first row are samples of the nadiral and oblique UAV images, and images in the second row are samples of the terrestrial images, including some of the challenging underexposed or overexposed images.	138
5.9	Dataset C_GT, used as the ground truth to evaluate the results on Dataset C. The red flags are the targets used as GCPs, while the yellow ones are those used as CPs.	139
5.10	Example of matched features with the different approaches on a challenging image pair (green or blue lines are the valid matches, while the red dots are the rejected keypoints): (a) SuperPoint + LightGlue (658 valid matches); (b) COLMAP RootSIFT (49 valid matches); (c) Agisoft Metashape (1 valid match).	140
5.11	(a) Reconstructed sparse point cloud and oriented camera with SuperPoint + LightGlue after the bundle in COLMAP; (b) the same solution from Metashape, georeferenced with 4 GCPs (red flags), while all the other points are used as CPs (yellow flags)	141

List of Tables

2.1	Summary of camera and flight characteristics for the five datasets.	22
2.2	Summary of characteristics of the SfM-MVS point clouds (PCD) in terms of number of points and average volumetric density. The Data Density parameter refers to the rasterized point cloud, and it is defined as the ratio between the number of nonempty cells in the original and interpolated DSMs.	34
2.3	Minimum and Maximum Altitudes (a.s.l.) of the Glacier at Different Epochs	34
2.4	Glacier Volume Gain/Loss in the Four Considered Periods	36
3.1	Summary of the characteristics of the surveys.	46
3.2	Summary of the characteristics of the cameras employed.	46
4.1	Summary of the characteristics of the two cameras. Fields marked with * are computed considering the distance between each camera and the ice cliff.	86
4.2	Spearman correlation coefficients between original (ρ_S) and detrended ρ_D signals for the daily volume variation (dV), mean air temperature (T), and surface velocity of points $P1$ and $P2$ (v_{P1} and v_{P2} respectively). In all the cases, the p-value was $< 10^{-5}$	111
5.1	Summary of the Winter dataset results obtained with DIM compared to those obtained with COLMAP (with RootSIFT features) and Agisoft Metashape with its proprietary feature extractor and matches.	133
5.2	Summary of the Nadar dataset results obtained with DIM compared to those obtained with COLMAP (with RootSIFT features) and Agisoft Metashape with its proprietary feature extractor and matches. (*) The dataset has been oriented by combining different local features: SIFT, KeyNey + HardNet, ALIKED, SuperPoint, and DISK.	136
5.3	Summary of the Castle dataset results obtained with DIM, compared to those obtained with COLMAP (with RootSIFT features) and Agisoft Metashape with its proprietary feature extractor and matches. (*) As COLMAP produced two non-linked reconstructions, the reported results refer to the reconstruction with the highest number of oriented images.	139

Acronyms

AAT Assisted Aerial Triangulation

AWS Automatic Weather Station

BA Bundle Adjustment

BBA Bundle Block Adjustment

CEST Central European Summer Time

CNN Convolutional Neural Network

CP Check Point

DIC Digital Image Correlation

DIM Deep-Image-Matching

DL Deep Learning

DoD DEM of Difference

DSLR Digital Single-Lens Reflex

DSM Digital Surface Model

EO Exterior Orientation

GB-SAR Ground-based Synthetic Aperture Radar

GCP Ground Control Point

GNSS Global Navigation Satellite System

GSD Ground Sample Distance

GT Ground Truth

INS Inertial Navigation System

IO Interior Orientation

MAD Median Absolute Deviation

MVS Multi-View Stereo

nRTK Network Real Time Kinematic

PCD Point Cloud

SAR Synthetic Aperture Radar

SfM Structure-from-Motion

SIFT Scale Invariant Feature Transform

TLS Terrestrial Laser Scanners

TP Tie Point

UAV Uncrewed Aerial Vehicle

vCP Virtual Check Point

vGCP Virtual Ground Control Point

VHR Very High-Resolution

1

Introduction

THIS CHAPTER IS BASED ON:

- De Gaetani, C. I., Ioli, F., & Pinto, L. (2021). Aerial and UAV Images for Photogrammetric Analysis of Belvedere Glacier Evolution in the Period 1977–2019. *Remote Sensing*, 13(18), 3787. <https://doi.org/10.3390/rs13183787>
- Ioli, F., Bianchi, A., Cina, A., De Michele, C., Maschio, P., Passoni, D., & Pinto, L. (2022). Mid-Term Monitoring of Glacier's Variations with UAVs: The Example of the Belvedere Glacier. *Remote Sensing*, 14(1), 28. <https://doi.org/10.3390/rs14010028>
- Ioli, F., Dematteis, N., Giordan, D., Nex, F., Pinto, L. (2024). Deep Learning Low-cost Photogrammetry for 4D Short-term Glacier Dynamics Monitoring. *PFG*. <https://doi.org/10.1007/s41064-023-00272-w>

1.1 MOTIVATION AND RELEVANCE

Glaciers worldwide are experiencing profound transformations due to the ongoing climate crisis (Oerlemans, 2005), and their sensitivity to temperature fluctuations renders them powerful indicators of global climate change (Barry, 2006). Alpine glaciers in temperate zones are particularly susceptible to rising temperatures. The accelerated rate of glacial retreat underscores the necessity for comprehensive monitoring programs (Zemp et al., 2006, Sommer et al., 2020). Therefore, they are often considered as a proxy for climate change evaluation. Projections point out that the European Alps may lose more than 60% of ice volume by the end of the century under the RCP2.6 scenario, whereas a more significant amount of ice loss is expected under worse scenarios (Zekollari et al., 2019).

However, mountain glaciers are a critical component of the local economy regarding hydroelectric production, tourist activities, and freshwater supply (Barnett et al., 2005, Hock et al., 2005). Additionally, glacier melting and retreat are triggering several glaciological processes, e.g., ice break-off, glacier outburst, snow/ice avalanches, and gravitational slope stability processes, such as rockfalls and collapses, and debris flow, which can threaten the population infrastructure of the nearby urban areas (Kääb et al., 2004, Deline et al., 2015, Giordan et al., 2020).

In the European Alps, the number of mass movements and hazardous events in high-elevation environments has experienced an increase in the past decade due to climate change (Chiarello et al., 2023, Nigrelli et al., 2024). A relevant and tragic example was the collapse of a section of the Marmolada Glacier (Dolomites, Italy), which occurred on July 3, 2022, at 13:43:20 CEST¹. The collapse caused an ice avalanche that killed 11 mountaineers trying to reach the Marmolada summit and injured 7 (Olivieri and Bettanini, 2023, Bondesan and Francese, 2023). The collapse occurred on the northern slope of the glacier at an elevation of 3213 m a.s.l. and involved a volume of ~96 000 m³ (Olivieri and Bettanini, 2023). The detachment was caused by a failure along a median crevasse, partially filled by meltwater due to highly anomalous temperatures, that reached 10.7 °C at the time of the event. The sudden glacier collapse was probably induced by hydraulic jacking and pressure within a thin layer of basal till (Bondesan and Francese, 2023).

A significant example of an ice failure-related hazard that demands continuous monitoring is the Planpincieux Glacier on the Italian side of the Grandes Jorasses in the Mont Blanc massif. The Planpincieux Glacier is a polythermal hanging glacier noted for its significant break-off activity (Fig. 1.1). The terminus of the Montitaz lobe features a 20-meter-high ice cliff, from which ice chunks exceeding 50 000 m³ cubic

¹<https://www.theguardian.com/world/2022/jul/03/deaths-glacier-breaks-marmolada-mountain-italy>

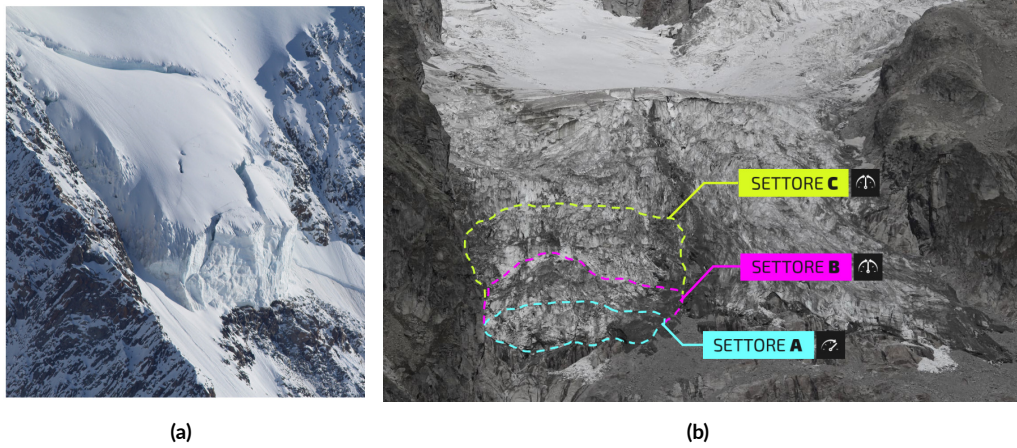


Figure 1.1: Images of the Planpincieux Glacier (Mont Blanc Massif). (a) Close-up photo of the Whymper Serac. The fracture fractures in the frontal part of the serac, from where several ice break-offs are triggered, are clearly visible (photo Fondazione Montagna Sicura, 2020, Chiarle et al. (2023)); (b) illustration of the Planpincieux Glacier with overlapped the area of three sectors identified by the permanent monitoring system based on their different kinematics properties (photo Fondazione Montagna Sicura, 2023, Giordan et al. (2020)).

meters frequently detach (Giordan et al., 2020). The most recent major break-off occurred during the night of May 31 to June 1, 1998, when nearly the entire Whymper glacier, approximately $\sim 150\,000\text{ m}^3$, broke off, triggering an ice avalanche that reached the valley floor, fortunately without causing any damage (Faijettaz et al., 2016, Chiarle et al., 2023). Additionally, this glacier was responsible for the deadliest ice failure event in the Italian Alps before the Marmolada tragedy: on August 2, 1993, an ice break-off exceeding $80\,000\text{ m}^3$ killed eight mountaineers ascending the normal route of the Grandes Jorasses from the Boccalatte Hut (Faijettaz et al., 2016, Chiarle et al., 2023). For this reason, the glacier has been monitored since 2013 using a visual-based system installed at 2305 meters elevation and 3800 meters from the glacier². This system, developed by the Research Institute for Geo-Hydrological Protection (IRPI) of the Italian National Research Council (CNR) and the Safe Mountain Foundation (FMS), consists of two consumer-grade cameras powered by solar panels and remotely controlled, capturing one image per hour (Dematteis et al., 2018, Giordan et al., 2020). Additionally, a Ground-based Synthetic Aperture Radar (GB-SAR) system captures images every 16 minutes, collecting over 2200 images during the study period, ensuring detailed monitoring of the glacier's movements (Dematteis et al., 2018).

Another significant slope instability process affecting an alpine glacier was the large debris flow that occurred on the Belvedere Glacier on August 27, 2023 (Anzasca Valley, Italian Alps)³. The debris flow

²<https://www.fondazionemontagnasicura.org/monitoraggio-planpincieux>

³<https://www.regenze.piemonte.it/web/temi/protezione-civile-difesa-suolo-opere-pubbliche/>



Figure 1.2: Impact of the August 27, 2023 debris flow on the Belvedere Glacier (Anscasca Valley, Italian Alps). **(a)** Aerial view acquired (August 30, 2023, author's photo) reveals the extent of debris accumulation within the Castelfranco gully and across the glacier's northern lobe; **(b)** Picture of the Belvedere Glacier northern lobe few hours after the debris flow event (August 28, 2023, 4:00 PM), captured by the fixed monitoring system. Note the muddy channels carved into the glacier's surface. These channels are remnants of the powerful flow that washed away much of the debris.

originated at the beginning of the steep Castelfranco gully, located at approximately 3600 m a.s.l. on the streamwise-left side of the Belvedere Glacier's northwest lobe (Fig. 1.2). During the event, a volume of $\sim 200\,000\text{ m}^3$ was accumulated on top of the Belvedere Glacier and obstructed the sinkhole that allowed the Castelfranco stream to flow below the ice sheet. This obstruction forced the water to flow over the glacier's surface, carving deep grooves into the ice (Fig. 1.2b). A substantial portion of the debris was transported towards the Macugnaga municipality by the river Anza. A similar but significantly smaller event occurred in 2008 and was documented by [Mortara and Tamburini \(2009\)](#), who estimated the debris volume to be a few thousand cubic meters. The 2023 debris flow profoundly impacted the glacier's dynamics, leading to the collapse of the central part of the terminal lobe surface and severe thinning over the following months. This was primarily due to the water flowing atop the glacier, which washed away the debris. This event underscores the importance of considering meteorological variables and other slope instability processes in studying glacier dynamics, as these factors can significantly influence glacier evolution.

In this context, systematically monitoring glaciers and related glaciological processes is crucial. To thoroughly understand these complex systems, accurate observations are essential ([Kääb et al., 2005](#)). A particular focus is usually placed on monitoring surface kinematics, as these can potentially offer early warning signs of impending instability or collapse events ([Faillettaz et al., 2015](#), [Giordan et al., 2020](#)).

Nevertheless, monitoring glaciers in remote areas and inaccessible terrains often presents logistical and safety challenges. Therefore, remote sensing techniques are widely used because they allow scientists and technicians to observe glacial processes with minimal risk.

1.2 REMOTE AND CLOSE-RANGE SENSING OF ALPINE GLACIERS

Remote sensing techniques have revolutionized the study and monitoring of mountain glaciers, providing invaluable insights into glacial processes and other natural phenomena in often inaccessible regions. These techniques can be classified based on the platform carrying the sensor, such as satellites, airplanes or helicopters, Uncrewed Aerial Vehicles (UAVs), and terrestrial systems, influencing the spatial and temporal resolution achievable, and the techniques employed to extract information from the data.

From the platform point of view, satellites have been central to glacier monitoring for several decades, offering the ability to survey large areas with various sensors, including optical sensors (Scherler et al., 2008, Dehecq et al., 2015, Winsvold et al., 2016, Rabatel et al., 2017), multispectral (Hall et al., 1995, Paul et al., 2004, Kargel et al., 2005), thermal infrared (Mihalcea et al., 2008, Shukla et al., 2010, Bhambri et al., 2011), Synthetic Aperture Radar (SAR) (Fang et al., 2016, Winsvold et al., 2018, Strozzi et al., 2020) and laser altimetry (Moholdt et al., 2010, Neckel et al., 2014). Optical and multispectral satellite imagery is widely used for various applications, including mapping glacier outlines (Paul et al., 2002, Winsvold et al., 2016), estimating glacier kinematics (Scherler et al., 2008, Dehecq et al., 2015), and assessing glacier mass balance (Bamber and Rivera, 2007, Berthier et al., 2016, Rabatel et al., 2017, Berthier et al., 2023).

The increasing availability of public and private satellite constellations has enabled access to high-resolution images with short revisit time, ranging from weekly to daily intervals. However, despite their utility for regional and global glacier monitoring, freely available satellite data often lack the spatial and temporal resolution required to monitor small alpine glaciers and their rapid changes, while recent commercial Very High-Resolution (VHR) satellite imageries are usually expansive and lack of long-term time series of images. Additionally, satellite imagery primarily provides 2D planimetric information, limiting the ability to generate 3D Digital Surface Models (DSMs) without multi-view acquisitions.

On a smaller spatial scale than the satellites, aircraft and helicopters can carry high-quality metric cameras for photogrammetric 3D reconstruction in remote mountain areas. This allows for achieving DSM at the decimeter to sub-meter resolution for middle to large-scale glaciers (Poli et al., 2020). While the cost of aerial photogrammetric flights remains a factor, the availability of regional mapping datasets presents a unique opportunity for long-term glacier monitoring, as historical aerial imagery allows for reconstructing glacier geometries far into the past, beyond the era of VHR satellites (De Gaetani et al., 2021).

In the past decade, UAVs have emerged as powerful and cost-effective tools for small to mid-scale mapping thanks to their minimal requirements and ability to access remote areas safely (Bhardwaj et al., 2016, Gaffey and Bhardwaj, 2020, Śledź et al., 2021). In the earliest, Whitehead et al. (2013), Immerzeel et al. (2014) and Kraaijenbrink et al. (2016) employed fixed-wing UAVs to generate orthophotos and DSMs and serving seasonal surface velocities. Afterward, UAV and photogrammetry have been used to map glacier extension (Belloni et al., 2023), derive glacier kinematics (Benoit et al., 2019, Chudley et al., 2019, Jouvet et al., 2020, Ioli et al., 2021, Cao et al., 2021, Lamsters et al., 2022), and estimate elevation changes and geodetic mass balance (Fugazza et al., 2018, Ioli et al., 2021, Van Tricht et al., 2021, Cao et al., 2021, Lamsters et al., 2022). Gindraux et al. (2017) investigated the impact of Ground Control Point (GCP) distribution on DSM accuracy, and she proposed a joint usage of DSMs and orthophotos to derive glacier kinematics.

Because of their flexibility, UAVs are particularly well suited for tracking glacier evolution at the decimeter or centimeter scale through seasonal or annual surveys over extended periods (Van Tricht et al., 2021, Cao et al., 2021, Ioli et al., 2021), as well as for capturing intra-seasonal dynamics through multiple surveys in a short time frame (Immerzeel et al., 2014, Chudley et al., 2019, Cao et al., 2021). However, they are unsuitable for continuous long-term monitoring due to the need for in situ intervention.

At the local scale, capturing short-term glacier dynamics at a high temporal frequency (e.g., daily) necessitates permanent in-situ monitoring systems. Low-cost time-lapse camera systems can provide daily observations for studying sub-seasonal glacier kinematics and responses to external factors within a warming climate (Maas et al., 2006, Messerli and Grinsted, 2015, Giordan et al., 2016, James et al., 2016). Recently, terrestrial SAR (Luzi et al., 2007) and permanent Terrestrial Laser Scanners (TLS) (Hendrickx et al., 2022, Voordendag et al., 2023) have gained attention for short-term monitoring and early warning systems implementation (Noferini et al., 2009, Dematteis et al., 2017). However, the high costs, complex logistics, and often site-specific focus of ground-based SAR and permanent TLS limit their widespread application for regional-scale monitoring.

From a technical perspective, monitoring glacier surface kinematics is crucial for understanding glacier dynamics and detecting early signs of instability (Falletta et al., 2015). Digital Image Correlation (DIC) is a powerful technique for this purpose, as it tracks distinctive pixel patterns across a series of images to measure their displacement and determine glacier flow velocity (Ahn and Box, 2010, Giordan et al., 2016, Hadhri et al., 2019). DIC works by dividing the reference image into small subsets, known as templates or interrogation windows, and then using cross-correlation techniques to identify the most similar region within a designated search area in subsequent images. This process, which can be performed in the spatial domain (Scambos et al., 1992) or frequency domain (Rølstad et al., 1997), effectively measures the move-

ment of tracked features on the glacier's surface. DIC can be applied to optical satellite imagery (Scherler et al., 2008, Heid and Kääb, 2012) or satellite SAR amplitude images for offset tracking (Schellenberger et al., 2015), high-resolution orthophotos from aerial or UAV photogrammetry (Immerzeel et al., 2014, Chudley et al., 2019, Cao et al., 2021), and terrestrial time-lapse cameras (Dematteis et al., 2024, Ioli et al., 2024).

Structure-from-Motion (SfM) (Westoby et al., 2012) and Multi-View Stereo (MVS) (Seitz et al., 2006) are widely used techniques for generating high-resolution DSMs and monitoring volume variations from pairs or multiple overlapping images. SfM-MVS photogrammetry involves reconstructing 3D models from unregistered, overlapping image sets. SfM specifically refers to the step in the workflow that estimates the camera's exterior (location and orientation) and interior parameters (mathematical models describing camera geometry, including lens distortions) (Brown, 1971). This step results in a sparse point cloud, representing the 3D coordinates of corresponding points detected in multiple images. MVS then builds on the SfM output to achieve dense 3D reconstruction, producing dense point clouds, orthophotos, DSMs, and triangulated mesh models. The combined process is often referred to as SfM-MVS. The principles and applications of SfM-MVS photogrammetry are extensively detailed in publications such as Westoby et al. (2012), James and Robson (2012), Eltner et al. (2016), Eltner and Sofia (2020).

SfM and MVS can be employed with aerial and UAV photogrammetric blocks (De Gaetani et al., 2021, Ioli et al., 2021), as well as in-situ stereo (Ioli et al., 2024) or multi-camera setups (Taylor et al., 2023), to create high-resolution 3D point clouds and orthophotos for reconstructing glacier 3D geometry and capturing detailed spatial and temporal changes in glacier dynamics. Similarly, these methods can be applied to stereo pairs or triplets from VHR satellites, such as WorldView, SPOT, Pleiades, and Pleiades Neo, to produce meter or sub-meter resolution DSMs (Rupnik et al., 2018, Perko et al., 2018, Giulio Tonolo et al., 2020).

1.3 THE BELVEDERE GLACIER

The Belvedere Glacier (Randolph Glacier Inventory code RGI60-11.02858) is an alpine glacier in the Anzasca Valley (Italy), on the east side of the Monte Rosa Massif ($N\ 45^{\circ}58' E\ 7^{\circ}55'$) (Fig. 1.3). The lower part of the Belvedere Glacier is a temperate debris-covered glacier that covers an area of $\sim 1.8\ km^2$ and extends from an altitude of $\sim 2250\ m\ a.s.l.$ to $\sim 1800\ m\ a.s.l..$ This region is characterized by a gentle slope, and it is fed by icefalls and snow avalanches coming from the Monte Rosa East Face (Haeberli et al., 2002). The Belvedere Glacier splits into two lobes in its low-relief sector, reaching $\sim 1800\ m\ a.s.l..$ The northern lobe, in particular, ends with a prominent ice cliff, from which the River Anza springs.

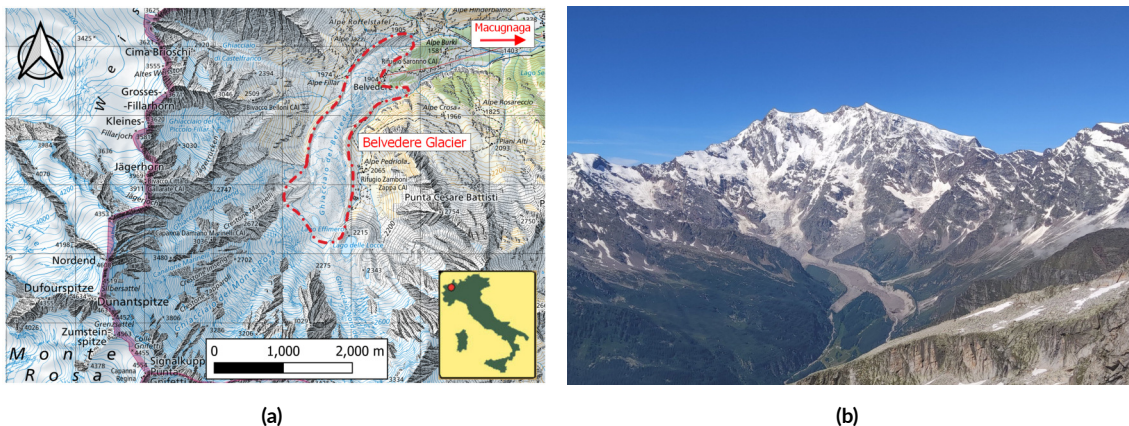


Figure 1.3: (a) Location of Belvedere Glacier, base map (source: Swisstopo www.geo.admin.ch); (b) Picture of the Belvedere Glacier taken from the nearby Monte Moro.

Similarly to Miage Glacier (Monte Bianco, Valle d'Aosta), the Belvedere Glacier is almost entirely covered by rocks and boulders with dimensions ranging from a few decimetres to some meters, which makes it a *black glacier*⁴. Due to the global warming trend, the number of black glaciers along the Italian Alps is rising (Diolaiuti et al., 2003). Up to the beginning of the century, the debris cover helped compensate for the increased temperature's effect, establishing a negative feedback in the temperature-ablation relationship (Roethlisberger et al., 1985, Diolaiuti et al., 2003). However, in recent years, the protection of debris cover has not been sufficient to limit the glacier retreat.

In the past, several hazardous events originated from the Belvedere Glacier, such as floods and slope instability, threatened the nearby village of Macugnaga and the Zamboni Zappa Hut at 2070 m a.s.l. (Kääb et al., 2004). At the beginning of the 21st century, the Belvedere Glacier was characterized by particular surge-type dynamics (Haeberli et al., 2002). During the late 1990s, the surface speeds of the whole glacier were ranging between 30 m y^{-1} and 45 m y^{-1} (Roethlisberger et al., 1985, Kääb et al., 2005). During 2000–2001, an accelerated flow in the Monte-Rosa Glacier produced a wave of compression-decompression stresses and strains in the Belvedere Glacier. Surface velocities soared: values up to 200 m y^{-1} were observed photogrammetrically during autumn 2001 (Kääb et al., 2004). The ice thickness increased more than 20 m, and the wave traveled downwards, creating a depression area in the accumulation zone that was filled by a super-glacial lake, the Lago Effimero (Haeberli et al., 2002, Mortara and Tamburini, 2009).

During spring 2002, the large depression at the foot of the Monte Rosa east face, caused by the surge-

⁴www.thebelvedereglacier.it



type movement, was temporarily filled by a lake with a volume of $3 \times 10^6 \text{ m}^3$, the so-called *Lago Effimero* (*short-lived lake*). Recognizing the potential danger of an outburst flood, the Italian Civil Defense Department rapidly implemented emergency measures, including evacuating parts of Macugnaga village, installing automatic alarm systems and pumps, and initiating detailed scientific investigations. Reduced meltwater input in July 2002, combined with natural subglacial drainage, stabilized and subsequently lowered the lake level. However, the lake reformed in the spring of 2003, bursting out in mid-June without causing significant damage (Kääb et al., 2004).

1.4 OBJECTIVES

This thesis explores the potential of multi-scale and multi-temporal photogrammetry for monitoring alpine glaciers, focusing on the debris-covered Belvedere Glacier in the Italian Alps.

This investigation integrates a spectrum of photogrammetric techniques. Firstly, historical aerial imagery analysis provides a long-term perspective on decades-long geomorphological changes at the meter scale. Secondly, in-situ UAV acquisitions enable annual reconstructions of glacier morphology, allowing for precise change analysis at a high spatial resolution. Finally, permanent in-situ monitoring using a low-cost stereo camera system allows for capturing the short-term dynamics of this rapidly changing environment.

This study uses archival aerial photogrammetry data collected by public agencies during mapping flights to investigate the glacier's long-term evolution. This technique allowed the reconstruction of past glacier morphology from 1977 to 2009, with approximately decadal intervals between models. The historical knowledge gained through this method is invaluable in documenting a natural heritage rapidly disappearing due to climate change. Of particular interest, archival photogrammetry reveals a significant period of glacier expansion in the early 21st century, allowing precise quantification of the increase in ice volume and glacier thickness.

This work integrates low-cost UAVs and GNSS for close-range photogrammetric monitoring to understand the glacier's current evolution. Annual in-situ surveys since 2015 provide a periodic and highly accurate record of the evolution. Through these UAV surveys, centimeter-scale resolution enables detailed mapping of the dynamic environment, including precise quantification of glacier volume loss and study of variations in glacier flow rate.

However, alpine glacier dynamics are inherently non-linear, with a pronounced acceleration of processes in summer compared to winter. This trend has intensified in recent years due to the increasing frequency of hot and dry summers associated with climate change. While annual high-precision in-situ

measurements provide essential insights into long-term geomorphological evolution, they lack the temporal resolution to fully capture the short-term kinematics of the glacier, which are crucial for understanding the relationship between glacier dynamics and external drivers such as air temperature. To address this need, a permanent monitoring system based on low-cost stereo cameras has been designed and installed on Belvedere Glacier. This system allows daily observations of glacier motion at a local spatial scale, providing the high-frequency data needed for in-depth kinematic analysis.

This thesis describes the technical design and implementation of a low-cost glacier monitoring system and the development of novel software tools for extracting relevant information from stereo camera images via photogrammetric processing. A new pipeline was designed and published to overcome the limitations of existing software in handling images with extremely wide baselines. This pipeline allows the analysis of time-series point clouds and the extraction of metrics such as velocity, volume variations, and displacement.

The harsh mountain environment was a significant challenge, which constrained the camera placement. This resulted in extremely wide baselines and significant viewpoint differences. These conditions made it difficult to find corresponding points using traditional local feature-matching techniques and hindered 3D reconstruction using existing commercial and open-source photogrammetric software. To overcome this obstacle, a novel pipeline was developed using state-of-the-art deep-learning algorithms for robust feature matching that successfully overcomes the limitations of wide baseline stereo image processing.

This thesis presents a successful pilot test of the low-cost glacier monitoring system. The current uses only two cameras installed at the northwest terminal lobe of the Belvedere glacier, focused on the terminal ice cliff, the portion of the glacier experiencing the most severe retreat and fast evolution. However, the system needs to be scaled up to achieve a more comprehensive and robust monitoring framework capable of capturing the glacier's entire dynamics. Expanding the camera network will increase the coverage and significantly improve the quality of daily 3D reconstructions through greater data redundancy. Motivated by this potential, the final part of this thesis focuses on developing a flexible multi-view library. This library enables image matching using state-of-the-art deep learning algorithms and traditional handcrafted features. Crucially, it integrates seamlessly with existing photogrammetric software for streamlined 3D reconstruction, thus supporting the monitoring system's future expansion.

1.5 THESIS OUTLINE

This thesis is introduced in **Chapter 1**. This chapter presents the motivation, the research problem, and the objectives of the thesis. It introduces the Belvedere Glacier as a primary case study. It presents an

overview of remote and close-range sensing techniques for alpine environments, focusing on image-based techniques for glacier monitoring at different spatial and temporal scales.

Chapter 2 analyzes the historical evolution of Belvedere Glacier (1977-2009) using archival aerial photogrammetry with sub-meter spatial resolution and decadal survey intervals.

Chapter 3 describes the annual UAV and GNSS survey methodology for contemporary monitoring of Belvedere Glacier (2015-2023). SfM-MVS techniques generate annual 3D models, orthophotos, and DSMs with decimeter resolution. Glaciological analysis reveals complex spatial and temporal patterns in surface velocities, volume variations, and thinning effects.

Chapter 4 presents a novel low-cost stereo camera system for daily monitoring of a section of Belvedere Glacier (May-November 2022). Deep learning algorithms overcome the challenges of large baselines, enabling accurate 3D reconstruction, surface velocity estimation, and quantification of ice loss with daily frequency.

Chapter 5 describes Deep-Image-Matching (DIM), a novel open-source toolkit for wide-baseline, multi-view image matching in complex scenarios. DIM's robustness, flexibility, and integration capabilities make it a powerful tool for expanding the use of deep learning in photogrammetry.

Chapter 6 synthesizes the key findings of the thesis, highlighting their significance within glaciological research and the broader context of climate change. It emphasizes the unique long-term insights gained for Belvedere Glacier and the transformative tools developed for broader glacier monitoring. The commitment to open science and data sharing encourages collaboration and future research.

References

- Ahn, Y. & Box, J. E. (2010). Glacier velocities from time-lapse photos: technique development and first results from the extreme ice survey (eis) in greenland. *J. Glaciol.*, 56(198), 723–734, <https://doi.org/10.3189/002214310793146313>.
- Bamber, J. L. & Rivera, A. (2007). A review of remote sensing methods for glacier mass balance determination. *Global and Planetary Change*, 59(1), 138–148, <https://doi.org/10.1016/j.gloplacha.2006.11.031>. Mass Balance of Andean Glaciers.
- Barnett, T. P., Adam, J. C., & Lettenmaier, D. P. (2005). Potential impacts of a warming climate on water availability in snow-dominated regions. *Nature*, 438, 303–309, <https://doi.org/10.1038/nature04141>.
- Barry, R. G. (2006). The status of research on glaciers and global glacier recession: a review. *Prog. Phys. Geog.: Earth and Environment*, 30(3), 285–306, <https://doi.org/10.1191/0309133306pp478ra>.
- Belloni, V., Rita, M. D., Fugazza, D., Traversa, G., Hanson, K., Diolaiuti, G., & Crespi, M. (2023). High-resolution high-accuracy orthophoto map and digital surface model of fornii glacier tongue (central italian alps) from uav photogrammetry. *Journal of Maps*, 19(1), 2217508, <https://doi.org/10.1080/17445647.2023.2217508>.
- Benoit, L., et al. (2019). A high-resolution image time series of the gorner glacier – swiss alps – derived from repeated unmanned aerial vehicle surveys. *Earth Syst. Sci. Data*, 11(2), 579–588, <https://doi.org/10.5194/essd-11-579-2019>.
- Berthier, E., Cabot, V., Vincent, C., & Six, D. (2016). Decadal region-wide and glacier-wide mass balances derived from multi-temporal aster satellite digital elevation models. validation over the mont-blanc area. *Frontiers in Earth Science*, 4, <https://doi.org/10.3389/feart.2016.00063>.
- Berthier, E., et al. (2023). Measuring glacier mass changes from space—a review. *Reports on Progress in Physics*, 86(3), 036801, <https://doi.org/10.1088/1361-6633/acaf8e>.
- Bhambri, R., Bolch, T., & Chaujar, R. (2011). Mapping of debris-covered glaciers in the Garhwal Himalayas using ASTER DEMs and thermal data. *International Journal of Remote Sensing*, 32(23), 8095–8119, <https://doi.org/10.1080/01431161.2010.532821>.
- Bhardwaj, A., Sam, L., Akanksha, Martín-Torres, F. J., & Kumar, R. (2016). UAVs as remote sensing platform in glaciology: Present applications and future prospects. *Remote Sens. Environ.*, 175, 196–204, <https://doi.org/10.1016/j.rse.2015.12.029>.
- Bondesan, A. & Francese, R. G. (2023). The climate-driven disaster of the marmolada glacier (italy). *Geomorphology*, 431, 108687, <https://doi.org/10.1016/j.geomorph.2023.108687>.
- Brown, C. D. (1971). Close-range camera calibration. *Photogramm. Eng*, 37(8), 855–866.

- Cao, B., Guan, W., Li, K., Pan, B., & Sun, X. (2021). High-resolution monitoring of glacier mass balance and dynamics with unmanned aerial vehicles on the ningchan no. 1 glacier in the qilian mountains, china. *Remote Sensing*, 13(14), <https://doi.org/10.3390/rs13142735>.
- Chiarle, M., Viani, C., Mortara, G., Deline, P., Tamburini, A., & Nigrelli, G. (2023). Large glacier failures in the Italian Alps over the last 90 years. *Geografia Fisica e Dinamica Quaternaria*, (45), 19–40, <https://doi.org/10.4461/GFDQ.2022.45.2>.
- Chudley, T. R., Christoffersen, P., Doyle, S. H., Abellan, A., & Snooke, N. (2019). High-accuracy UAV photogrammetry of ice sheet dynamics with no ground control. *Cryosphere*, 13(3), 955–968, <https://doi.org/10.5194/tc-13-955-2019>.
- De Gaetani, C. I., Ioli, F., & Pinto, L. (2021). Aerial and UAV Images for Photogrammetric Analysis of Belvedere Glacier Evolution in the Period 1977–2019. *Remote Sensing 2021, Vol. 13, Page 3787*, 13(18), 3787, <https://doi.org/10.3390/RS13183787>.
- Dehecq, A., Gourmelen, N., & Trouve, E. (2015). Deriving large-scale glacier velocities from a complete satellite archive: Application to the pamir–karakoram–himalaya. *Remote Sensing of Environment*, 162, 55–66, <https://doi.org/10.1016/j.rse.2015.01.031>.
- Deline, P., et al. (2015). Chapter 15 - ice loss and slope stability in high-mountain regions. In J. F. Shroder, W. Haeberli, & C. Whiteman (Eds.), *Snow and Ice-Related Hazards, Risks, and Disasters*, Hazards and Disasters Series (pp. 521–561). Boston: Academic Press.
- Dematteis, N., Giordan, D., Zucca, F., Luzi, G., & Allasia, P. (2018). 4d surface kinematics monitoring through terrestrial radar interferometry and image cross-correlation coupling. *Journal of Photogrammetry and Remote Sensing*, 142, 38–50, <https://doi.org/10.1016/j.jprs.2018.05.017>.
- Dematteis, N., Luzi, G., Giordan, D., Zucca, F., & Allasia, P. (2017). Monitoring alpine glacier surface deformations with gb-sar. *Remote Sensing Letters*, 8, 947–956, <https://doi.org/10.1080/2150704X.2017.1335905>.
- Dematteis, N., Troilo, F., Scotti, R., Colombaroli, D., Giordan, D., & Maggi, V. (2024). The use of terrestrial monoscopic time-lapse cameras for surveying glacier flow velocity. *Cold Reg. Sci. Technol.*, 222, 104185, <https://doi.org/10.1016/j.coldregions.2024.104185>.
- Diolaiuti, G., D'Agata, C., & Smiraglia, C. (2003). Belvedere Glacier, Monte Rosa, Italian Alps: Tongue Thickness and Volume Variations in the Second Half of the 20th Century. *Arctic, Antarctic, and Alpine Research*, 35(2), 255–263, [https://doi.org/10.1657/1523-0430\(2003\)035\[0255:BGMRIA\]2.0.CO;2](https://doi.org/10.1657/1523-0430(2003)035[0255:BGMRIA]2.0.CO;2).
- Eltner, A., Kaiser, A., Castillo, C., Rock, G., Neugirg, F., & Abellán, A. (2016). Image-based surface reconstruction in geomorphometry – merits, limits and developments. *Earth Surface Dynamics*, 4(2), 359–389, <https://doi.org/10.5194/esurf-4-359-2016>.
- Eltner, A. & Sofia, G. (2020). Chapter 1 - Structure from motion photogrammetric technique. volume 23 of *Remote Sensing of Geomorphology* (pp. 1–24). Elsevier.
- Faillettaz, J., Funk, M., & Vagliansindi, M. (2016). Time forecast of a break-off event from a hanging glacier. *The Cryosphere*, 10(3), 1191–1200, <https://doi.org/10.5194/tc-10-1191-2016>.

- Faillettaz, J., Funk, M., & Vincent, C. (2015). Avalanching glacier instabilities: Review on processes and early warning perspectives. *Reviews of Geophysics*, 53(2), 203–224, <https://doi.org/10.1002/2014RG000466>.
- Fang, L., Xu, Y., Yao, W., & Stilla, U. (2016). Estimation of glacier surface motion by robust phase correlation and point like features of SAR intensity images. *ISPRS J Photogramm*, 121, 92–112, <https://doi.org/10.1016/j.isprsjprs.2016.08.012>.
- Fugazza, D., et al. (2018). Combination of UAV and terrestrial photogrammetry to assess rapid glacier evolution and map glacier hazards. *Natural Hazards and Earth System Sciences*, 18(4), 1055–1071, <https://doi.org/10.5194/nhess-18-1055-2018>.
- Gaffey, C. & Bhardwaj, A. (2020). Applications of unmanned aerial vehicles in cryosphere: Latest advances and prospects. *Remote Sensing*, 12(6), <https://doi.org/10.3390/rs12060948>.
- Gindraux, S., Boesch, R., & Farinotti, D. (2017). Accuracy assessment of digital surface models from unmanned aerial vehicles' imagery on glaciers. *Remote Sensing*, 9(2).
- Giordan, D., Allasia, P., Dematteis, N., Dell'Anese, F., Vagliasindi, M., & Motta, E. (2016). A Low-Cost Optical Remote Sensing Application for Glacier Deformation Monitoring in an Alpine Environment. *Sensors*, 16(10), 1750, <https://doi.org/10.3390/s16101750>.
- Giordan, D., Dematteis, N., Allasia, P., & Motta, E. (2020). Classification and kinematics of the planpin-cieux glacier break-offs using photographic time-lapse analysis. *Journal of Glaciology*, 66(256), 188–202, <https://doi.org/10.1017/jog.2019.99>.
- Giulio Tonolo, F., Cina, A., Manzino, A., & Fronteddu, M. (2020). 3D glacier mapping by means of satellite stereo images: the Belvedere Glacier case study in the Italian Alps. *The International Archives of the Photogrammetry, Remote Sensing and Spatial Information Sciences, Volume XLIII-B2-2020*, <https://doi.org/10.5194/isprs-archives-XLIII-B2-2020-1073-2020>.
- Hadhri, H., Vernier, F., Atto, A. M., & Trouvé, E. (2019). Time-lapse optical flow regularization for geophysical complex phenomena monitoring. *J. Photogramm. Remote Sens.*, 150, 135–156, <https://doi.org/10.1016/j.jprs.2019.02.007>.
- Haeberli, W., et al. (2002). A surge-type movement at Ghiacciaio del Belvedere and a developing slope instability in the east face of Monte Rosa, Macugnaga, Italian Alps. *Norsk Geografisk Tidsskrift*, 56(2), 104–111, <https://doi.org/10.1080/002919502760056422>.
- Hall, D. K., Riggs, G. A., & Salomonson, V. V. (1995). Development of methods for mapping global snow cover using moderate resolution imaging spectroradiometer data. *Remote Sensing of Environment*, 54(2), 127–140, [https://doi.org/10.1016/0034-4257\(95\)00137-P](https://doi.org/10.1016/0034-4257(95)00137-P).
- Heid, T. & Kääb, A. (2012). Evaluation of existing image matching methods for deriving glacier surface displacements globally from optical satellite imagery. *Remote Sens. Environ.*, 118, 339–355, <https://doi.org/https://doi.org/10.1016/j.rse.2011.11.024>.
- Hendrickx, H., et al. (2022). Timing, volume and precursory indicators of rock- and cliff fall on a permafrost mountain ridge (Mattertal, Switzerland). *Earth Surf. Process. Landforms*, 47(6), 1532–1549, <https://doi.org/10.1002/esp.5333>.

- Hock, R., Jansson, P., & Braun, L. N. (2005). Modelling the response of mountain glacier discharge to climate warming. *Global change and mountain regions: An overview of current knowledge*, (pp. 243–252), https://doi.org/10.1007/1-4020-3508-x_25.
- Immerzeel, W. W., Kraaijenbrink, P. D., Shea, J., Shrestha, A. B., Pellicciotti, F., Bierkens, M. F., & de Jong, S. M. (2014). High-resolution monitoring of himalayan glacier dynamics using unmanned aerial vehicles. *Remote Sensing of Environment*, 150, 93–103.
- Ioli, F., Bianchi, A., Cina, A., De Michele, C., Maschio, P., Passoni, D., & Pinto, L. (2021). Mid-term monitoring of glacier's variations with uavs: The example of the belvedere glacier. *Remote Sens.*, 14(1), 28.
- Ioli, F., Dematteis, N., Giordan, D., Nex, F., & Pinto, L. (2024). Deep learning low-cost photogrammetry for 4d short-term glacier dynamics monitoring. *PFG-Journal of Photogrammetry, Remote Sensing and Geoinformation Science*, (pp. 1–22).
- James, M. R., How, P., & Wynn, P. M. (2016). Pointcatcher software: analysis of glacial time-lapse photography and integration with multitemporal digital elevation models. *J. of Glaciol.*, 62(231), 159–169, <https://doi.org/10.1017/jog.2016.27>.
- James, M. R. & Robson, S. (2012). Straightforward reconstruction of 3D surfaces and topography with a camera: Accuracy and geoscience application. *Journal of Geophysical Research: Earth Surface*, 117(F3), <https://doi.org/10.1029/2011JF002289>.
- Jouvet, G., van Dongen, E., Lüthi, M. P., & Vieli, A. (2020). In situ measurements of the ice flow motion at Eqip Sermia Glacier using a remotely controlled unmanned aerial vehicle (UAV). *Geosci. Instrum. Meth.*, 9(1), 1–10, <https://doi.org/10.5194/gi-9-1-2020>.
- Kääb, A., Huggel, C., Barbero, S., Chiarle, M., Cordola, M., Epifani, F., & Haeberli, W. (2004). Glacier Hazards At Belvedere Glacier and the Monte Rosa East Face , Italian Alps: Processes and Mitigation. *Inter nationales Symposion INTERPRAEVENT 2004 – RIVA / TRIENT*, (Vc), 67–78.
- Kääb, A., et al. (2005). Remote sensing of glacier-and permafrost-related hazards in high mountains: an overview. *Natural Hazards and Earth System Science*, 5(4), 527–554, <https://doi.org/10.5194/nhess-5-527-2005>.
- Kargel, J., et al. (2005). Multispectral imaging contributions to global land ice measurements from space. *Remote Sensing of Environment*, 99(1-2), 187–219.
- Kraaijenbrink, P., Meijer, S. W., Shea, J. M., Pellicciotti, F., De Jong, S. M., & Immerzeel, W. W. (2016). Seasonal surface velocities of a Himalayan glacier derived by automated correlation of unmanned aerial vehicle imagery. *Ann. Glaciol.*, 57(71), 103–113, <https://doi.org/10.3189/2016AoG71A072>.
- Lamsters, K., Ješkins, J., Sobota, I., Karušs, J., & Džeriňš, P. (2022). Surface characteristics, elevation change, and velocity of high-arctic valley glacier from repeated high-resolution uav photogrammetry. *Remote Sensing*, 14(4), <https://doi.org/10.3390/rs14041029>.
- Luzi, G., Pieraccini, M., Mecatti, D., Noferini, L., Macaluso, G., Tamburini, A., & Atzeni, C. (2007). Monitoring of an alpine glacier by means of ground-based SAR interferometry. *IEEE Geoscience and Remote Sensing Letters*, 4(3), 495–499, <https://doi.org/10.1109/LGRS.2007.898282>.

- Maas, H.-G., Dietrich, R., Schwalbe, E., Bäßler, M., & Westfeld, P. (2006). Analysis of the motion behaviour of Jakobshavn Isbræ glacier in Greenland by monocular image sequence analysis. *Int. Arch. Photogramm. Remote Sens. Spat. Inf. Sci. - ISPRS Arch.*, 36.
- Messerli, A. & Grinsted, A. (2015). Image georectification and feature tracking toolbox: ImGRAFT. *Geoscientific Instrumentation, Methods and Data Systems*, 4(1), 23–34, <https://doi.org/10.5194/gi-4-23-2015>.
- Mihalcea, C., et al. (2008). Spatial distribution of debris thickness and melting from remote-sensing and meteorological data, at debris-covered Baltoro glacier, Karakoram, Pakistan. *Annals of Glaciology*, 48, 49–57, <https://doi.org/10.3189/172756408784700680>.
- Moholdt, G., Nuth, C., Hagen, J., & Kohler, J. (2010). Recent elevation changes of Svalbard glaciers derived from ICESat laser altimetry. *Remote Sensing of Environment*, 114(11), 2756–2767, <https://doi.org/10.1016/j.rse.2010.06.008>.
- Mortara, G. & Tamburini (2009). *Il ghiacciaio del Belvedere e l'emergenza del Lago Effimero*. Societa' Meteorologica Subalpina.
- Neckel, N., Kropáček, J., Bolch, T., & Hochschild, V. (2014). Glacier mass changes on the Tibetan Plateau 2003–2009 derived from ICESat laser altimetry measurements. *Environmental Research Letters*, 9(1), <https://doi.org/10.1088/1748-9326/9/1/014009>.
- Nigrelli, G., et al. (2024). First national inventory of high-elevation mass movements in the Italian Alps. *Comput. Geosci.*, 184, 105520, <https://doi.org/10.1016/j.cageo.2024.105520>.
- Noferini, L., Mecatti, D., Macaluso, G., Pieraccini, M., & Atzeni, C. (2009). Monitoring of Belvedere Glacier using a wide angle GB-SAR interferometer. *Journal of Applied Geophysics*, 68(2), 289–293, <https://doi.org/10.1016/j.jappgeo.2009.02.004>.
- Oerlemans, J. (2005). Extracting a Climate Signal from 169 Glacier Records. *Science*, 308(5722), 675–677, <https://doi.org/10.1126/science.1107046>.
- Olivieri, L. & Bettanini, C. (2023). Preliminary observation of Marmolada glacier collapse of July 2022 with space-based cameras. *Remote Sensing Letters*, 14(1), 21–29, <https://doi.org/10.1080/2150704X.2022.2152754>.
- Paul, F., Huggel, C., & Kääb, A. (2004). Combining satellite multispectral image data and a digital elevation model for mapping debris-covered glaciers. *Remote Sensing of Environment*, 89(4), 510–518, <https://doi.org/10.1016/j.rse.2003.11.007>.
- Paul, F., Kääb, A., Maisch, M., Kellenberger, T., & Haeberli, W. (2002). The new remote-sensing-derived Swiss glacier inventory: I. methods. *Annals of Glaciology*, 34, 355–361, <https://doi.org/10.3189/172756402781817941>.
- Perko, R., Raggam, H., Schardt, M., & Roth, P. M. (2018). Very high resolution mapping with the Pléiades satellite constellation. *American Journal of Remote Sensing*, 6(2), 89–99, <https://doi.org/10.11648/j.ajrs.20180602.14>.
- Poli, D., Casarotto, C., Strudl, M., Bollmann, E., Moe, K., & Legat, K. (2020). Use of historical aerial images for 3d modelling of glaciers in the province of Trento. *The International Archives of the Photogrammetry, Remote Sensing and Spatial Information Sciences*, 43, 1151–1158, <https://doi.org/10.5194/isprs-archives-XLIII-B2-2020-1151-2020>.

- Rabatel, A., et al. (2017). Annual and seasonal glacier-wide surface mass balance quantified from changes in glacier surface state: A review on existing methods using optical satellite imagery. *Remote Sensing*, 9(5), <https://doi.org/10.3390/rs9050507>.
- Roethlisberger, H., Haeberli, W., Schmid, W., Biolzi, M., & Pika, J. (1985). Studi Sul Comportamento Del Ghiacciaio Del Belvedere. *Comunità montana della Valle Anzasca*, (97.3).
- Rolstad, C., Amlien, J., Hagen, J.-O., & Lundén, B. (1997). Visible and near-infrared digital images for determination of ice velocities and surface elevation during a surge on osbornebreen, a tidewater glacier in svalbard. *Annals of Glaciology*, 24, 255–261.
- Rupnik, E., Pierrot-Deseilligny, M., & Delorme, A. (2018). 3d reconstruction from multi-view vhr-satellite images in micmac. *ISPRS Journal of Photogrammetry and Remote Sensing*, 139, 201–211, <https://doi.org/https://doi.org/10.1016/j.isprsjprs.2018.03.016>.
- Scambos, T. A., Dutkiewicz, M. J., Wilson, J. C., & Bindschadler, R. A. (1992). Application of image cross-correlation to the measurement of glacier velocity using satellite image data. *Remote Sens. Environ.*, 42(3), 177–186, [https://doi.org/10.1016/0034-4257\(92\)90101-0](https://doi.org/10.1016/0034-4257(92)90101-0).
- Schellenberger, T., Dunse, T., Kääb, A., Kohler, J., & Reijmer, C. H. (2015). Surface speed and frontal ablation of kronebreen and kongsbreen, nw svalbard, from sar offset tracking. *The Cryosphere*, 9(6), 2339–2355, <https://doi.org/10.5194/tc-9-2339-2015>.
- Scherler, D., Leprince, S., & Strecker, M. R. (2008). Glacier-surface velocities in alpine terrain from optical satellite imagery—Accuracy improvement and quality assessment. *Remote Sensing of Environment*, 112(10), 3806–3819, <https://doi.org/10.1016/j.rse.2008.05.018>.
- Seitz, S. M., Curless, B., Diebel, J., Scharstein, D., & Szeliski, R. (2006). A comparison and evaluation of multi-view stereo reconstruction algorithms. In *Proceedings of the IEEE Computer Society Conference on Computer Vision and Pattern Recognition*, volume 1 (pp. 519–526).
- Shukla, A., Arora, M., & Gupta, R. (2010). Synergistic approach for mapping debris-covered glaciers using optical-thermal remote sensing data with inputs from geomorphometric parameters. *Remote Sensing of Environment*, 114(7), 1378–1387, <https://doi.org/10.1016/j.rse.2010.01.015>.
- Sommer, C., Malz, P., Seehaus, T. C., Lippl, S., Zemp, M., & Braun, M. H. (2020). Rapid glacier retreat and downwasting throughout the European Alps in the early 21st century. *Nature Communications* 2020, 11(1), 1–10, <https://doi.org/10.1038/s41467-020-16818-0>.
- Strozzi, T., et al. (2020). Monitoring Rock Glacier Kinematics with Satellite Synthetic Aperture Radar. *Remote Sensing* 2020, Vol. 12, Page 559, 12(3), 559, <https://doi.org/10.3390/RS12030559>.
- Taylor, L. S., Quincey, D. J., & Smith, M. W. (2023). Evaluation of low-cost raspberry pi sensors for structure-from-motion reconstructions of glacier calving fronts. *Nat. Hazards Earth Sys.*, 23(1), 329–341, <https://doi.org/10.5194/nhess-23-329-2023>.
- Van Tricht, L., Huybrechts, P., Van Breedam, J., Vanhulle, A., Van Oost, K., & Zekollari, H. (2021). Estimating surface mass balance patterns from unoccupied aerial vehicle measurements in the ablation area of the morteratsch–pers glacier complex (switzerland). *The Cryosphere*, 15(9), 4445–4464, <https://doi.org/10.5194/tc-15-4445-2021>.

- Voordendag, A., Goger, B., Klug, C., Prinz, R., Rutzinger, M., Sauter, T., & Kaser, G. (2023). Uncertainty assessment of a permanent long-range terrestrial laser scanning system for the quantification of snow dynamics on hintereisferner (austria). *Frontiers in Earth Science*, 11, <https://doi.org/10.3389/feart.2023.1085416>.
- Westoby, M., Brasington, J., Glasser, N., Hambrey, M., & Reynolds, J. (2012). ‘structure-from-motion’ photogrammetry: A low-cost, effective tool for geoscience applications. *Geomorphology*, 179, 300–314, <https://doi.org/https://doi.org/10.1016/j.geomorph.2012.08.021>.
- Whitehead, K., Moorman, B. J., & Hugenholtz, C. H. (2013). Brief communication: Low-cost, on-demand aerial photogrammetry for glaciological measurement. *Cryosphere*, 7(6), 1879–1884, <https://doi.org/10.5194/tc-7-1879-2013>.
- Winsvold, S. H., Kääb, A., Nuth, C., Andreassen, L. M., van Pelt, W. J. J., & Schellenberger, T. (2018). Using sar satellite data time series for regional glacier mapping. *The Cryosphere*, 12(3), 867–890, <https://doi.org/10.5194/tc-12-867-2018>.
- Winsvold, S. H., Kääb, A., & Nuth, C. (2016). Regional glacier mapping using optical satellite data time series. *IEEE Journal of Selected Topics in Applied Earth Observations and Remote Sensing*, 9(8), 3698–3711, <https://doi.org/10.1109/JSTARS.2016.2527063>.
- Zekollari, H., Huss, M., & Farinotti, D. (2019). Modelling the future evolution of glaciers in the european alps under the euro-cordex rcm ensemble. *The Cryosphere*, 13(4), 1125–1146, <https://doi.org/10.5194/tc-13-1125-2019>.
- Zemp, M., Haeberli, W., Hoelzle, M., & Paul, F. (2006). Alpine glaciers to disappear within decades? *Geophys. Res. Lett.*, 33(13), <https://doi.org/10.1029/2006GL026319>.
- Śledź, S., Ewertowski, M. W., & Piekarczyk, J. (2021). Applications of unmanned aerial vehicle (uav) surveys and structure from motion photogrammetry in glacial and periglacial geomorphology. *Geomorphology*, 378, 107620, <https://doi.org/10.1016/j.geomorph.2021.107620>.

2

Back to the Past: Reconstructing Glacier Topography with Archival Aerial Images (1977-2009)

THIS CHAPTER IS BASED ON:

De Gaetani, C. I., Ioli, F., & Pinto, L. (2021). Aerial and UAV Images for Photogrammetric Analysis of Belvedere Glacier Evolution in the Period 1977–2019. *Remote Sensing*, 13(18), 3787. <https://doi.org/10.3390/rs13183787>

2.1 INTRODUCTION

To understand the long-term dynamics of an alpine glacier, gathering information from the past becomes mandatory. Geomorphological studies benefit from three-dimensional topographic representations, which accurately describe the topography surfaces and quantify their variation over time (Chandler and Brunsden, 1995). Traditionally, image datasets acquired by metric cameras mounted onboard planes have been used to build maps through analytical stereo plotters and traditional photogrammetric techniques. Image orientation experienced improvements with the incorporation of GNSS/INS sensors for precise camera positioning and orientation (Forlani and Pinto, 2001, Jacobsen, 2004).

The emergence of digital photogrammetry in the late 1990s and the advent of automated methods for finding homologous points between images catalyzed a shift towards automated processing of extensive image collections. Since then, photogrammetry has become a widely used, cost- and time-effective approach for geoscience research (Lane et al., 2000). This transformation, coupled with the development of SfM/MVS algorithms and the availability of affordable digital cameras, has established photogrammetry as an indispensable technique for geomorphological research and glacier monitoring.

Despite millions of analog photographs documenting land surface change taken in the past century being available in historical archives, only a tiny fraction of these photographs have been digitally scanned and can be used with modern photogrammetric techniques. Scanned historical aerial image archives allow for *going back in time* and derive accurate historical DSMs and orthophotos for long-term measurements of surface change (Micheletti et al., 2015).

Examples of applications of historical archive photogrammetry for documenting geomorphological processes include fluvial geomorphology (Bakker and Lane, 2017, Lane et al., 2010), gravitational mass movement processes (Chandler and Brunsden, 1995, Walstra et al., 2007, Schwab et al., 2008), mapping and land cover estimation (Giordano et al., 2018) and permafrost and glacial processes (Kääb, 2002, Kauffmann and Ladstädter, 2003, Keutterling and Thomas, 2006, Borgogno Mondino and Chiabrando, 2008, Fischer et al., 2011).

Recently, several modern photogrammetric software packages, including Agisoft Metashape¹, Pix4DMapper², ERDAS IMAGINE³, MicMac (Rupnik et al., 2017, Zhang et al., 2021) together with a recent sPyMicMac addition (McNabb et al., 2020) and NASA AMES Stereo Pipeline (Beyer et al., 2018), have implemented support for processing archival images with fiducial marks defining the

¹<https://www.agisoft.com/>

²<https://www.pix4d.com/product/pix4dmapper-photogrammetry-software/>

³<https://hexagon.com/products/imagine-photogrammetry>

camera interior orientation. Moreover, the Swiss Federal Office of Topography SwissTopo has recently digitalized, cataloged, and published a large collection of grayscale and color historical aerial images on their website (Heisig and Simmen, 2021), representing a virtuosus example of promoting open data practices. In this context, several authors employed modern photogrammetric techniques with historical archive images for reconstructing glaciers' 3D topography in the past, including glaciers in Antarctica (Child et al., 2021, Dahle et al., 2024), North America (Knuth et al., 2023) and in the Alpine region (Mölg and Bolch, 2017, Poli et al., 2020).

This chapter aims to reconstruct the long-term evolution of the Belvedere Glacier between 1977 and 2019 by utilizing historical archival images and modern digital photogrammetry. To this end, three archival datasets captured by analog metric cameras in 1977, 1991, and 2001 were combined with data from a more recent aerial survey (2009) and a UAV flight (2019). These surveys are distributed across the timeline with a relatively consistent interval of approximately ten years, allowing us to track the glacier's morphological evolution and quantify volumetric changes.

Notably, the 2001 dataset captured the 3D topography of the Belvedere Glacier during a peculiar surge-type event (Haeberli et al., 2002) occurred between 2000 and 2002 (see Sec. 1.3 for more details). This event marked the glacier's maximum extension since the Little Ice Age, and its resulting moraines remain visible today. Consequently, analyzing the Belvedere Glacier's long-term evolution since 1977 enables us to quantify the progression of a glacier that underwent a rapid expansion followed by a critical regression and thinning. This process continues to this day.

2.2 DATASETS

The study utilized data from five photogrammetric surveys conducted between 1977 and 2019. The earlier datasets, referred to as *historical* datasets, were conducted in September 1977, August 1991, and September 2001. These surveys involved the acquisition of images for regional mapping purposes by the Italian company CGR S.p.A. (Compagnia Generale Riprese Aeree S.p.A.) using analog photogrammetric cameras mounted on planes. The images were cataloged, and their metadata were organized in the SITAD (Sistema Informativo Territoriale Ambientale Diffuso) database (Cipriano, 2005), now integrated with the GeoPortale Piemonte⁴. CGR S.p.A. digitized the images of the Belvedere Glacier and provided them to the authors upon request. The analog films were digitized using a photogrammetric scanner with a resolution of $21 \mu\text{m px}^{-1}$. The 2009 dataset was acquired with a digital photogrammetric camera by CGR S.p.A. for mapping purposes and was made available to the authors upon request. The authors directly

⁴<https://www.geoportale.piemonte.it/>

Table 2.1: Summary of camera and flight characteristics for the five datasets.

Year	Camera	Support/sensor	Lens	Focal length (mm)	Pixel size (μm^2)
1977	Wild RC ₁₀	230 × 230 mm film	15 UAG I	153.260	21 × 21 ¹
1991	Wild RC ₂₀	230 × 230 mm film	15/4 UAGA-F	152.820	21 × 21 ¹
2001	Wild RC ₃₀	230 × 230 mm film	15/4 UAG-S	153.928	21 × 21 ¹
2009	Z/I-Imaging DMC	CCD sensor	4 × f = 120 mm/f:4.0 integrated	120.000	12 × 12
2019	Hawkeye Firefly 8S	1/2.3" CMOS sensor	-	3.8	1.34 × 1.34

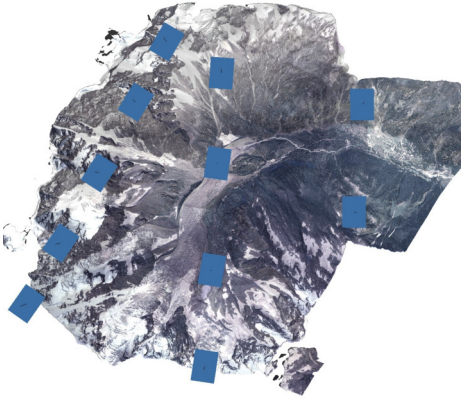
Year	Avg flight h a.g.l. (m)	Avg image scale	Avg GSD (m)
1977	3600	1:23,000	0.50 ¹
1991	6400	1:42,000	0.90 ¹
2001	3500	1:23,000	0.50 ¹
2009	3800	1:32,000	0.40
2019	120	1:32,000	0.05

¹ Pixel size and GSD of the analog images refer to those of the digitalized images.

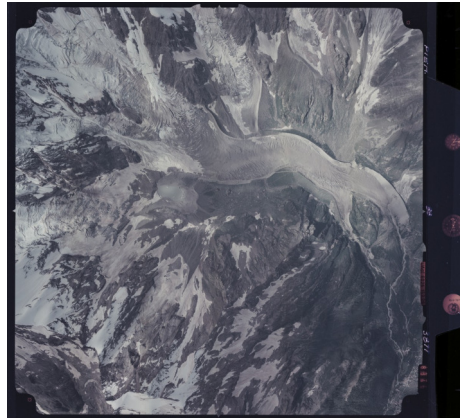
acquired the most recent dataset from 2019 using a fixed-wing UAV with a small and lightweight action camera mounted on board. A summary of the characteristics of the cameras and flights for each of the five datasets is presented in Tab. 2.1.

2.2.1 HISTORICAL AERIAL DATASETS OF 1977, 1991 AND 2001

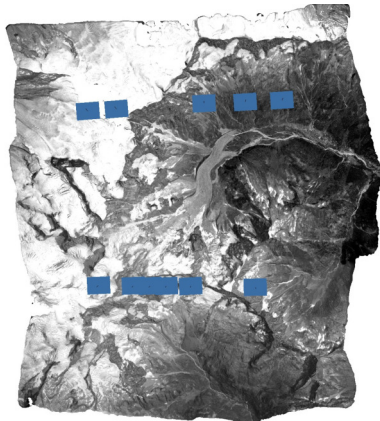
The earliest dataset considered in the study was acquired by CGR S.p.A. on 16/09/1977 with an analog photogrammetric camera Wild RC₁₀, equipped with a 15 UAG I lens with a focal length of 153.26 mm. The flight consisted of three stripes performed at an average altitude of 5600 m a.s.l., with approximately 60% along-flight overlap and transversal overlap varying from 30% to 60% because the stripes were not parallel. A total of 11 RGB images were acquired (Fig. 2.1a). Considering the average altitude of the glacier of 2000 m a.s.l., the scale of the images was about 1:23,000, leading to an average Ground Sample Distance (GSD) of 0.5 m. The camera reference system was materialized on the film with four fiducial



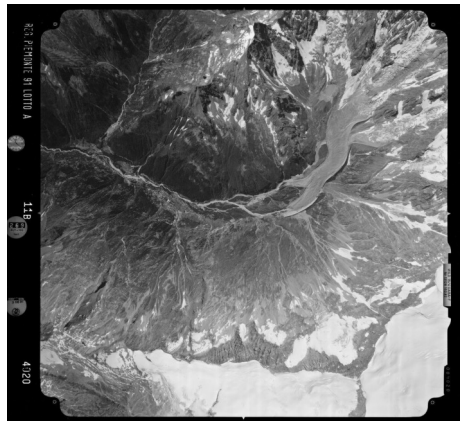
(a)



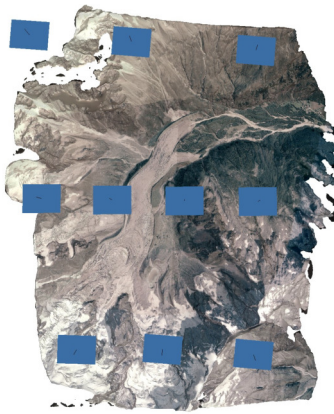
(b)



(c)



(d)



(e)



(f)

Figure 2.1: Historical datasets of a,b 1977, c,d 1991, e,f and 2001. A picture depicting the image acquisition geometry (left) and a sample of the scanned analog images (right) is presented for each dataset.

marks placed at the four corners of the image. As is visible in Fig. 2.1b, some of the fiducial marks were faded due to the aging of the films, but they were still identifiable in the digitalized images.

The 1991 survey was carried out on two different days: 03/08/1991 and 07/08/1991. Eleven grayscale images were taken with an analog photogrammetric camera, a Wild RC20 equipped with a 15/4 UAGA F lens (focal length of 153.26 mm). The flight consisted of only two stripes (Fig. 2.1c), conducted at 8200 m a.s.l. and 8500 m a.s.l., leading to an average GSD for the images of about 0.9 m. The along-flight overlap was approximately between 70% and 80%, while the transversal overlap was about 50%. As in the images of 1977, four fiducial marks allowed for the definition of the camera reference system (Fig. 2.1d).

The most recent among the three historical datasets dates back to 2001. Images were acquired with a film camera Wild RC30 equipped with a 15/4 UAG-S lens (focal length of 153.928 mm). The flight consisted of three stripes acquired between 06/09/2001 and 11/09/2001, producing a total of ten RGB images with overlaps of 70% along flight and 50% in the transversal direction (Fig. 2.1e). The two external stripes were conducted at an altitude of about 6100 m a.s.l., while the central one was conducted at a lower altitude of about 4800 m a.s.l., for an average of 5800 m a.s.l.. The mean scale of the images was 1:23,000, producing a GSD of 0.5 m, comparable to that of the 1977 flight. The camera reference frame was materialized by eight fiducial marks, well identifiable on the digitalized images (Fig. 2.1b).

Historical aerial images were digitalized using a photogrammetric scanner PhotoScan2000, developed by Z/I Imaging and Carl Zeiss, capable of scanning analog film rolls. The images were digitalized by CGR S.p.A. with a resolution of 21 $\mu\text{m}/\text{px}$, producing eight-bit TIF images with dimensions of 12 098 px \times 11 144 px. To assess the quality of the digitalized images, the actual pixel size was computed as the average ratio of the distance (in millimeters) between the fiducial marks with the corresponding distance in pixels. The estimated pixel size was 21 $\mu\text{m} \times 21 \mu\text{m}$ for each dataset, with a standard deviation of about three orders of magnitude less, in agreement with the technical scanner specifications.

2.2.2 DIGITAL AERIAL DATASET OF 2009

In October 2009, CGR S.p.A. flew over Belvedere Glacier for mapping purposes. This time, a digital photogrammetric camera was employed. A Z/I-Imaging DMC camera equipped with a 120 mm focal length lens and a CCD sensor with a pixel size of 12 $\mu\text{m} \times 12 \mu\text{m}$, acquiring RGB digital images at a resolution of 7680 \times 13,824 pixels, was mounted on an airplane. Eleven images with along-flight and transversal overlaps of 70% and 50%, respectively, were gathered along two stripes with altitudes between 5600 and 6000 m a.s.l (Fig. 2.2a-b). The average image scale was 1:32,000, and the GSD was 0.4 m.

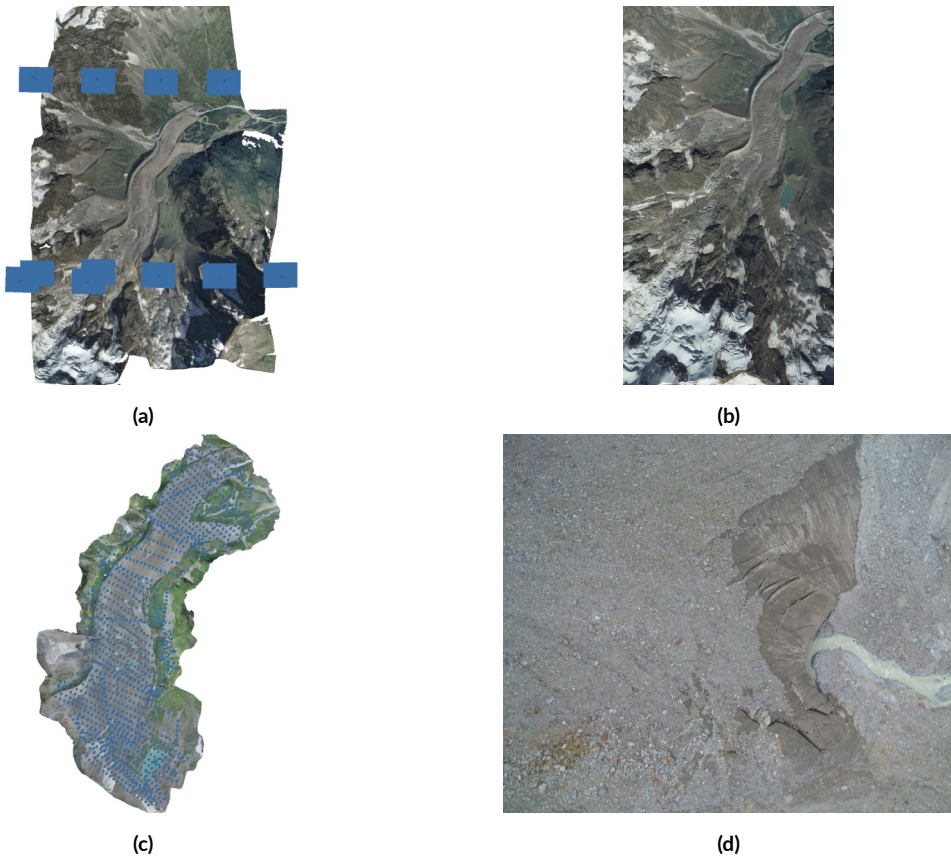


Figure 2.2: Digital datasets of **a,b** 2009 (aerial), **c,d** 2019 (UAV). For each dataset, a picture depicting the image acquisition geometry (left) and a sample image (right) is presented.

2.2.3 DIGITAL UAV DATASET OF 2019

The authors gathered images from the latest dataset during fieldwork on the Belvedere Glacier between 29/07/2019 and 02/08/2019 ([Ioli et al., 2022](#)). A fixed-wing UAV Parrot Disco was adapted to carry a low-cost and lightweight action camera, a HawkEye Firefly 8S. The action camera was equipped with a 12 Mpx 1/2.3" CMOS sensor, with a pixel size of $1.34 \mu\text{m} \times 1.34 \mu\text{m}$ and a focal length of 3.8 mm (90° field of view). The flights were conducted at an average height of 120 m a.g.l. (above ground level), in agreement with Italian UAV regulations, and images were taken with longitudinal and transversal overlap of 80% and 60%, respectively (except for a small portion in the middle of the glacier with a slightly smaller transversal overlap of 50%; see Fig. 2.2c). Therefore, the average image scale was approximately 1:32,000, and the GSD was 5 cm, one order of magnitude smaller than the aerial datasets. Because of UAV technical

limitations, the survey area was restricted to the glacier body only, and five flights with the fixed-wing UAV were performed (Fig. 2.2c)

2.2.4 GNSS SURVEY FOR BLOCK GEOREFERENCING

To constrain the UAV photogrammetric block from 2019, 36 squared targets consisting of 50 cm × 50 cm polypropylene sheets with high color contrast were deployed over the survey area, anchored to large rocks on both the glacier and the moraines. Among the 36 targets, 26 were used as GCPs and 10 as Check Points Check Points (CPs). The targets were measured on the field with a dual frequency (L_1/L_2) geodetic quality GNSS receiver Leica Viva GS14. Because a GSM internet connection was available in the lower part of the glacier, the targets were measured in Network Real Time Kinematic (nRTK) relative to the HxGN SmartNet network of permanent stations. All the points measured in nRTK were occupied for 10 s with a 1 Hz acquisition rate. In the upper part of the glacier, where nRTK was not possible, the targets were measured by static positioning. For each of those points, carrier-phase raw observations were logged for a timespan of ~10 min (1 Hz sampling rate). These were postprocessed relative to a local master station (Leica GPS1200) placed over a target next to the Zamboni-Zappa hut (2070 m a.s.l.). Coordinates of the master station were repeatedly measured in different years, with both static and nRTK measurements, and accuracy on the order of 0.5 cm in planimetry and 2 cm in height was obtained. GNSS observations were post-processed with Leica Infinity software (version 3.2.0) in the official Italian reference system ETRF2000 at epoch 2008.0. The resulting accuracies of the GCPs' coordinates were 1.5 cm in planimetry and 3 cm in height in terms of average RMSE.

2.3 METHODOLOGY

2.3.1 SFM-MVS

The photogrammetric blocks were processed with the commercial software package Agisoft Metashape (version 1.7.2), which allows for image orientation and model reconstruction with digital cameras and scanned films with fiducial marks. Fig. 2.3 summarizes the workflow to orient the five photogrammetric blocks.

Concerning the most recent UAV survey from 2019, the 1486 images were oriented by traditional aerial triangulation based on the 26 targets spread over the survey area (see Sec. 2.2.4) used as GCPs in the Bundle Block Adjustment (BBA). The location of the GCPs is presented in Fig. 2.4. The targets were manually collimated on the images. A 1 px collimation accuracy was assumed as the a priori standard deviation

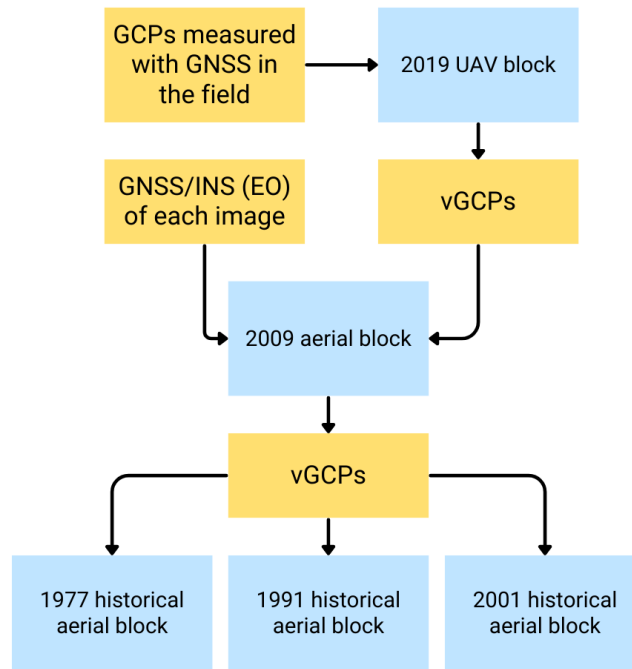


Figure 2.3: Workflow for image orientation of the five photogrammetric blocks. Virtual Ground Control Points (vGCPs) refer to GCPs extracted from a previous photogrammetric model by identifying characteristic features (either natural or artificial) that have remained unchanged over time across multiple images of the previous photogrammetric block. The 3D coordinates of the Virtual Ground Control Points (vGCPs) are obtained through forward triangulation of their image coordinates in 3D space.

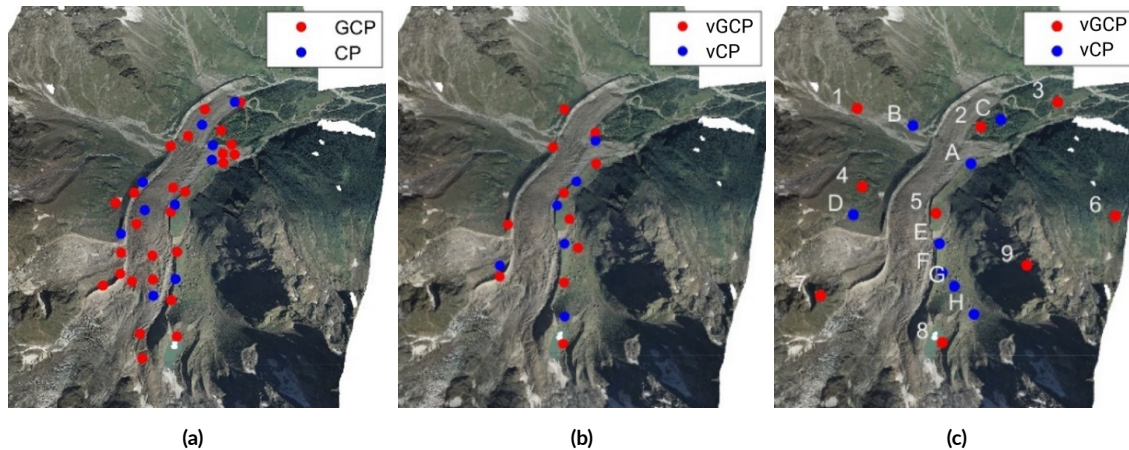


Figure 2.4: Sketches of the GCPs and CPs locations for the different photogrammetric block: (a) 2019 block; (b) 2009 block; (c) 1977, 1991 and 2001 block. For the 2009 block and the historical blocks, the points are vGCPs and vCPs.

of the observations because of the rather poor image quality derived from the low-cost action camera. Tie Points (TPs) were automatically detected and matched by Metashape on full-resolution images. Camera Interior Orientation (IO) parameters of the Hawkeye Firefly 8S action camera were estimated during the BBA by self-calibration. To this end, approximated IO parameters were pre-calibrated using a traditional checkerboard ([Zhang, 2000](#)). These initial values were adjusted for each flight because of the internal instability of the camera and thanks to the high density of the GCPs available.

Regarding the 2009 digital dataset, the Z/I-Imaging DMC system included high-precision GNSS/INS instrumentation, providing the camera Exterior Orientation (EO) ([Hinz et al., 2001](#)). The coordinates of the camera projection centers were provided with an accuracy of 30 cm, while the camera attitude angles had an accuracy of 8 mgon for roll and pitch angles and 10 mgon for yaw ([Forlani and Pinto, 2001](#)). To improve the quality of the photogrammetric block within a small area such as that of Belvedere Glacier, 11 features identifiable on the images (e.g., sharp rocks) were used as Virtual Ground Control Points (vGCPs). The 3D coordinates of vGCPs were estimated by forward triangulation from multiple collimations of the same point on different images of the 2019 UAV block, which has a significantly higher spatial resolution Tab. 2.1 than the aerial blocks. This procedure allows for estimating the triangulation error of the 3D point, which was considered as the uncertainty of the 3D coordinates for subsequent BBA in the 2009 block. EO of the images was estimated through Assisted Aerial Triangulation (AAT) ([Ioli et al., 2021](#)), as the BBA was solved by combining GNSS/INS information with TPs automatically detected by the software and the vGCPs manually collimated on the images. The quality of the photogrammetric model was finally assessed by employing 6 Virtual Check Points (vCPs), which were not used to solve the BBA.

The three historical aerial datasets were oriented by aerial triangulation based on the 2009 block. The coordinates of 9 vGCPs (marked with numbers 1 to 9 in Fig. 2.4c) and eight vCPs (marked with letters A to H), well distributed over the whole area, were retrieved from the 2009 aerial images. Points such as buildings edges, corners, sharp rocks along the glacier moraines, and particular morphological patterns that remained reasonably unchanged over time were selected in such a way as to be clearly identified in most of the four datasets (1977, 1991, 2001, and 2009), as shown in Fig. 2.5). Note that it was not always possible to identify the same point in all four datasets because of the different image scales, different image quality (e.g., RGB versus grayscale images), or changes in the morphology over 30 years. Therefore, if one point was not visible in one dataset, another was searched nearby. To clarify, if one point (e.g., Point 2) was not found in images from 1991, then another feature, named Point 2b, was searched for close to the original location of Point 2 in the 2009 images and used as GCP for the 1991 dataset. However, in the statistics, Points 2 and 2b were considered one point because of their spatial proximity. The vGCPs used

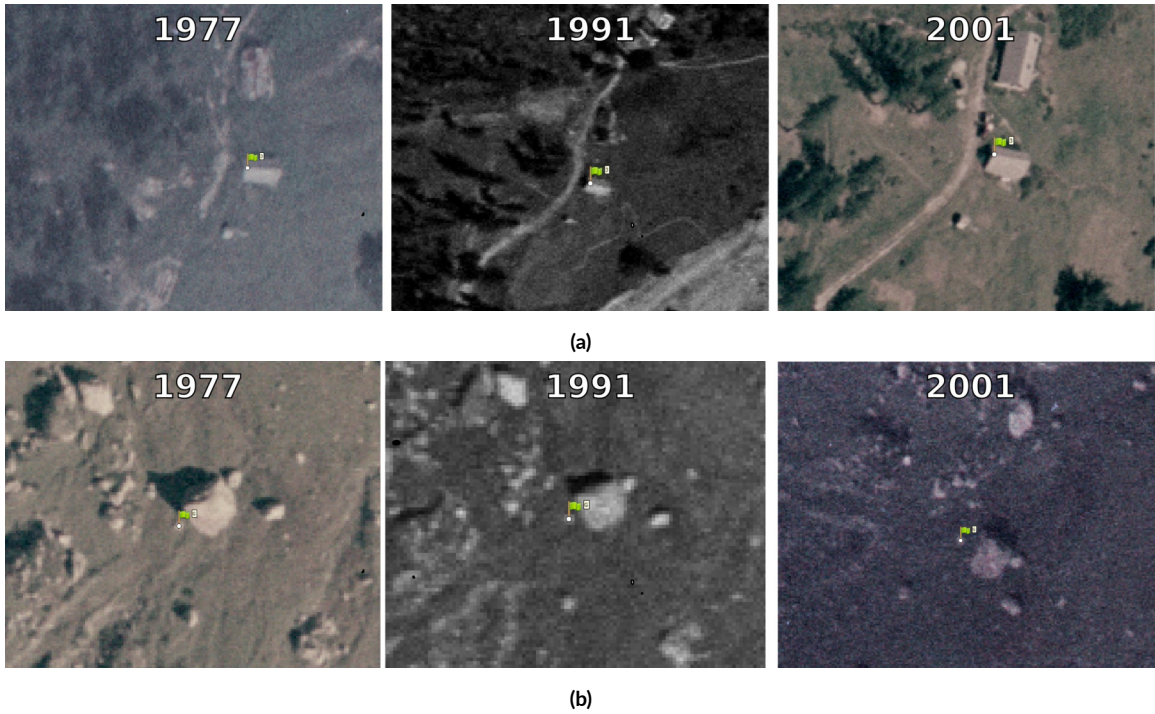


Figure 2.5: Examples of points chosen as vGCPs or vCPs: (a) artificial features in 1977, 1991, and 2001 aerial images; (d) natural features in 1977, 1991, and 2001 aerial images.

to solve the BBA of the three historical datasets were properly weighted with their variance, which was computed by forward triangulation in the 2009 photogrammetric block.

While using vGCPs to orient historical photogrammetric blocks does introduce a correlation between the models, causing error propagation from the more recent models to the older ones, this effect is partially mitigated by the increasing GSD from newer to older blocks. Specifically, the error in the vGCPs extracted from the UAV block is well below the GSD of the 2009 images. Similarly, the error in the vGCPs extracted from the 2009 model remains below the GSD of the older blocks. Even though the GSD of the 1977 and 2001 blocks are more comparable to the 2009 block, the significantly higher quality of the 2009 images reduces the impact of error propagation. Provided that the vGCPs were consistently weighted with their variances and no significant systematic errors (such as doming effects) were present in the models used to extract the vGCPs (which was verified by comparing DSMs on stable areas), we can assume that the effect of variance propagation from the more recent to the older models was limited and remained within the pixel level of the images.

Concerning the camera interior orientation, the three analog cameras were calibrated by the produc-

ers, and calibration certificates were available. Therefore, the calibrated focal length and the principal point coordinates were provided as initial values in the BBA. These were then adjusted based on the vgcp using a self-calibration procedure (Jacobsen, 2004). Additionally, two radial (k_1 and k_2) and tangential (p_1 and p_2) distortion parameters were estimated to correct the lens distortions of the photogrammetric cameras and, mostly, the distortion introduced by external factors, e.g., the deterioration of the films over the years or by the scanning procedure.

After BBA, dense Point Cloud (PCD), orthophotos, and DSMs were computed (a downscale factor of 2 was set to make the PCDs more manageable) and used as a starting point for glacier analyses.

2.3.2 POINT CLOUD PRE-PROCESSING

The obtained point clouds referring to the different surveys required additional preprocessing to make them consistent regarding spatial resolution and coverage area for further analyses. The point clouds were initially rasterized by using CloudCompare (v2.12 alpha). East–North gridded data with 0.5 m grid spacing were derived by averaging the height of the points inside each cell. Empty cells were initially filled with null values.

The rasterized DSM was then manipulated in the MATLAB (R2020a) environment. As the surveys' coverage areas are significantly different, the first step was automatically detecting the valid area for each photogrammetric DSM. This was done by first defining a binary mask with value 1 in correspondence with the DSM's non-null cells. The mask was then blurred by iterative convolutions with a circular kernel (10 m of radius), and unitary values were assigned to resulting cells with values greater than 0 until no voids were present in the inner area. A binary mask defining the valid surveyed area of each point cloud was obtained by applying the converse procedure (i.e., blurring with the same kernel and assigning 0 to the resulting cells with values smaller than 1) for the same number of iterations. Finally, empty cells of the initial rasterized DSM within the valid surveyed area were filled via triangulation-based bi-dimensional linear interpolation. As a result, rasterized point clouds at a consistent resolution of 0.5 m were obtained for all five surveys (Fig. 2.6).

A joint mask referring to the glacier body only and excluding surrounding areas was required to compare DSM from different surveys, which are now at a consistent spatial resolution. To this end, the five binary masks defining the valid areas of each survey were superimposed (Fig. 2.7a), and only fully overlapped cells were considered (Fig. 2.7b). A data-driven approach was pursued to identify the glacier body boundaries. In the surrounding areas, low or even null altitude variability over time was expected, while cells referring to the glacier body were expected to show detectable changes in altitude. Fig. 2.7c shows the

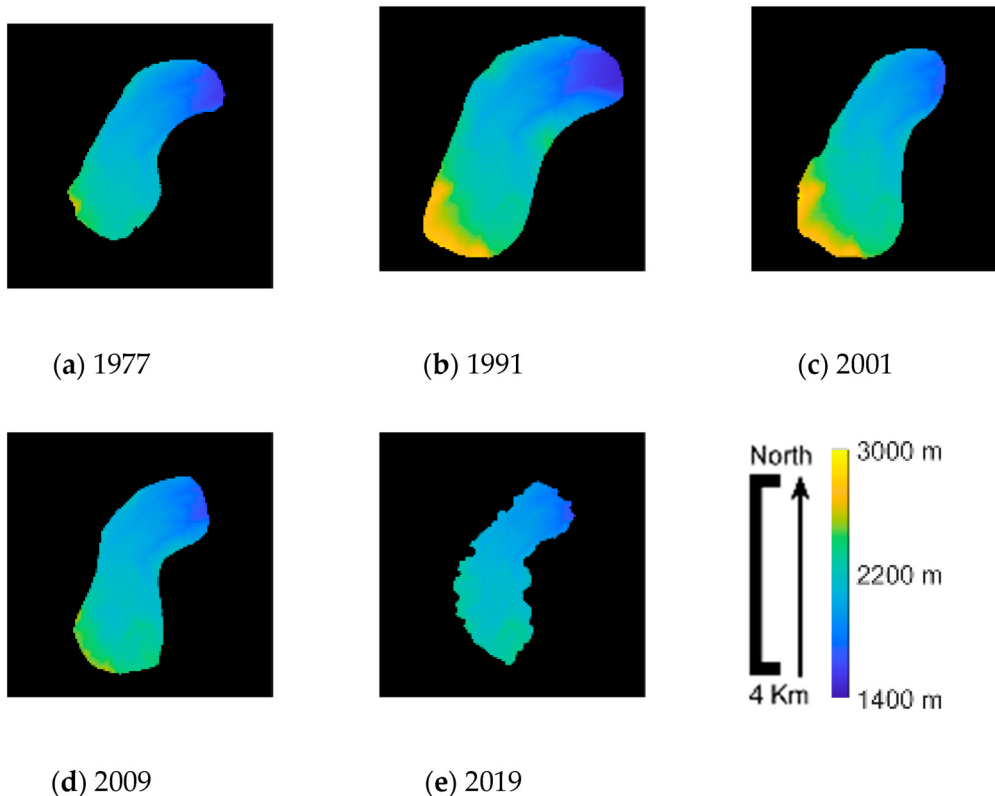


Figure 2.6: Interpolated gridded point clouds: (a) 1977; (b) 1991; (c) 2001; (d) 2009; (e) 2019.

binary mask representing the cells for which the height difference between consecutive survey epochs was larger than 10 m. The shape of the glacier's body is recognizable. This mask was then refined by applying the same iterative procedure previously presented for the valid area identification, which first removed isolated areas and cleaned glacier borders (Fig. 2.7d) and then applied a buffer around it also to comprise lateral moraines expected to remain almost unchanged over time (Fig. 2.7e). The obtained final glacier mask (now covering about a surface of 1.78 km^2) was then applied to the interpolated DSMs.

2.3.3 GLACIER EVOLUTION ANALYSIS

The final masked DSMs allowed spatial analyses of the glacier surface by comparing the measured altitude variations, quantifying volume variations, and evaluating the long-term morphology evolution from 1977 to 2019. First, the DSMs were analyzed in absolute terms. Additionally, relative comparisons were conducted to quantify the effects of accumulation and ablation processes on Belvedere Glacier over time.

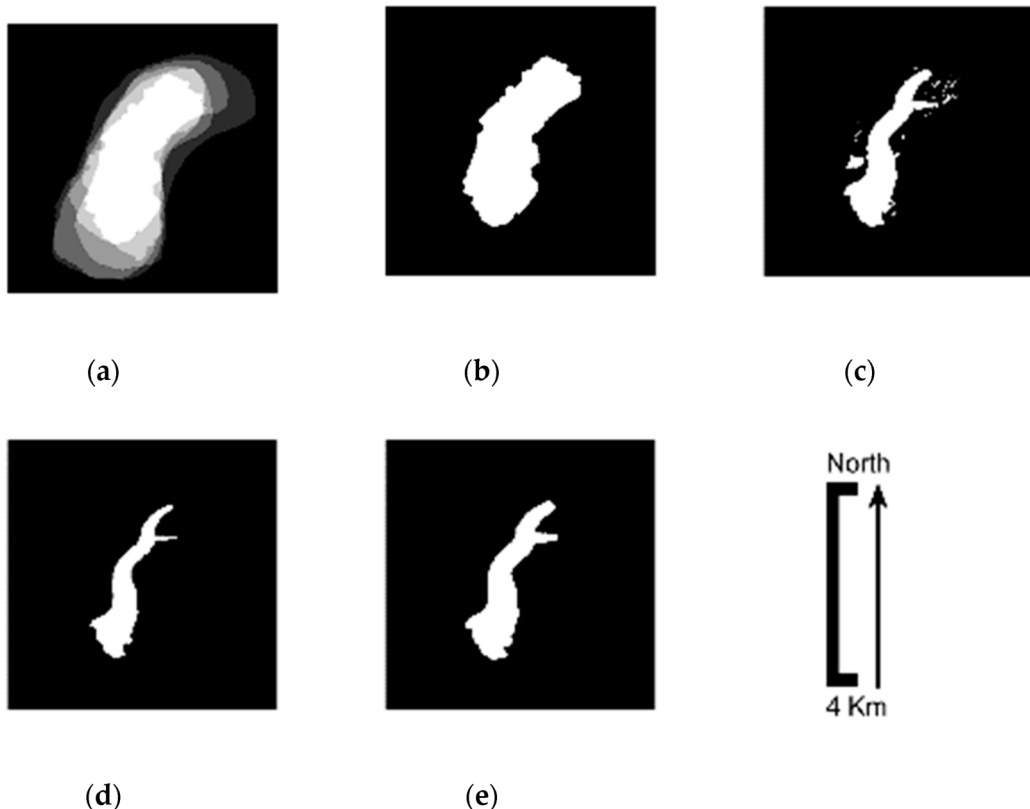


Figure 2.7: Steps for defining the final mask for defining the glacier boundaries: (a) binary mask defining the valid area of each survey overlapped; (b) common area between the masks; (c) high-variability area (i.e., areas for which the height difference between consecutive survey epochs was greater than 10 m); (d) filtered high-variability area; (e) buffered high-variability area, i.e., considered glacier shape.

As the different DSMs were georeferenced and consistent in spatial resolution, volume variations were computed by DEM of Difference (DoD). Cumulated volume variations were obtained, taking the 1977 DSM as a reference, while average annual volume losses/gains were obtained in the considered periods.

2.4 RESULTS

2.4.1 SFM-MVS

Eight vCPs distributed mainly along the glacier moraines were used to assess the accuracy of the three historical models, while six vCPs were used for the 2009 dataset. Fig. 2.8 reports the RMSEs computed on

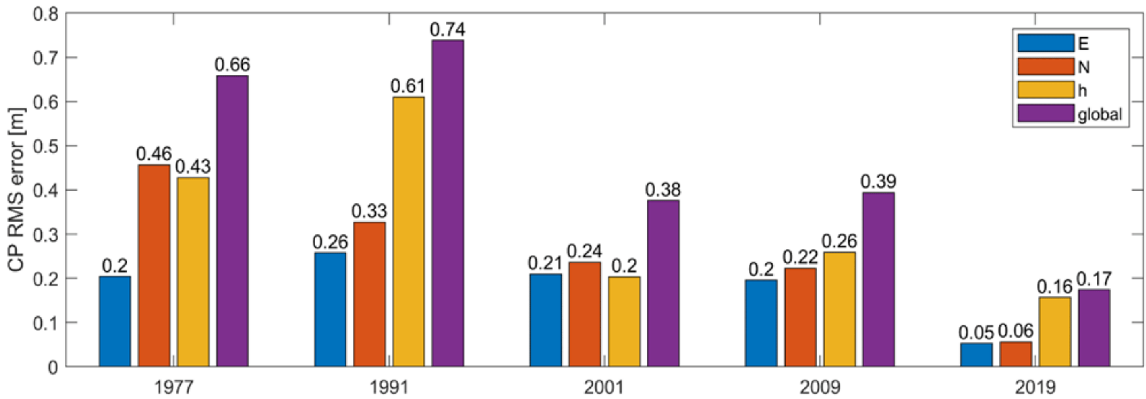


Figure 2.8: Model accuracy comparison in terms of RMS error on CPs.

the vCPs. The 1977 and 1991 models obtained global RMSEs of 0.66 m and 0.74 m, respectively, while the 2001 and 2009 models obtained similar RMSEs of approximately 0.4 m. In all cases, these values were comparable to the average GSD of the aerial images. Regarding the 2019 survey, the model accuracy was assessed by 10 CPs, resulting in an RMSE error of 0.17 m, comparable to three times the GSD. This was due to the low quality of the camera employed. Nevertheless, as the GSD was on the order of magnitude of the centimeter, the model accuracy was still higher than that of the older flights.

Starting from the solution obtained with the Agisoft Metashape SfM pipeline, an MVS approach was used to compute image depth maps, dense point clouds, orthophotos, and DSMs. The PCD number of points and the average volumetric density (i.e., the number of points per unit of volume) are summarized in Tab. 2.2. While the PCD size was strictly related to the survey coverage, the PCD average density was directly related to the GSD of the original photogrammetric survey, indicating the capability of resolving finer details.

Orthophotos and DSMs were computed with a GSD of 0.50 m for the historical datasets of 1977, 1991, and 2001, 0.40 m for the digital aerial dataset of 2009, and 0.20 m for the UAV dataset of 2019. The computed orthophotos are visible in Appendix A.

2.4.2 POINT CLOUD PRE-PROCESSING

According to the pre-processing described in Sec. 2.3.2, we computed the data density within the rasterized point clouds as the ratio between non-empty cells in the original and interpolated DSMs. Tab. 2.2 highlights the impact of grid spacing choice on point cloud gridding. For the most detailed 2019 survey, a 0.5 m grid spacing required minimal interpolation ($\sim 6\%$ empty cells), effectively fully exploiting its high spa-

Table 2.2: Summary of characteristics of the SfM-MVS point clouds (PCD) in terms of number of points and average volumetric density. The Data Density parameter refers to the rasterized point cloud, and it is defined as the ratio between the number of nonempty cells in the original and interpolated DSMs.

	1977	1991	2001	2009	2019
Points [#]	8,962,182	4,296,638	12,504,582	17,595,703	112,293,439
PCD density [pts/m ³]	1.56	1.08	1.58	2.67	26.40
Data density [cells/m ²]	37%	11%	39%	60%	94%

Table 2.3: Minimum and Maximum Altitudes (a.s.l.) of the Glacier at Different Epochs

Epoch	1977	1991	2001	2009	2019
Min Altitude (m)	1820.72	1823.60	1824.44	1826.23	1825.64
Max Altitude (m)	2381.11	2385.07	2350.37	2339.43	2349.36

tial resolution. Finer grids would increase interpolation and computational demands without significant informational gain, especially for the lower-resolution historical surveys. Conversely, coarser grids would risk losing detail in more recent, high-resolution data. Thus, the chosen 0.5 m grid spacing minimized interpolation while preserving the full potential of higher-resolution surveys.

2.4.3 GLACIER EVOLUTION ANALYSIS

The minimum and maximum altitudes of the glacier extracted from each DSM are shown in Tab. 2.3. The minimum values ranged between 1820 m and 1826 m, while maximum values ranged between 2339 m and 2385 m. The stability of the minimum values can be justified by the PCD masking. Minimum altitudes likely occurred near the glacier terminus, and the mask buffering could have comprised points surveyed at the terminal lobes. Conversely, the maximum glacier heights occurred in the upper part of the glacier, close to the main accumulation area. In this area, the glacier can benefit from events like ice avalanches or localized large ice mass accumulation related to particular meteorological conditions or glaciological processes, such as that occurred during the surge event.

Fig. 2.9 presents glacier contour altitudes between 1800 and 2400 m, to comprise the maximum altitude range measured by the five surveys with a contour interval of 50 m. Compared to the 1977 DSM (Fig. 2.9a), 1991 DSM cells classified in the range 2200–2400 m remained almost unchanged while the following contour lines gradually moved toward a valley, clearly indicating a mass accumulation (Fig. 2.9b). The following 2001 survey showed a continuation in these areas of the trend of increasing altitude toward the glacier terminus. Still, an altitude decrease was observed in the SW cells of the accumulation area (note

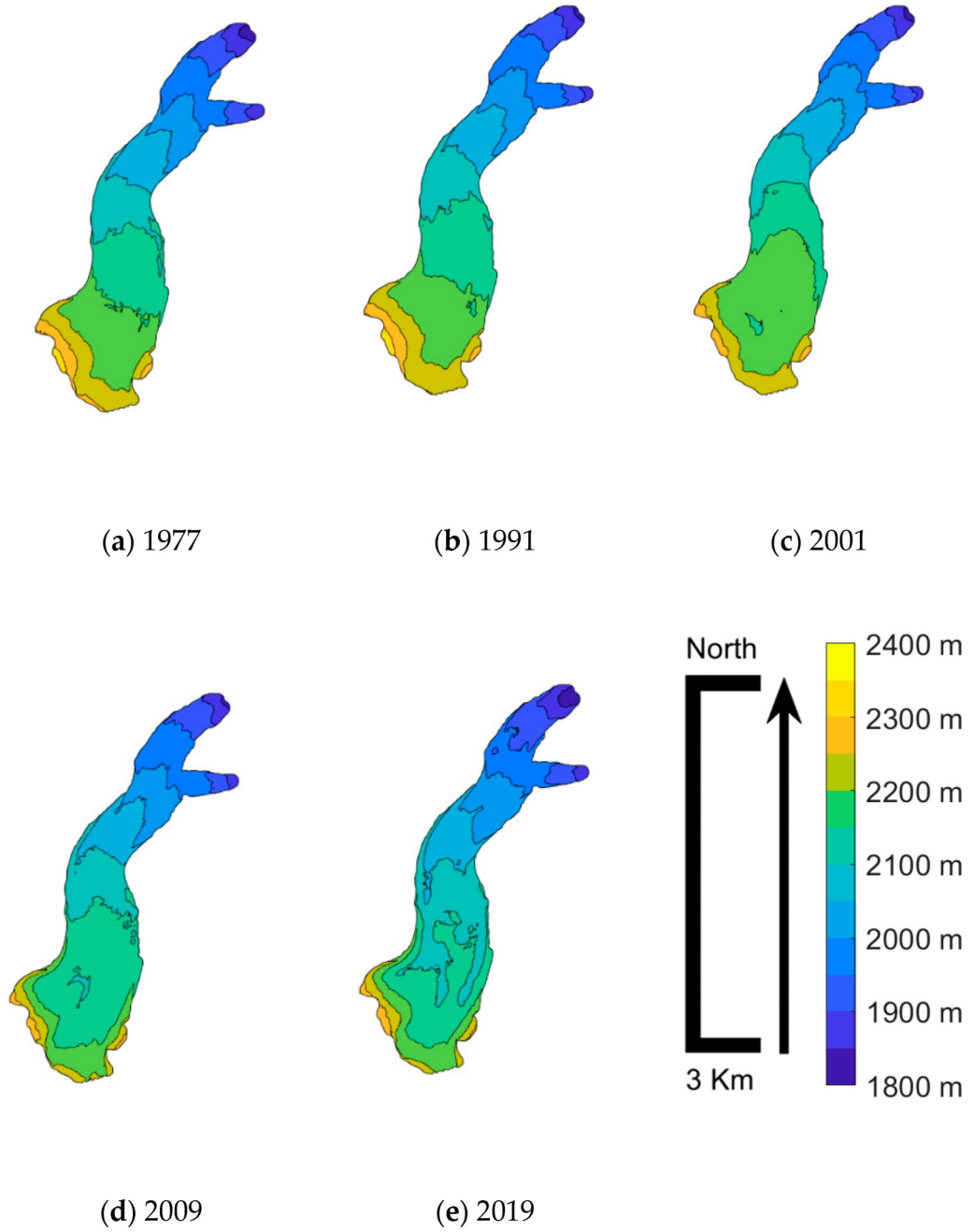


Figure 2.9: Glacier contours at different epochs: (a) 1977; (b) 1991; (c) 2001; (d) 2009; (e) 2019.

the extension of the altitude class 2200–2250 m in Fig. 2.9c), and cells of the highest altitude class were practically absent (see Tab. 2.3). The 2009 DSM showed different behavior (Fig. 2.9d). Lower contour lines retreated toward peaks, approximately in the same location as in 1977, while the 2150–2200 m range greatly retreated and covered a large part of the glacier toward the accumulation area. The most recent 2019 DSM (Fig. 2.9e) again showed a general retreat trend of lower contour lines, with no sharp transition in the range of 2100–2200 m (probably due to high surface ablation phenomena) and no great variation in the remaining areas in the range of 2200–2350 m.

Table 2.4: Glacier Volume Gain/Loss in the Four Considered Periods

Period	1977–1991	1991–2001	2001–2009	2009–2019
ΔVol (millions m ³)	+10.06	+10.61	-47.78	-27.16
Yearly ΔVol (millions m ³ /year)	+0.72	+1.06	-5.97	-2.72
Cumulated ΔVol (millions m ³)	+10.06	+20.66	-27.12	-54.28

Volume variations obtained by DoD are shown in Tab. 2.4. Cumulated volume variations are computed considering the 1977 DSM as a reference. Between 1977 and 2001, the glacier's volume increased substantially by $+20.66 \times 10^6$ m³. Notably, the rate of expansion accelerated during the period 1991–2001. During this period, the glacier gained volume 50% faster than the previous decade, increasing from $+0.72 \times 10^6$ m³ y⁻¹ to $+1.06 \times 10^6$ m³ y⁻¹. The glacier expansion continued until the surge event of 2000–2002 (Haeberli et al., 2002, Kääb et al., 2004, Mortara and Tamburini, 2009).

Since 2001, the glacier has undergone severe retreat, losing a total of -74.94×10^6 m³ of ice volume between 2001 and 2019. From 2001 to 2009, the average yearly volume decrease was -5.97×10^6 m³ y⁻¹, reducing the volume by -27.12×10^6 m³ relative to the initial 1977 measurement, despite prior accumulation. While the negative trend persisted from 2009 to 2019, the rate of loss slowed (-2.72×10^6 m³ y⁻¹). Over the 42-year observation period (1977–2019), the glacier experienced a net loss of -54.28×10^6 m³.

The reported volume gains or losses refer to the whole glacier surface, but it could be interesting to investigate local variations. Fig. 2.10 classifies glacier areas in terms of altitude variation, with contour intervals of 25 m. The volume increase was quite distributed in the first considered period, from 1977 to 1991. Glacier terminus advancement was visible, and volume decrease was measured in small portions at higher altitudes. The following period, 1991–2001, saw an important volume accumulation in the central part of the glacier, which was partially counterbalanced at higher altitudes. The following periods showed general volume loss, which was particularly important in the higher portion between 2001 and 2009 and was distributed until the terminus (see the northern one) in the period 2009–2019.

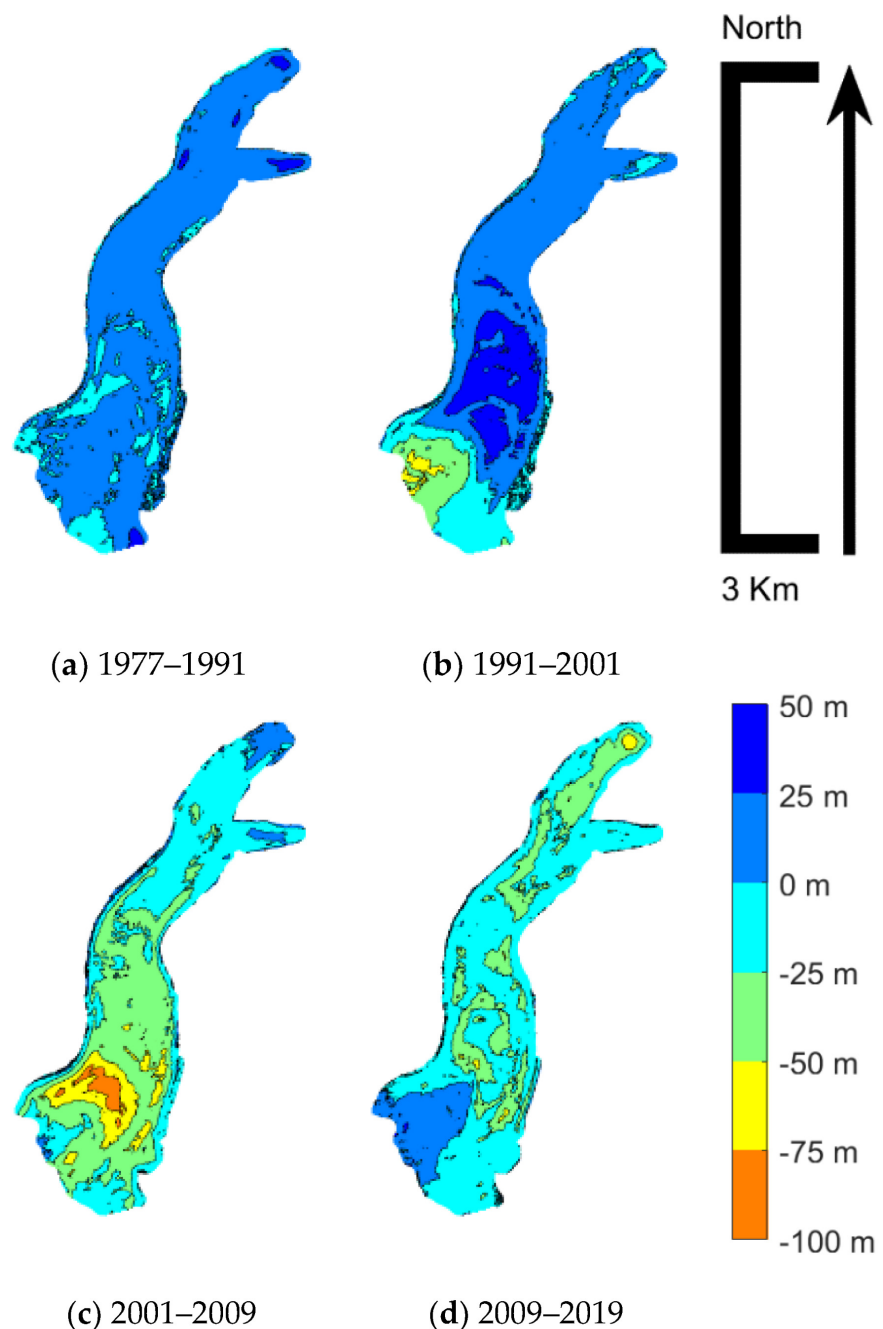


Figure 2.10: Binned glacier altitude variations in different periods with bin size set to 25 m: (a) 1977–1991; (b) 1991–2001; (c) 2001–2009; (d) 2009–2019.

2.4.4 COMPARISON WITH PREVIOUS STUDIES

Several studies focused on understanding and quantifying Belvedere Glacier dynamics. [Diolaiuti et al. \(2003\)](#) digitalized two large-scale topographic maps to interpolate DSMs and estimate volume variations between 1957 and 1991. They found a positive volume difference of $22.7 \times 10^6 \text{ m}^3$, which translates to an average rate of $\sim 0.69 \times 10^6 \text{ m}^3 \text{ y}^{-1}$ (assuming a linear volume variation between 1957 and 1991). This aligns with the yearly volume variation rate estimated in this study between 1977 and 1997, equal to $0.72 \times 10^6 \text{ m}^3 \text{ y}^{-1}$. The results obtained by [Diolaiuti et al. \(2003\)](#) agrees with those obtained by [Roethlisberger et al. \(1985\)](#), who estimated an increase of the glacier height of 1.5 m y^{-1} between 1983 and 1985.

References

- Bakker, M. & Lane, S. N. (2017). Archival photogrammetric analysis of river–floodplain systems using structure from motion (sfm) methods. *Earth Surface Processes and Landforms*, 42(8), 1274–1286, <https://doi.org/10.1002/esp.4085>.
- Beyer, R. A., Alexandrov, O., & McMichael, S. (2018). The ames stereo pipeline: Nasa’s open source software for deriving and processing terrain data. *Earth and Space Science*, 5(9), 537–548, <https://doi.org/10.1029/2018EA000409>.
- Borgogno Mondino, E. & Chiabrando, R. (2008). Multi-temporal block adjustment for aerial image time series: The belvedere glacier case study. *The International Archives of the Photogrammetry, Remote Sensing and Spatial Information Sciences*, 37(B2).
- Chandler, J. & Brunsden, D. (1995). Steady state behaviour of the black ven mudslide: the application of archival analytical photogrammetry to studies of landform change. *Earth Surface Processes and Landforms*, 20(3), 255–275.
- Child, S. F., Stearns, L. A., Girod, L., & Brecher, H. H. (2021). Structure-from-motion photogrammetry of antarctic historical aerial photographs in conjunction with ground control derived from satellite data. *Remote Sensing*, 13(1), <https://doi.org/10.3390/rs13010021>.
- Cipriano, P. (2005). Sitad: Building spatial data infrastructure in italy. In *GIS for Sustainable Development* (pp. 489–499).: CRC Press: Boca Raton, FL, USA.
- Dahle, F., Lindenbergh, R., & Wouters, B. (2024). Revisiting the past: A comparative study for semantic segmentation of historical images of adelaide island using u-nets. *ISPRS Open Journal of Photogrammetry and Remote Sensing*, 11, 100056, <https://doi.org/10.1016/j.oophoto.2023.100056>.
- Diolaiuti, G., D’Agata, C., & Smiraglia, C. (2003). Belvedere Glacier, Monte Rosa, Italian Alps: Tongue Thickness and Volume Variations in the Second Half of the 20th Century. *Arctic, Antarctic, and Alpine Research*, 35(2), 255–263, [https://doi.org/10.1657/1523-0430\(2003\)035\[0255:BGMRIA\]2.0.CO;2](https://doi.org/10.1657/1523-0430(2003)035[0255:BGMRIA]2.0.CO;2).
- Fischer, L., Eisenbeiss, H., Kaab, A., Huggel, C., & Haeberli, W. (2011). Monitoring topographic changes in a periglacial high-mountain face using high-resolution dtms, monte rosa east face, italian alps. *PERMAFROST AND PERIGLACIAL PROCESSES*, 22(2), 140–152, <https://doi.org/10.1002/ppp.717>.
- Forlani, G. & Pinto, L. (2001). Integrated ins/dgps systems: Calibration and combined block adjustment. In *Proceedings of the OEEPE workshop Integrated Sensor Orientation*: Hannover, Germany.
- Giordano, S., Le Bris, A., & Mallet, C. (2018). Toward automatic georeferencing of archival aerial photogrammetric surveys. *ISPRS Annals of the Photogrammetry, Remote Sensing and Spatial Information Sciences*, IV-2, 105–112, <https://doi.org/10.5194/isprs-annals-IV-2-105-2018>.

- Haeberli, W., et al. (2002). A surge-type movement at Ghiacciaio del Belvedere and a developing slope instability in the east face of Monte Rosa, Macugnaga, Italian Alps. *Norsk Geografisk Tidsskrift*, 56(2), 104–111, <https://doi.org/10.1080/002919502760056422>.
- Heisig, H. & Simmen, J.-L. (2021). Re-engineering the past: countrywide geo-referencing of archival aerial imagery. *PFG-Journal of Photogrammetry, Remote Sensing and Geoinformation Science*, 89(6), 487–503.
- Hinz, A., Dörstel, C., & Heier, H. (2001). The digital sensor technology of z/i-imaging. In *Photogrammetric Week* (pp. 93–103).: Cite Seerx: University Park, PA, USA.
- Ioli, F., Bianchi, A., Cina, A., De Michele, C., Maschio, P., Passoni, D., & Pinto, L. (2022). Mid-term monitoring of glacier's variations with UAVs: The example of the belvedere glacier. *Remote Sensing*, 14(1), 28, <https://doi.org/10.3390/rs14010028>.
- Ioli, F., Pinto, L., & Ferrario, F. (2021). Low-cost dgps assisted aerial triangulation for sub-decimetric accuracy with non-rtk uavs. *Int. Arch. Photogramm. Remote Sens. Spatial Inf. Sci.*, XLIII-B2-2021, 25–32, <https://doi.org/10.5194/isprs-archives-XLIII-B2-2021-25-2021>.
- Jacobsen, K. (2004). Issues and method for in-flight and on-orbit calibration. *Post-Launch Calibration of Satellite Sensors; ISPRS Book Series; Taylor & Francis Group: London, UK*, 2, 83–92.
- Kääb, A. (2002). Monitoring high-mountain terrain deformation from repeated air-and spaceborne optical data: examples using digital aerial imagery and aster data. *ISPRS Journal of Photogrammetry and remote sensing*, 57(1-2), 39–52.
- Kääb, A., Huggel, C., Barbero, S., Chiarle, M., Cordola, M., Epifani, F., & Haeberli, W. (2004). Glacier Hazards At Belvedere Glacier and the Monte Rosa East Face , Italian Alps: Processes and Mitigation. *Inter nationales Symposium INTERPRAEVENT 2004 – RIVA / TRIENT*, (Vc), 67–78.
- Kaufmann, V. & Ladstädter, R. (2003). Quantitative analysis of rock glacier creep by means of digital photogrammetry using multi-temporal aerial photographs: Two case studies in the austrian alps. *Proceedings of the 8th International Conference on Permafrost*, (pp. 525–530).
- Keutterling, A. & Thomas, A. (2006). Monitoring glacier elevation and volume changes with digital photogrammetry and gis at gepatschferner glacier, austria. *International Journal of Remote Sensing*, 27(19), 4371–4380.
- Knuth, F., et al. (2023). Historical structure from motion (hsfm): Automated processing of historical aerial photographs for long-term topographic change analysis. *Remote Sensing of Environment*, 285, 113379, <https://doi.org/10.1016/j.rse.2022.113379>.
- Lane, S., et al. (2010). Quantification of braided river channel change using archival digital image analysis. *Earth Surface Processes and Landforms*, 35(8), 971–985.
- Lane, S. N., James, T. D., & Crowell, M. D. (2000). Application of digital photogrammetry to complex topography for geomorphological research. *The Photogrammetric Record*, 16(95), 793–821, <https://doi.org/10.1111/0031-868X.00152>.
- McNabb, R., Girod, L., Nuth, C., & Kääb, A. (2020). An open-source toolset for automated processing of historic spy photos: spymicmac. In *EGU General Assembly 2020*, volume EGU2020-11150. <https://doi.org/10.5194/egusphere-egu2020-11150>.

- Micheletti, N., Lane, S. N., & Chandler, J. H. (2015). Application of archival aerial photogrammetry to quantify climate forcing of alpine landscapes. *The Photogrammetric Record*, 30(150), 143–165, <https://doi.org/10.1111/phor.12099>.
- Mortara, G. & Tamburini (2009). *Il ghiacciaio del Belvedere e l'emergenza del Lago Effimero*. Societa' Meteorologica Subalpina.
- Mölg, N. & Bolch, T. (2017). Structure-from-motion using historical aerial images to analyse changes in glacier surface elevation. *Remote Sensing*, 9(10), <https://doi.org/10.3390/rs9101021>.
- Poli, D., Casarotto, C., Strudl, M., Bollmann, E., Moe, K., & Legat, K. (2020). Use of historical aerial images for 3d modelling of glaciers in the province of trento. *The International Archives of the Photogrammetry, Remote Sensing and Spatial Information Sciences*, 43, 1151–1158, <https://doi.org/10.5194/isprs-archives-XLIII-B2-2020-1151-2020>.
- Roethlisberger, H., Haeberli, W., Schmid, W., Biolzi, M., & Pika, J. (1985). Studi Sul Comportamento Del Ghiacciaio Del Belvedere. *Comunità montana della Valle Anzasca*, (97.3).
- Rupnik, E., Daakir, M., & Pierrot Deseilligny, M. (2017). Micmac—a free, open-source solution for photogrammetry. *Open Geospat. Data, Softw. Stand.*, 2(1), 1–9.
- Schwab, M., Rieke-Zapp, D., Schneider, H., Liniger, M., & Schlunegger, F. (2008). Landsliding and sediment flux in the central swiss alps: A photogrammetric study of the schimbrig landslide, entlebuch. *Geomorphology*, 97(3-4), 392–406.
- Walstra, J., Dixon, N., & Chandler, J. H. (2007). Historical aerial photographs for landslide assessment: two case histories. *Quarterly Journal of Engineering Geology and Hydrogeology*, 40(4), 315–332.
- Zhang, L., Rupnik, E., & Pierrot-Deseilligny, M. (2021). Feature matching for multi-epoch historical aerial images. *ISPRS Journal of Photogrammetry and Remote Sensing*, 182, 176–189, <https://doi.org/10.1016/j.isprsjprs.2021.10.008>.
- Zhang, Z. (2000). A flexible new technique for camera calibration. *IEEE Trans. Pattern Anal. Machine Intell.*, 22(11), 1330–1334, <https://doi.org/10.1109/34.888718>.

3

UAV photogrammetry for annual glacier reconstruction (2015-2023)

THIS CHAPTER IS BASED ON:

- Ioli, F., Bianchi, A., Cina, A., De Michele, C., Maschio, P., Passoni, D., & Pinto, L. (2022). Mid-Term Monitoring of Glacier's Variations with UAVs: The Example of the Belvedere Glacier. *Remote Sensing*, 14(1), 28. <https://doi.org/10.3390/rs14010028>
- Ioli, F., De Gaetani, C., Barbieri, F., Gaspari, F., Pinto, L., & Rossi, L. (2024). Belvedere Glacier long-term monitoring Open Data [Data set]. Zenodo. <https://zenodo.org/doi/10.5281/zenodo.7842347>

3.1 INTRODUCTION

This chapter investigates the potential of high-resolution UAV photogrammetry and in-situ GNSS measurements to comprehensively monitor the Belvedere Glacier. Originally, our understanding of glacier dynamics was constrained by the limitations of traditional aerial photogrammetry, which provided data at approximately decadal intervals and sub-meter resolution. A UAV-based approach offers a paradigm shift, enabling annual reconstructions with sub-decimeter resolution. With this enhanced capability, we can delve into the glacier's yearly kinematics, gaining deeper insights into its evolution and responses to climate change.

The Belvedere Glacier monitoring campaign, which started in 2015, was designed and conducted jointly by the Department of Civil and Environmental Engineering (DICA) of Politecnico di Milano and the Department of Environment, Land and Infrastructure Engineering (DIATI) of Politecnico di Torino. Moreover, the DREAM projects (DRone tEchnnology for wAter resources and hydrologic hazard Monitoring), involving teachers and students from Alta Scuola Politecnica (ASP) of Politecnico di Torino and Milano, contributed to the campaign from 2015 to 2017.

Every year, fixed-wing UAVs and quadcopters were used to remotely sense the glacier and build high-resolution 3D photogrammetric models, DSMs, and orthophotos. The series of point clouds was used to estimate the glacier volume variations and estimate the thinning of the glacier. The orthophotos and the DSMs were also used to investigate the glacier kinematics and derive ice flow velocity and glacier retreat. This was carried out by exploiting DIC techniques to track the movement of the glacier surface.

The Belvedere Glacier monitoring campaign has produced a rich dataset of GNSS measurements, 3D point clouds, DSMs, and orthophotos. Recognizing the transformative potential of open science, we have made this entire dataset publicly available, and we have also developed a suite of web-based tools to make the data user-friendly for researchers and non-experts¹. This chapter will finally describe the solutions to promote the widespread use of our monitoring data, accelerate scientific progress in glacier research, and encourage knowledge sharing across the scientific community.

3.2 INSTRUMENTS AND DATASETS

This section introduces the data acquired in this study from 2015 to 2023, including the periodic GNSS measurements of targets deployed over the glacier and UAV images acquired to build the photogrammetric reconstructions.

¹<https://thebelvedereglacier.it/>

3.2.1 GNSS MEASUREMENTS

Yearly GNSS measurements of permanent targets deployed across the glacier were conducted. These targets served a dual purpose: as GCPs/CPs for photogrammetric block processing and as high-accuracy reference points for evaluating glacier kinematics derived from photogrammetry. The targets were materialized using square cross patterns printed on polypropylene sheets and anchored to large rocks and boulders (Fig. 3.1b).

Approximately 25 targets were deployed on the glacier itself (designated as *moving targets* or $M\#$ in Fig. 3.1a), while 24 targets were placed on stable areas along the moraines (labelled as *stable targets* or $S\#$ in Fig. 3.1a). Annually, we evaluated the condition of each target. Damaged or destroyed targets were replaced with new polypropylene plates, maintaining the original center location using the existing plugs. Over time, some targets were lost and replaced with new ones near the original locations (e.g., M29bis).

All targets were surveyed with dual frequency geodetic quality GNSS receivers: Leica Viva GS14 and Leica GPS1200+. The measurements were framed within the official Italian reference system ETRF2000 at the epoch 2008.0, projected in UTM 32N (RDN2008 / UTM zone 32N, EPSG:7791). The measurement techniques employed in the survey have evolved. Before 2021, target positions on the lower glacier, where GSM network coverage was available, were determined using nRTK relative to CORS permanent stations (HxGN SmartNet or SPIN GNSS). These points were occupied for at least 20 seconds. In contrast, upper glacier targets were surveyed using static sessions of approximately 10 minutes, with raw data post-processed relative to local master stations located in stable areas (S_{12} or S_{20} , see Fig. 3.1a). Since 2021, GNSS measurements have been conducted in RTK mode using a local base station (S_{12} or S_{20}). A radio link connection streamed the real-time corrections from the base to the rover. This approach has significantly reduced measurement time in the upper glacier, requiring seconds rather than minutes per occupation, as was for static processing of the upper glacier targets. Additionally, the local-base RTK method improves internal coherence among measurements, as well as tropospheric and ionospheric error modeling due to shorter baselines compared to the nRTK approach.

The accuracy of GNSS measurements was evaluated empirically by comparing repeated measurements over stable targets carried out in different years. RMSE of 1.5 cm in planimetry and 3 cm in elevation were obtained.

3.2.2 UAV FLIGHTS

The long duration of the monitoring campaign, the challenging environment, and the involvement of multiple research groups led to the use of various UAV platforms and cameras over time. Tab. 3.1 provides

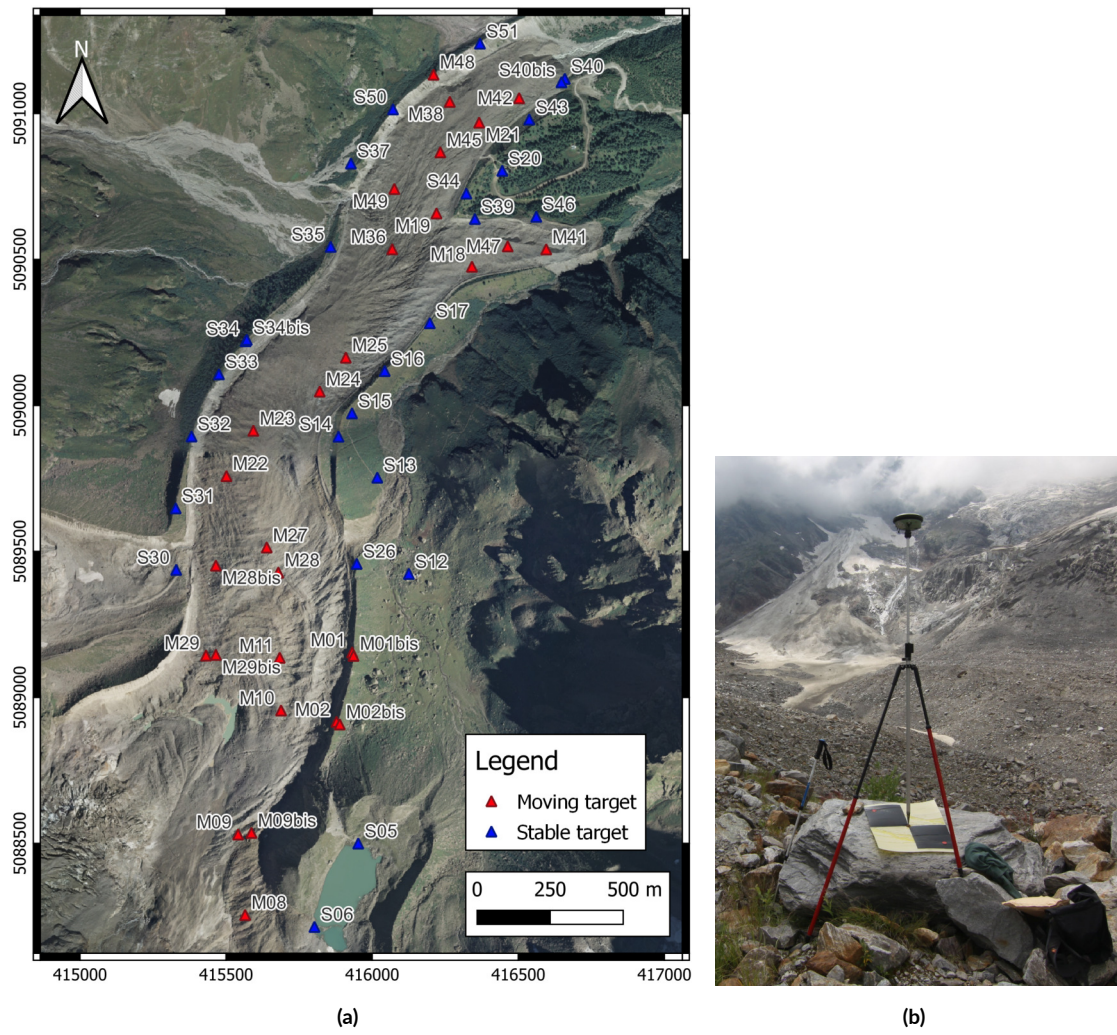


Figure 3.1: (a) Location of the targets used for the photogrammetric surveys. For each year, a subset of the targets were used as GCPs, while the remaining as CPs; (b) an example of a photogrammetric target deployed over the glacier moraine.

Table 3.1: Summary of the characteristics of the surveys.

Year	Date	UAV	Camera	GSD [m/px]	GCP [#]	CP [#]
2015	A. 8.10	SenseFly eBee	Canon PowerShot S110	0.07	24	11
	B. 23.10					
2016	20.10	SenseFly eBee	Canon PowerShot S110	0.09	31	15
2017	A. 5.10	A. SenseFly eBee	A. Canon PowerShot S110			
	B. 15.11	B. SenseFly eBee Plus	B. SenseFly S.O.D.A	0.06	27	8
	C. 16.11	C. DJI Phantom 4 Pro	C. DJI FC6310			
2018	23-25.07	Parrot Disco	Hawkeye Firefly 8S	0.05	27	13
2019	29.07-2.08	Parrot Disco	Hawkeye Firefly 8S	0.06	26	10
2020	A. 26-27.07	A. Parrot Disco	A. Hawkeye Firefly 8S			
	B. 9.08	B. DJI Phantom 4 Pro	B. DJI FC6310	0.05	29	12
2021	29.07-2.08	DJI Matrice 210 V2	DJI ZenMuse x5s	0.04	23	9
2022	28.07-29.07	DJI Matrice 300 RTK	DJI Zenmuse P1 - 35 mm	0.03	22	19
2023	25.07-27.07	DJI Matrice 300 RTK	DJI Zenmuse P1 - 35 mm	0.03	23	9

Table 3.2: Summary of the characteristics of the cameras employed.

Camera	Sensor	Sensor Size [mm ²]	Focal length [mm]	Image size [px]	Pixel size [μm]
Canon PowerShot S110	1/1.7" CMOS	7.44 × 5.58	5.2	4000 × 3000	1.9
SenseFly S.O.D.A	1" CCD	13.2 × 8.8	10.6	5472 × 3648	2.4
DJI FC6310	1" CMOS	13.2 × 8.8	8.8	5472 × 3648	2.4
Hawkeye Firefly 8S	1/2.3" CMOS	6.17 × 4.56	3.8	5472 × 3648	1.34
DJI ZenMuse x5s	4/3" CMOS	17.3 × 13	15	5280 × 3956	3.3
DJI Zenmuse P1 - 35 mm	FullFrame CMOS	35.9 × 24	35	8192 × 5460	4.4

a detailed summary of the equipment (UAV and camera) employed while Tab. 3.2 lists the sensor and lens specifications for each camera.

In 2015 and 2016, a ready-to-fly fixed-wing SenseFly eBee equipped with a compact camera, Canon PowerShot S110, was used for whole glacier surveys. Due to technical problems, the year 2017 saw the use of different UAVs (both fixed-wing and quadcopters) and camera combinations (Tab. 3.1). From 2018 to 2020, a low-cost recreational Parrot Disco FPV fixed-wing UAV (wingspan 1.15 m, weight 750 g) was adapted to carry a lightweight Hawkeye Firefly 8S action camera.

In 2021, a professional-grade DJI Matrice 210 V2 quadcopter was employed, carrying a DJI ZenMuse X5s camera featuring a Micro 4/3 sensor and a 15 mm lens. Since 2022, the UAV platform has been upgraded to a DJI Matrice 300 RTK quadcopter with a full-frame DJI Zenmuse P1 camera and a DL 35 mm F2.8 LS ASPH lens. While this setup offered superior image quality, the longer focal length required higher flight altitudes to maintain a consistent GSD with the previous surveys. Furthermore, the DJI Matrice 300 RTK was equipped with an RTK GNSS receiver, enabling decimeter-level accuracy in recording the camera position for each shot. This precision was achieved through a local GNSS base station positioned near the take-off location, which streamed real-time corrections to the drone via DJI's proprietary link.

UAV flights were conducted automatically by using ground station software packages developed by UAV manufacturers and UgCS² flight planning software. The flights were designed to have GSD ranging between 5 cm and 10 cm, and to guarantee ~80 % of longitudinal and ~60 % of transversal overlap. Average image GSD values and number of GCPs and CPs, used respectively to orient the images and to assess the quality of the photogrammetric blocks are summarized in Tab. 3.1.

3.2.3 CHALLENGES AND ADAPTATIONS IN THE 2017, 2018 AND 2020 SURVEYS

Conducting annual monitoring campaigns in alpine environments poses logistical and environmental challenges, including limited accessibility in certain areas and unpredictable weather. These factors directly impacted the 2017 and 2020 surveys.

Adverse weather and logistical constraints necessitated splitting the 2017 survey across multiple dates, requiring using different UAVs and cameras (see Tab. 3.1). Consequently, the photogrammetric model was built in three parts. The central portion corresponds to a survey carried out in October, while the snow-covered upper and lower sections were acquired in November.

²<https://www.sphengineering.com/flight-planning/ugcs>

Technical issues arose during the 2020 survey when an elevon servo failed during landing and caused the fixed-wing UAV to crash. To complete the survey, a DJI Phantom 4 Pro quadcopter was employed 14 days later to survey the upper part of the glacier (see the different colors in the orthophoto of Fig. 3.3f). However, the harsh terrain and the presence of crevasses in the upper part of the glacier prevented the measurement of additional GCPs to constrain the model in this region. This necessitated co-registering the Phantom 4 Pro model with the 2019 data, using stable rock features along the moraines as reference points. This approach was less accurate than measuring GCPs directly on the field and yielded an RMSE on CPs of 0.36 m (see Fig. 3.2), ~7 times the GSD. Nevertheless, this problem affected only the upper accumulation area, which was limited compared to the whole Belvedere Glacier.

The project timeline also led to a shift in survey periods from autumn (2015–2017) to summer (2018–2023). This change means that the timespan between the October/November 2017 and July 2018 surveys do not encompass the summer (neither August 2017 nor August 2018 was included), which is the period of maximum glacier ablation and surface velocity. Consequently, volume variation and ice flow velocity estimated between 2017 and 2018 reflect primarily winter conditions and are not directly comparable to other years, as they underestimate the actual annual average statistics.

3.3 METODOLOGY

3.3.1 SFM WORKFLOW

To generate photogrammetric models of the glacier, UAV imagery was processed using Agisoft Metashape 1.8.5³. Each year, a minimum of 22 GCPs distributed across the glacier were used for image orientation, while at least 8 CPs served for model quality assessment. All GCPs and CPs were manually collimated within the images.

TP were detected and matched by Metashape on full-resolution images (which corresponds to *high accuracy* parameter in Metashape). Image EO and TPs world coordinates were estimated by solving the BBA. TPs with the worst reprojection error on images were removed, and the BBA was solved again to improve the quality of the solution. This process was iterated more times until the TP mean reprojection error had dropped below ~0.8 px. Camera internal orientation was estimated by self-calibration (Fraser, 2013, Cramer et al., 2017) because of the intrinsic instability of the low-cost cameras' IO.

Agisoft Metashape computed dense 3D reconstruction with proprietary MVS algorithms (Dall'asta and Roncella, 2014). Depth maps and dense point clouds were obtained from images downsampled by a

³<https://www.agisoft.com>

factor of 4 to reduce the computational time (*medium quality* parameter of the dense cloud generation in Metashape). Triangulated mesh surfaces and photorealistic textures were computed.

DSMs with a resolution of 0.5 m px^{-1} were derived from the mesh model. Finally, orthophotos with a GSD of 0.10 m px^{-1} were obtained by projecting the most nadiral images over the mesh models.

3.3.2 GLACIER FLOW VELOCITY

In debris-covered glaciers, surface debris and boulders primarily move in conjunction with the underlying ice flow, making them valuable proxies for evaluating glacier kinematics through tracking techniques (Dehecq et al., 2015, Blöthe et al., 2021).

In-situ GNSS measurements of the *moving targets* (see Sec. 3.2.1) were employed for deriving glacier surface flow velocities. These punctual measurements, labeled as GNSS, provided high-accuracy, estimated at approximately $\sim 3 \text{ cm}$ (see Section 3.2.1). Assuming measurements of the same target at two consecutive years as independent, the expected standard deviation of the velocity was computed by propagating the variance as $\pm 0.04 \text{ m y}^{-1}$. Therefore, GNSS measurements were considered the most reliable reference for flow velocity estimation.

However, due to the limited number of GNSS measurement points across the glacier, they are insufficient for deriving a complete glacier velocity field. Therefore, DIC algorithms were employed to derive a complete description of the surface kinematics. DIC allows for determining the displacement of an image patch between two images (master and slave) of the same scene and acquired at different epochs by the same camera. The displacement d is obtained as (Eq. 3.1):

$$d = \operatorname{argmax}_{(r,q)} S(A(i,j), B(i+r, j+q)) \quad (3.1)$$

To compute displacement by DIC, we employed the open-source Local Adaptive Multiscale Image Matching Algorithm (LAMMA) (Dematteis et al., 2022). LAMMA adopts a hierarchy structure of patch grids of increasing spatial resolution and uses locally adaptive search area sizes according to the displacements already obtained in the neighboring region. LAMMA was originally written in Matlab⁴, but it has been recently translated into Python. A collaborative effort with Niccolò Dematteis is underway to publish pyLamma as open-source⁵.

As a correlation function, we used the cosine similarity applied to orientation images (Dematteis and Giordan, 2021), which is less sensitive to chromatic variation changes (e.g., due to shadows or snow pat-

⁴LAMMA: <https://github.com/niccolodematteis/LAMMA>

⁵pyLamma: <https://github.com/franioli/pylamma>

ters) and is known to perform well in glacier environments (Heid and Kääb, 2012, Dematteis et al., 2019). The cosine similarity function is defined as (Dematteis et al., 2022):

$$\text{CXC}(r, c) = \frac{1}{RC} \sum_{r,c} \text{Re} (A_{\text{or}}^*(i,j) \cdot B_{\text{or}}(i+r, j+c)) \quad (3.2)$$

where A_{or} and B_{or} denotes the complex conjugate and are the orientation images of the reference and slave patches, respectively. An orientation image is defined as $I_{\text{or}} = \frac{I_x}{|I_x|} + i \frac{I_y}{|I_y|}$, where are the first derivatives of the image intensity in the two dimensions (Fitch et al., 2002).

From 2018 onwards, consistent acquisition periods (end of July) and snow-free conditions enabled the use of DIC on UAV orthophotos for comprehensive velocity field derivation. On the other hand, the presence of snow and significant environmental variations between orthophotos from 2015 to 2018 made them unsuitable for DIC techniques. Consequently, we applied DIC on pairs of DSMs (Gindraux, 2019) to extract glacier surface displacements for this period.

All image pairs processed with pyLamma (DSM pairs for 2015-2018 and orthophotos from 2019-2023) maintained a consistent ground resolution of 0.2 m px^{-1} . To analyze these images, we established a regular grid of nodes spaced 64 px apart (equivalent to 12.8 m on the ground). The interrogation template (i.e., the size of the area defined around each node in the master image that is searched in the slave image) was set to 64 px, equal to the same size of the grid step. This was empirically chosen as a trade-off to balance the benefit of a stronger correlation peak (achieved with a larger area for computing the correlation function) with the constraints of maintaining similar kinematics within the interrogation template. In fact, an excessively large interrogation template may include regions with different kinematics within it, potentially weakening the correlation results.

We employed pyLamma's multiscale processing with a 3-step scale approach to optimize the interrogation area hierarchically. This strategy involved calculating displacement at a coarser scale, using an interrogation template of 256 px. This provided an initial displacement estimate, which we leveraged to refine the search area at finer scales. We based the initial interrogation template size on expected minimum and maximum glacier displacements derived from GNSS measurements, ensuring our analysis was tailored to the specific glacier's movement.

To achieve subpixel displacement sensitivity, LAMMA considers the sub-region of the similarity function centered in its maximum value, and it oversamples this sub-region using bicubic interpolation (Dematteis et al., 2022). Then, the subpixel displacement is the peak's position of the oversampled correlation function (Debella-Gilo and Kääb, 2011). We used an upsampling factor of 10 to derive sub-pixel displacements.

The displacement velocity fields were finally filtered in the spatial domain by implementing the filter implemented in LAMMA. This filter works in the spatial domain, and for each node, it considers the median displacement of the four closest nodes (Dematteis et al., 2024)

3.3.3 VOLUME VARIATIONS

To compute glacier volume variation ΔV , consecutive DSMs were differentiated by employing a DoD approach. To this end, the tool *Compute 2.5D volume* implemented in CloudCompare⁶ was used. First, photogrammetric dense clouds were gridded by projecting points along the vertical direction onto a planar surface, resulting in DSMs with a $0.5 \text{ m} \times 0.5 \text{ m}$ ground resolution. This resolution balances robust height estimation (by averaging a sufficient number of points per cell) with the ability to resolve finer-scale glacier morphology. A manually created mask delineated the glacier surface within each DSM, ensuring only relevant areas were analyzed. DSMs from consecutive years were then subtracted pixel-by-pixel, yielding the height difference for each raster cell.

A simplified approach was initially used to estimate volume variation variance, treating each DSM as a mono-dimensional random variable with variance equal to the squared vertical RMSE computed on CPs. Assuming DSMs computed at different years as independent, the volume variation variance was calculated as follows:

$$\sigma_{\Delta V^{(i+1,i)}}^2 = (n \times A_c)^2 (\sigma_{DSM^{(i+1)}}^2 + \sigma_{DSM^{(i)}}^2), \quad (3.3)$$

where n is the number of cell in the DSMs, A_c is the area of the cells and σ_{DSM}^2 is the squared vertical error of the photogrammetric model.

While providing a preliminary idea, this is clearly a simplified approach. However, a more rigorous uncertainty estimation would require several additional considerations. Firstly, to propagate variance accurately, we need the full covariance matrix of each DSM, including the covariances between neighboring DSM cells, not to underestimate the actual DOD variance. However, Agisoft Metashape does not provide this information, but only the 3×3 covariance matrix of each point of the sparse point cloud derived from the bundle adjustment. However, this may not capture systematic biases like the doming effect (James and Robson, 2014, James et al., 2020). Finally, these variances pertain only to the sparse point cloud, and an interpolation onto the DSM grid is required. A potential solution for a more robust DSM covariance estimation would require Monte Carlo simulations, as carried out by James et al. (2017) and Roncella et al. (2021).

⁶Cloudcompare: <https://www.danielgm.net/cc/>

Between 2015 and 2018, the partial snow cover (Fig. 3.3a–c) introduced additional uncertainty in volume estimation. To address this, snow depth data measured from the meteorological station located close to the Zamboni Zappa Hut⁷ was used as a first estimate of the snow depth for the upper part of the glacier. The snow depths measured on survey dates are the following

- 2015 (Oct. 23): 22 cm
- 2016 (Oct. 20): 20 cm
- 2017 (Nov. 15): 40 cm

These depths were incorporated into the DSM standard deviations. However, the snow-driven uncertainty was weighted by half the total glacier area during variance propagation due to the partial snow cover.

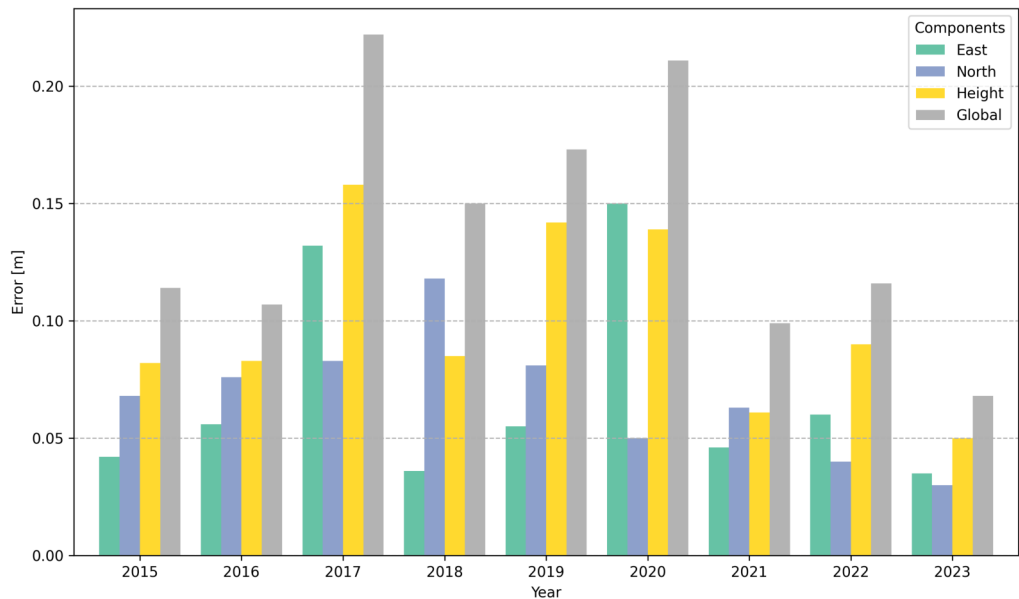


Figure 3.2: Barplot of reprojection RMSE computed on CPs for each photogrammetric model. Due to the technical problems that occurred in 2020 (see Sec. 3.2.3), the 2020 RMSE refers only to the survey of the lower part of the glacier, excluding the upper accumulation sector.

⁷https://www.arpa.piemonte.it/rischinaturali/accesso-ai-dati/annali_meteoidrologici/annali-meteo-idro/banca-dati-meteorologica.html

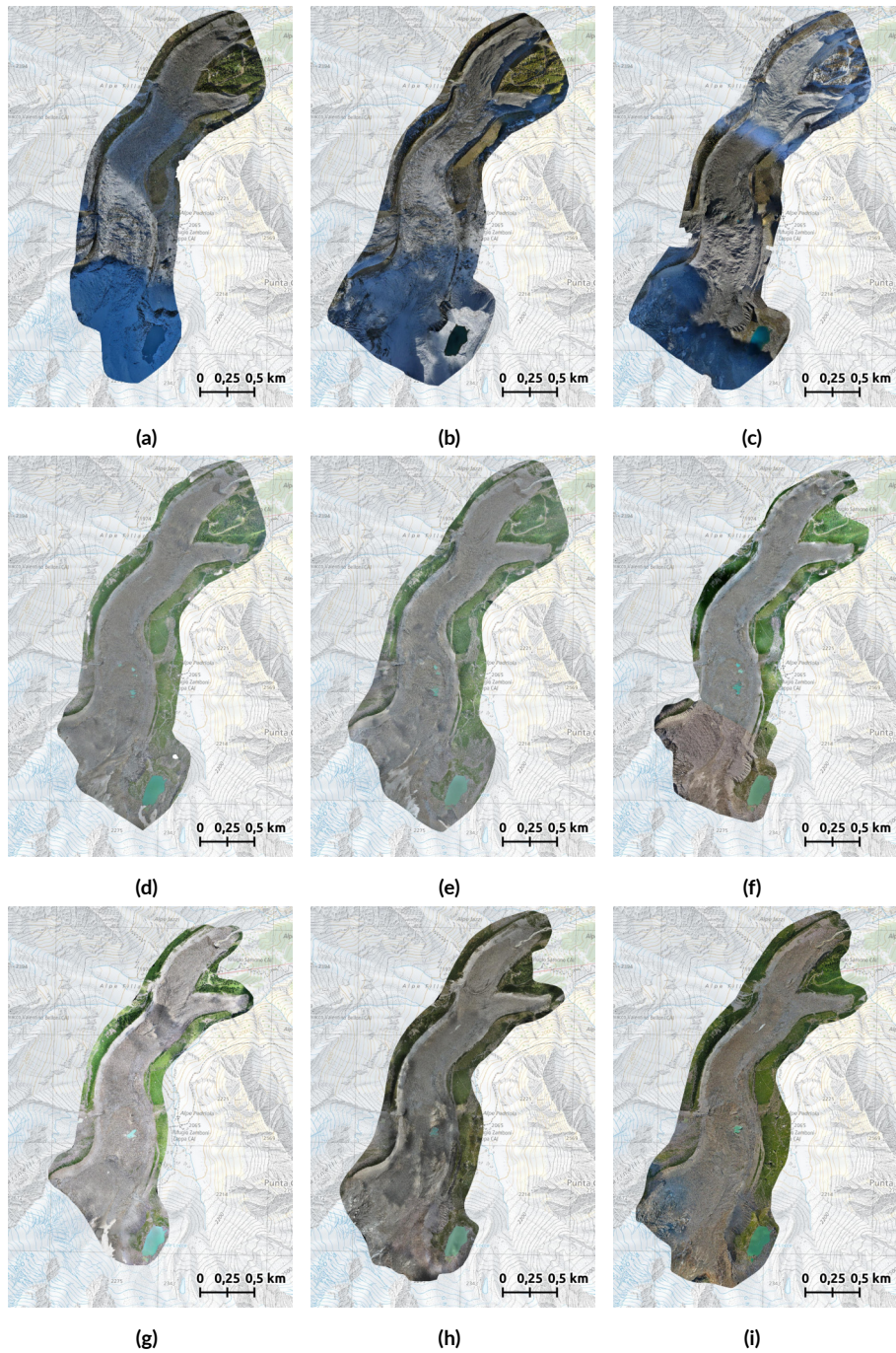


Figure 3.3: Orthophotos obtained from the photogrammetric model for each year. (a) 2015, (b) 2016, (c) 2017, (d) 2018, (e) 2019, (f) 2020, (g) 2021, (h) 2022, (i) 2023. Orthophotos are overlapped to the SwissTopo base map (source: SwissTopo www.geo.admin.ch). Refer to the Appendix A for a better visualization of the orthophotos.

3.4 RESULTS

3.4.1 SfM

Each SfM process yielded a 3D point cloud, a textured mesh, a DSM, and an orthophoto of the glacier. Point cloud density increased over time: point clouds from 2015 to 2020 contained 0.5×10^8 to 1×10^8 points, while those from 2021 onwards had 1.5×10^8 to 2.5×10^8 points. DSMs and orthophotos were produced at a resolution of 20 centimeters per pixel. Due to autumn surveys, orthophotos from 2015 to 2017 show some snow cover (Fig. 3.3).

The geometrical accuracy of the SfM models was evaluated for all years using CPs. Fig. 3.2 RMSE of on-ground error in all three directions and globally. RMSE values range between 0.1 m and 0.2 m across all years. Note that for 2020, errors reflect the lower part of the glacier only, as the upper part was surveyed with a separate photogrammetric flight that lacked GNSS-measured GCPs but relied on natural features identified in the 2019 model as GCPs (see Sec. 3.2.3).

3.4.2 GLACIER FLOW VELOCITY

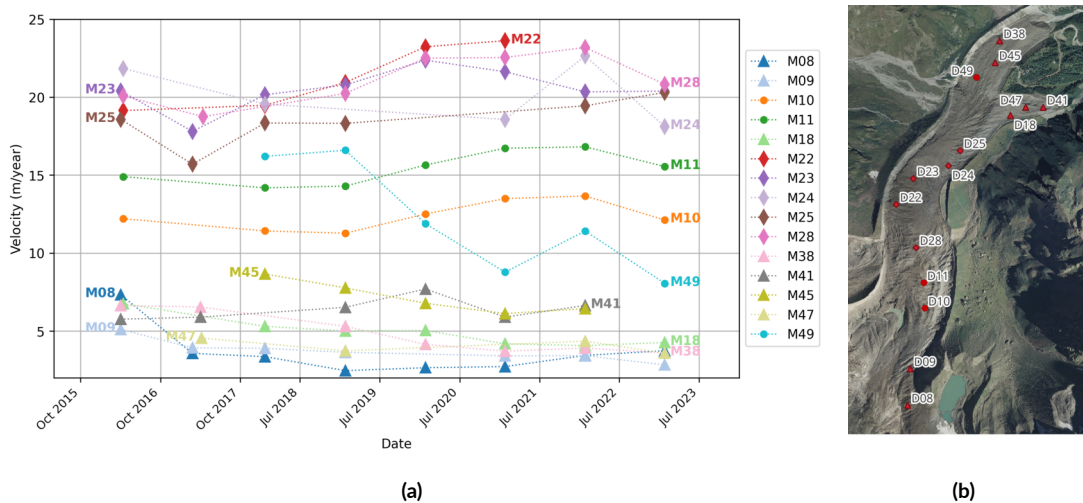


Figure 3.4: (a) Time series of the velocity computed from the GNSS measurements of the targets deployed across the glacier. (b) Location of the targets in the last surveying year.

Annual ice flow velocities were first computed using in-situ GNSS measurements of moving targets (Fig. 3.4). Most of the moving targets were found and measured for three more years, and some of them

have been continuously tracked since 2015 (e.g., M_{10} , M_{28} , M_{38}). While some targets were inevitably lost (e.g., due to the presence of crevasses), they were replaced with new ones materialized nearby to maintain data continuity.

Analysis of the graph in Fig. 3.4 reveals three distinct velocity clusters. The first cluster exhibits the lowest velocities ranging between 2 m y^{-1} and 8 m y^{-1} and encompasses points in the upper part of the glacier and glacier terminal lobes (e.g., targets M_{08} , M_{09} , M_{41} , M_{45}). The glacier's central part is characterized by significantly faster speeds between 16 m y^{-1} and 25 m y^{-1} (e.g., targets M_{22} , M_{23} , M_{24} , M_{25} , M_{28}). The third cluster represents a transition zone with intermediate velocities found between the central sector and the upper accumulation area (targets M_{10} , M_{11}) and between the central sector and the terminal lobes (e.g., target M_{49}).

The surface velocity fields, derived from both orthophotos and DSMs, are presented in Fig. 3.5. We employed DIC on DSM pairs for the 2015-2018 period and orthophotos for 2019-2023 (see Sec. 3.3.2 for methodological details). The results agree with those obtained from GNSS measurements, highlighting the same velocity distribution along the glacier. Additionally, DIC results allow us to appreciate the velocity distribution along the glacier transects. As expected, the highest velocities are found along the centerline, gradually decreasing towards the moraines due to increased friction between the glacier and the underlying bedrock and the glacier's thinner ice at the edges.

The 2017-2018 velocity field (Fig. 3.5c) exhibits significantly lower velocities than other years. This discrepancy is attributed to the shift in survey dates from autumn to summer (see Sec. 3.2.3). The DSMs used for this period (acquired in October/November 2017 and July 2018) do not encompass the peak glacier ablation and velocity season during summer. In contrast, all other surveys were consistently carried out either in autumn (pre-2017) or summer (2018 onwards), ensuring comparability. Additionally, the surface fields from 2019-2021 lack results in the glacier's upper portion due to the limitations in the 2020 SfM model (Sec. 3.2.3).

The grid nodes used for DIC computations were subdivided into groups with similar kinematics according to the clusters identified by the GNSS measurements (Fig. 3.6b). These groups included the slow-moving terminal lobes, a transition zone between the lobes and the glacier's main transfer zone, the fast central zone, and the upper zone. Nodes near glacier moraines (where friction reduces surface velocity) and nodes in areas prone to decorrelation between years were excluded, e.g., the heavily crevassed region near the terminal lobe junction, areas with recurrent supraglacial lake formation, or areas where subglacial streams create cavities and pronounced ice cliffs. The remaining nodes were used to calculate the median annual velocity of each cluster. Fig. 3.6a visualizes these time series of the median velocity, along with the Interquartile Range (IQR, i.e., the difference between the 0.75 and 0.25 percentiles of the empirical dis-

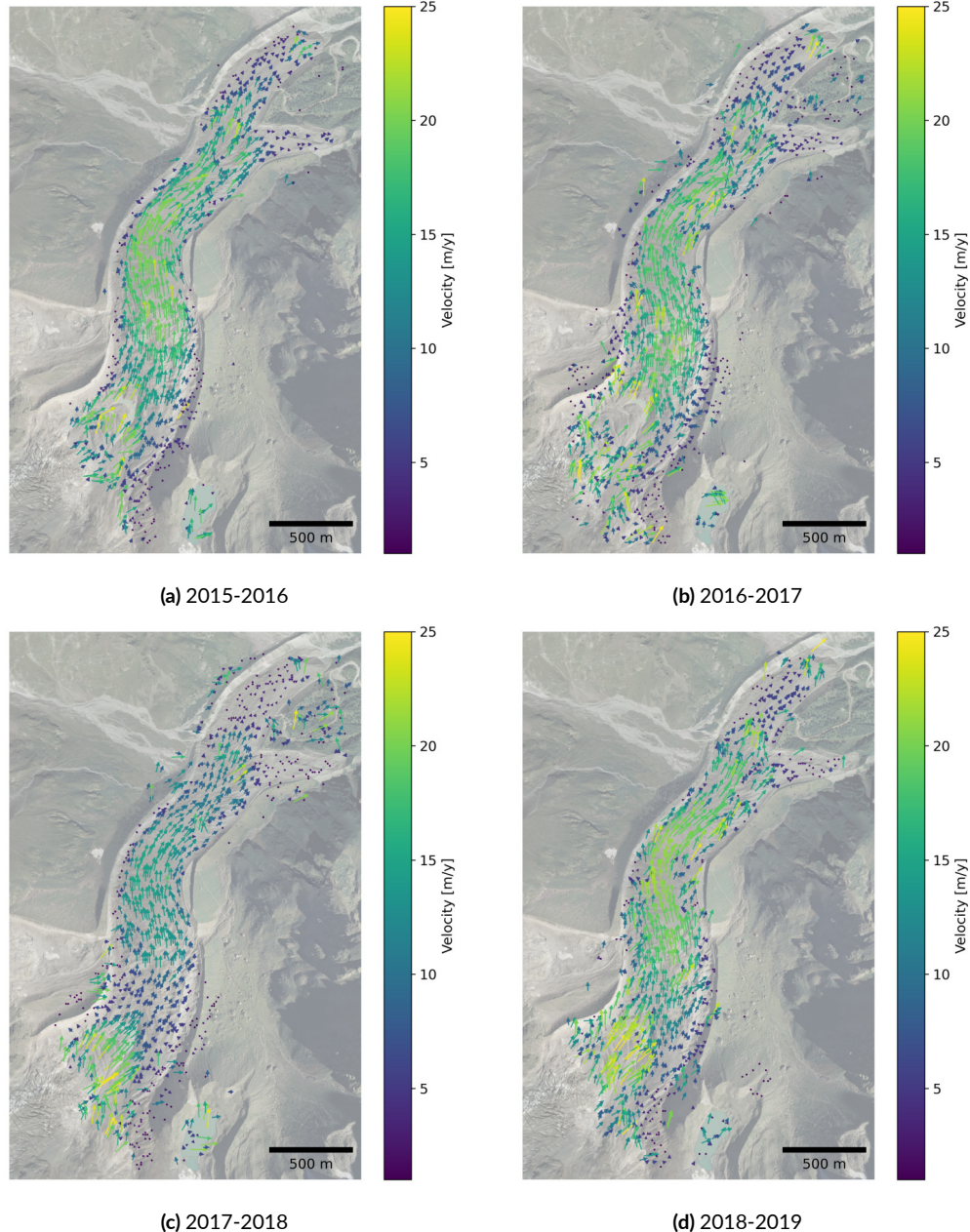


Figure 3.5: Surface velocity fields derived by DIC on pair of consecutive DSM between 2015 and 2018 and orthophotos between 2019 and 2023. (a) 2015-2016, (b) 2016-2017, (c) 2017-2018, (d) 2018-2019. All the surface velocity fields are overlapped to the 2009 orthophoto (De Gaetani et al., 2021) as reference. Refer to the Appendix B for better visualization of the orthophotos (continue on the next page).

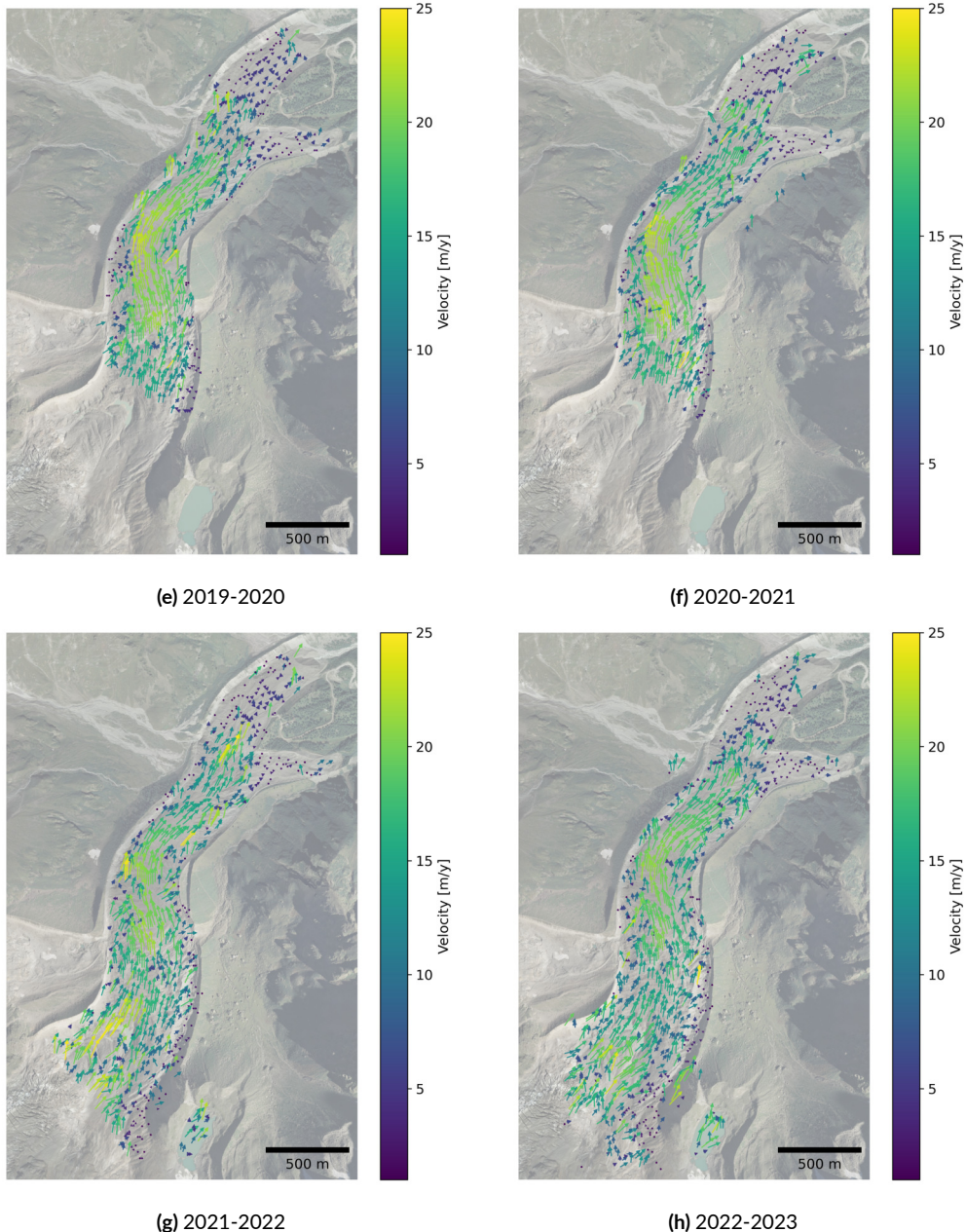


Figure 3.5: Surface velocity fields derived by DIC on pair of consecutive DSM between 2015 and 2018 and orthophotos between 2019 and 2023. (e) 2019-2020, (f) 2020-2021, (g) 2021-2022, (h) 2022-2023. All the surface velocity fields are overlapped to the 2009 orthophoto (De Gaetani et al., 2021) as reference. Refer to the Appendix B for better visualization of the orthophotos (cont.).

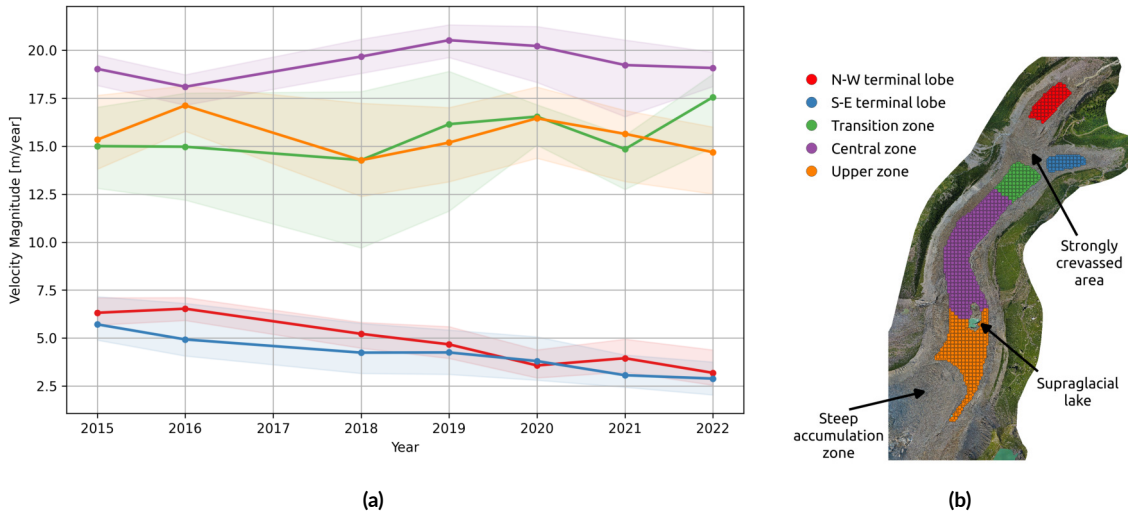


Figure 3.6: (a) Time series of median annual velocities for each cluster derived from DIC. The solid lines represent the median velocity, while the light-colored bands indicate the interquartile range, visualizing velocity variability within each cluster. Cluster colors correspond to the spatial mapping in (b). Marker positions correspond to the year of the master image used in DIC processing (i.e., the first image of each pair). The velocity value obtained from 2017–2018 was excluded from the time series; (b) Location of clusters with homogeneous movement patterns.

tribution) of the velocity vectors of each cluster for each year. Velocity values obtained by DIC between 2017 and 2018 were excluded from the analysis due to the velocity underestimation related to the change in the survey date.

A strong velocity contrast exists between the glacier’s slower terminal lobes and its faster-flowing central zone. The gradual velocity decline observed in the two terminal lobes is particularly interesting. This trend is probably related to the extreme ice thinning documented in this region in recent years, as a reduced ice thickness leads to slower flow velocities (Cuffey and Paterson, 2010, Jiskoot, 2011). A generalized glacier slowdown linked to a negative mass balance trend was also sensed in various regions around the globe between 1953 and 2009 (Heid and Kääb, 2012) and in High Mountain Asia between 2000 and 2017 (Dehecq et al., 2019). In fact, at the terminal lobes, where the ice thickness is smaller, the ice thinning is particularly relevant (see Sec. 3.4.3). Conversely, other clusters do not exhibit statistically significant velocity trends. Transition area (green) and upper zone (orange) clusters exhibit a higher IQR than others, indicating more significant variability in estimated velocity vectors within these regions. In contrast, velocities within other clusters appear more homogeneous.

The velocities obtained with DIC were compared with those measured by GNSS. To this end, pyLamma was employed to calculate displacements based on templates centered around GNSS-measured

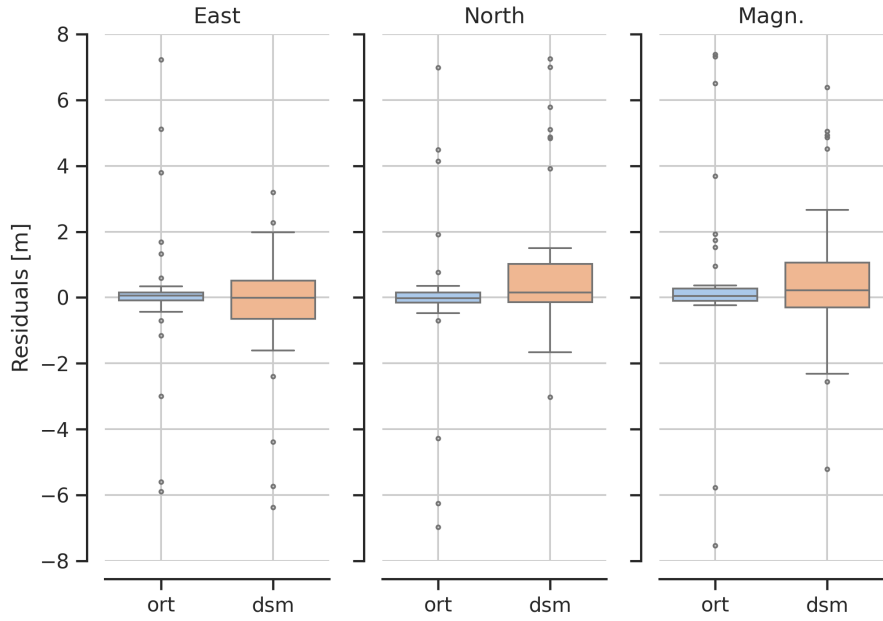


Figure 3.7: Boxplots of the differences between the displacements computed by GNSS measurements and those obtained by DIC on DSMs (from 2015 to 2018) and orthophotos (from 2018 to 2023). The differences are grouped by the image source (orthophoto –*ort* – and DSM) and divided into the East and North components and the magnitude of the displacement vectors.

target coordinates each year. To ensure a reliable comparison, 23 measurements of points located in particularly troublesome glacier areas, such as those near crevasses or where other morphological changes disrupt the image coherence between two consecutive years upon which DIC relies, were excluded from the comparison. Thus, a dataset of 106 GNSS measurements spanning the glacier was used to compute the differences in East and North directions and magnitude between GNSS and DIC displacement vectors.

Overall, the Median Absolute Deviation (MAD) of differences was 0.20 m, 0.18 m, and 0.22 m for East, North, and magnitude components, respectively. These values are comparable to the GSD of the orthophotos and DSMs, highlighting an overall accuracy in displacement estimation at the pixel level. Boxplots in Fig. 3.7 illustrate differences categorized by image source (DSM or orthophotos). While both groups show outliers exceeding 2 m, orthophotos yield significantly less dispersion than DSMs. Considering the magnitude of the displacement vectors, MAD for orthophotos was 0.17 m, contrasting with DSM's three times larger 0.58 m, highlighting a more robust performance of DIC on orthophotos compared to DSMs. Despite the challenges posed by snow partially covering the glacier and critical illumination conditions that forced the use of DSMs, the glacier surface displacement field was successfully com-

puted by DIC for the period between 2015 and 2018, albeit with a coarser accuracy.

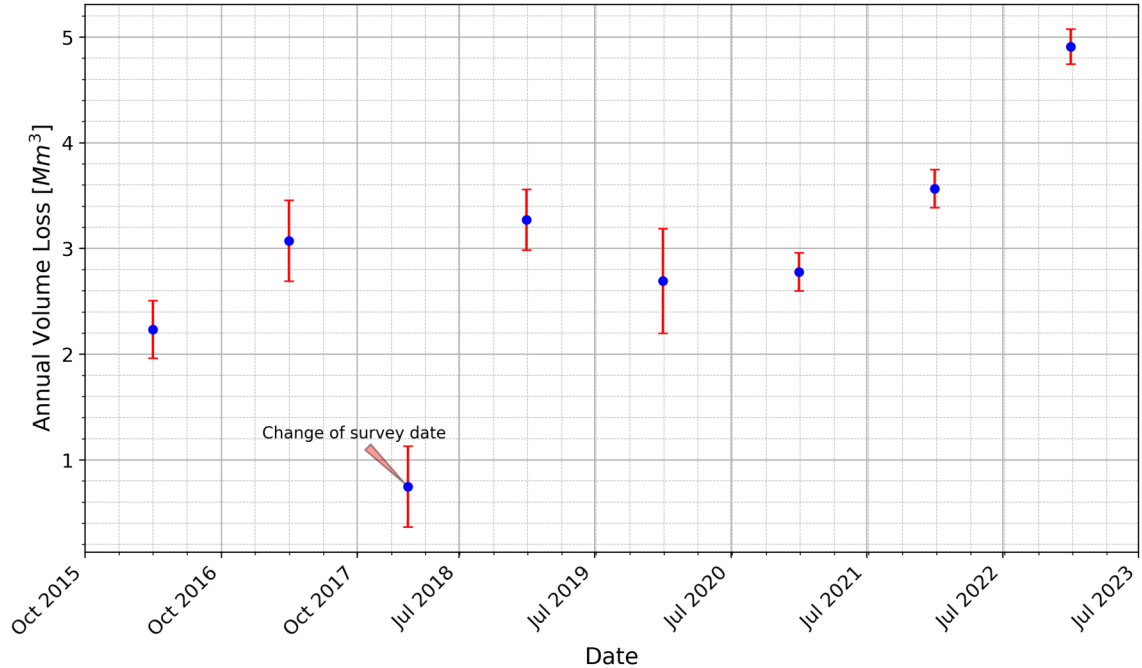
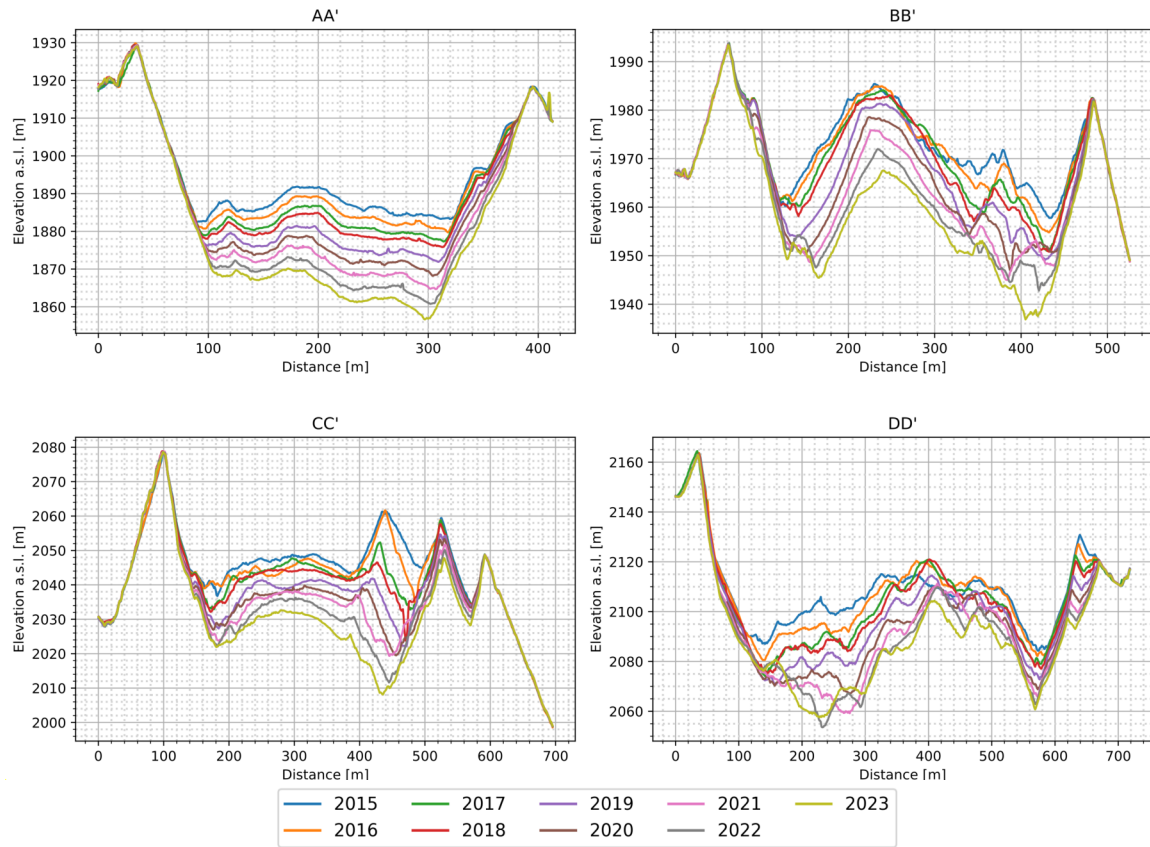


Figure 3.8: Yearly volume variation computed as the difference between DSM of consecutive years. The error bars represent the uncertainty of each value.

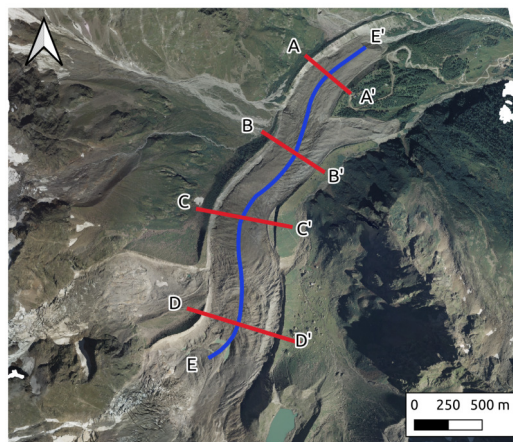
3.4.3 VOLUME VARIATIONS

Fig. 3.8 shows the annual ice volume loss for the glacier, with error bars indicating the estimated uncertainty in volume change (details in Section 3.3.3). On average, the glacier lost about $3.21 \times 10^6 \text{ m}^3$ of ice per year between 2015 and 2023. Notably, the time series reveals a concerning trend: ice loss is accelerating, with a non-linear increase in volume reduction from 2020 to 2023. In particular, the exceptionally hot and dry summer of 2022 left a significant mark, resulting in a notable volume loss of $4.90 \times 10^6 \text{ m}^3$ during 2022–2023. These findings align with those observed in other alpine glaciers, such as the Mont Blanc glaciers (Berthier et al., 2023).

Due to the transition of fieldwork from Autumn to Summer between 2017 and 2018, the volume loss computed from October 2017 to July 2018 primarily reflects wintertime and springtime variations. Therefore, it can not be directly compared with the annual average estimated for the other years. Moreover,



(a)



(b)

Figure 3.9: (a) Elevation profiles obtained from the DSM computed for the years 2015-2023 along four different cross-sections. (b) Location of cross-sections. Cross-sections are viewed from south to north.

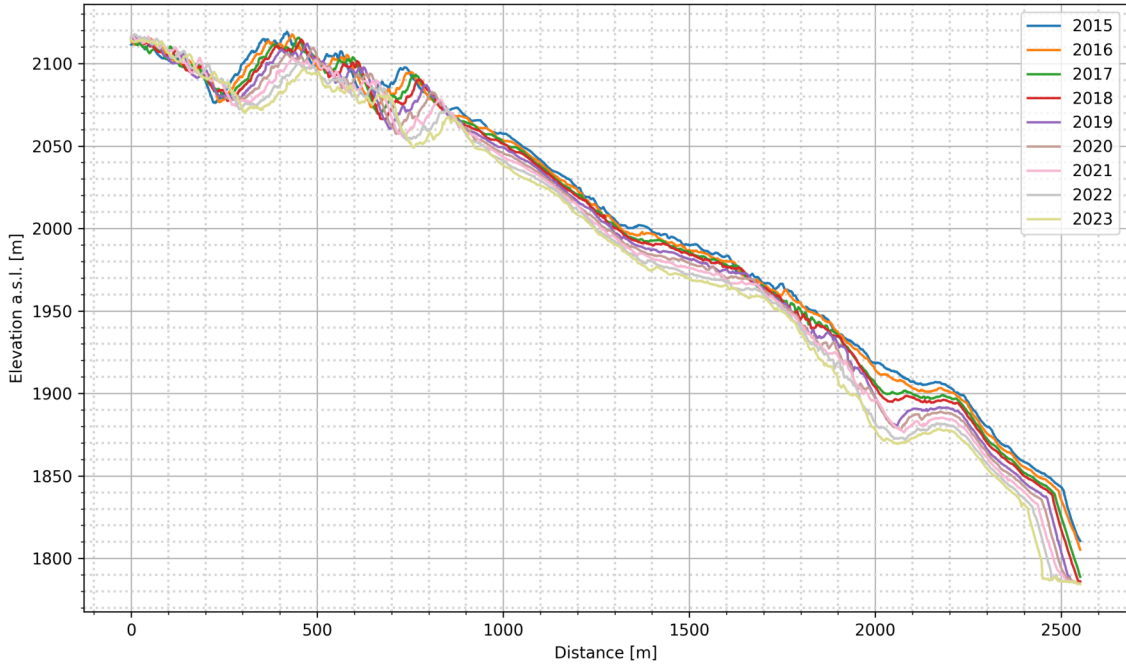


Figure 3.10: Longitudinal profiles of the glacier extracted each year along the centerline. The location of the profile is marked in Fig. 3.9b.

ice volume loss for 2019–2020 might be marginally underestimated due to significant geometric discrepancies in the photogrammetric model of the glacier’s upper portion, attributed to the absence of GCPs measured in situ during photo acquisition.

Excluding the period of 2017–2018, the year with the least ice ablation occurred between 2015 and 2016, amounting to $2.23 \times 10^6 \text{ m}^3$, while ice ablation peaked during 2022–2023. This trend emphasizes the sensitivity of glacier systems to climate variations and the need for continued monitoring to understand the evolving dynamics of glacial environments.

Fig. 3.9 presents elevation profiles of the glacier obtained annually at four distinct cross sections. The series of cross-section AA' extracted at the northern terminal lobe (Fig. 3.9a) shows a regular decrease in the glacier thickness ice loss rate of approximately 2 m y^{-1} . In the other sections situated in the central and upper parts of the glacier (sections BB', CC', and DD', Fig. 3.9b-d), the height reduction displays less regularity owing to the presence of crevasses. Moreover, the formation of local peaks and valleys within the debris, arising from locally different melting processes, significantly disrupts the glacier’s transfer zone. These features are particularly noticeable in the cross-sections BB' and DD'. Notably, the glacier’s stream-

wise right moraine experiences progressive sliding processes and collapses due to the diminishing support of the thinning glacier. This phenomenon is prominently observed in sections AA' and DD'.

Fig. 3.10 shows the evolution of the glacier's elevation profile along its centerline from 2015 to 2023. The most striking feature is the pronounced decrease in elevation near the heavily crevassed area separating the central body of the glacier from the northwestern terminal lobe (about 2000 m along the profile). There is a progressive increase in surface slope here, reflecting the recent formation of irregular valleys with steep ice cliffs. This has led to an increasingly chaotic distribution of debris cover, which has intensified in recent years. In addition, the profiles show a gradual downslope movement of the irregular ice mass accumulation in the upper glacier. Finally, the glacier's terminal ice cliff experienced a significant retreat of about 200 meters between 2015 and 2023.

3.5 GLACIER MASS VARIATIONS FROM 1977 TO 2023

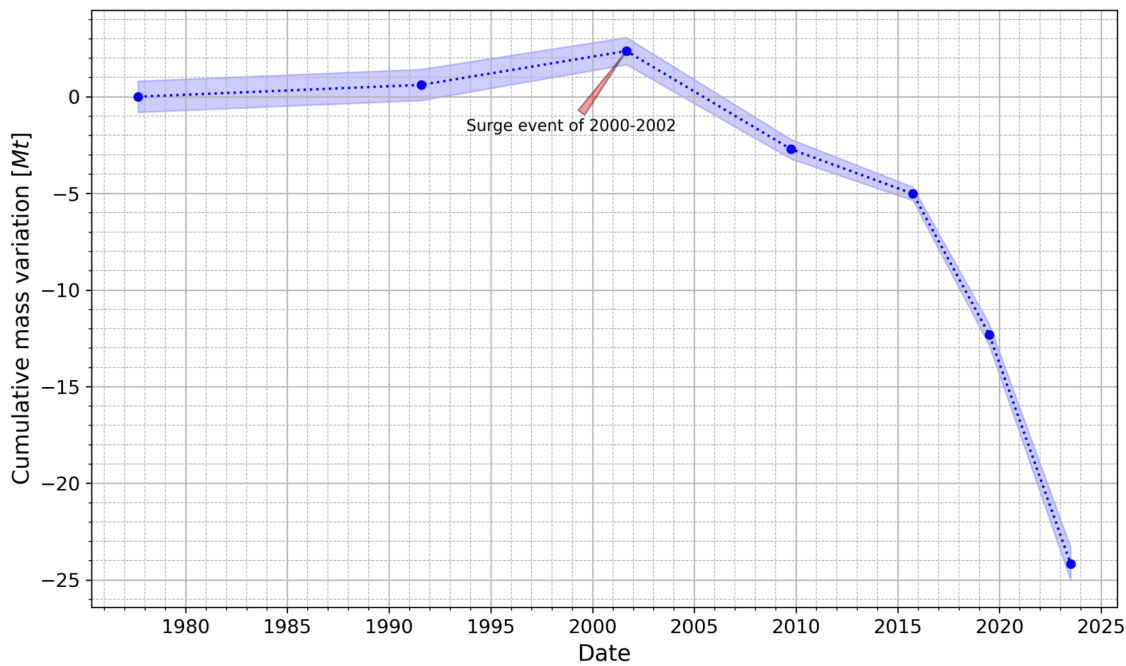


Figure 3.11: (a) Cumulative volumes variations Belvedere Glacier (1977-2023) with 1977 as the reference year (b) Cumulative ice mass variations (in megatonnes), assuming an ice density of $(850 \pm 60) \text{ kg m}^{-3}$, considering periods longer than 5 years (Huss, 2013).

By integrating historical aerial surveys (chapter 2) with repeated in-situ UAV measurements, this study

quantified long-term cumulative volume changes in Belvedere Glacier from 1977 to 2023. To convert volume variations into mass changes, an average ice density of $(850 \pm 60) \text{ kg m}^{-3}$ was assumed (Huss, 2013). However, as emphasized in Huss (2013), this constant density assumption is only reliable for geodetic mass balance assessments over periods longer than five years. Shorter intervals (< 3 years) introduce significant uncertainty due to potential density variations within the firn layer. To address this, geodetic mass balance calculations focused on three UAV surveys spaced approximately five years apart (2015, 2019, 2023) in addition to the previous aerial surveys.

Fig. 3.11 shows the estimated mass variations. The Belvedere Glacier increased in mass from 1977 to 2001, highlighting its expansion period. This trend abruptly ended with the 2000-2002 surge event, resulting in a significant mass gain around 2001. Subsequently, the glacier has undergone a continuous and dramatic retreat. As of 2023, the Belvedere Glacier has lost ~ 24 Mt of ice mass compared to its 1977 state.

3.6 AN OPEN-SOURCE FRAMEWORK FOR SHARING MONITORING RESULTS

The long-term monitoring campaign of Belvedere Glacier has produced a rich dataset that includes high-accuracy in-situ GNSS measurements, 3D point clouds, DSMs, and orthophotos derived from UAV photogrammetry. In recognition of the value of collaboration and open science, all point clouds, DSMs, and orthophotos for the entire glacier have been made publicly available under the GNU General Public License (GPL) version 3 license through a Zenodo repository⁸ (Ioli et al., 2023). All data are accompanied by a structured JSON file containing essential metadata, which allows researchers to use the data efficiently and encourages further scientific exploration by researchers across disciplines. This will allow replication of the analyses performed in this thesis, such as estimates of glacier velocity and volume change, and facilitate the study of other geomorphological processes, such as moraine collapse, or derive new insights into glacier dynamics.

To maximize accessibility for non-expert users, the 3D point clouds derived from all the surveys were converted to a Potree-compatible structure (Schütz et al., 2016) and uploaded to a web server. Potree is an open-source WebGL-based JavaScript library designed for web-based rendering of large-point clouds, and it offers versatile tools for handling 2D and 3D objects, scene navigation, and interaction, including measurements and cross-section profile extraction (Gaspari et al., 2024, Fascia et al., 2024). The 3D glacier models are accessible from any web browser (Fig. 3.12), allowing users to navigate through different years

⁸Belvedere Open Data: <https://doi.org/10.5281/zenodo.7842347>

and experience the evolution of the glacier over time⁹.

Additionally, a robust open-source relational database serves as the central repository for the monitoring campaign's outcomes, ensuring easy storage, use, and sharing. We chose PostgreSQL for its flexibility, permissive open-source license, and seamless ability to manage geospatial data through the PostGIS extension. Using a PostgreSQL database centralizes data storage, allows direct use within GIS software packages as well as remote public access (e.g., via a read-only web interface) while protecting sensitive internal data through customizable permission levels. The database primarily serves as a repository for field survey data, including details such as survey dates, instrument specifications, key acquisition parameters, and selected processing statistics. It also contains periodic GNSS measurements of photogrammetric targets and outputs from photogrammetric processes, including DSMs, orthophotos, derived glacier velocities, and volume changes.

Following the principles of relational databases, data is structured across multiple tables, with access facilitated by defined relationships using primary and foreign keys. The logical model of the database, shown in Fig. 3.13, describes the main tables and their relationships. Key components of the database include the *surveys* table, which contains information about each survey; the *points* table, which catalogs points that have been periodically GNSS surveyed; and the *measurements* table, which contains the actual GNSS measured coordinates. Each measurement is associated with a survey record, which allows retrieval of survey timing and instrumentation information used to collect the measurement, and a point record, which associates the measurement with a specific point label, allowing tracking of points in time. Each measurement can be associated with an image, stored in a separate table, to document the acquisition. In the *surveys* table, each survey is linked to its corresponding metadata stored in the *instruments* table, which contains information on all instruments used over the years, and the *flights* table, which includes details of each photogrammetric flight performed. In addition, each survey is associated with the products derived from the photogrammetric processing. This organizational structure streamlines data retrieval using SQL queries, enabling tasks such as extracting measurements from individual surveys or ranges of surveys and deriving displacement time series for specific points.

This structure defines the core of the database, which is intended for internal use. However, to improve accessibility and streamline data retrieval, a set of predefined queries has been used to create read-only views (i.e., read-only subsets of a database based on a query that runs on one or more tables) within a separate public schema. These views provide a higher level of abstraction and functions for accessing information such as the measured points for each year, identifying active points (i.e., targets still present on the glacier and not lost) by providing their most recent measurement, and automatically calculating a time

⁹Potree web app: <https://thebelvedereglacier.it/potree/index.php>



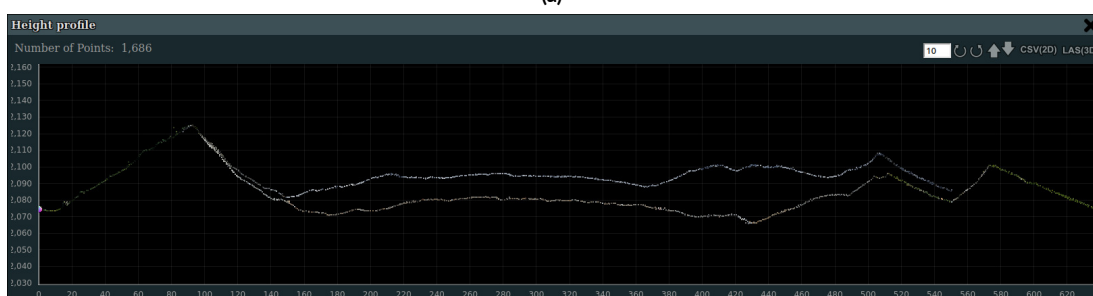
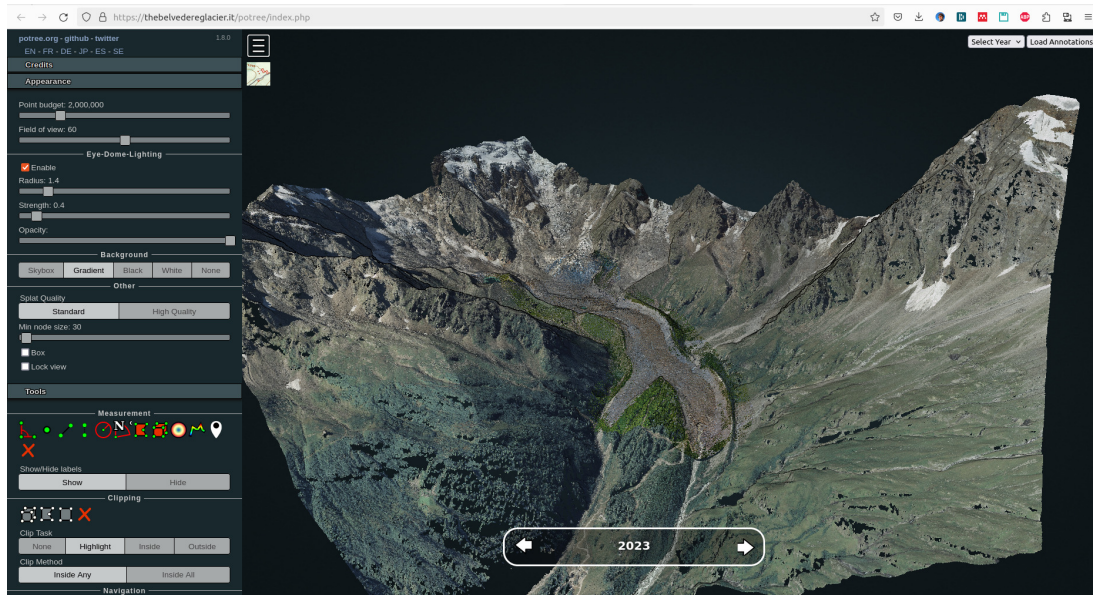


Figure 3.12: (a) Web platform based on Potree (Schütz et al., 2016) for exploring the photogrammetric point clouds of the Belvedere Glacier acquired during the different surveys. (b) Example of two cross sections extracted directly from the Potree web interface from the point clouds of 2023 and 2015 to easily estimate the glacier thinning.

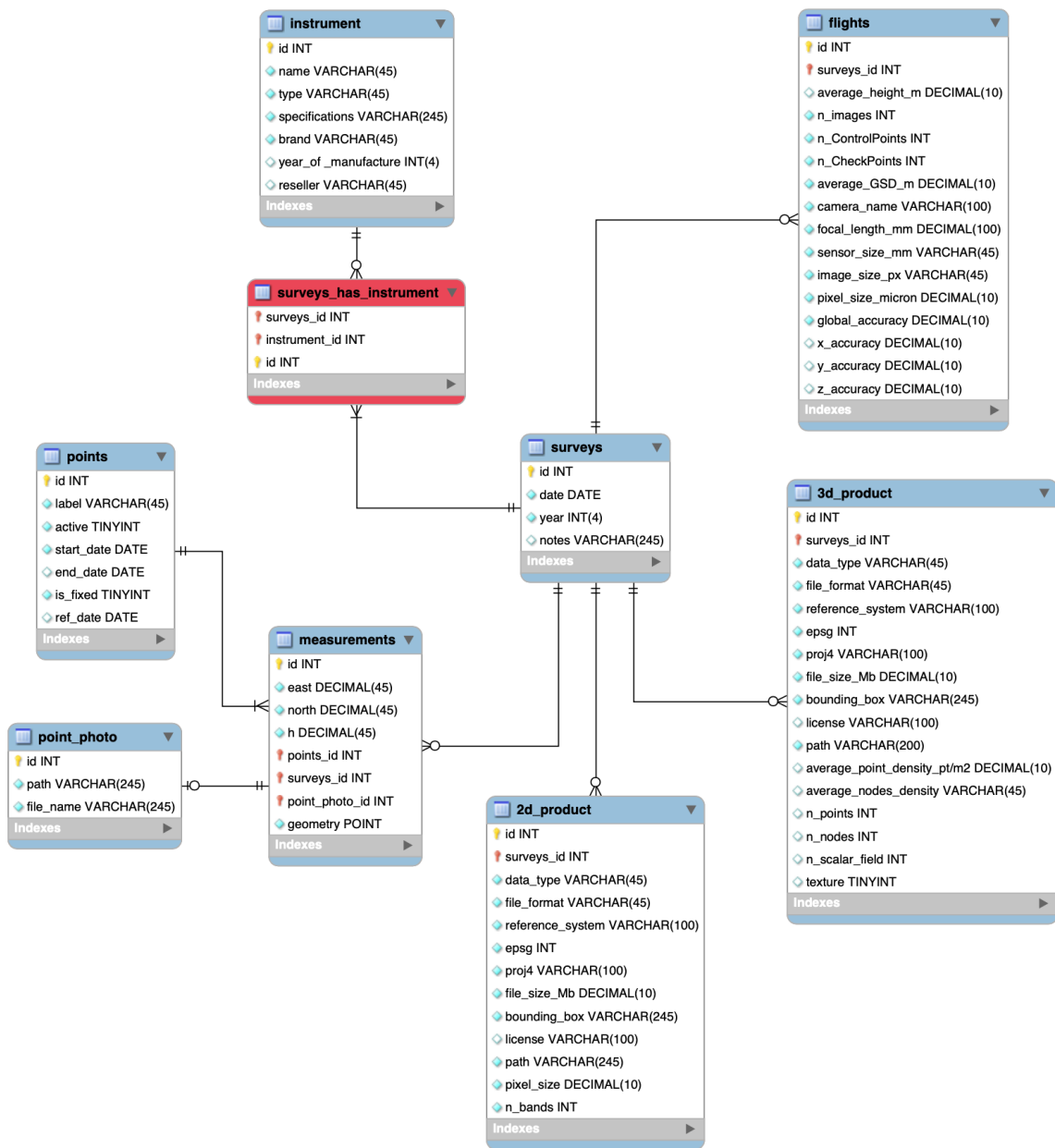


Figure 3.13: ERD diagram of the PostgreSQL database used for storing the Belvedere results.

series of displacements, velocities, and accelerations for each point by differentiating consecutive measurements. Additional functionalities encompass the automatic conversion of GNSS coordinates from the

geographic WGS84 reference system to the projected RDN2008 / UTM zone 32N reference system and vice versa. Furthermore, the database facilitates the computation of orthometric heights for each measurement via bilinear interpolation using the Italian Geoid model ITALGEO05 (Barzaghi et al., 2007).

The database currently stores 456 GNSS measurements from 85 distinct points measured across 19 surveys. Thanks to the PostGIS extension, information can be easily displayed on a map canvas in GIS software like QGIS, together with predefined visualization styles, facilitating visual analysis (Fig. 3.14). Furthermore, researchers and non-expert users can access the public schema of the database via a dedicated web platform¹⁰. Here, users can effortlessly view the GNSS measurements on a web map, extract time-series information, and download them for their scientific inquiries. Combining this with a web-based visualization of the 3D point clouds with Potree gives a complete overview of the outcomes of the Belvedere Glacier monitoring campaign.

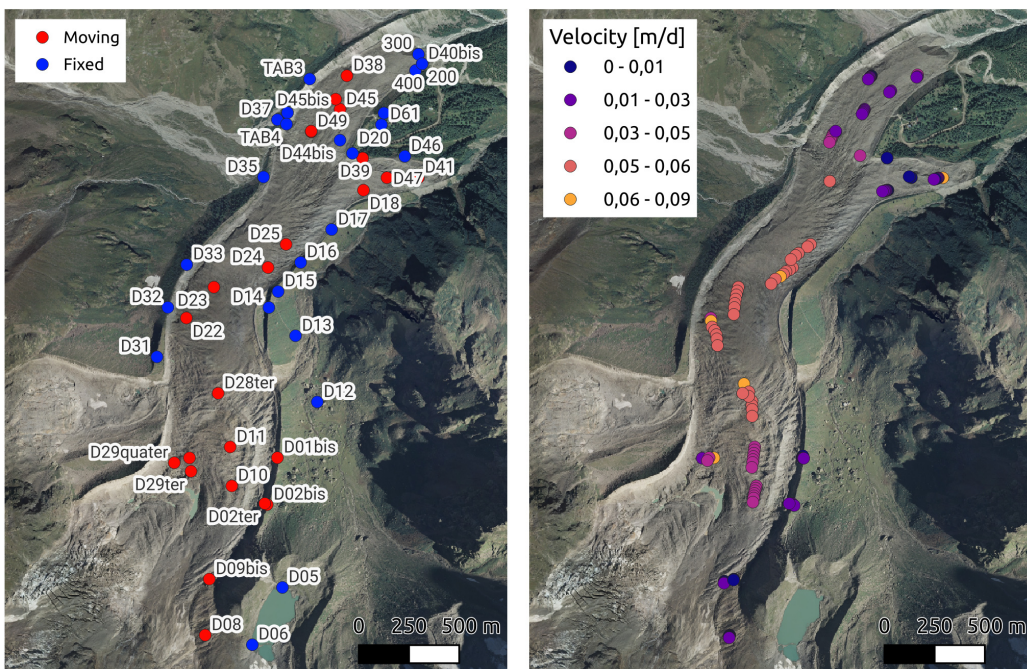


Figure 3.14: Example of georeferenced layer queries from the PostgreSQL database using QGIS. The layer symbology is directly stored within the database and is automatically loaded into the QGIS project upon layer loading.

¹⁰Web app <https://thebelvedereglacier.it>

References

- Barzaghi, R., Borghi, A., Carrion, D., & Sona, G. (2007). Refining the estimate of the italian quasi-geoid. *Bollettino di Geodesia e Scienze Affini, Anno LXVI*, 145–160.
- Berthier, E., Vincent, C., & Six, D. (2023). Exceptional thinning through the entire altitudinal range of mont-blanc glaciers during the 2021/22 mass balance year. *Journal of Glaciology*, (pp. 1–6), <https://doi.org/10.1017/jog.2023.100>.
- Blöthe, J. H., Halla, C., Schwalbe, E., Bottegal, E., Trombotto Liaudat, D., & Schrott, L. (2021). Surface velocity fields of active rock glaciers and ice-debris complexes in the central andes of argentina. *Earth Surface Processes and Landforms*, 46(2), 504–522, <https://doi.org/10.1002/esp.5042>.
- Cramer, M., Przybilla, H. J., & Zurhorst, A. (2017). UAV cameras: Overview and geometric calibration benchmark. *Int. Arch. Photogramm. Remote Sens. Spatial Inf. Sci.*, 42(2W6), 85–92, <https://doi.org/10.5194/isprs-archives-XLII-2-W6-85-2017>.
- Cuffey, K. & Paterson, W. (2010). *The physics of glaciers*. Burlington : Butterworth Heinemann-Elsevier.
- Dall'asta, E. & Roncella, R. (2014). A comparison of semiglobal and local dense matching algorithms for surface reconstruction. In *Int. Arch. Photogramm. Remote Sens. Spatial Inf. Sci.*, volume XL-5 (pp. 187–194).
- De Gaetani, C. I., Ioli, F., & Pinto, L. (2021). Aerial and UAV Images for Photogrammetric Analysis of Belvedere Glacier Evolution in the Period 1977–2019. *Remote Sensing* 2021, Vol. 13, Page 3787, 13(18), 3787, <https://doi.org/10.3390/RS13183787>.
- Debella-Gilo, M. & Kääb, A. (2011). Sub-pixel precision image matching for measuring surface displacements on mass movements using normalized cross-correlation. *Remote Sens. Environ.*, 115(1), 130–142, <https://doi.org/10.1016/j.rse.2010.08.012>.
- Dehecq, A., et al. (2019). Twenty-first century glacier slowdown driven by mass loss in high mountain asia. *Nat. Geosci.*, 12(1), 22–27, <https://doi.org/10.1038/s41561-018-0271-9>.
- Dehecq, A., Gourmelen, N., & Trouve, E. (2015). Deriving large-scale glacier velocities from a complete satellite archive: Application to the pamir–karakoram–himalaya. *Remote Sensing of Environment*, 162, 55–66, <https://doi.org/10.1016/j.rse.2015.01.031>.
- Dematteis, N. & Giordan, D. (2021). Comparison of digital image correlation methods and the impact of noise in geoscience applications. *Remote Sensing*, 13(2), <https://doi.org/10.3390/rs13020327>.
- Dematteis, N., Giordan, D., & Allasia, P. (2019). Image classification for automated image cross-correlation applications in the geosciences. *Applied Sciences*, 9(11), <https://doi.org/10.3390/app9112357>.
- Dematteis, N., Giordan, D., Crippa, B., & Monserrat, O. (2022). Fast local adaptive multiscale image matching algorithm for remote sensing image correlation. *Computers & Geosciences*, 159, 104988, <https://doi.org/10.1016/j.cageo.2021.104988>.

- Dematteis, N., Troilo, F., Scotti, R., Colombaroli, D., Giordan, D., & Maggi, V. (2024). The use of terrestrial monoscopic time-lapse cameras for surveying glacier flow velocity. *Cold Reg. Sci. Technol.*, 222, 104185, <https://doi.org/10.1016/j.coldregions.2024.104185>.
- Fascia, R., Barbieri, F., Gaspari, F., Ioli, F., & Pinto, L. (2024). From 3d survey to digital reality of a complex architecture: A digital workflow for cultural heritage promotion. *The International Archives of the Photogrammetry, Remote Sensing and Spatial Information Sciences*, XLVIII-2/W4-2024, 205–212, <https://doi.org/10.5194/isprs-archives-XLVIII-2-W4-2024-205-2024>.
- Fitch, A., Kadyrov, A., Christmas, W. J., & Kittler, J. (2002). Orientation correlation. In *BMVC* (pp. 1–10).: Citeseer.
- Fraser, C. S. (2013). Automatic camera calibration in close range photogrammetry. *Photogramm. Eng. Rem. S.*, 79(4), 381–388, <https://doi.org/10.14358/PERS.79.4.381>.
- Gaspari, F., Barbieri, F., Fascia, R., Ioli, F., & Pinto, L. (2024). An open-source web platform for 3d documentation and storytelling of hidden cultural heritage. *Heritage*, 7(2), 517–536, <https://doi.org/10.3390/heritage7020025>.
- Gindraux, S. (2019). *The potential of UAV photogrammetry for hydro-glaciological forecasts*. Doctoral thesis, ETH Zurich.
- Heid, T. & Kääb, A. (2012). Repeat optical satellite images reveal widespread and long term decrease in land-terminating glacier speeds. *The Cryosphere*, 6(2), 467–478, <https://doi.org/10.5194/tc-6-467-2012>.
- Heid, T. & Kääb, A. (2012). Evaluation of existing image matching methods for deriving glacier surface displacements globally from optical satellite imagery. *Remote Sens. Environ.*, 118, 339–355, <https://doi.org/https://doi.org/10.1016/j.rse.2011.11.024>.
- Huss, M. (2013). Density assumptions for converting geodetic glacier volume change to mass change. *The Cryosphere*, 7(3), 877–887, <https://doi.org/10.5194/tc-7-877-2013>.
- Ioli, F., De Gaetani, C., Barbieri, F., Gaspari, F., Pinto, L., & Rossi, L. (2023). Belvedere glacier long-term monitoring open data. Zenodo. <https://doi.org/10.5281/zenodo.7842348>.
- James, M. R., Antoniazza, G., Robson, S., & Lane, S. N. (2020). Mitigating systematic error in topographic models for geomorphic change detection: accuracy, precision and considerations beyond off-nadir imagery. *Earth Surface Processes and Landforms*, 45(10), 2251–2271, <https://doi.org/10.1002/esp.4878>.
- James, M. R. & Robson, S. (2014). Mitigating systematic error in topographic models derived from uav and ground-based image networks. *Earth Surface Processes and Landforms*, 39(10), 1413–1420, <https://doi.org/10.1002/esp.3609>.
- James, M. R., Robson, S., & Smith, M. W. (2017). 3-d uncertainty-based topographic change detection with structure-from-motion photogrammetry: precision maps for ground control and directly georeferenced surveys. *Earth Surface Processes and Landforms*, 42(12), 1769–1788, <https://doi.org/10.1002/esp.4125>.
- Jiskoot, H. (2011). Dynamics of glaciers. *physical Research*, 92, 9083–9100.

Roncella, R., Forlani, G., & Diotri, F. (2021). A monte carlo simulation study on the dome effect. *The International Archives of the Photogrammetry, Remote Sensing and Spatial Information Sciences*, XLIII-B2-2021, 53–60, <https://doi.org/10.5194/isprs-archives-XLIII-B2-2021-53-2021>.

Schütz, M. et al. (2016). Potree: Rendering large point clouds in web browsers. *Technische Universität Wien, Wieden*.

4

Deep learning low-cost photogrammetry for 4D short-term glacier monitoring (2022-2023)

THIS CHAPTER IS BASED ON:

- Ioli, F., Dematteis, N., Giordan, D., Nex, F., Pinto, L. (2024). Deep Learning Low-cost Photogrammetry for 4D Short-term Glacier Dynamics Monitoring. *PFG*, <https://doi.org/10.1007/s41064-023-00272-w>.
- Ioli, F., Barbieri, F., Gaspari, F., Nex, F., and Pinto, L. (2023). ICEPy4D: a Python Toolkit for Advanced Multi-epoch Glacier Monitoring with Deep-learning Photogrammetry, *Int. Arch. Photogramm. Remote Sens. Spatial Inf. Sci.*, XLVIII-1/W2-2023, 1037-1044, <https://doi.org/10.5194/isprs-archives-XLVIII-1-W2-2023-1037-2023>.

- Ioli, F., Bruno, E., Calzolari, D., Galbiati, M., Mannocchi, A., Manzoni, P., Martini, M., Bianchi, A., Cina, A., De Michele, C., and Pinto, L. (2023). A Replicable Open-source Multi-camera system for Low-cost 4D Glacier Monitoring, *Int. Arch. Photogramm. Remote Sens. Spatial Inf. Sci.*, XLVIII-M-1-2023, 137–144, <https://doi.org/10.5194/isprs-archives-XLVIII-M-1-2023-137-2023>.

4.1 INTRODUCTION

Climate change is accelerating the evolution of alpine glaciers, leading to rapid ice melt and increased frequency of collapses during summer months. This accelerated melting can trigger various glaciological, geomorphological, and slope stability hazards, including avalanches, glacier outbursts, rockfalls, permafrost-related collapses, and moraine instability (Käab et al., 2005, Faillettaz et al., 2015, Chiarle et al., 2023, Nigrelli et al., 2024). Consequently, short-term observations (e.g., daily) are crucial for deeply understanding glaciers' associated processes and their relation with external forces, particularly the air temperature.

Permanent ground-based solutions are generally the preferred solution for short-term monitoring. Among these, terrestrial SAR (Strozzi et al., 2020) and TLS (Hendrickx et al., 2022, Voordendag et al., 2023) have recently gained significant attention. SAR, in particular, offers the advantage of all-weather and day-and-night imaging, making it suitable for real-time monitoring and early-warning systems (Dematteis and Giordan, 2021, Noferini et al., 2009). However, both ground-based SAR and permanent TLS are expensive and require complex logistics. These limitations prevent their applications in distributed sites at the regional scale, but their usage may be limited to investigating hazardous locations.

Fixed time-lapse cameras are affordable alternatives to SAR and permanent TLS to acquire short-term qualitative and quantitative information on glacier dynamics (Giordan et al., 2016, James et al., 2016, Maas et al., 2006, Messerli and Grinsted, 2015). DIC can be used on sequences of images from terrestrial time-lapse cameras to estimate glacier surface velocity by tracking patterns on image sequences. However, with a single camera, external DSMs are required to convert 2D-pixel displacements obtained by DIC into 3D displacement vectors.

Although most of the existing literature focuses on single time-lapse cameras, in recent years, some studies have been conducted on multi-camera systems for monitoring glaciologic and geomorphological processes. Even though it was not applied to glaciers, Roncella et al. (2014) first developed a pure stereoscopic system for monitoring a moving landslide, proposing a fully photogrammetric approach to derive a 3D model of the scene and detecting collapses without the need for a priori DSMs. Schwalbe and Maas (2017) proposed an application of multiple time-lapse cameras for deriving a coarse digital surface model using SfM to estimate a distance map, which was used to scale displacement vectors derived by DIC. Marsy et al. (2020) used a stereo camera system to construct a glacier DSM and back-projected the DIC-derived velocity field. However, their main focus was on deriving glacier kinematics rather than achieving a short-term 3D reconstruction of the glacier. Recently, Kneib et al. (2022) used a multi-camera system to estimate sub-seasonal variability of supraglacial ice cliff melt rates. Taylor et al. (2023) successfully tested a low-cost Raspberry Pi with a high-quality camera module and a telephoto lens mounted on a boat for reconstruct-

ing a glacier calving front by SfM, achieving sub-meter accuracy when compared to a UAV benchmark. [Blanch et al. \(2023\)](#) proposed a low-cost fixed multi-camera system for natural hazard monitoring using a photogrammetric approach, and they achieved sub-decimetric change detection sensitivity in rockfall detection.

Nevertheless, all of the aforementioned studies used small or normal camera baselines, which makes it easier for traditional photogrammetric methods to find corresponding points between images and achieve 3D scene reconstruction. However, in mountainous terrain, finding stable, accessible locations with ideal baseline and viewing geometry can be challenging. Conversely, wide baselines or highly convergent views hinder a 3D reconstruction by traditional photogrammetry.

This chapter presents a pilot study on short-term 4D monitoring of the Belvedere Glacier glacier using a low-cost stereo-camera system with a wide baseline. The study investigates daily glacier dynamics by calculating surface movement, ice volume loss, and glacier retreat of a debris-covered alpine glacier. The proposed methodology integrates 3D reconstruction from stereo cameras for volume estimation and utilizes DIC on monoscopic cameras to derive surface velocities. By utilizing state-of-the-art Deep Learning (DL) matching techniques, this approach overcomes the challenges posed by the wide camera baselines, and it allows for accurately reconstructing the scene under sub-optimal viewing conditions.

The objective of this work is twofold: (i) to demonstrate the feasibility and effectiveness of using a cost-effective photogrammetric solution for short-term glacier monitoring using a DL approach; (ii) to investigate the short-term relationship between air temperature, ice volume variations, and glacier surface velocity for an alpine debris-covered glacier. By combining stereo and monoscopic image sequence analysis, this study contributes to a better understanding of sub-seasonal glacier dynamics, particularly in the context of changing climate conditions and rising temperatures.

4.2 IMAGE MATCHING IN CHALLENGING SCENARIOS

Identifying homologous or tie points in pairs of images is the foundational task in photogrammetry for non-contact 3D measuring methods. These points allow for orienting single, stereo, or multi-image configurations. Applications span a wide range, depending on object size and the requisite level of accuracy, encompassing industrial, architectural, engineering, and remote sensing applications, requiring measurements on sparse control points or evaluations on dense reconstructions via multi-view dense image matching. Classical photogrammetric outputs include 3D point clouds, orthophotos, and digital surface models.

Historically, local image features (also known as keypoints or interest points) were initially identified manually on images. Automatic approaches gradually emerged between the 1980s and the early 2000s

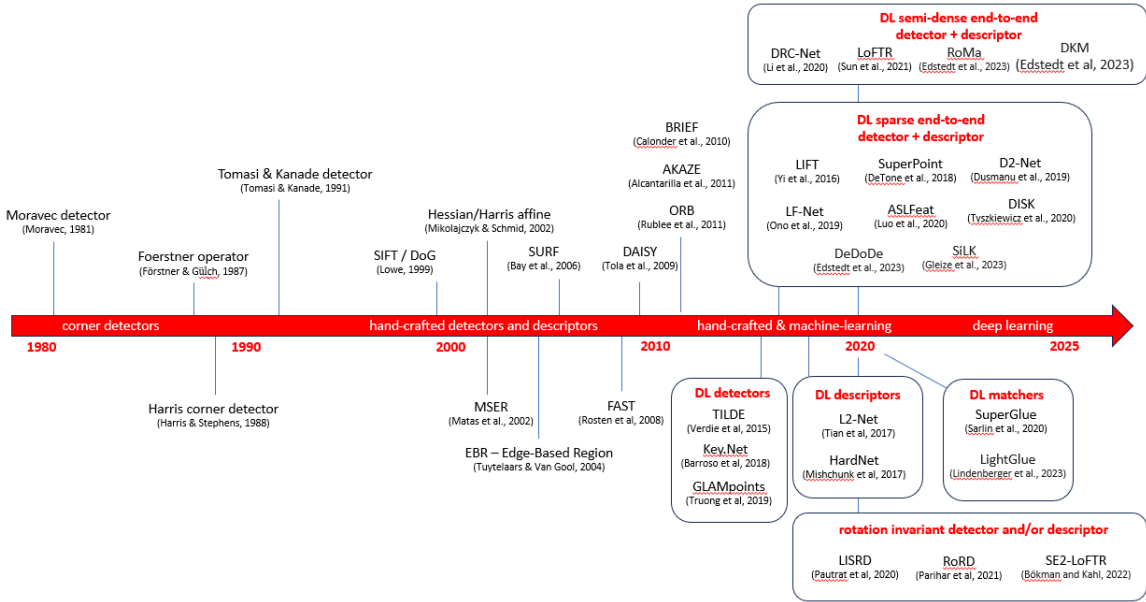


Figure 4.1: Timeline development of detectors, descriptors, and matches from preliminary works, hand-crafted, machine-learning, and deep-learning local features (figure adapted from Remondino et al. (2022)).

by developing algorithms that effectively identify characteristic features on images (Lowe, 2004). Image detectors should identify repeatable keypoints across different images, described by a descriptor vector that characterizes the keypoint’s neighborhood. This allows for similarity matching across different image views. These detectors and descriptors should exhibit invariance to scale differences, arbitrary rotations, radiometric changes, and multi-view perspective projections. Moreover, descriptors should be distinctive and unambiguous.

Several groundbreaking works emerged, significantly contributing to the advancement of fully automatic SfM software packages. Particularly noteworthy is SIFT (Scale Invariant Feature Transform) (Lowe, 2004), which, despite its acknowledged limited invariance to illumination and affine transformations, marked a significant milestone as the first detector and descriptor demonstrating sufficient invariance to scale and rotations, making it suitable for a broad spectrum of applications. Even today, SIFT remains the benchmark feature among traditional approaches (i.e., non-deep learning-based, often referred to as hand-crafted methods) (Jin et al., 2021).

Fig. 4.1 illustrates a timeline of the evolution of local features. Initially, corner detectors were utilized in the early works (Harris and Stephens, 1988), transitioning to blob detectors that achieved a broader degree of scale and rotation invariance (Lowe, 2004). As computational efficiency played a pivotal role,

SURF (Bay et al., 2006) was developed with the explicit goal of improving upon SIFT computation time, whilst ORB (Rublee et al., 2011) was engineered as a binarized feature tailored for real-time applications.

However, these methods have limitations when dealing with large camera baselines, strong viewpoint differences, and strong radiometric or scale variations (Yao et al., 2021). Large camera baselines and changes in viewpoint lead to complex distortions, missing content, and occlusions between corresponding objects, making matching difficult (Jin et al., 2021, Ioli et al., 2024). Other challenging scenarios for traditional local features include matching historical images with contemporary datasets, e.g., for cultural heritage valorization (Maiwald et al., 2021, 2023) or multitemporal aerial datasets (Farella et al., 2022, Zhang et al., 2021).

Since 2015, a novel category of DL-based approaches has emerged to address the limitations of existing features. Initially, these methods involved independently training detectors and descriptors on extensive datasets comprising multi-temporal images, challenging illumination and perspective conditions, and wide baselines (Mishchuk et al., 2018). Subsequently, there has been a shift towards jointly training detectors and descriptors, starting with the seminal work of LIFT (Yi et al., 2016), followed by other end-to-end DL approaches such as LF-Net (Ono et al., 2018), SuperPoint (DeTone et al., 2018), and ASLFeat (Luo et al., 2020). Generally, any combination of hand-crafted and DL approaches is feasible (Jin et al., 2021).

Additionally, the matcher component can also be trained using DL techniques. A pioneering and groundbreaking approach in this regard was SuperGlue (Sarlin et al., 2020), which makes use of an attention-based architectures (Vaswani et al., 2023) to dramatically improve matching results by exploiting self- (intra-image) and cross- (inter-image) attention to leverage both spatial relationships of the keypoints and their visual appearance. SuperGlue has been recently followed by a faster update named LightGlue (Lindenberger et al., 2023). Recently, semi-dense matchers such as LoFTR (Sun et al., 2021) and RoMa (Edstedt et al., 2023) have been developed. However, as they are detector-free matchers, they can identify tie points only on image pairs. As these semi-dense matchers are not designed to build tracks of features in multiple images, they are not suitable for multi-view image orientation.

Several works have proved the effectiveness of DL approaches against varying illumination conditions, multi-temporal datasets, wide baselines, and significantly different view angles. These challenging scenarios include glacier monitoring with wide camera baselines (Ioli et al., 2023, 2024), multi-temporal image matching (Maiwald et al., 2023), multi-temporal co-registration problems (Maiwald et al., 2021, Morelli et al., 2022), visual-odometry and SLAM (Morelli et al., 2023), aerial triangulation (Remondino et al., 2022) and in terrestrial laser scanning point cloud registration (Markiewicz et al., 2023). Despite these advantages, well-known limitations of DL approaches are their computational complexity, limited scale and rotation invariance of the descriptors and their application on high-resolution images.

4.3 THE LOW-COST STEREOSCOPIC SYSTEM

A low-cost stereoscopic camera system was designed to monitor the Belvedere Glacier's short-term evolution. The stereoscopic system consists of two autonomous and independent monitoring units. Each unit consists of an off-the-shelf Digital Single-Lens Reflex (DSLR) camera, a circuit for scheduling image acquisition and controlling the system, a solar-based power supply system, and a case for protecting the system from the harsh environment. The core of each monitoring unit is the controlling circuit, which is composed of an Arduino microcontroller for camera triggering and a Raspberry Pi Zero with a SIM card for sending images to a remote server via a GSM network (Fig. 4.2). The total cost of each unit was less than €2000, including camera and lens (Ioli et al., 2023).

The system was designed and built by adapting to the alpine environment an existing open-source model developed by Greig Sheridan and published on GitHub¹. A key aspect of the project was to ensure easy assembly and realization of the system to guarantee future replications and improvements.

This section describes the monitoring system in detail and its installation at the Belvedere Glacier.

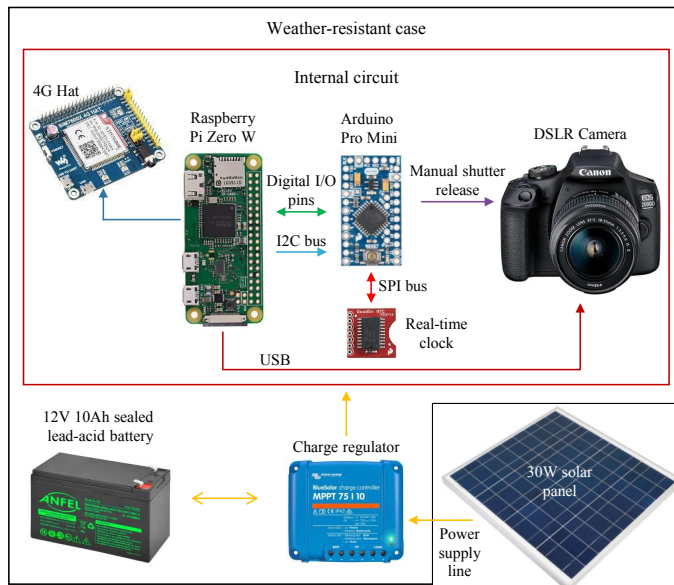


Figure 4.2: Scheme of a single monitoring station's proposed acquisition system configuration. Arrows indicate the direction of signal initiation. Image adapted from Greig Sheridan's repository.

¹Greig Sheridan's Intervalometer repository: <https://github.com/greiginsydney/Intervalometer>

4.3.1 POWER SUPPLY

Each monitoring unit has its autonomous power supply line (yellow arrows in Fig. 4.2) provided by a solar panel combined with a sealed lead-acid battery. An MPPT (Maximum Power Point Tracker) charge regulator directly connects with the unit's internal circuit, providing a regular current supply to the battery and the load and exploiting all the power generated by the panel. This regulator prevents any excess current that may damage the connected device, thus increasing the system's reliability. Its battery-life-saving algorithm modulates the load disconnection level so that a nearly 100% recharge is achieved about once every week. In case of battery discharging, the whole system is switched off until the battery is fully recharged.

The whole monitoring system is designed to minimize power consumption, e.g., by powering off devices responsible for the highest power consumption when not needed. Estimating the system's energy consumption guided the choice of the power supply line components, including the battery and the associated panel. To this end, the Photovoltaic Geographical Information System (PVGIS)², a tool provided by the European Commission, was used. PVGIS can estimate the performance of off-grid photovoltaic systems according to the installation site, and it is supported by a database and algorithms for calculating solar radiation. After tuning the parameters for the Belvedere Glacier location and the system consumption, we ended up with the specifications of a solar panel power of 30 W, a battery voltage of 12 V, and a capacity of 10 Ah. Some compromises were made, accepting that the system might not be sufficiently powered for a few days in the months with the lowest solar radiation (November, December, January, and February).

4.3.2 CONTROLLING CIRCUIT AND ACQUISITION SCHEDULING

The internal electronic circuit (red box in Fig. 4.2) of the monitoring unit is the only load connected to the power supply and is responsible for all the system's control and scheduling functionalities. Its components are a real-time clock (number 3 in Fig. 4.3) with a 12 mm coin-cell backup battery, an Arduino microcontroller (Pro Mini 328 3.3V 8MHz, number 4 in Fig. 4.3), a Raspberry Pi Zero W with 128 GB SD memory card (number 6 in Fig. 4.3), and minor elements for connections, isolation (capacitors and optoisolators numbers 1 and 5 in Fig. 4.3), and voltage regulations (numbers 2 in Fig. 4.3). The circuit was realized manually by soldering wires and components on a stripboard (see Fig. 4.3). After some testing, the final version of the circuit was implemented on a more compact PCB (Printed Circuit Board), with all the components soldered in pre-defined positions, connected by conductive transmission lines printed directly on the board (Fig. 4.4).

²PVG tool https://re.jrc.ec.europa.eu/pvg_tools/en/

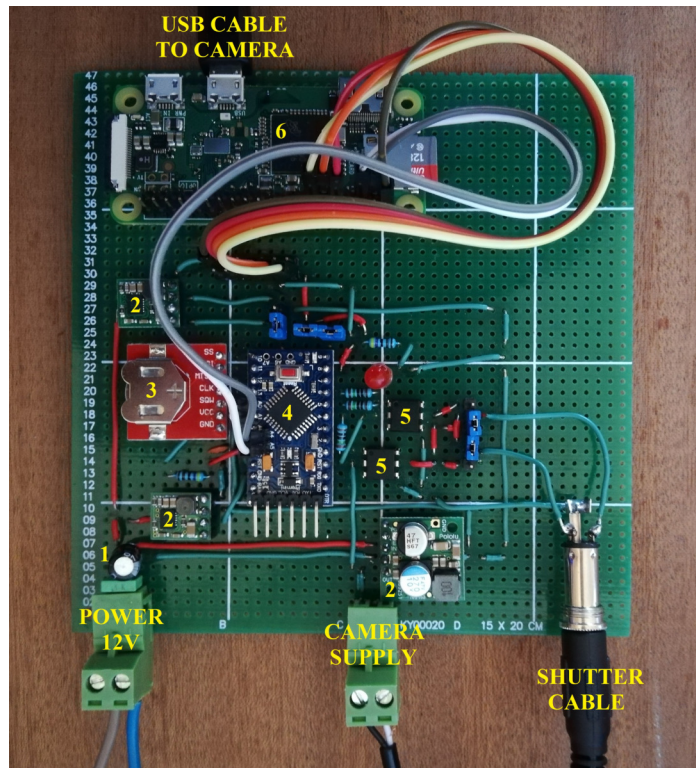


Figure 4.3: Prototyping stripboard on which are soldered the main components of the internal circuit: capacitors (1), voltage regulators (2), real-time clock with coin-cell battery (3), Arduino Pro Mini (4), optoisolators (5), and Raspberry Pi Zero W (6).

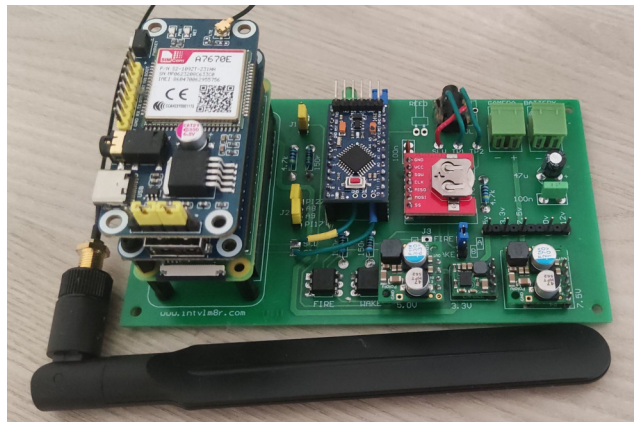


Figure 4.4: Final circuit version with the components soldered on a smaller PCB. The 4G hat for internet connection is attached to the Raspberry Pi.

The Arduino communicates through an SPI (Serial Peripheral Interface) bus with an accurate real-time clock to schedule its actions: waking the camera, firing the shutter to take a photo, and turning on/off the Raspberry. The Raspberry can access the camera images and transfer them to a remote server via internet connectivity. A large storage memory is added to the unit to save photos before remote transferring. The Raspberry also provides a web-based, user-friendly interface (Fig. 4.5) to configure and monitor the system remotely ([Sheridan, 2021](#)). An I₂C (Inter Integrated Circuit) bus and digital pin connections enable higher-level communication between these two boards. Among the minor components, we mention the role of the three voltage regulators. They allow each unit to be powered at the appropriate voltage and current: starting from the 12 V in input, one delivers 3.3 V and 500 mA to the Arduino, one 5 V and 2.5 A to the Raspberry and its hat, and the other 7.5 V and 2.4 A to the camera. The Arduino controls the Raspberry's 5 V regulator to reduce quiescent power consumption when the Raspberry board is off.

The acquisition of a defined number of images, camera triggering and timing, and sending of images to a remote server can be scheduled thanks to adequate programming of a cyclic executive program in C++ for Arduino and services that automatically execute Python scripts for the Raspberry. All the monitoring station activities can be remotely scheduled from the terminal or a user-friendly web interface ([Sheridan, 2021](#)). This useful feature allows one to change the settings and check the system's behavior, avoiding the need for manual intervention. The Raspberry uses the gPhoto2, a Python-based protocol developed to specifically interact with popular cameras' firmware, to communicate with the camera and access new photos. The web-based interface service is based on NGINX and Gunicorn, open-source software for web servers. The interface (Fig. 4.5) consists of a web page accessible with credentials and provides a summary of the system state and the exact time of the last operations (time of the last shot and the last upload of images), temperatures of the components, previews of the last images, buttons to wake up the camera, take a preview photo and schedule the system routine (time and number of photo acquisition, wake-up time of the Raspberry) and some camera settings.

All the components were chosen because of their low power consumption and their intercompatibility. The circuit is robust against power losses due to battery discharging and can auto-recover when power is regained. A low energy consumption policy is also followed when selecting the scheduling. The camera is switched on only during the data capture activity. The Raspberry is switched on only once daily when the remote server connection and image transfer are scheduled.

System Information	
System date:	2020 Sep 26 14:21:46
Last shot:	Saturday 14:00
Next shot:	Saturday 14:30
Camera:	USB PTP Class Camera
Lens:	EF24mm f/2.8
Images on camera:	1303
Last image on camera:	2020-09-26 14:02:48
Available shots:	127098
Battery:	100%
Images on Pi:	1286
Last image on Pi:	2020-09-25 18:32:48
Pi storage free:	100.07 GB
Last transfer:	2020/09/26 14:02:27 Commencing upload using Google Drive



Unknown model

Intervalometer Settings	
Shoot day of week:	<input type="checkbox"/> Monday <input type="checkbox"/> Tuesday <input type="checkbox"/> Wednesday <input checked="" type="checkbox"/> Thursday <input type="checkbox"/> Friday <input type="checkbox"/> Saturday <input type="checkbox"/> Sunday
Daily start hour:	07
Daily end hour:	20
Interval (minutes):	30
Shots / day:	26
Est days in camera:	Unknown
<input type="button" value="Apply"/>	

Thermal	
Units:	<input checked="" type="radio"/> °C <input type="radio"/> °F
Arduino temperature:	17 °C
Arduino min:	<input type="button" value="Reset"/> 8 °C
Arduino max:	<input type="button" value="Reset"/> 46 °C
Pi temperature:	37 °C

Figure 4.5: Example of some of the pages of the web-based interface to remotely control the monitoring units.

4.3.3 CONNECTIVITY

Internet connectivity is crucial to transfer images and control the units remotely. To this end, the Raspberry is equipped with the SIM7600E-H 4G hat by Waveshare. The module supports 4G/3G/2G communication via a SIM card. Raspberry and hat operations are the most expensive in terms of power consumption. For this reason, the board is switched on only once a day for a limited period, which is kept adequately low to be sustainable for the system power supply but still sufficient for transferring new images to the server. We adopted IoT (Internet of Things) SIM cards provided by the multi-operator service Emnify ([Emnify, 2023](#)), as it allows connecting to the best-quality cellular network available and includes flexible and customizable data plans. A VPN (Virtual Private Network) allows remote access to the devices. The service costs €33 per month for a data plan with 6 GB.

4.3.4 CASE AND PROTECTION

The majority of the components need to be protected. Therefore, a solid and compact case that allows all the parts (except the solar panel) to be kept in the same location is desirable for the system's functioning and convenient transportation, installation, and maintenance. The case should also satisfy the thermal insulation requirements according to each component's working temperature range. The case should also be waterproof and robust against different and harsh weather conditions but also provide access for connecting the solar panel and taking pictures. We chose an HPRC 2250 lightweight, waterproof resin case with internal insulating foam. The foam was found to enhance the temperature seal and stabilize the location of some components, preventing unwanted movements. Holes were drilled in the case: one sealed with an 82 mm UV filter to allow the camera to take shots, two others to access the solar panel wires, and others to fix the system to a tripod. The internal case dimensions (236 mm × 182 mm × 155 mm) posed a significant challenge in accommodating all the components inside. In particular, the camera lens dimensions were constrained by space availability.

4.3.5 GENERAL PERFORMANCES

The system was subject to several tests before being used in its final application at the Belvedere glacier site. During these tests, the system proved to be autonomous, robust to sudden shutdowns, cold-resistant, water-resistant, and self-sufficient for a prolonged period with no direct sunlight on the solar panels. Specifically, without sunlight, the battery can power the system for about nine days before it is completely discharged. Battery voltage and temperatures of components were monitored, simulating the absence of solar radiation and low environmental temperatures. Fig. 4.6 shows the system's performances during these tests.

4.3.6 THE CHOICE OF THE CAMERA

The choice of the DSLR camera and the optics can be considered application-dependent. Therefore, specifications regarding these components refer to the Belvedere glacier case study. Each monitoring station had a DSLR camera, Canon EOS 2000D, with 24.1 MP CMOS APS-C sensor. This model was chosen because of its limited costs, high image resolution, and compactness, as it must fit inside the case. Another fundamental requirement was camera compatibility with the *gPhoto2* software. The choice of the lenses is mostly site-specific, as it is driven by the required GSD of the images. In addition, dimensional constraints limit the choices of the optics to rather small lenses that can fit into the protective case. The lenses chosen

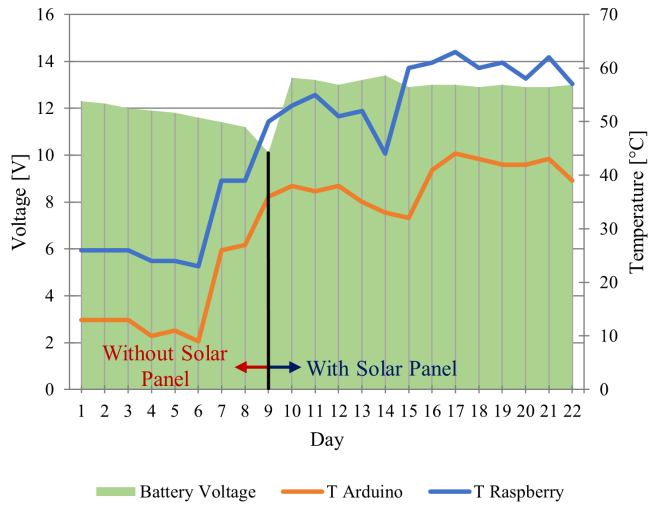


Figure 4.6: Battery voltage and temperature of boards with and without the solar panel during a period of tests. Starting from a fully charged condition, the system was kept without the solar panel at around 2 °C for the first six days. After nine days, the battery was fully discharged, and the system was reconnected to the panel and exposed to solar radiation.

for the two cameras are described in Sec. 4.3.7.

In the installation inside the system case, the traditional rechargeable battery was replaced by a special battery ("fake battery") equipped with a power supply cable that provides 7.5V from the circuit. The camera is attached to a sliding plate that can vary within a limited range but that fixes the camera orientation along the longitudinal axis. Screws fix the camera to the plate and the plate to the case.

It is worth mentioning the performance of the system in terms of costs: our monitoring system can be fully reproduced with an average cost of €2000 per station (November 2023), including camera (€400), lens (€500) and material for the on-site installation (€150). In comparison, commercial time-lapse cameras are expensive (e.g., PhotoSentinel³ cameras cost more than \$ 5,000.00) and hardly customizable.

4.3.7 SITE SELECTION FOR PERMANENT INSTALLATION

A preliminary survey was conducted to identify suitable locations for the two monitoring units. The primary goal was to ensure both cameras had a clear view of the northwest terminal lobe, particularly the terminal ice cliff, as this area experiences substantial transformation and retreat. However, the harsh glacial environment presented significant challenges. The glacier's steep moraines are mostly unstable due to

³PhotoSentinel: <https://photosentinel.com/>

reduced support from the melting ice, making them prone to sliding and collapsing.

Another critical consideration for a good acquisition geometry is the baseline (i.e., the distance between cameras). This distance should be sufficiently large relative to the camera-object distance to avoid compromising depth estimation accuracy due to narrow perspective ray intersection. Consequently, installing the cameras close together on the same side of the glacier was not feasible.

Ultimately, two large boulders located on opposite moraines flanking the glacier's terminal lobe were identified as the only suitable and stable locations (Fig. 4.7). The cameras, labeled as C1 and C2 (Tab. 4.1), were installed in July 2021 approximately at ~ 230 m and ~ 350 m from the terminal ice cliff, respectively, with a strongly convergent pose.

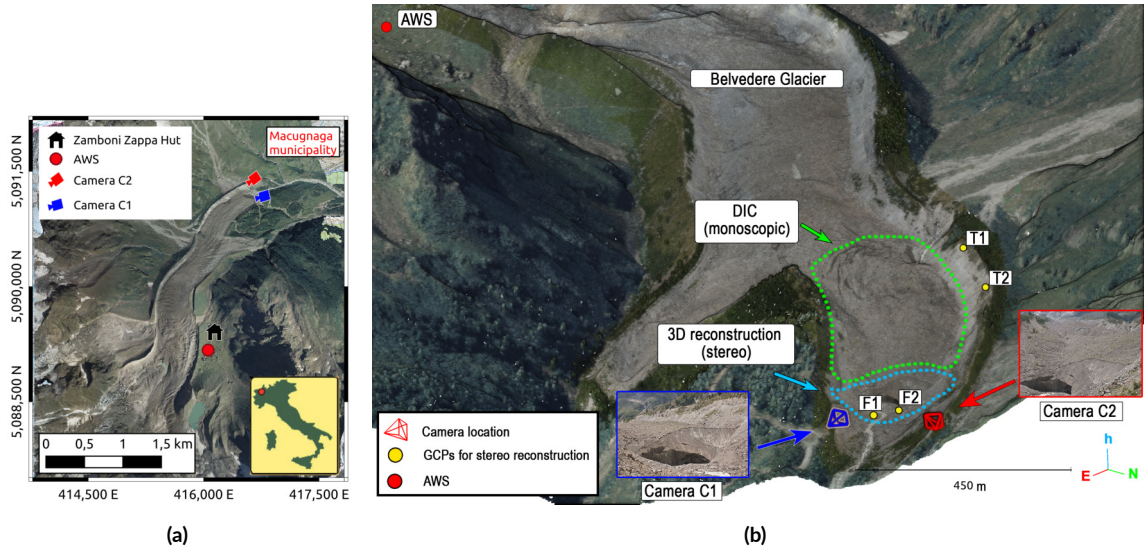


Figure 4.7: (a) Map of the Belvedere Glacier, with marked the location of the two cameras C1 and C2, the Automatic Weather Station (AWS) and the Zamboni Zappa Hut; (b) The area of study: the stereoscopic reconstruction is focused on the terminal ice cliff (dashed light blue line), while the monoscopic DIC processing from camera C2 image sequence is focused on the upper area of the north lobe (dashed green line).

To ensure comparable GSD of the images (~ 3.5 cm px $^{-1}$), lenses with different focal lengths were employed. Camera C1 (streamwise right) was equipped with a Canon EF 24 mm f/2.8 IS USM, and camera C2 (streamwise left) had a Canon EF 35 mm f/2 IS USM. The cameras and lenses' characteristics are summarized in Tab. 4.1.

The baseline between the two cameras of ~ 261 m ensured a good viewing geometry because of the large parallax between corresponding points. However, the baseline comparable to the camera-object distance (base-height ratio close to 1, Tab. 4.1) led to complex affinity-like distortions and occlusions between

Table 4.1: Summary of the characteristics of the two cameras. Fields marked with * are computed considering the distance between each camera and the ice cliff.

	C ₁	C ₂
Camera	Canon Eos 1200D	Canon Eos 1200D
Sensor	APS-C	APS-C
Pixel size	3.7 μm	3.7 μm
Image	6000 px \times 4000 px	6000 px \times 4000 px
Lens	Canon EF 24mm f/2.8 IS USM	Canon EF 35mm f/2 IS USM
Distance*	230 m	350 m
Average GSD*	3.5 cm px ⁻¹	3.5 cm px ⁻¹

corresponding areas in the two images (Yao et al., 2021). Additionally, C₁ was positioned at a lower viewpoint compared to C₂, due to site geometry constraints. Therefore, camera C₁ provides a limited view that primarily encompasses the frontal ice cliff but does not capture the glacier surface, which is only visible from camera C₂ (Fig. 4.7b).

Considering a nominal situation of a normal stereo case, it is possible to compute the theoretical depth precision of the reconstructed 3D points. To this end, we consider two cameras identical to Camera C₂, positioned with an average camera-object distance of 350 m, corresponding to the distance of the closest point of the sub-vertical terminal ice cliff from Camera C₂. Assuming an a priori collimation accuracy of 1 px (due to the lack of sub-pixel accuracy of the SuperPoint descriptor used for feature matching, as described in Sec. 4.5.4), the theoretical depth precision is approximately 3.7 cm. It is important to note that these values may be underestimated, as the a priori collimation accuracy could easily exceed 1 pixel due to the strongly convergent viewing angles and the inherent difficulties in finding corresponding points.

4.3.8 CAMERA INSTALLATION

The cameras were mounted on large, stable rocks along the moraines using aluminum topographic tripods anchored with steel dowels and cables (Fig. 4.8). A central steel tie rod secures each system. This agile installation approach allows for relatively easy on-site assembly and disassembly within the challenging environment, minimizing cost and time requirements. The equipment was transported to the site via backpacks, often traversing unmarked terrain.

Despite these efforts, analysis of the acquired images revealed minor instability in both cameras, particularly small rotations around the vertical axis and wind-induced vibrations. While achieving perfect stability in a mountain environment is challenging, the use of GCPs located in stable areas will enable the

estimation of camera orientation during image processing.

The final prototype of the monitoring station is shown in Fig. 4.8.

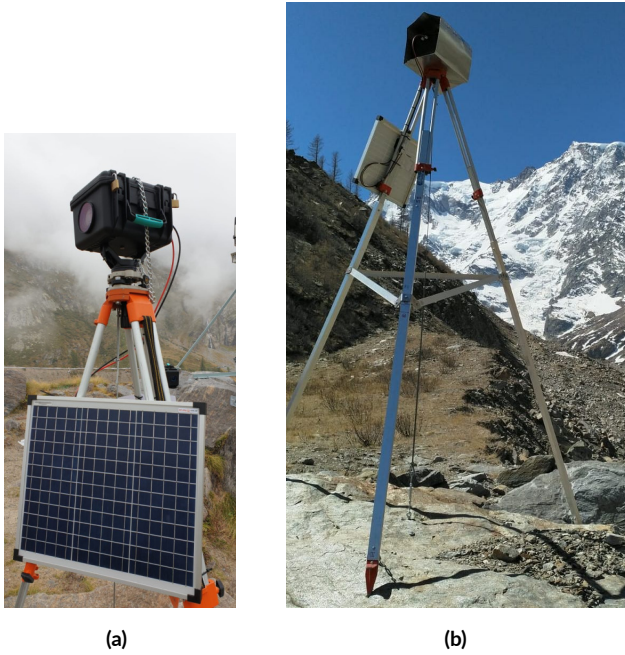


Figure 4.8: (a) Picture of the monitoring unit prototype installed for tests at the Belvedere Glacier site. (b) Picture of the final camera installation installed on the streamwise right moraine.

The stereoscopic system operated from August 2021 until December 2022, when it was temporarily unmounted for ordinary maintenance and finally mounted again in June 2023. During the operational period, the system was programmed to acquire two images per day, but only one image per day was used for the multitemporal processing. Only daily images taken during the snow-free period between 01/05/2022 and 13/11/2022 were considered. The glacier experienced the most significant flow velocity and ablation rate changes during this period. On the other hand, during winter and spring seasons, the glacier was covered by snow, making it difficult to extract relevant information from optical images for tasks such as 3D reconstruction and surface velocity estimation.

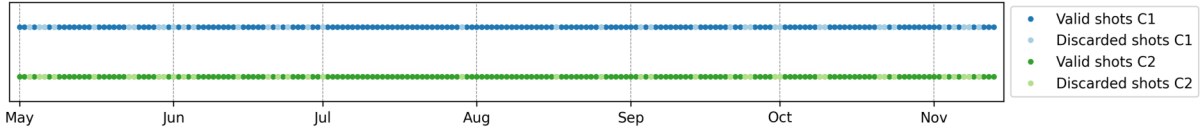


Figure 4.9: Days with images acquired by the two cameras C1 and C2. Valid shots are represented with dark colors, while discarded days due to bad weather conditions are represented with light colors.

4.4 DATASETS

4.4.1 STEREOSCOPIC IMAGE SEQUENCES

During the snow-free study period (from 1/05/2022 to 13/11/2022), both camera C1 and camera C2 acquired 197 images daily. However, 39 images were discarded due to bad weather conditions, such as rain, low clouds, or fog, resulting in 158 days with valid data for stereo and monoscopic processing (Fig. 4.9).

4.4.2 UAV SURVEYS

Two UAV flights, spaced by a 10-day interval, were conducted in the summer of 2022 to acquire ground truth data for assessing the proposed methodology. The first UAV flight, labeled as UAV-A, was carried out on 28/07/2022 with a DJI Matrice 300 RTK quadcopter and a DJI Zenmuse P1 camera with a 35 mm lens. During the survey, 436 images were captured, encompassing both nadiral and oblique perspectives. Additionally, 19 GCPs were measured using a combination of a total station and Differential GPS (DGPS), employing a topographic-grade GNSS receiver. The GCPs included both artificial targets and natural features. During the flight, the UAV was equipped with an onboard RTK GNSS receiver, enabling the acquisition of camera projection centers with decimetric accuracy. The photogrammetric block (Fig. 4.10a) was processed with the commercial software package Agisoft Metashape ([Metashape, 2023](#)) by using 14 GCPs and 5 CPs to evaluate the block accuracy. The global RMSE evaluated on the CPs was equal to 4.0 cm.

The second UAV flight, UAV-B, was carried out on 05/08/2022 with a DJI Phantom 4 RTK, focusing on a smaller portion of the northern lobe of the Belvedere Glacier. However, due to technical constraints, moving GCPs located inside the glacier body were not measured again. Therefore, only the fixed targets located outside the glacier were employed. Among these, 8 targets were designated as GCPs, while the remaining 4 were used as CPs. The photogrammetric block encompassed 428 nadiral and oblique images, which were processed using Agisoft Metashape (Fig. 4.10b). A global RMSE of 7.5 cm was obtained on

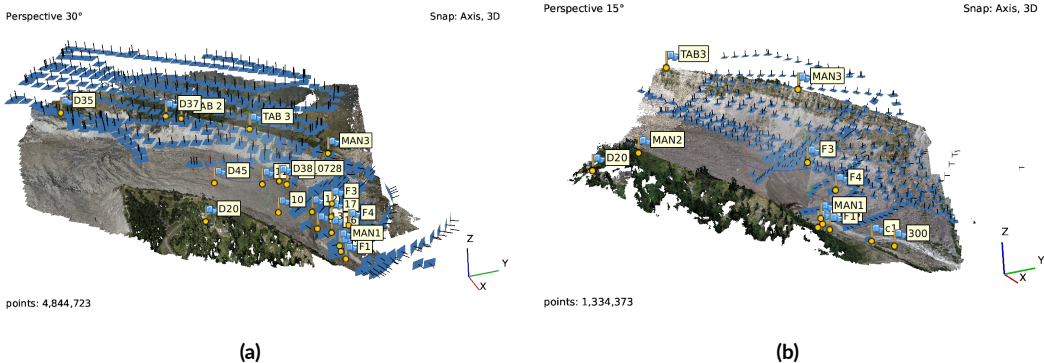


Figure 4.10: (a) UAV-A block and (b) UAV-B block processed with Agisoft Metashape. The flags represent the targets used either as GCPs in the BA or as CPs to evaluate the quality of the photogrammetric block.

the 4 CPs.

4.4.3 METEOROLOGICAL MONITORING STATION

To analyze the correlation between the Belvedere Glacier dynamics and external environmental variables, data measured from an Automatic Weather Station (AWS) located close to the Zamboni Zappa Hut were used. The AWS is located at an altitude of 2075 m a.s.l. and at a distance of 2 km from the area of study. The data from the AWS can be downloaded from the Arpa Piemonte website⁴. In our study, we analyzed mean daily values of air temperature, precipitation, and incoming solar radiation from 01/05/22 to 15/11/22.

4.5 METHODOLOGY

This chapter outlines the methodology developed to monitor the evolution of the Belvedere Glacier northern lobe. The daily images were processed using a framework consisting of two parallel processing chains (Fig. 4.11): (i) a photogrammetric-based stereoscopic approach; (ii) a DIC-based monoscopic approach. The daily stereo pairs were used to generate 3D models of the glacier terminus, enabling the estimation of ice volume loss on a daily basis by computing point cloud differences along the main flow direction. However, due to limited overlapping views of the two cameras, the stereoscopic approach primarily provides a 3D reconstruction of the terminal ice cliff (dashed-blue area in Fig. 4.7b). Consequently, deriving the

⁴https://www.arpa.piemonte.it/rischi_naturali/snippets_arpa_graphs/dati_giornalieri_meteo/?staid=PIE-003086-906-2007-07-05¶m=T

3D surface velocity field of the glacier solely from photogrammetry was not feasible. The image sequence captured by camera C₂, which offers a higher viewpoint and a broader coverage of the glacier surface, was employed to determine the glacier's surface velocity over a larger area of the north lobe of the Belvedere Glacier (dashed-green area in Fig. 4.7b).

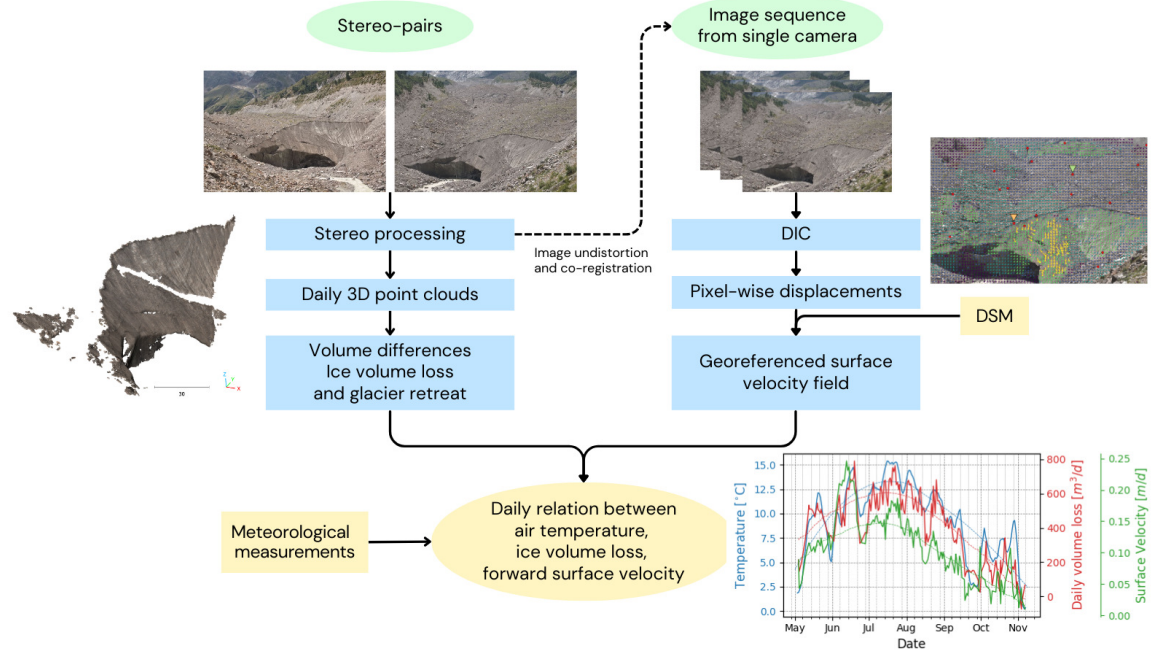


Figure 4.11: General workflow with two parallel processing chains involving stereoscopic reconstruction of terminal ice cliff from stereo-pairs of images to derive ice volume losses at the glacier terminus and glacier retreat and monoscopic digital image correlation to derive surface velocities.

4.5.1 IMAGE SELECTION

Once the acquired images have been received from the monitoring system, an automatic selection of the images was performed to exclude the ones acquired in rainy, foggy, or poor lighting conditions. This selection was based on the analysis of the images' median entropy (Tsai et al., 2008): the images with a low value over the entire image were rejected. Additionally, a visual inspection was performed on the entire image dataset. The inspection had the following objectives: (i) selecting only one image per day; (ii) rejecting poor-quality images that were not automatically rejected, and images in which the fixed targets placed along the moraines were not visible; (iii) detecting sudden changes in the morphology of the glacier terminus (e.g., icefall).

4.5.2 CAMERA CALIBRATION

Each camera was mounted with all its electronics inside a waterproof case and protected by a neutral filter that was glued to the case and fixed in front of the cameras. Since the filter introduced additional distortion, the cameras must be calibrated inside the boxes to reproduce the final setup. Therefore, a two-step approach was taken: first, a 120 cm x 70 cm calibration board with a checkerboard printed on it was used to estimate an initial set of parameters for the interior orientation ([Zhang, 2000](#)). To this end, the cameras were mounted on tripods inside their cases while the calibration board was moved and rotated in front of the camera to simulate a convergent hemispheric acquisition. About 30 images were collected and processed in Agisoft Metashape for each camera to obtain a first estimate of the interior orientation. However, the average camera-to-panel distance was much smaller than the actual camera-to-glacier distance. Therefore, a calibration refinement was performed *in situ* by incorporating the stereo pair acquired by the cameras on 28/07/22 within the UAV-A block, carried out on the same day. This block was processed with Agisoft Metashape to refine the interior camera orientation of the stereo cameras, aided by the increased robustness of the block given by the additional matches between the two images taken by cameras C1 and C2 and the UAV.

An additional challenge was represented by camera interior orientation stability over time. From experimental evidence, the interior orientation parameter that suffered the most because of temperature variations that occur in a mountain environment was the camera principal distance ([Elias et al., 2020](#)), while the other parameters remained more stable over time. To mitigate the impact of temperature-induced variations, it was crucial to incorporate camera self-calibration during the stereoscopic processing at each epoch to refine the pre-calibrated principal distance.

4.5.3 CAMERA STABILITY AND GCPs

Since the two cameras were mounted on topographic tripods, their stability was not perfectly guaranteed. In particular, the two cameras experienced small vibrations around their pivots due to wind gusts. On the other hand, the position of the cameras was constrained by topographic heads that kept the position of the camera center constant at the centimeter level. Therefore, the baseline of the cameras can be reasonably considered constant, with a value of 261.55 m. On the other hand, camera angular vibrations implied that the relative orientation of the cameras must be estimated at each epoch. Moreover, to fix the world reference system over time, the absolute orientation of the stereo model was required. To this end, the position of the cameras was measured *in situ* using a topography-grade GNSS receiver in RTK. In addition, four GCPs were materialized with plastic targets, anchored to stable rocks in front of the terminal ice cliff

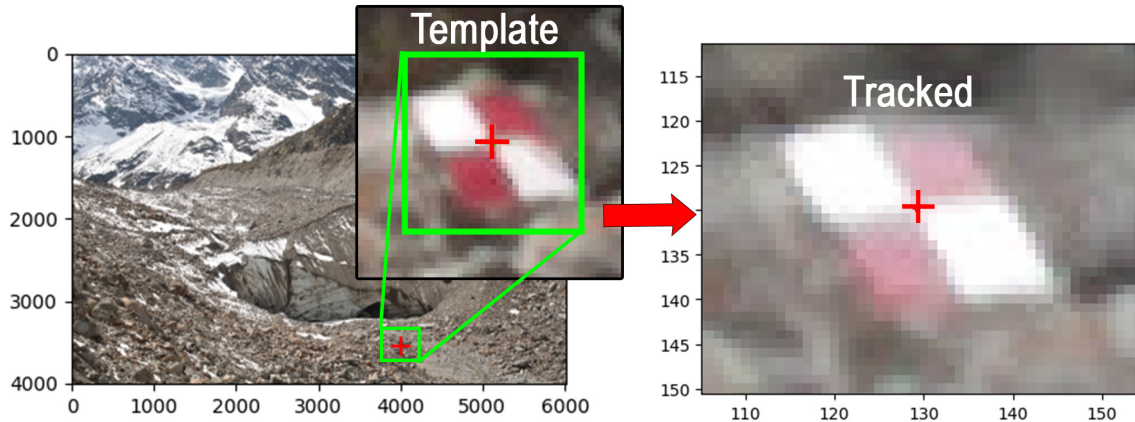


Figure 4.12: Example of template matching used to track GCPs on a monocular image sequence. The green square represents the template on the reference image that is searched in all the other images of the sequence. The red cross marks the estimated position of the center of the template in a new image.

and along the streamwise left moraine (Fig. 4.7a). While the minimum requirement to estimate a Helmert transformation would have been just the two cameras’ location and one GCP, having a redundant number of GCPs overcomes the possibility that, on some days, not all GCPs were clearly visible in the images due to low clouds or fog. Additionally, GCPs can be included in the Bundle Adjustment (BA) to refine the cameras’ interior orientation, particularly their focal length.

As the cameras are subjected to slight rotations, the image coordinates of the GCPs’ projections must be detected at each epoch. To this end, a feature tracking routine was developed based on the ImGRAFT TemplateMatch method (Messerli and Grinsted, 2015) to track a GCP on all images in the time series by DIC (Fig. 4.12). This involves defining a template on a reference image and search orientation correlation algorithm (Fitch et al., 2002), which is more robust against illumination changes compared to normalized cross-correlation and achieves sub-pixel accuracy (Dematteis and Giordan, 2021, Heid and Kääb, 2012).

4.5.4 STEREOSCOPIC IMAGE PROCESSING WORKFLOW

ICEPy4D was developed to achieve a daily stereoscopic reconstruction of the glacier snout. ICEPy4D⁵ is a Python-based toolkit that allows for solving different steps of scene reconstruction (Fig. 4.13). In particular, the main steps consist of: (i) finding corresponding points by deep-learning feature matching; (ii) tracking features on the sequence of images acquired from the same camera; (iii) performing 3D scene

⁵ICEPy4D <https://github.com/franioli/icepy4d>

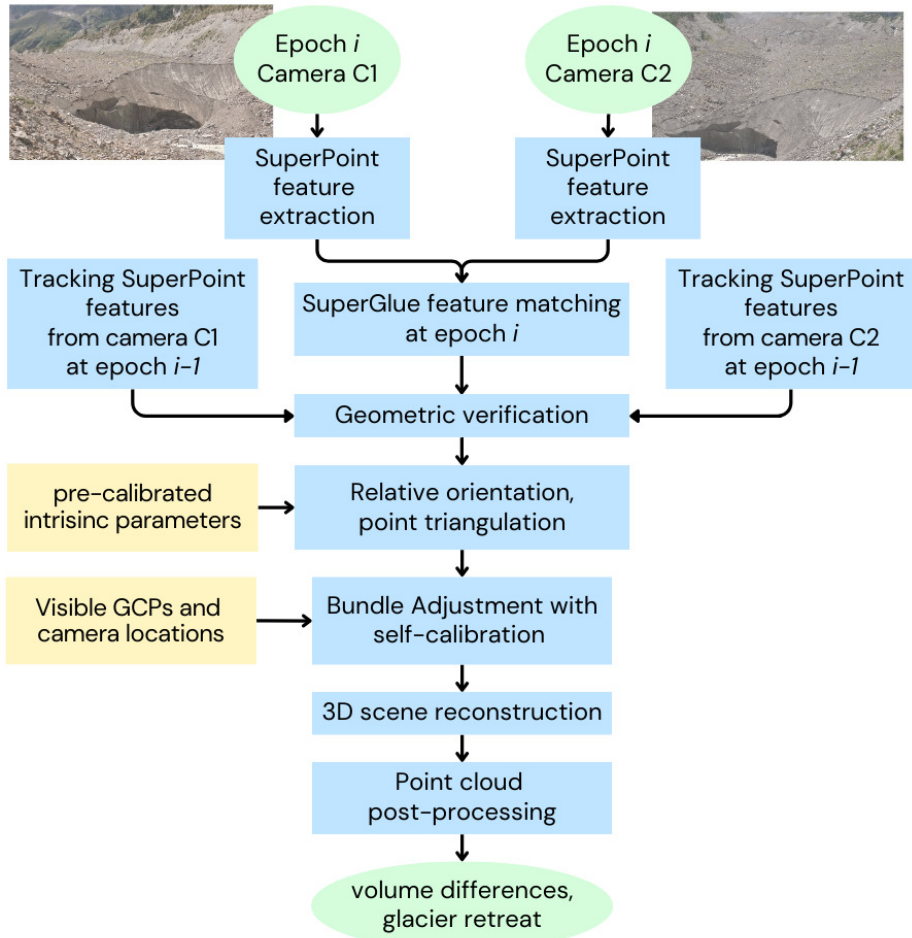


Figure 4.13: Scheme of the stereoscopic workflow performed with ICEPy4D. At a generic epoch i , new features are extracted and matched. At the same time, features from the previous epoch $i-1$ are tracked on the current epoch images. After geometric verification, features successfully matched are used for 3D scene reconstruction. Point clouds obtained on different days are used to compute ice volume differences and glacier retreat.

reconstruction and point cloud post-processing. All the processing was done with a mid-class workstation equipped with a 20-core i7-12700 CPU, 32 Gb of DDR5 RAM and a GPU NVIDIA RTX A2000 12 GB.

4.5.4.1 WIDE-BASELINE IMAGE MATCHING

To find corresponding points, the combination of DL feature-matching algorithms SuperPoint ([DeTone et al., 2018](#)) and SuperGlue ([Sarlin et al., 2020](#)) was used, and fully integrated into the ICEPy4D package. SuperPoint is a Convolutional Neural Network (CNN) with an encoder-decoder structure, which detects interesting points and computes 256-value descriptors in a single forward pass. [DeTone et al. \(2018\)](#) trained SuperPoint to detect corner-like features first using corners of synthetic shape datasets as ground truth. They employed a self-supervised approach by applying random homographies to warped copies of the input training images and combining the results ([DeTone et al., 2018](#)). SuperGlue is an attention-based graph CNN used for local feature matching. It was specifically designed to match SuperPoint features based on their descriptors. [Sarlin et al. \(2020\)](#) trained SuperGlue in a supervised manner and published two different sets of weights: one for indoor environments and another for outdoor environments. The outdoor environment model was trained on the Megadepth dataset ([Li and Snavely, 2018](#)).

The SuperPoint and SuperGlue models were not fine-tuned to ensure the replicability of the proposed pipeline in different scenarios without the need for a dedicated ground truth dataset. Acquiring a ground truth dataset can be challenging, especially for natural scenarios and mountain environments. Typically, generating datasets for training wide baseline matching requires collecting a considerable number of image sequences with a normal baseline and artificially creating a wide baseline by skipping intermediate images. However, this approach would demand numerous field campaigns to capture a series of UAV images under different environmental conditions and throughout various seasons, making it generally unfeasible. Moreover, the matching results obtained with the Belvedere stereo pairs were already satisfactory using pre-trained weights for outdoor environments without any fine-tuning (see results in Sec. 4.6.2).

Since feature matching was performed on a GPU with limited memory, it was necessary to decompose the full-resolution images into smaller tiles and match pairs of tiles one after the other. Therefore, a two-step approach was implemented: first, a matching is performed with SuperPoint and SuperGlue on downsampled images. Subsequently, the full-resolution images were subdivided into regular tiles, and only the tiles with corresponding features in the low-resolution images were selected as candidates for a second matching step. In the second step, the selected tiles were matched using the same procedure as before. The features matched in each tile were then reassembled to recover their image coordinates on the original image for geometric verification. Incorrectly matched keypoints, which did not satisfy the epipolar

constraint, were rejected using Pydegensac (Mishkin et al., 2015), by imposing a maximum re-projection error of 1.5 px.

4.5.4.2 TRACKING POINTS OVER EPOCHS

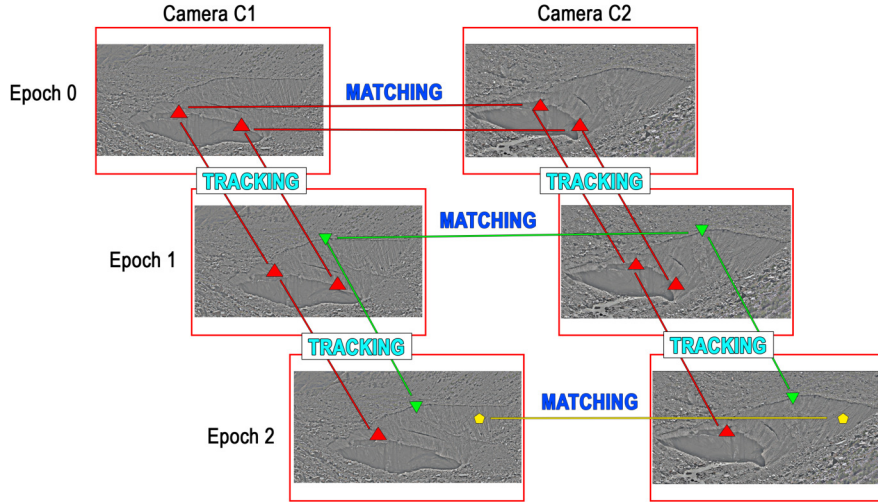


Figure 4.14: Scheme of feature tracking in stereo-cameras sequence. At each epoch, new features are matched on the stereo pair (horizontal lines), but also tracked from previous epochs (oblique lines). At epoch 0, the matches are only the corresponding features matched between current the stereo pair (red triangles). At epoch 1, the valid matches are the new corresponding features matched (green triangles) plus the successfully tracked features from epoch 0 (red triangles). The same holds for epoch 2, where the matches are the new corresponding features (yellow pentagons), plus the features tracked from both epoch 0 and 1.

Matched points are tracked over time on single-camera image time series (Fig. 4.14). This procedure led to two main advantages: (i) increasing the number of matches at every epoch; (ii) obtaining a time series of corresponding points that can be triangulated to derive their 3D coordinates over time. For brevity, images are labeled with the camera labels $C1$ and $C2$, while a superscript indicates the acquisition epoch. At a generic epoch i , keypoints were detected and matched between images $C1^i$ and $C2^i$ with the procedure described in Sec. 4.5.4.1. SuperPoint features were then extracted on $C1^{(i+1)}$ and $C2^{(i+1)}$. Valid matched features from $C1^i$ were tracked to $C1^{(i+1)}$, by matching their descriptors with the SuperGlue algorithm. The same holds for camera $C2$. If a matched feature at epoch i was tracked successfully both from images $C1^i$ to $C1^{(i+1)}$ and from images $C2^i$ to $C2^{(i+1)}$, then this feature was considered a valid match also for epoch $i + 1$ and merged to the new corresponding features detected at epoch $i + 1$. Duplicate features

(e.g., a feature that was successfully tracked from epoch i to epoch $i + 1$ but also matched again at epoch $i + 1$) were removed and a new geometric verification was carried out to reject outliers.

4.5.4.3 3D SCENE RECONSTRUCTION

At each epoch, the terminal ice cliff was reconstructed using ICEPy4D in two main steps: (i) relative-absolute orientation and (ii) bundle adjustment. In the first step, matches between each stereo pair were utilized to estimate the relative pose of the two cameras based on the camera's pre-calibrated intrinsic matrix. Subsequently, the absolute orientation was determined by calculating a Helmert transformation, considering the cameras' locations and the available GCPs. A full BA was performed in the second step to refine the relative-absolute solution. For this purpose, the Agisoft Metashape software package was employed via its Python API. The choice of Agisoft Metashape was driven by its support for GCPs, the possibility to assign different a-priori weights to observations, and the availability of a Python API, enabling the software to be run from a Python routine in headless mode. The Metashape BA was seamlessly integrated into ICEPy4D, enabling the entire workflow chain to run automatically without any interaction with the GUI.

During the BA, the cameras' locations and the available GCPs were used as observations. A centimetric a-priori accuracy was assigned to the world coordinates of the GCPs. A centimetric accuracy was also given to the camera locations to constrain their positions while still allowing for an estimation of the cameras' rotations. Additionally, during the BA process, the principal distance of the two cameras was refined by self-calibration based on the available GCPs, while the remaining interior orientation parameters were kept fixed at their pre-calibrated values.

The dense reconstruction of the ice cliff terminus was again carried out using the Agisoft Metashape API. In fact, although Agisoft Metashape couldn't perform feature matching with wide baselines due to its reliance on hand-crafted features, it was effective in performing dense matching through semi-global matching algorithms ([Hirschmüller et al., 2012](#)), when accurate camera poses were available for image rectification. Depth maps were generated from full-resolution images (i.e., *highest* quality parameter in Agisoft Metashape) with mild filtering. The estimated depth maps were then used to reconstruct a dense point cloud and a triangulated mesh.

4.5.5 VOLUME VARIATION ESTIMATION

The daily variation of ice volume was determined by DOD along the streamwise direction. A local reference system was established by defining the X-direction as the streamwise direction, the Z-direction as

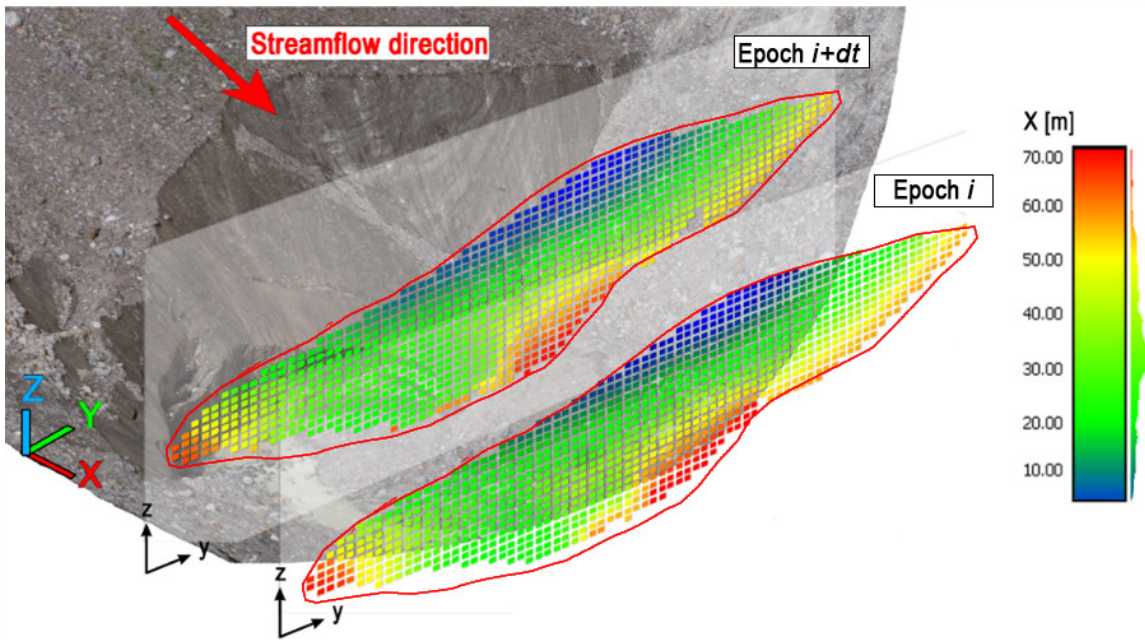


Figure 4.15: Scheme of Dem of Difference (DOD) approach used to compute volume variations at the glacier terminal ice cliff. Two point clouds built at epoch i and $i+dt$ (we used $dt=5$ days to increase the signal-to-noise ratio), were rasterized to a vertical Y-Z planes, with normals parallel to the glacier flow direction (X direction). Before rasterization, the point clouds are clipped with the same convex polygon in the Y-Z plane (red line). The colors of the grids represent the depth of each cell of the two rasters along the X direction (i.e., the distance along X from a reference plane). Volume variation was computed by DOD of the two rasters along X.

the geodetic height, and the Y-direction to complete the right-hand reference system. The point clouds of two different epochs were rasterized to a reference YZ plane, corresponding to the frontal view of the terminal ice cliff, using a grid step of 0.3 m, while maintaining the same raster origin and extent (i.e., the two point clouds were first clipped with the same convex polygon). The volume change between two epochs was then calculated by differentiating the two rasters cell-by-cell (Fig. 4.15). To account for possible incomplete coverage and holes in the 3D reconstruction, which may result in volume underestimating, the computed volume difference was normalized by the percentage of filled cells (i.e., cells with at least one point in the original point cloud) in both rasters. The normalization was computed as in Eq. 4.1:

$$dV_{\text{norm}} = dV \times \frac{n_{\text{filled}}}{n_{\text{total}}} \quad (4.1)$$

where n_{filled} is the number of filled cells in both the rasters and n_{total} is the total number of cells within

the clipping polygon. During the considered study period, the percentage of filled cells in the rasterized point clouds of the terminal ice cliff ranged from 90% to 98.8%, with a mean value of 96.8%.

4.5.5.1 TEMPORAL LAG BETWEEN POINT CLOUDS FOR VOLUME AND VELOCITY ESTIMATION

The point clouds were processed using pairs spaced 5 days apart to estimate volume variation and surface velocity. This interval was selected by the average glacier surface displacement, as computed in Sec. 3.4.2. Given a decimetric accuracy of the stereo point clouds (see the results presented in Sec. 4.6.5), a 5-day interval was considered appropriate to achieve a good signal-to-noise ratio. Therefore, each point cloud acquired on a particular day was compared to that captured five days earlier to compute volume differences. However, in case of adverse weather conditions that hindered stereo reconstruction and resulted in the unavailability of a point cloud on a certain date, the closest one acquired within a range of 5 to 7 days earlier was chosen as a substitute. This approach balanced preserving temporal resolution and minimizing data gaps caused by unfavorable weather conditions.

To ensure consistency between volume variations and surface velocities, the same pairs of days utilized for estimating volume differences from point clouds were also employed for selecting pairs of images to compute surface velocities using DIC on monoscopic image sequences (see Sec. 4.5.7).

4.5.6 AUTOMATIC EXTRACTION OF ICE CLIFF TOP EDGE

To calculate the glacier retreat over time, the top edge of the ice cliff was chosen as a reference point. This decision was made because the top edge remained rather stable and experienced limited changes in morphology compared to the rest of the terminal ice cliff, which is often affected by deformation and other processes that altered its shape, such as ice block collapses.

The top edge of the ice cliff was automatically extracted from point clouds by exploiting the geometric features of each point compared to its neighborhood (Hackel et al., 2016). To identify elongated features situated at the edges of the ice cliff within the point cloud, the linearity and normal change rate were computed for each point compared to a neighborhood sphere of radius 2 m. By employing empirically determined thresholds specifically tailored to the study site, these geometric properties facilitated the identification and extraction of the top edge of the glacier terminus from the point cloud data.

4.5.7 DIGITAL IMAGE CORRELATION FROM SINGLE CAMERAS

Glacier surface displacements were computed on the image sequence acquired by the monoscopic camera C2 (see Fig. 4.7). To this end, we used LAMMA ([Dematteis et al., 2022](#)) and the cosine similarity applied to orientation images as a correlation function (see Sec. 3.3.2 for a description of LAMMA). This method offers superior robustness to shadow pattern changes and is well-suited to glacier environments ([Heid and Kääb, 2012](#)).

We applied DIC to the undistorted images, which were corrected according to the interior orientation parameters estimated at every epoch within stereo BA. Moreover, assuming a zero-translation of the camera perspective centers, but only small rotations (Sec. 4.5.3), the transformation between the image plane at an arbitrary epoch with respect to a reference one (named *master*) is described by a homography transformation. We adopted the image taken on 28/07/2022 as a master image, which was coeval with the DSM built from the UAV-A survey. All the other images acquired were warped to be coregistered to the master image by computing a homography transformation H (Eq. 4.2):

$$H = KRK^{-1} \quad (4.2)$$

where K is the camera intrinsic matrix and R is the relative rotation between the image planes ([Förstner and Wrobel, 2016](#)). The relative rotation R between the camera pose at a generic epoch, and the pose of the master camera was known from stereo processing.

The same image pairs used for volume variation computation, spaced by a time lag of 5 days, were selected for DIC (Sec. 4.5.5.1). The resulting displacement maps on the image plane, in pixel units, were finally post-processed using a local filter to remove outliers. To geocode the displacement maps, we used the open-source ImGRAFT Matlab toolbox ([Messerli and Grinsted, 2015](#)). Given a set of camera interior parameters (from stereo automatic calibration), ImGRAFT allows the projection of 3D world coordinates (x, y, z) into the 2D image coordinates and the back projection of image coordinates onto a DSM, expressed as $f(i, j) \rightarrow (x, y, z)$. Thereby, the metric conversion of the image displacement vectors, with components (du, dv) , is obtained by $v(dx, dy, dz) = f(i + du, j + dv) - f(i, j)$, where v is the 3D displacement vector. The f function is a form of ray tracing carried out based on the input DSM and the interior and exterior camera parameters ([Messerli and Grinsted, 2015](#)). To estimate the transformation between 2D and 3D coordinate systems, we adopted the DSM acquired by UAV photogrammetry on 28/07/2022, resampled at 1 m resolution to smooth small local DSM variations.

4.5.7.1 ORTHORECTIFICATION UNCERTAINTY

The orthorectification of the 2D DIC displacement vectors to obtain 3D vectors is influenced by the chosen DSM and its associated uncertainty (Travelletti et al., 2012). Ideally, using an updated DSM derived from daily stereo-processing, as performed in Marsy et al. (2020), would be the optimal approach. However, due to the camera's viewing location, reconstructing the daily DSM of the upper surface of the glacier lobe was not feasible. Consequently, we utilized the UAV-A DSM acquired on 28/07/2022.

To estimate the uncertainty derived by the use of a single DSM over the study period, we conducted the following experiment: using the DSM of 28/07/2022 as the reference, we virtually translated the glacier DSM along the flow direction to create two synthetic DSMs representing the most advanced and the most retreated positions that the glacier snout experienced in 2022. The selection of these positions was based on the actual results of the stereo-processing (Sec. 4.6.4): the most advanced location of the snout was approximately 12 meters downstream (May 2022), while the most retreated location was about 5 meters upstream (November 2022). This rigid translation of the glacier body not only affected the front position but also resulted in a variation in the glacier surface elevation, i.e., thinning in the case of retreat. Subsequently, we back-projected the DIC displacement values of 28/07/2022 onto the original DSM and the two synthetic DSMs. Finally, we compared the metric displacement values considering the MAD between the original and synthetic results.

4.5.8 CORRELATION BETWEEN GLACIER DYNAMICS AND METEOROLOGICAL VARIABLES

We compared the behavior of glacier velocity and ice volume loss at the snout with the mean daily air temperature, precipitation, and incoming solar radiation measured by the AWS located 2 km from the glacier terminus (Sec. 4.4.3). Since both volume loss and velocity were obtained by comparing point clouds and images acquired with a temporal lag of five days, we applied a moving average with a window of five days to the weather data. Subsequently, to filter out the main signal due to the seasonal trend, we detrended the time series by subtracting a robust loess smoothing function (Cleveland, 1979) evaluated on a period of 180 days. Finally, we calculated the Spearman correlation with the original data and obtained residuals, which indicates how well the relationship between two variables can be described using a monotonic function. We adopted the Spearman correlation because it is more robust against outliers compared to the linear correlation and because it allows the modelling of any kind of correlation (i.e., linear and non-linear) between meteorological variables, ice volume losses and glacier surface velocities.

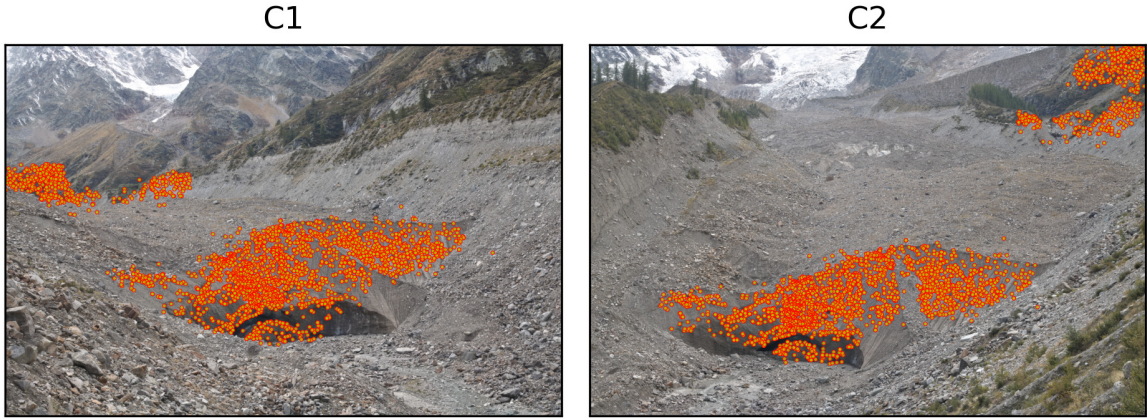


Figure 4.16: Example of features successfully matched on the stereo-pair acquired on 27/09/2022.

4.6 RESULTS

4.6.1 AUTOMATIC DETECTION OF GCPs

Automatic target tracking of GCPs on monocular image sequences allowed successful tracking of GCPs in 99% of image sequences from both cameras. Only in two out of 158 epochs did template matching fail, requiring target manual collimation. Manual collimation was performed on all the images to validate template-matching results. For camera C1, the MAD between the image coordinates of the automatically tracked targets and the manually collimated one was 0.46 px, with a standard deviation of 0.25 px. Similarly to camera C2, the MAD was 0.55 px, with a standard deviation of 0.23 px, denoting the template matching routine's sub-pixel accuracy.

4.6.2 WIDE-BASELINE FEATURE MATCHING AND TRACKING

The features matched by ICEpy4D on each stereo pair extended over the entire frontal ice cliff, with some features detected in overlapping regions along the streamwise left moraine (Fig. 4.16), near targets T1 and T2 (see Fig. 4.7b). For each epoch, a number of features ranging from 1000 to 3500 were successfully matched and validated following geometric verification (Fig. 4.17a). Among them, approximately 30-40% of the matched features were effectively tracked from previous epochs, increasing the total number of matches available for camera pose estimation while establishing a linkage between consecutive epochs.

After BA, the global average reprojection error was computed by projecting the 3D coordinates of all the tie points to the two images and averaging the norm of the reprojection errors for all the points.



Figure 4.17: (a) Number of valid matches extracted from the stereo pair at each epoch and number of points tracked from the previous epoch. (b) Average and standard deviation of the reprojection error obtained by projecting the 3D coordinates of the tie points to the images. The average reprojection error was computed as the mean reprojection error for all the point on the two images.

Fig. 4.17b show the global reprojection error, which exhibited a consistent fluctuation around 0.45 px, with a standard deviation of approximately 0.3 px.

4.6.3 3D SCENE RECONSTRUCTION

At each epoch, the dense point cloud consisted of 5 to 7 million points, with a spacing of ~ 3 cm, which is comparable to the image GSD. Due to the wide baseline and the different camera viewpoints, only the sub-vertical part of the terminal ice cliff and a few boulders near the upper edge of the ice cliff was reconstructed.

For clarity, Fig. 4.18 shows a point cloud for each month highlighting glacier retreat: ~ 17.5 m in total. Fig. 4.19a-d shows four vertical cross-sections extracted parallel to the streamwise direction at specific locations indicated in Fig. 4.18. The higher rate of ice ablation during the summer, especially from June to September, is evidenced by the greater shift to the left and downward of the corresponding cross sections (i.e., light green, light blue, and red curves) compared to those taken during the fall (i.e., yellow, dark green, and dark blue curves). Cross-section AA' reveals the occurrence of an ice block collapse in August (Fig. 4.19a). This can be observed from the rightmost section of the profile, which appears to detach from the main body of the ice cliff and slide to the right and downward. At the same time, the remaining sections of the profile exhibit a leftward movement. This behavior is consistent until the September profile (yellow curve), at which point the detached ice block is no longer present.

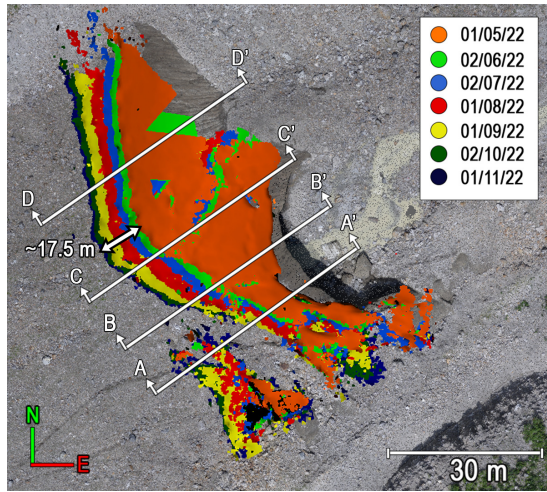


Figure 4.18: Series of the point clouds built at the beginning of each month from 01/05/22 to 01/11/22. The basemap is derived from a previous UAV survey carried out by the authors in July 2022

4.6.4 VOLUME VARIATIONS AND GLACIER RETREAT

Estimation of ice volume variation was performed by DOD along the streamwise direction (Sec. 4.5.5). Fig. 4.20 presents the daily ice volume variations and the cumulated curve, highlighting the varying ablation rate throughout the study period. Every value of the time series is referred to as the mean instant between the date of the two-point clouds from which it was derived (see Sec. 4.5.5.1). The ice loss rate increases during summer and significantly reduces in autumn, particularly after mid-September. A total ice loss of 63 000 m³ was observed from 01/05/2022 to 13/11/2022.

The daily glacier was estimated continuously tracking a point located at the center of the top edge of the terminal ice cliff, extracted as described in Sec. 4.5.6. The glacier retreat curve is shown in Fig. 4.21b and, similarly to that of volume variations, it shows a higher rate of retreat during the summer months, while the retreat velocity decreased between September and November. From 01/05/2022 to 13/11/2022, a retreat of 17.8 meters was estimated.

4.6.5 VALIDATION OF THE STEREO MODELS WITH UAV DATA

To validate the stereo models, both in terms of internal geometric and absolute georeferencing errors, the dense stereo point clouds were compared with those obtained from UAV-A (28/07/2022) and UAV-B (05/08/2022) flights. The signed difference between the UAV point clouds and the stereo point clouds acquired on the same day were computed using the M₃C₂ algorithm (Lague et al., 2013), in CloudCom-

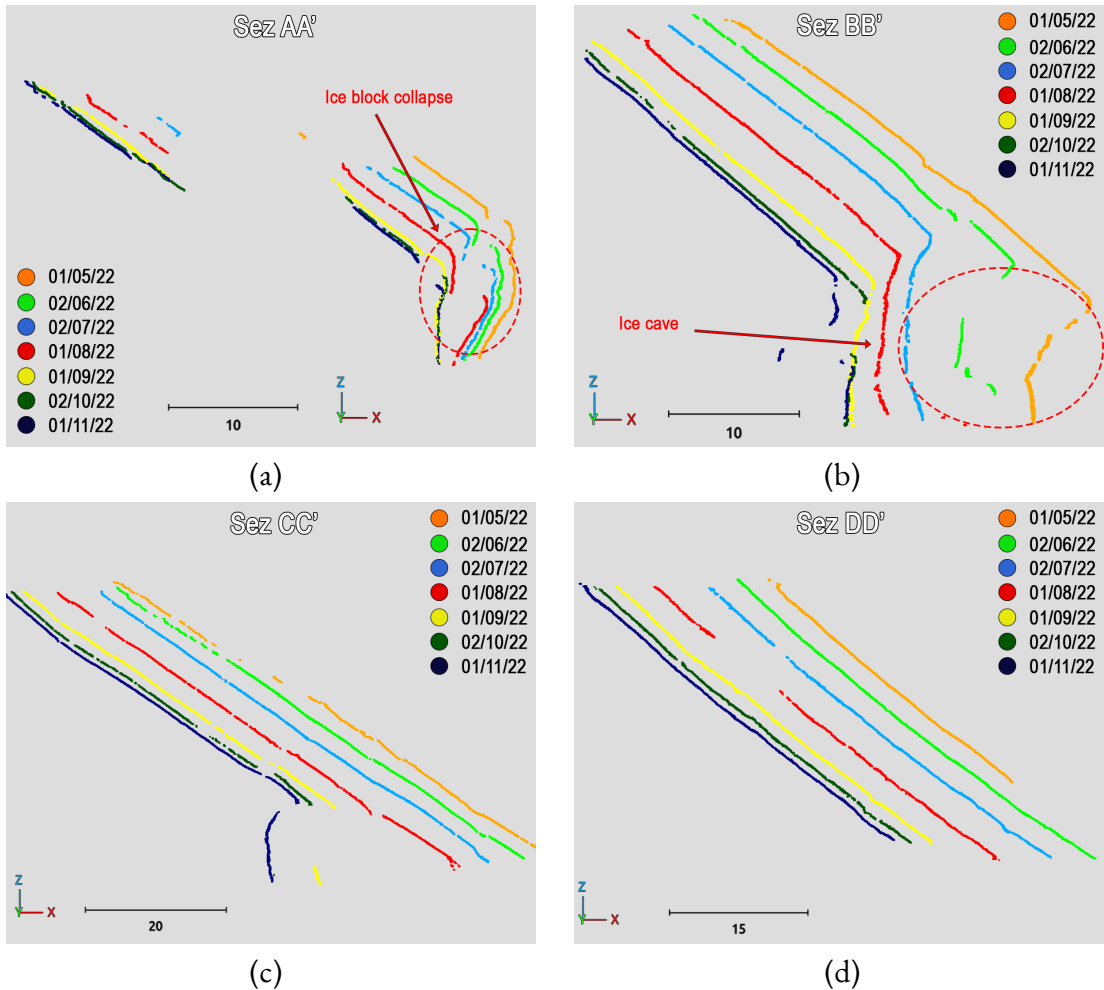


Figure 4.19: Vertical cross-sections extracted at the location marked in Fig. 4.18. All the cross-sections are extracted in a local reference system, with the X-direction pointing in the direction of the glacier flow, the Z-direction pointing upward, and the Y-direction completing the right-hand reference system. Please note the different scales of the figures, indicated by the scale bar (in meters).

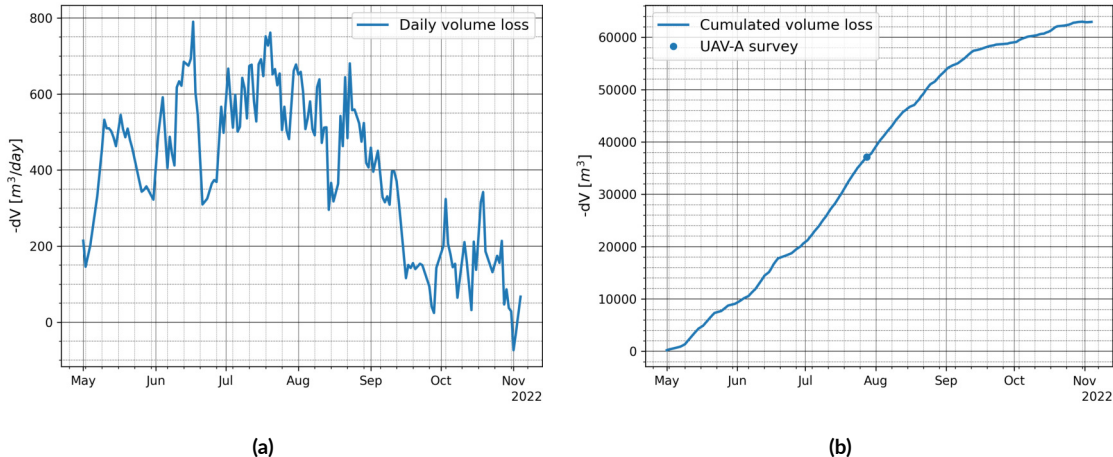


Figure 4.20: (a) Daily ice volume lost at the glacier terminus, estimated by DOD of pairs of point clouds spaced by 5 days. (b) Cumulative curve of the ice volume loss during the study period.

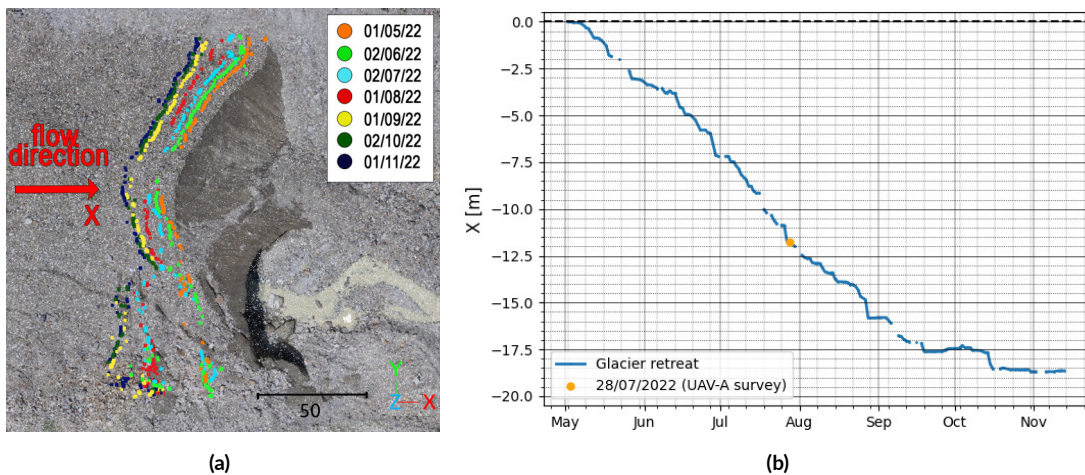


Figure 4.21: (a) Location of the segmented ice cliff top edge at the beginning of each month from May to November 2022; (b) Estimation of daily retreat based on the displacement of the top edge along the flow direction (X-direction). The location of the ice cliff on 01/05/2022 is considered as a baseline for the retreat. The orange marker indicates the day of the UAV-A survey.

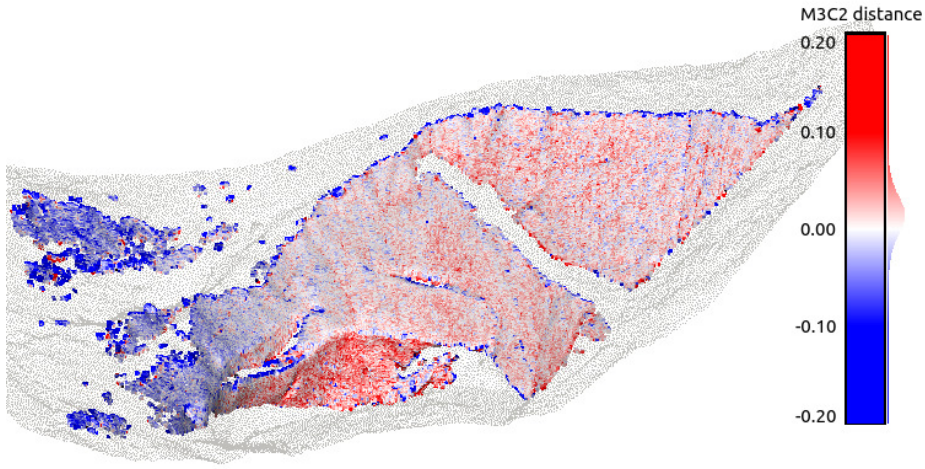


Figure 4.22: Comparison of the 28/07/22 stereo point cloud with the reference UAV point cloud acquired on the same day, computed with M3C2 algorithm ([Lague et al., 2013](#)). The stereo-point cloud is represented by a color scale indicating the distances relative to the UAV point cloud (represented by a light gray color as a reference).

pare. M₃C₂ first computes a 3D local surface normal for each core point at a scale D, by fitting a plane to the core points located within a radius of size $D/2$. Once the normal vectors are defined, the local distance is computed for each core point as the mean distance of the target points that fall inside a cylinder oriented as the normal vector, projected to the cylinder axis.

The comparison with the UAV-A point cloud resulted in a non-significant mean difference between the point clouds of 0.01 m, with a standard deviation of 0.04 cm, indicating an absence of systematic errors in stereo point cloud georeferencing. The largest differences were observed at the edges of the stereo point cloud and inside the ice cave (Fig. 4.22). Considering the UAV-B block, the mean difference was 0.05 m, with a standard deviation of 0.03 m. The non-negligible mean difference was likely due to a combination of the georeferencing accuracy of the stereo point cloud and the georeferencing error in the UAV model, which was in the order of a few centimeters (see Sec. 4.4.2). UAV-B block, in fact, had limited coverage in the surveyed area and fewer GCPs compared to the UAV-A block. Overall, both comparisons showed an overall error of stereo models smaller than 10 cm. Therefore, a decimetric level of precision can be reasonably considered for the stereo models.

4.6.6 GLACIER SURFACE VELOCITY AND MORPHOLOGY

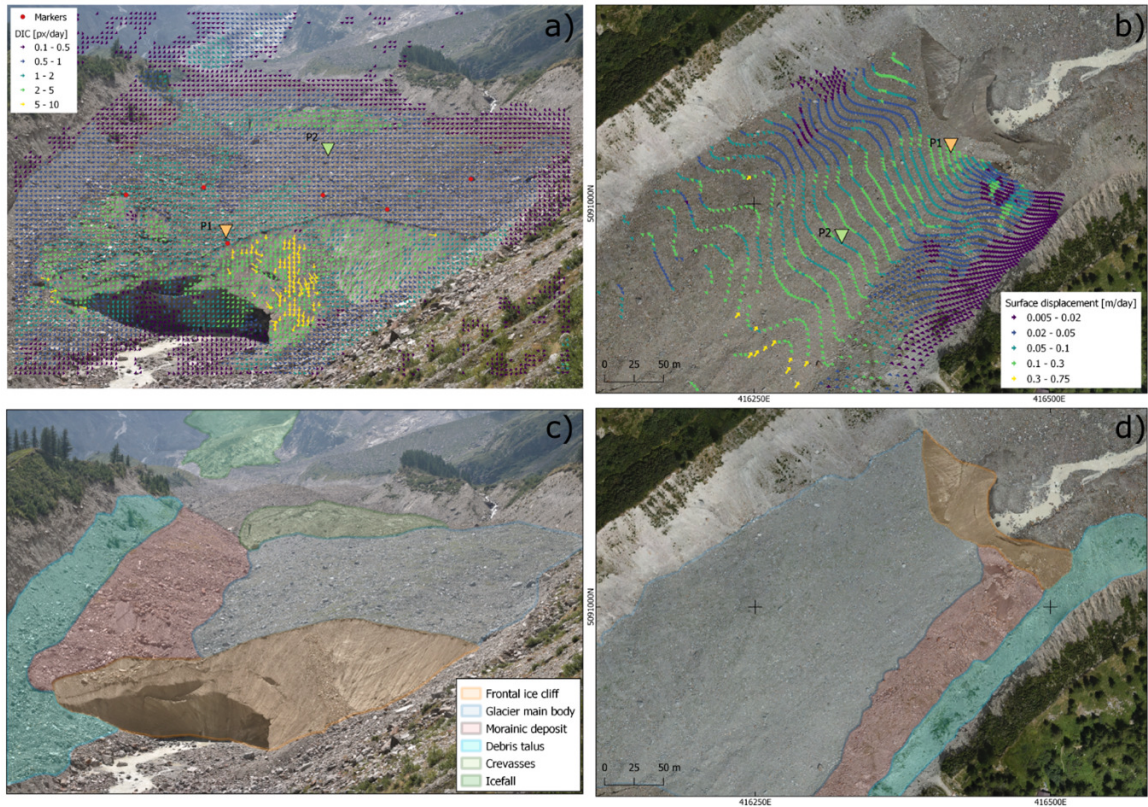


Figure 4.23: (a) DIC displacement map between 25 and 30 July 2022. (b) Orthorectified DIC displacement map between 25 and 30 July 2022. The triangles indicate the points P1 and P2, where we extracted the velocity time series. (c, d) Glacier domains are characterized by specific morphology and kinematics.

DIC displacement maps allow for evaluating the surface kinematics of the glacier and the moraines (Fig. 4.23a). We orthorectified the results only in the area of the right lobe up to 1 km distance from the terminal ice cliff, covering most of the north lobe of the glacier. Since the morphology of the frontal ice cliff evolved and moved significantly during the year, we did not orthorectify the displacement vectors in this area (Fig. 4.23b).

From the displacement maps of the oblique (Fig. 4.23a,c) and georeferenced images (Fig. 4.23b,d), it was possible to identify different domains, based on their morphology and kinematic behavior (Fig. 4.23c):

1. The frontal ice cliff of the glacier, where the ablation process was more concentrated. The slope was very steep, and several ice and rock falls occurred, particularly at the upper edge, at the limit

with the rear part of the glacier.

2. The debris-covered main body of the glacier, covering the last 400 m of the lobe. This region was gentler, and the velocity was higher in the central part.
3. The lateral morainic deposit, where the lack of lateral pressure from the glacier due to the loss of volume, destabilized the original moraines. The internal part collapsed onto the glacier and moved downslope due to glacier traction.
4. The debris talus resulting from erosional processes on the moraine, where the boundary between the glacier and the stable morainic deposit was partially covered by a debris deposit formed from superficial erosional processes on the steep morainic side.

Compared to the glacier's main body, the two latter domains moved at progressively lower rates, with the morainic talus showing the slowest velocity. Besides the kinematic regimes, these domains are clearly distinct due to long longitudinal fractures indicating displacement gradients. In the oblique images (Fig. 4.23c), it is possible to recognize other portions of the glacier outside the area of interest of this study, including a lower crevassed area and the icefall that feeds the glacier lobes.

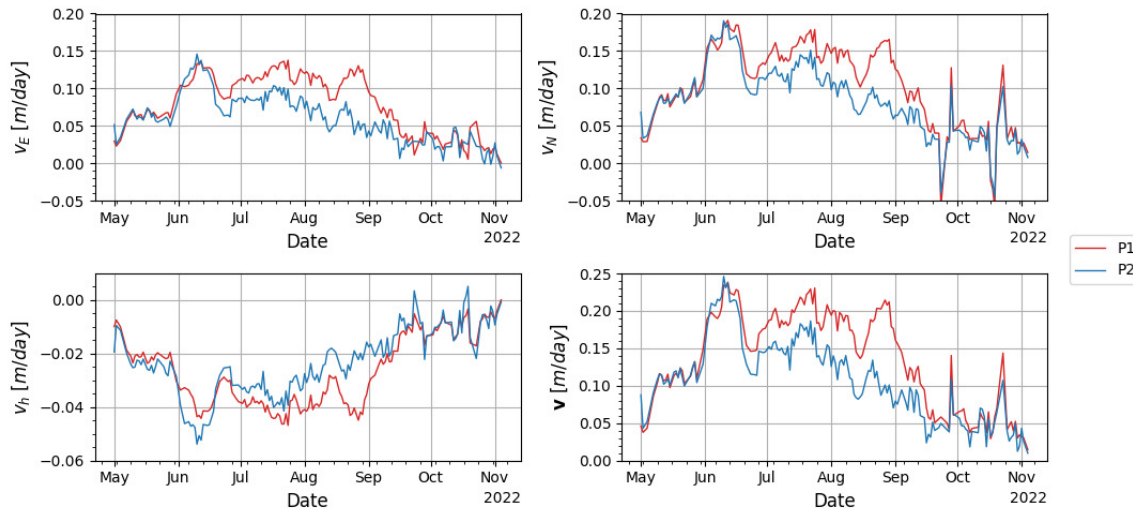


Figure 4.24: Time series of displacement extracted in the terminal part of the glacier lobe. The red curves correspond to point P1, located 10 m from the terminal ice cliff (considering the location of the terminal ice cliff on 28/07/2022), and the blue curves correspond to point P2, located 120 m far from the ice cliff. The location of points P1 and P2 is marked in Fig. 4.23.

We considered the displacement time series of two points on the glacier surface: one at 10 meters from the frontal ice cliff at the end of the considered period (P1) and one in the central part approximately 120 m

from the front (P_2), as indicated in Fig. 4.23a,b. The orthorectified 3D components of daily velocity and the velocity module, calculated between pairs of images spaced 5 days apart (see Sec. 4.5.5.1), are shown in Fig. 4.24. The time series exhibit similar behavior, with a Spearman correlation coefficient of 0.88, and show comparable velocity values between May and the first half of June and from the second half of September until the end of the period. However, P_1 has a 30% higher velocity during the warm season, with values ranging from 0.15 m d^{-1} , occurring on a few days during the second week of August and at the beginning of September to 0.23 m d^{-1} in mid-July. The South-North velocity component is the highest, varying during the warm season between 0.10 m d^{-1} to 0.18 m d^{-1} (P_1) and 0.06 m d^{-1} to 0.15 m d^{-1} (P_2). The East-West component is approximately 0.05 m d^{-1} lower, while the vertical component assumes smaller values, approximately 0.03 m d^{-1} .

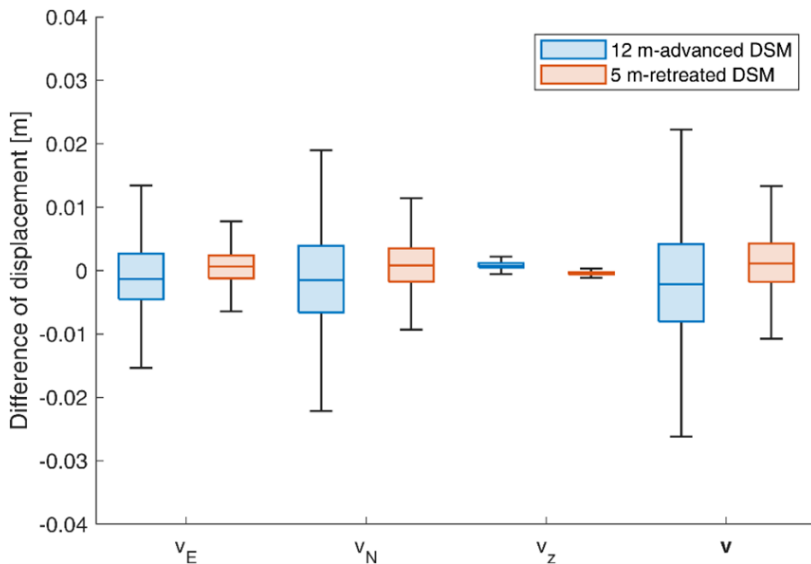


Figure 4.25: Uncertainty analysis of velocity vector orthorectification against possible DSM variation. Blue boxes represent the difference between the velocity vectors back-projected on the true DSM of 28/07/2022 and those back-projected on a simulated DSM advanced downstream by 12m (as it was in May 2022). Red boxes represent the difference between the true velocity vectors and those obtained with a simulated DSM with the glacier front retreating 5 meters upstream (as it was in November 2022). v_E , v_N , v_z , and v are respectively the three components in the east, north, and height directions and the magnitude of the differences of the velocity vectors.

4.6.7 VELOCITY ORTHORECTIFICATION UNCERTAINTY

To estimate the error related to DSM variations, we simulated two different snout positions, as described in Sec. 4.5.7.1. The first simulated snout position was 12 meters downstream of the location of the ter-

minal ice cliff on 28/07/2022, which was the most advanced front position at the beginning of the season (Fig. 4.21b). The second simulated snout position was 5 meters upstream, representing the most retreated position at the end of the season (Fig. 4.21b). On average, the different front locations caused a glacier elevation change of 1.76 m and -0.88 m for the advanced and retreated positions, respectively. The differences between the velocity vectors orthorectified with the true and the simulated DSMs are summarized in Fig. 4.25. The considered velocity vectors were measured by DIC between 25 and 30 July 2022, during a five-day period centered around the acquisition of the UAV-A DSM of 28/07/2022. It was observed that the velocity vertical component v_b was the least influenced, with a normalized MAD_z of 2.6% for the advanced simulated position and 1.3% for the retreated position. The $MADs$ of the East and North planimetric components v_E, v_N were similar and approximately 2.5 times higher than MAD_z , while the normalized $MADs$ of the velocity modules were 5.2% and 2.6% (advanced and retreated positions).

4.6.8 COMPARISON BETWEEN SURFACE VELOCITY, FRONTAL ICE LOSS AND METEOROLOGICAL VARIABLES

We compared the time series of ice volume variation dV , obtained with the stereo cameras, and the magnitude of the surface velocity v obtained by the monoscopic camera approach at the locations of points $P1$ and $P2$ (labeled as \mathbf{v}_{P1} and \mathbf{v}_{P2}) with the series of daily meteorological measurements acquired by the AWS. We observed a significant relationship between the daily average air temperature T , glacier surface velocity, and volume variations, while precipitation and incoming solar radiation were correlated. Fig. 4.26 shows the time series and the seasonal trend. All the series exhibit the same behavior, which is in phase. To remove the main seasonal trend and analyze the detrended signal, we subtracted the robust loess fit (Cleveland, 1979) from the original series and computed the Spearman correlation coefficients for each pair of variables (Tab. 4.2). The correlations were always larger than 0.49 for the detrended signal and larger than 0.81 for the original series.

4.7 DISCUSSION

4.7.1 HAND-CRAFTED VS DEEP LEARNING MATCHING

In the case of the Belvedere Glacier, the wide baseline between the two cameras posed a challenge for traditional hand-crafted matching techniques, which failed to find sufficient corresponding points for estimating camera poses. Traditional feature matching, including well-known commercial solutions like Agisoft Metashape, yielded a limited number of poorly distributed tie points, ranging from a dozen to a hundred

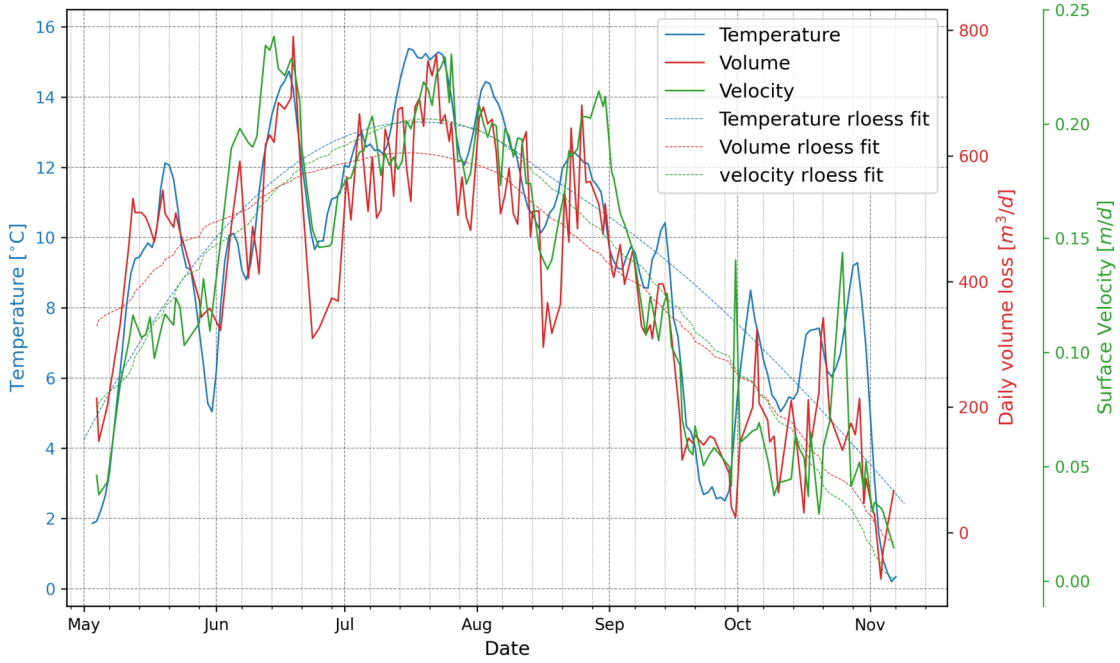


Figure 4.26: Time series of the daily volume loss due to the glacier terminus retreat, compared to the time series of glacier surface velocity extracted by monoscopic DIC at the location of point P1 (located close to the ice cliff terminus and marked with an orange triangle in Fig. 4.23) and the 5-day smoothed time series air temperature measured by the AWS at the location marked in Fig. 4.7.

Table 4.2: Spearman correlation coefficients between original (ρ_S) and detrended (ρ_D) signals for the daily volume variation (dV), mean air temperature (T), and surface velocity of points $P1$ and $P2$ (v_{P1} and v_{P2} respectively). In all the cases, the p-value was $< 10^{-5}$.

	ρ_S	ρ_D
$dV \& T$	0.89	0.80
$dV \& v_{P1}$	0.87	0.64
$dV \& v_{P2}$	0.81	0.49
$T \& v_{P1}$	0.88	0.59
$T \& v_{P2}$	0.82	0.59
$v_{P1} \& v_{P2}$	0.88	0.64

tie points. In all the cases, the tie points were concentrated mainly in the central part of the ice cliff, where the ice cliff was nearly vertical, and it was impossible to determine the camera's relative orientation.

On the other hand, DL feature matching algorithms outperformed traditional hand-crafted methods, successfully finding a significant number of corresponding features. SuperPoint and SuperGlue matched between 1000 and 3500 features, which were well distributed over the entire ice cliff, with some along the streamwise right moraine in the background. This substantial matching success allowed for estimating a sparse but complete 3D reconstruction of the terminal ice cliff, serving as the starting point for a dense scene reconstruction. With a reliable camera pose and sparse reconstruction in place, traditional dense matching algorithms, like semi-global matching, proved to be effective. To further enhance the result, state-of-the-art algorithms can be employed for even better performance.

4.7.2 MERGING STEREOSCOPIC AND MONOSCOPIC PROCESSINGS TO STUDY THE GLACIER DYNAMICS

The stereoscopic and monoscopic workflows focused on different aspects of the glacier's dynamics, and the combined use of these two pieces of information is useful for characterizing the glacier behavior of the studied area. The installation of two cameras allowed for the stereoscopic reconstruction of the glacier snout and the computation of volume variations, while the use of a single camera (C_2) allowed for the characterization of the movement of the debris-covered sector of the lobe.

The proposed system was able to monitor the evolution of the glacier in its different sectors and supports the identification of different kinematic sectors (Fig. 4.23). The north lobe of the Belvedere Glacier exhibited a complex motion that involved multiple components. This included a retreat along the streamwise direction, a downslope forward motion due to glacier sliding, and a thinning of the glacier surface caused by ablation. From the stereoscopic processing, it was possible to extract the morphology and position of the terminal lobe, which retreated by 17.6 m between May and November 2022 (Fig. 4.21), and ice volume loss (Fig. 4.20). On the other hand, the monoscopic approach allowed us to derive the forward motion of the glacier by tracking features on the glacier's surface. Additionally, the availability of volumetric and kinematic data allowed the combined analysis of the potential relationship between volume variation, surface velocity and external meteorological factors such as air temperature.

4.7.3 GLACIER VELOCITY, FRONTAL ABLATION AND TEMPERATURE

Typically, mountain glacier motion is dominated by basal sliding (Willis, 1995), which is related to the state of the hydraulic drainage system (Vincent et al., 2016). In particular, the water pressure is higher in

the presence of distributed small channels (Pimentel and Flowers, 2011), while it diminished when large cavities form and a more efficient drainage develops (Nienow et al., 2005). Consequently, glacier flow is often faster in early summer than at the end of the warm season (Sanders et al., 2018, Vincent et al., 2016). Therefore, at the seasonal scale, glacier surface velocity is sometimes not linked to air temperature (Sanders et al., 2018). At hourly to daily scale, several studies showed that the flow velocity is linked to subglacial water pressure (Sugiyama et al., 2010) and air temperature (Liu et al., 2019), even though Allstadt et al. (2015) did not observe a significant variation in the diurnal cycle. Moreover, in many cases, the flow velocity was observed to rise after intense rainstorms (Benoit et al., 2015, Horgan et al., 2015, Sugiyama et al., 2010).

We showed that the daily air temperature variations are strictly linked to glacier surface velocity at a daily to weekly scale. On a monthly scale, we registered the highest velocity in July, even though the absolute peak was reached in the first half of June, concurrently with high air temperature. Contrary to the findings of other scholars (Benoit et al., 2015, Horgan et al., 2015, Sugiyama et al., 2010), we did not register any relationship with rainfall episodes. These observations suggest that the subglacial hydraulic system remained homogeneous during the season (at least in the lower portion of the north lobe). Besides, we also observed an even stronger relationship between air temperature and frontal ablation, which, to our knowledge, has never been documented before. This was possible thanks to the stereoscopic system that produced volumetric data, increasing the understanding of the glacier snout dynamics.

4.7.4 TRANSFERABILITY OF THE SYSTEM

The transferability of the low-cost camera system used in this study to other test sites is a crucial aspect to consider. The installation process of the system is relatively straightforward, as the cameras are mounted on topographic tripods, eliminating the need for complex and permanent structures. This ease of installation enables the system to be replicated in different sites without significant difficulty. While a more robust installation with minimal vibrations and camera rotations would be beneficial, the simplicity of the setup allows for efficient deployment by a small team without requiring specialized equipment.

The Belvedere glacier, characterized by debris cover and a dirty ice terminal cliff, presents favorable conditions for 3D reconstruction due to the presence of distinct patterns in the images. However, previous studies have also achieved successful 3D reconstructions of bare ice or snow-covered areas. Belloni et al. (2023) and Gindraux et al. (2017) utilized UAV-SfM to generate 3D models of debris-free or partially debris-covered glaciers. Taylor et al. (2023) demonstrated the effectiveness of an extremely low-cost camera for 3D reconstruction of a debris-free glacier calving front in Iceland. Additionally, Avanzi et al. (2018)

and [De Michele et al. \(2016\)](#) employed UAV-based photogrammetric reconstruction to map snow depth. Despite snow having even fewer discernible patterns than bare ice, multi-camera photogrammetry allowed for accurate 3D reconstructions.

It is worth noting that these examples utilized traditional feature-matching techniques. Results can be further improved with state-of-the-art DL sparse and dense matching techniques. Even though the Belvedere glacier's characteristics facilitate 3D reconstruction, successful reconstructions of debris-free ice and snow-covered areas using similar techniques have been demonstrated in the literature, supporting the broader applicability of the low-cost camera system for monitoring glaciers in diverse environments.

References

- Allstadt, K. E., Shean, D. E., Campbell, A., Fahnestock, M., & Malone, S. D. (2015). Observations of seasonal and diurnal glacier velocities at mount rainier, washington, using terrestrial radar interferometry. *The Cryosphere*, 9, 2219–2235, <https://doi.org/10.5194/tc-9-2219-2015>.
- Avanzi, F., et al. (2018). Centimetric accuracy in snow depth using unmanned aerial system photogrammetry and a multistation. *Remote Sensing*, 10(5), <https://doi.org/10.3390/rs10050765>.
- Bay, H., Tuytelaars, T., & Van Gool, L. (2006). SURF: Speeded Up Robust Features. In *Computer Vision – ECCV 2006*, Lecture Notes in Computer Science (pp. 404–417). Berlin, Heidelberg: Springer.
- Belloni, V., Rita, M. D., Fugazza, D., Traversa, G., Hanson, K., Diolaiuti, G., & Crespi, M. (2023). High-resolution high-accuracy orthophoto map and digital surface model of fornii glacier tongue (central italian alps) from uav photogrammetry. *Journal of Maps*, 19(1), 2217508, <https://doi.org/10.1080/17445647.2023.2217508>.
- Benoit, L., et al. (2015). Multi-method monitoring of glacier d'argentièrre dynamics. *Annals of Glaciology*, 56, 118–128, <https://doi.org/10.3189/2015AoG70A985>.
- Blanch, X., Guinau, M., Eltner, A., & Abellan, A. (2023). Fixed photogrammetric systems for natural hazard monitoring with high spatio-temporal resolution. *Natural Hazards and Earth System Sciences Discussions*, 2023, 1–19, <https://doi.org/10.5194/nhess-2023-79>.
- Chiarle, M., Viani, C., Mortara, G., Deline, P., Tamburini, A., & Nigrelli, G. (2023). Large glacier failures in the Italian Alps over the last 90 years. *Geografia Fisica e Dinamica Quaternaria*, (45), 19–40, <https://doi.org/10.4461/GFDQ.2022.45.2>.
- Cleveland, W. (1979). Robust locally weighted regression and smoothing scatterplots. *Journal of the American Statistical Association*, 74(368), 829–836, <https://doi.org/10.1080/01621459.1979.10481038>.
- De Michele, C., et al. (2016). Using a fixed-wing uas to map snow depth distribution: an evaluation at peak accumulation. *The Cryosphere*, 10(2), 511–522, <https://doi.org/10.5194/tc-10-511-2016>.
- Dematteis, N. & Giordan, D. (2021). Comparison of digital image correlation methods and the impact of noise in geoscience applications. *Remote Sensing*, 13(2), <https://doi.org/10.3390/rs13020327>.
- Dematteis, N., Giordan, D., Crippa, B., & Monserrat, O. (2022). Fast local adaptive multiscale image matching algorithm for remote sensing image correlation. *Computers & Geosciences*, 159, 104988, <https://doi.org/10.1016/j.cageo.2021.104988>.
- DeTone, D., Malisiewicz, T., & Rabinovich, A. (2018). Superpoint: Self-supervised interest point detection and description. In *Proceedings of the IEEE Conference on Computer Vision and Pattern Recognition (CVPR) Workshops*.
- Edstedt, J., Sun, Q., Bökman, G., Wadenbäck, M., & Felsberg, M. (2023). Roma: Robust dense feature matching.

- Elias, M., Eltner, A., Liebold, F., & Maas, H.-G. (2020). Assessing the influence of temperature changes on the geometric stability of smartphone- and raspberry pi cameras. *Sensors*, 20(3), <https://doi.org/10.3390/s20030643>.
- Emnify (2023). <https://www.emnify.com/>. [Online; visited on 22/2/2023].
- Faillettaz, J., Funk, M., & Vincent, C. (2015). Avalanching glacier instabilities: Review on processes and early warning perspectives. *Reviews of Geophysics*, 53(2), 203–224, <https://doi.org/10.1002/2014RG000466>.
- Farella, E. M., Morelli, L., Remondino, F., Mills, J. P., Haala, N., & Crompvoets, J. (2022). The eurasdr time benchmark for historical aerial images. *The International Archives of the Photogrammetry, Remote Sensing and Spatial Information Sciences*, XLIII-B2-2022, 1175–1182, <https://doi.org/10.5194/isprs-archives-XLIII-B2-2022-1175-2022>.
- Fitch, A., Kadyrov, A., Christmas, W. J., & Kittler, J. (2002). Orientation correlation. In *BMVC* (pp. 1–10).: Citeseer.
- Förstner, W. & Wrobel, B. (2016). *Photogrammetric Computer Vision*. Springer Nature: Cham.
- Gindraux, S., Boesch, R., & Farinotti, D. (2017). Accuracy assessment of digital surface models from unmanned aerial vehicles' imagery on glaciers. *Remote Sensing*, 9(2).
- Giordan, D., Allasia, P., Dematteis, N., Dell'Anese, F., Vagliasindi, M., & Motta, E. (2016). A Low-Cost Optical Remote Sensing Application for Glacier Deformation Monitoring in an Alpine Environment. *Sensors*, 16(10), 1750, <https://doi.org/10.3390/s16101750>.
- Hackel, T., Wegner, J., & Schindler, K. (2016). Contour detection in unstructured 3d point clouds. In *Proc. CVPR IEEE* (pp. 1610–1618).
- Harris, C. G. & Stephens, M. J. (1988). A combined corner and edge detector. In *Alvey Vision Conference*.
- Heid, T. & Kääb, A. (2012). Evaluation of existing image matching methods for deriving glacier surface displacements globally from optical satellite imagery. *Remote Sens. Environ.*, 118, 339–355, <https://doi.org/https://doi.org/10.1016/j.rse.2011.11.024>.
- Hendrickx, H., et al. (2022). Timing, volume and precursory indicators of rock- and cliff fall on a permafrost mountain ridge (Mattertal, Switzerland). *Earth Surf. Process. Landforms*, 47(6), 1532–1549, <https://doi.org/10.1002/esp.5333>.
- Hirschmüller, H., Buder, M., & Ernst, I. (2012). MEMORY EFFICIENT SEMI-GLOBAL MATCHING. In *Annals of the Photogrammetry, Remote Sensing and Spatial Information Sciences*, volume I-3 (pp. 371–376).: Copernicus GmbH. ISSN: 2194-9042.
- Horgan, H. J., Anderson, B., Alley, R. B., Chamberlain, C., Dykes, R., Kehrl, L. M., & Townend, J. (2015). Glacier velocity variability due to rain-induced sliding and cavity formation. *Earth and Planetary Science Letters*, 432, 273–282, <https://doi.org/10.1016/j.epsl.2015.10.016>.
- Ioli, F., et al. (2023). A replicable open-source multi-camera system for low-cost 4d glacier monitoring. *Int. Arch. Photogramm.*, XLVIII-M-1-2023, 137–144, <https://doi.org/10.5194/isprs-archives-XLVIII-M-1-2023-137-2023>.

- Ioli, F., Dematteis, N., Giordan, D., Nex, F., & Pinto, L. (2024). Deep learning low-cost photogrammetry for 4d short-term glacier dynamics monitoring. *PFG-Journal of Photogrammetry, Remote Sensing and Geoinformation Science*, (pp. 1–22).
- James, M. R., How, P., & Wynn, P. M. (2016). Pointcatcher software: analysis of glacial time-lapse photography and integration with multitemporal digital elevation models. *J. of Glaciol.*, 62(231), 159–169, <https://doi.org/10.1017/jog.2016.27>.
- Jin, Y., Mishkin, D., Mishchuk, A., Matas, J., Fua, P., Yi, K. M., & Trulls, E. (2021). Image matching across wide baselines: From paper to practice. *International Journal of Computer Vision*, 129(2), 517–547, <https://doi.org/10.1007/s11263-020-01385-0>.
- Kääb, A., et al. (2005). Remote sensing of glacier-and permafrost-related hazards in high mountains: an overview. *Natural Hazards and Earth System Science*, 5(4), 527–554, <https://doi.org/10.5194/nhess-5-527-2005>.
- Kneib, M., et al. (2022). Sub-seasonal variability of supraglacial ice cliff melt rates and associated processes from time-lapse photogrammetry. *The Cryosphere*, 16(11), 4701–4725, <https://doi.org/10.5194/tc-16-4701-2022>.
- Lague, D., Brodu, N., & Leroux, J. (2013). Accurate 3d comparison of complex topography with terrestrial laser scanner: Application to the rangitikei canyon (nz). *ISPRS J. Photogramm. Remote Sens.*, 82, 10–26.
- Li, Z. & Snavely, N. (2018). Megadepth: Learning single-view depth prediction from internet photos. In *Proc. CVPR IEEE* (pp. 2041–2050).
- Lindenberger, P., Sarlin, P.-E., & Pollefeyns, M. (2023). Lightglue: Local feature matching at light speed.
- Liu, L., Jiang, L., Sun, Y., Wang, H., Sun, Y., Xu, H., et al. (2019). Diurnal fluctuations of glacier surface velocity observed with terrestrial radar interferometry at laohugou no. 12 glacier, western qilian mountains, china. *Journal of Glaciology*, 65, 239–248, <https://doi.org/10.1017/jog.2019.1>.
- Lowe, D. G. (2004). Distinctive image features from scale-invariant keypoints. *International Journal of Computer Vision*, 60(2), 91–110.
- Luo, Z., et al. (2020). Aslfeat: Learning local features of accurate shape and localization.
- Maas, H.-G., Dietrich, R., Schwalbe, E., Bäßler, M., & Westfeld, P. (2006). Analysis of the motion behaviour of Jakobshavn Isbræ glacier in Greenland by monocular image sequence analysis. *Int. Arch. Photogramm. Remote Sens. Spat. Inf. Sci. - ISPRS Arch.*, 36.
- Maiwald, F., Feurer, D., & Eltner, A. (2023). Solving photogrammetric cold cases using ai-based image matching: New potential for monitoring the past with historical aerial images. *ISPRS Journal of Photogrammetry and Remote Sensing*, 206, 184–200, <https://doi.org/https://doi.org/10.1016/j.isprsjprs.2023.11.008>.
- Maiwald, F., Lehmann, C., & Lazariv, T. (2021). Fully automated pose estimation of historical images in the context of 4d geographic information systems utilizing machine learning methods. *ISPRS Int. of Geo-Inf.*, 10(11).

Markiewicz, J., Kot, P., Markiewicz, L., & Muradov, M. (2023). The evaluation of hand-crafted and learned-based features in terrestrial laser scanning-structure-from-motion (tls-sfm) indoor point cloud registration: the case study of cultural heritage objects and public interiors. *Heritage Science*, 11, 1–26, <https://doi.org/10.1186/s40494-023-01099-9>.

Marsy, G., Vernier, F., Bodin, X., Cusicanqui, D., Castaings, W., & Trouvé, E. (2020). MONITORING MOUNTAIN CRYOSPHERE DYNAMICS BY TIME LAPSE STEREO PHOTOGRAMMETRY. *ISPRS Annals of the Photogrammetry, Remote Sensing and Spatial Information Sciences*, V-2, <https://doi.org/10.5194/isprs-annals-V-2-2020-459-2020>.

Messerli, A. & Grinsted, A. (2015). Image georectification and feature tracking toolbox: ImGRAFT. *Geoscientific Instrumentation, Methods and Data Systems*, 4(1), 23–34, <https://doi.org/10.5194/gi-4-23-2015>.

Metashape, A. (2023). <https://www.agisoft.com>.

Mishchuk, A., Mishkin, D., Radenovic, F., & Matas, J. (2018). Working hard to know your neighbor's margins: Local descriptor learning loss.

Mishkin, D., Matas, J., & Perdoch, M. (2015). Mods: Fast and robust method for two-view matching. *Computer Vision and Image Understanding*, 141, 81–93, <https://doi.org/https://doi.org/10.1016/j.cviu.2015.08.005>.

Morelli, L., Bellavia, F., Menna, F., & Remondino, F. (2022). Photogrammetry now and then – from hand-crafted to deep-learning tie points –. *The International Archives of the Photogrammetry, Remote Sensing and Spatial Information Sciences*, XLVIII-2/W1-2022, 163–170, <https://doi.org/10.5194/isprs-archives-XLVIII-2-W1-2022-163-2022>.

Morelli, L., Ioli, F., Beber, R., Menna, F., Remondino, F., & Vitti, A. (2023). Colmap-slam: A framework for visual odometry. *Int. Arch. Photogramm.*, 48, 317–324.

Nienow, P. W., Hubbard, A. L., Hubbard, B. P., Chandler, D. M., Mair, D. W., Sharp, M. J., & Willis, I. C. (2005). Hydrological controls on diurnal ice flow variability in valley glaciers. *Journal of Geophysical Research: Earth Surface*, 110, F04015, <https://doi.org/10.1029/2003JF000112>.

Nigrelli, G., et al. (2024). First national inventory of high-elevation mass movements in the Italian Alps. *Comput. Geosci.*, 184, 105520, <https://doi.org/10.1016/j.cageo.2024.105520>.

Noferini, L., Mecatti, D., Macaluso, G., Pieraccini, M., & Atzeni, C. (2009). Monitoring of Belvedere Glacier using a wide angle GB-SAR interferometer. *Journal of Applied Geophysics*, 68(2), 289–293, <https://doi.org/10.1016/j.jappgeo.2009.02.004>.

Ono, Y., Trulls, E., Fua, P., & Yi, K. M. (2018). Lf-net: Learning local features from images.

Pimentel, S. & Flowers, G. (2011). A numerical study of hydrologically driven glacier dynamics and subglacial flooding. *Proceedings of the Royal Society A: Mathematical, Physical and Engineering Sciences*, 467, 537–558, <https://doi.org/10.1098/rspa.2010.0211>.

Remondino, F., Morelli, L., Stathopoulou, E., Elhashash, M., & Qin, R. (2022). Aerial triangulation with learning-based tie points. *Int. Arch. Photogramm.*, XLIII-B2-2022, 77–84, <https://doi.org/10.5194/isprs-archives-XLIII-B2-2022-77-2022>.

- Willis, I. C. (1995). Intra-annual variations in glacier motion: A review. *Progress in Physical Geography*, 19, 61–106, <https://doi.org/10.1177/03091339501900104>.
- Yao, G., Yilmaz, A., Meng, F., & Zhang, L. (2021). Review of Wide-Baseline Stereo Image Matching Based on Deep Learning. *Remote Sensing*, 13(16), 3247, <https://doi.org/10.3390/rs13163247>.
- Yi, K. M., Trulls, E., Lepetit, V., & Fua, P. (2016). Lift: Learned invariant feature transform.
- Zhang, L., Rupnik, E., & Pierrot-Deseilligny, M. (2021). Feature matching for multi-epoch historical aerial images. *ISPRS Journal of Photogrammetry and Remote Sensing*, 182, 176–189, <https://doi.org/10.1016/j.isprsjprs.2021.10.008>.
- Zhang, Z. (2000). A flexible new technique for camera calibration. *IEEE Trans. Pattern Anal. Machine Intell.*, 22(11), 1330–1334, <https://doi.org/10.1109/34.888718>.

5

Towards a low-cost multi-camera multi-epoch monitoring with deep learning photogrammetry

THIS CHAPTER IS BASED ON:

- Morelli, L., Ioli, F., Maiwald, F., Mazzacca, G., Menna, F., and Remondino, F. (2024). DEEP-IMAGE-MATCHING: A TOOLBOX FOR MULTI-VIEW IMAGE MATCHING OF COMPLEX SCENARIOS, Int. Arch. Photogramm. Remote Sens. Spatial Inf. Sci., XLVIII-2/W4-2024, 309–316, <https://doi.org/10.5194/isprs-archives-XLVIII-2-W4-2024-309-2024>.

5.1 INTRODUCTION

Chapter 4 demonstrated the potential of a low-cost stereoscopic camera system for short-term monitoring of glacier dynamics. However, using a stereo camera only limits the viewing area that the system can cover, especially under sub-optimal viewing conditions and acquisition geometry. This chapter introduces a transition to a multi-camera approach, which offers several advantages for glaciological studies to further enhance 3D reconstruction capabilities. Firstly, it allows for reducing occlusions, ensuring better coverage of complex glacier environments. Secondly, a multi-view approach can improve the 3D reconstructions, providing more observation redundancy and more robust photogrammetric estimation. Finally, a multi-camera framework guarantees flexibility, allowing the integration of additional cameras over time for long-term monitoring within the same processing pipeline.

As discussed in Chapter 4, wide camera baselines, strong viewpoint changes, and the often low-texture surfaces inherent to glacial environments pose significant challenges for traditional feature-matching techniques. Therefore, standard SfM software packages are often unsuitable for performing photogrammetric reconstruction. This complexity introduces the need for cutting-edge approaches like the Deep-Image-Matching (DIM) toolbox¹ presented in this chapter. DIM is a versatile toolbox for traditional and DL-based multi-view image matching. It addresses a crucial gap in existing libraries: the lack of tools specifically tailored for multi-view matching under challenging conditions using hand-crafted and DL local features and matching algorithms.

The development of DIM was a collaborative effort between myself and Luca Morelli, a PhD student at 3DOM - FBK. We both contributed equally to the software development, as evidenced by the commit history on GitHub. Specifically, I was responsible for the backbone implementation of the software package, which included defining the main object-oriented structure for the extractors and matchers that are inherited by all the specific algorithms. Additionally, I handled image resolution management, tiling approaches, geometric verification, and integration with MICMAC and pycolmap. Conversely, Luca focused on the image rotation problem and integration with COLMAP and OpenMVG.

This chapter will explore the potential of DIM by testing it against challenging scenarios (e.g., wide baselines, viewpoint differences, low texture), highlighting its potential advantages over traditional feature-matching methods. The goal is to assess the suitability of DL local features for photogrammetric applications by exploiting the DIM library. Unfortunately, a multi-camera monitoring system has not been installed yet at the Belvedere Glacier. Therefore, this chapter will focus on the software component, and we will simulate a multi-view scenario of the Belvedere Glacier using UAV images.

¹<https://github.com/3DOM-FBK/deep-image-matching>

5.2 LIMITATIONS OF DEEP LEARNING LOCAL FEATURES

As discussed in Sec. 4.2, a large number of trainable algorithms for robust local feature extraction and matching have been developed in the past few years (Remondino et al., 2022). DL techniques, and particularly attention-based architectures (Vaswani et al., 2023), have emerged as powerful techniques for extracting and matching features under challenging conditions, such as wide baselines and significant radiometric differences (Jin et al., 2021, Yao et al., 2021).

Although DL local features offer several advantages, their limited rotational invariance remains a constraint, particularly when analyzing images with diverse orientations, such as those typical of aerial and UAV photogrammetric acquisitions. While some initial studies highlighted this issue, many approaches have not prioritized the solution to this problem, as datasets with minimal rotational variability (e.g., upright images) are commonly used within the computer vision community. Recently, some end-to-end approaches like LIFT (Yi et al., 2016) and LFNet (Ono et al., 2018), and semi-dense methods like RoRD (Parihar et al., 2022) and SE2-LoFTR (Bökman and Kahl, 2022), demonstrate progress in achieving rotational invariance. Recent works with Steerable CNNs (Cohen and Welling, 2016), which are group equivariant neural networks that allow for *steering* the descriptors to make them invariant by the rotation, further address this limitation (Bökman and Kahl, 2022, Bökman et al., 2023). Nevertheless, the number of approaches specifically addressing this problem is minimal compared to the overall interest in DL-based feature-matching algorithms. On the other hand, the most common approach to address large rotation is still to compensate by iteratively rotating images during matching, but this becomes computationally intensive for large datasets.

Another limitation of DL approaches is their computational expense, which makes them unsuitable for processing high-resolution images, mainly when consumer-grade GPUs are employed. However, the ability to process high-resolution images is crucial for leveraging the available image radiometric information in high-accuracy photogrammetric applications. In addition, it's worth noting that training itself is often carried out on low-resolution images. The impact of the resolution discrepancy between the training and the inference is still uncertain (Wu et al., 2024). In fact, training must be generalized enough not to require additional training on high-resolution images to guarantee a robust inference.

While the potential of these approaches under extreme lighting conditions and radiometric variations is increasingly evident, some preliminary experiences suggest that these approaches may lack locally accurate identification (Morelli et al., 2024). Indeed, despite the existence of DL approaches for several years, their utilization in photogrammetric applications remains relatively limited.

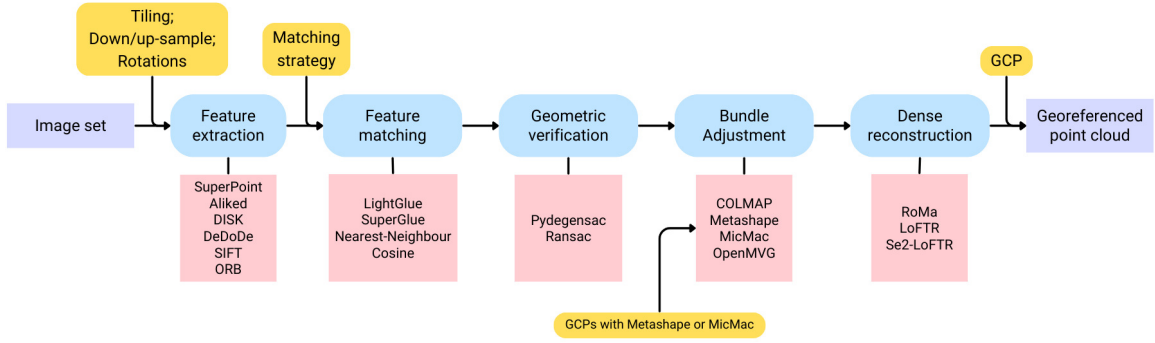


Figure 5.1: Scheme of the DIM workflow.

5.3 DEEP-IMAGE-MATCHING

Deep-Image-Matching² (DIM) is a flexible, open-source Python library designed for robust multi-view image matching, leveraging both hand-crafted and DL matching techniques, that aims to overcome the major limitations of DL local features for photogrammetric applications. Given a set of unordered images, DIM can perform the matching operations and return the corresponding points between images, providing the essential foundation for bundle adjustment and accurate photogrammetric reconstruction.

DIM’s primary goal is to provide a user-friendly interface to a wide selection of state-of-the-art computer vision algorithms for matching and tracking corresponding points across unordered images. Additionally, DIM aims to overcome the main limitations of DL-based matching approaches that pose challenges for their practical usage in photogrammetry and remote sensing. These limitations include sensitivity to rotation changes, computational bottlenecks with high-resolution images (e.g., larger than 3000 px on the longest edge), inefficient image pair selection for large datasets, difficulties in achieving sub-pixel accuracy, and compatibility issues with existing SfM software packages.

DIM employs a modular workflow designed for effective multi-view matching Fig. 5.1. DIM itself does not perform the bundle adjustment and scene reconstruction, but it is designed to ensure seamless integration with various popular SfM software packages within the remote sensing and computer vision communities. These include COLMAP (Schönberger and Frahm, 2016), OpenMVG (Moulon et al., 2016), MicMac (Rupnik et al., 2017), Agisoft Metashape³, and any other software package that supports the import from a Bundler solution format (Li and Snavely, 2018). Additionally, DIM can be easily integrated into a multi-camera multi-epoch pipeline, e.g., by exploiting the multi-temporal functionalities of

²<https://github.com/3DOM-FBK/deep-image-matching>

³<https://www.agisoft.com/>

ICEPy4D (see Chapter 4).

The DIM processing pipeline begins with a pre-processing stage where users select from different matching strategies (brute-force, low-resolution guided, sequential, image retrieval, or custom) to intelligently select the pair of images for optimized matching. DIM provides a module for addressing the challenge of rotated images within datasets (e.g., in the case of aerial or UAV surveys) by automatically identifying the ideal rotation angle between image pairs, significantly boosting matching accuracy. Additionally, users can opt to match images at their original resolution or employ down-sampling or up-sampling techniques. DIM offers the added capability of image tiling to handle high-resolution imagery, ensuring efficient processing without reducing detection precision.

For the actual matching, DIM supports various combinations of local feature and matching algorithms, named *pipelines*, optimized for diverse problem domains. This allows users to tailor the workflow to their specific needs. Each pipeline consists of two main components: (i) an *extraction* step that is responsible for extracting local features from all images in the dataset and (ii) a *matching* step that matches the extracted local features across the image pairs selected by the chosen matching strategy.

DIM supports a wide range of local features and matching algorithms, from traditional ones to recent state-of-the-art learning approaches. Available local features include ORB (Rublee et al., 2011), SIFT (Lowe, 2004), SuperPoint (DeTone et al., 2018), ALIKE (Zhao et al., 2022), ALIKED (Zhao et al., 2023), DISK (Tyszkiewicz et al., 2020), Key.Net (Barroso-Laguna et al., 2019) + HardNet (Pultar, 2020), DeDoDe (Edstedt et al., 2024) and XFeat (Potje et al., 2024). DIM implements SuperGlue (Sarlin et al., 2020), LightGlue (Lindenberger et al., 2023), and traditional nearest-neighbor algorithms based on the KORNIA library (Riba et al., 2019) as local features matchers. Additionally, the detector-free matchers algorithms LoFTR (Sun et al., 2021), SE2-LoFTR (Bökman and Kahl, 2022), and RoMA (Edstedt et al., 2023) are included in DIM and allows for a semi-dense scene reconstruction.

5.3.1 MATCHING STRATEGIES

The matching strategy defines how the pairs of images to be matched are selected. The choice of matching strategy plays a crucial role in optimizing image matching, especially with large datasets.

DIM offers a versatile range of strategies to address diverse use cases. The brute-force approach provides the most comprehensive exploration by attempting to match every image with every other (Fig. 5.2b). This method is computationally intensive but can be valuable for small datasets or complex scenarios where other strategies may yield insufficient matches. The image pairs are obtained by computing combinations of n elements in 2 places (i.e., the pair), where n is the number of images in the dataset. Therefore, the

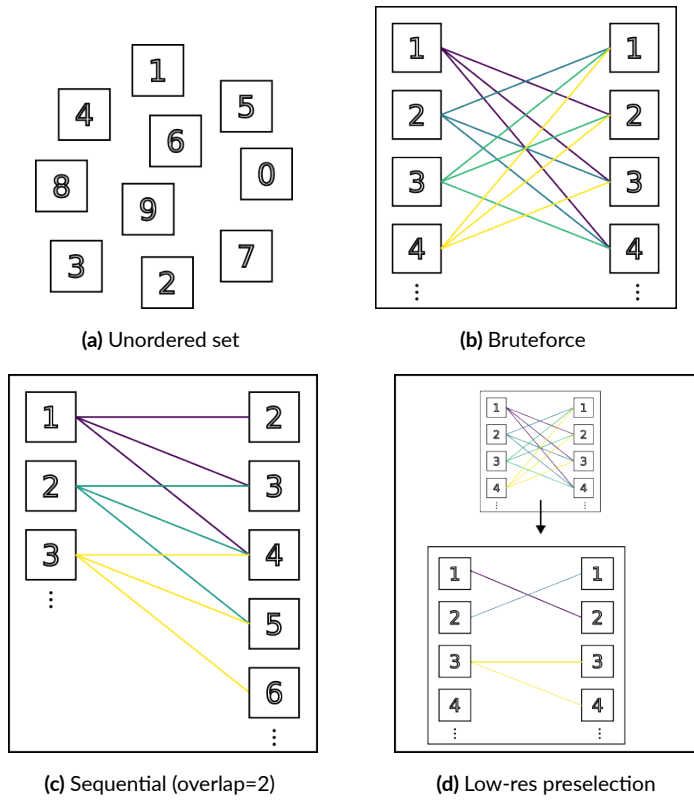


Figure 5.2: Scheme of the main different matching strategies implemented in DIM given an unordered image set (a). (b) Brute-force strategy (i.e., *all-to-all*); (c) Sequential strategy with overlap equal to 2 (i.e., match all images with next 3 images, note that the overlap parameter is zero-based); (d) Low-resolution guided matching strategy (i.e., perform a fast brute-force on low-resolution images and match only good candidates at high resolution).

computation complexity by $p = C(n, 2) = \frac{n*(n-1)}{2}$, where p is the number of pairs.

For image sequences acquired in order by a moving camera (e.g., Visual Odometry or SLAM), the sequential strategy offers optimized efficiency by matching each image with a defined number of subsequent images. The overlap parameter defines the number of consecutive images to match sequentially (Fig. 5.2c). The computational complexity is given by $p = (n - O) * O$, where O is the overlap parameter.

The `matching_lowres` enhances computational efficiency on large datasets by initially analyzing downsampled images to pre-filter pairs based on geometrically verified matches detected at lower resolution (Fig. 5.2d). By default, the minimum number of valid matches for each low-resolution pair is 20, but the user can tune it.

The `retrieval` strategy allows the use of global features to determine the pairs of images that are likely

to see the same scene (Yang and Newsam, 2013). Global features allow for describing the full image globally by encoding it into a neural network. Therefore, they are widely used to tackle visual place recognition problems (Napoletano, 2017). Candidate pairs are selected among all the images by matching the global descriptors. DIM makes use of hloc (Sarlin et al., 2019) for extracting and matching global features, and it supports NetVLAD (Arandjelović et al., 2016), openIBL (Ge et al., 2020), and CoSpace (Hong et al., 2019) global features.

Finally, the `custom_pairs` option grants users precise control over the matching process, allowing the specification of exact image pairs via a text file.

5.3.2 IMAGE RESOLUTION AND TILING

DIM provides extensive control over image resolution before feature extraction and matching. This functionality is particularly important when using DL-based local feature extractors and matchers that rely on GPU parallelization for best performance. They face limitations when processing large images on consumer-grade GPUs, which typically have limited memory resources. The image size threshold varies depending on the available GPU memory and the specific algorithms used (detector-free matchers tend to be particularly memory-intensive). As a general guideline, images with a long edge of up to 3000 px can be processed on a 12 GB GPU using the SuperPoint+LightGlue pipeline.

To address this challenge, DIM offers several resolution management strategies: images can be down-sampled by a factor of 2, 4, or 8 (controlled by the *medium*, *low*, or *lowest* quality parameter in DIM) using OpenCV’s pixel-area relation⁴ (i.e., bilinear interpolation). Image downsampling may be appropriate when computational efficiency is a priority. Alternatively, for DL features that operate with pixel-level accuracy (e.g., SuperPoint), upsampling by a factor of 2 (*highest* quality parameter) using bicubic interpolation can improve subpixel detection capabilities.

DIM supports breaking images into smaller, regular tiles to process large images without losing high-resolution details. DIM’s tiling allows the user to specify tile dimensions or the number of tiles per row/column. An overlap between neighboring tiles can be specified to avoid having no features extracted along the tile boundaries. The software automatically handles zero padding to maintain consistent tile sizes throughout. Image tiling is critical when high accuracy is needed or when using end-to-end detector-free matchers (e.g., LoFTR, RoMa), as their combined extraction and matching steps are particularly memory intensive.

⁴OpenCV interpolation algorithms: https://docs.opencv.org/4.x/d4/d54/group__imgproc__transform.html

When using image tiling, DIM handles local feature extraction separately, processing each tile sequentially. However, tile-based feature matching offers several strategies: **exhaustive**, **preselection**, and **grid** mode. In exhaustive mode, features from each tile of the first image are matched against features extracted from all tiles of the second image. This mirrors the brute-force approach to image pair selection (see Sec. 5.3.1) and ensures comprehensive exploration of potential matches, but can be computationally intensive. The **preselection** mode prioritizes efficiency and is the default approach. An initial low-resolution matching step identifies tile pairs likely to contain corresponding features, reducing computational cost by focusing subsequent full-resolution matching efforts on the selected tiles only. **Grid** mode assumes high similarity between the two images. It matches features from each tile in the first image to features from the corresponding tile (i.e., the tile that shares the same boundaries in image coordinates) in the second image. This approach is well suited for scenarios such as VSLAM, where images are captured sequentially by a moving camera and represent similar scenes.

5.3.3 IMAGE ROTATIONS

DL-based local features often struggle with extreme image rotations because they are trained on datasets with largely consistent orientations. DIM addresses this challenge with two management approaches, ensuring images are properly rotated according to a *principal direction* before feature extraction and matching. Features are extracted and matched from the rotated images, and only after matching are keypoints mapped back to their positions in the original image.

If the images' orientation relative to a principal direction is known (e.g., from on-board positioning systems), DIM accepts a text file specifying these rotations and rotates the images accordingly. Alternatively, in the absence of prior rotation knowledge, a *z-cluster approach* relative to a reference image (either random or user-selected) can be used to determine the principal direction (Fig. 5.3). This iterative method starts with a single reference image in the first cluster (*Group 0*) and all remaining images in the second cluster (*Group 1*). Each image I_i in *Group 1* is iteratively matched against a reference image I_r in *Group 0*, testing rotations of [90, 180, 270] degrees. The rotation with the highest number of geometrically verified matches is selected. If the number of matches exceeds a predefined threshold, I_i is moved to *Group 0*, expanding that cluster and reducing *Group 1*. This procedure is parallelizable, with *Group 1* images divided into subgroups for independent matching against *Group 0* images on independent processes. This significantly speeds up the computational time compared to a brute-force approach.

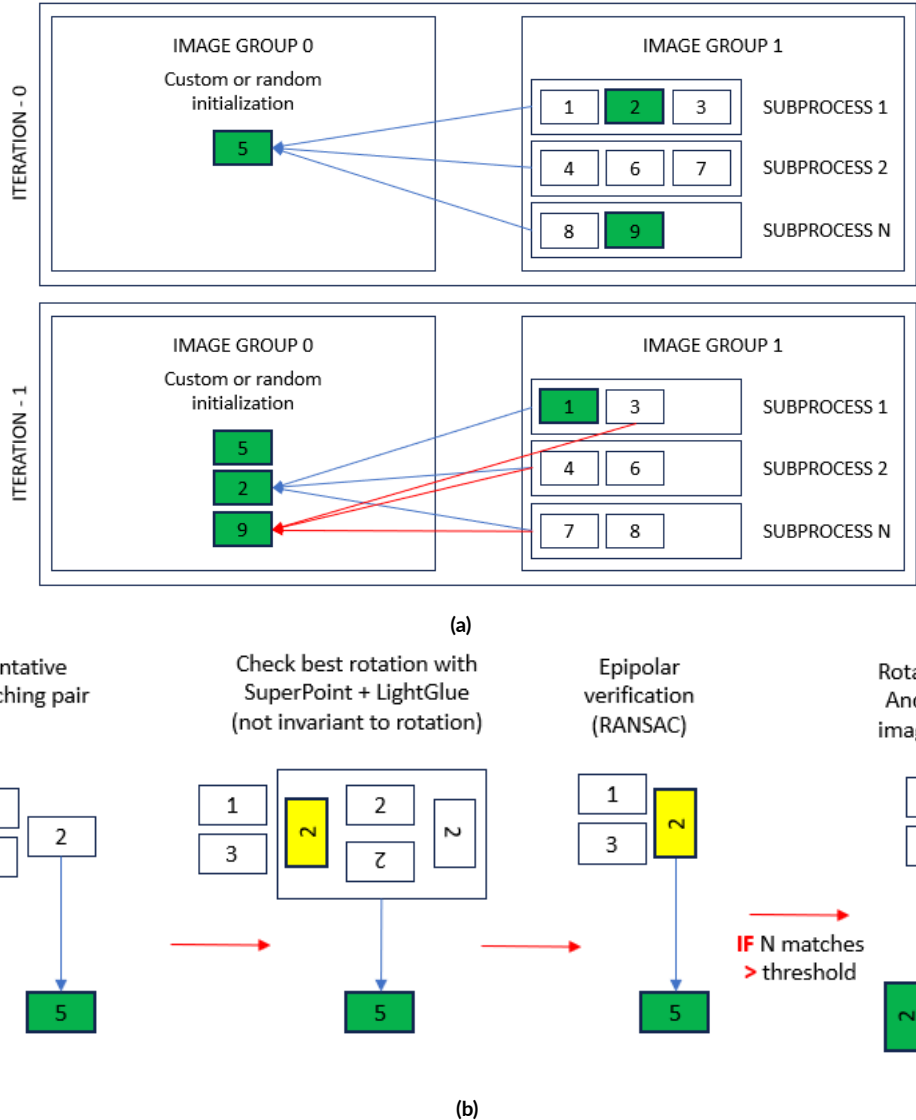


Figure 5.3: Scheme of the DIM's cluster-based approach to estimate the best rotation of the images before performing the image matching.

5.3.4 MATCHING PIPELINES

DIM offers flexibility by supporting diverse pipelines for image matching. A pipeline combines a local feature extractor and its corresponding matching algorithm. As compatibility constraints exist between feature extractors and matching algorithms within DL-based methods, DIM currently supports the fol-

lowing pipelines:

- SuperPoint+LightGlue
- SuperPoint+SuperGlue
- DISK+LightGlue
- Aliked+LightGlue
- ORB+nearest neighbor matching
- SIFT+nearest neighbor matching
- KeyNetAffNetHardNet+nearest neighbor matching
- DeDoDe+nearest neighbor matching
- XFeat+nearest neighbor matching
- LOFTR (detector-free matcher)
- RoMa (detector-free matcher)

DIM streamlines the process with a unified interface, allowing users to run pipelines with minimal configuration when default settings are suitable. Advanced users can provide configuration files to customize local feature extractor or matcher parameters.

DIM efficiently stores extracted features and matches in local HDF5 (Hierarchical Data Format) databases by using the h5py library⁵. Pipeline outputs are stored in two HDF5 files: *features.h5* containing keypoints image coordinates, descriptors, and scores and *matches.h5* containing the indices of matched features for each image pair. The features database organizes features by image, with datasets (i.e., a structure similar to a table in a relational database) representing extracted features on each image. The matches database contains datasets per image pair, storing an $n \times 2$ array (n = number of matches) where columns reference the corresponding feature indices within the feature database. This matches indexing approach enables the construction of tracks of features matched across multiple images and enhances flexibility and maintainability.

The use of HDF5 databases facilitates the combination of pipelines and merging different local features, exploiting their peculiar strengths together. For example, the same set of images can be processed

⁵h5py library: <https://docs.h5py.org/en/stable/>

both with SIFT for matching accuracy and reliability with standard baselines and with DL-based algorithms like SuperPoint+LightGlue due to its robustness for wide baselines and significant viewpoint changes.

After completing the matching pipelines, outlier correspondences must be rejected. DIM assumes non-calibrated cameras and employs fundamental matrix estimation for this purpose, rejecting matches with large epipolar errors. DIM offers robust algorithms for fundamental matrix estimation and geometric verification. Among these, PyDegensac ([Mishkin et al., 2015](#)), implementing LO-Ransac ([Chum et al., 2003](#)) and DEGENSAC ([Chum et al., 2005](#)), provides the most robust solution. Additionally, DIM supports all robust estimation algorithms implemented in OpenCV⁶, including traditional RANSAC, the least-median of squares algorithm (LMedS), and LO-Ransac (USAC_DEFAULT).

5.4 CASE STUDIES

This section presents a few case studies on challenging multi-view datasets, showcasing DIM’s versatility in diverse remote sensing scenarios. While these studies may not directly focus on the Belvedere Glacier, they address common complexities encountered in the remote sensing field. Furthermore, a case study specific to the Belvedere Glacier demonstrates how DIM, integrated with ICEPy4D (see Sec. 4.5.4), can enable the creation of effective multi-view monitoring systems using low-cost cameras.

5.4.1 LOW-TEXTURES SCENES

Hand-crafted descriptors like SIFT often struggle in low-texture environments like snow-covered glaciers, as the lack of distinctive features significantly complicates finding corresponding points for image orientation. Since glaciers are commonly snow-covered for large parts of the year, addressing this challenge is essential for robust, long-term monitoring. While the time series analysis discussed in Chapter 4 was limited to the May–November period, the planned expansion to a multi-camera system and the need to make the system an all-year monitoring platform motivated a focused investigation into this scenario.

To simulate a multi-view setup, we integrated the 24/03/2024 images captured by the existing two fixed cameras with three additional images acquired by a Parrot Anafi UAV (1/1.2.4” CMOS sensor with 4.8 mm focal length - 23 mm in 35mm format equivalent). Dataset A - Winter - is composed of these three UAV images, acquired from positions near potential future camera locations along the glacier moraines and with convergent view angles, combined with two terrestrial images acquired by the in-situ monitoring

⁶OpenCV robust estimators: https://docs.opencv.org/4.x/d9/d0c/group__calib3d.html

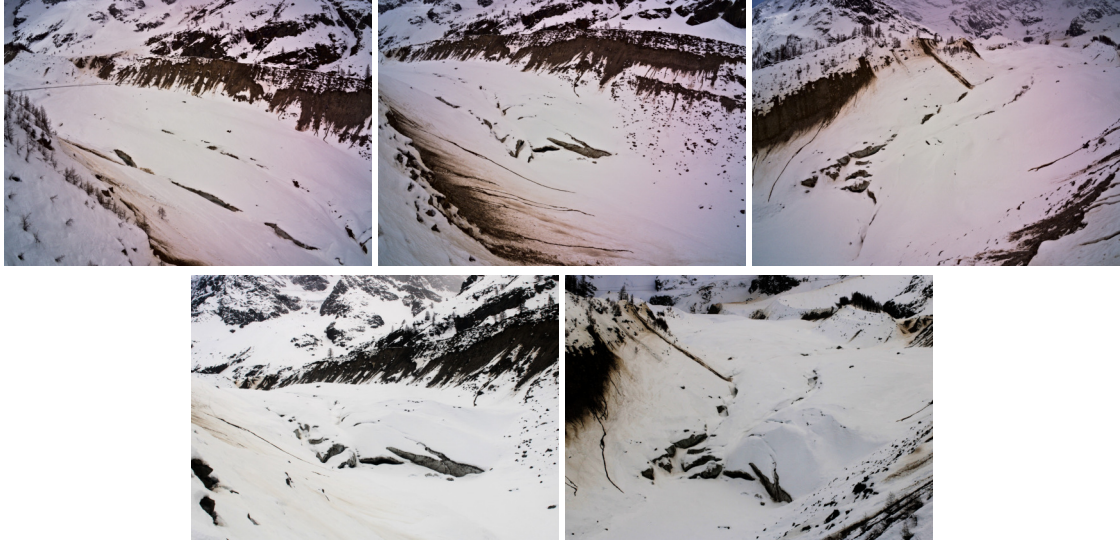


Figure 5.4: Images of Dataset A - Winter. Images in the first row are taken by UAV, while those in the second row are acquired by terrestrial cameras.

cameras (Fig. 5.4). Unfortunately, a ground truth acquired on the same day was unavailable to validate the multi-view reconstruction. Therefore, a qualitative assessment of the resulting multi-view reconstruction is presented.

For image orientation, dataset A images were processed using DIM with the SuperPoint+LightGlue pipeline (A₁) and subsequently compared with results obtained using RootSIFT implemented within the traditional COLMAP matching pipeline (A₂) and the proprietary feature matching algorithm implemented in Agisoft Metashape (A₃).

Given the limited dataset size, we used a DIM brute-force matching strategy to try to match all possible pairs. To accommodate SuperPoint's lack of subpixel refinement capability, we preprocessed images by upsampling them by a factor of two with bicubic interpolation. This enabled subpixel accuracy at the half-pixel level. Furthermore, due to the limited consumer-grade GPU memory, the upscaled images were subdivided into regularly sized tiles of 3000x2000 pixels. This tile dimension was a compromise between limiting the total number of tiles and facilitating processing on an NVIDIA RTX A2000 with 12 GB of memory. Since the images were acquired with an upright orientation and with minimal in-plane sensor rotations, the pipeline for pre-selection of the best image rotation was unnecessary. Pydegensac was used for the geometric verification of putative matches, and the final bundle adjustment was performed using COLMAP. In contrast, Metashape and COLMAP used full-resolution images for feature extraction and bundle adjustment procedures with their traditional workflow.

Table 5.1: Summary of the Winter dataset results obtained with DIM compared to those obtained with COLMAP (with RootSIFT features) and Agisoft Metashape with its proprietary feature extractor and matches.

	Local features and matcher	Oriented/ total images	Mean repro- jection error [px]	Mean track length	3D tie points
A ₁	DIM: SuperPoint + LightGlue	5/5	0.95	2.1	11973
A ₂	COLMAP (RootSIFT)	4/5	1.01	2.5	823
A ₃	Metashape (proprietary)	4/5	0.20	2.1	1424

The results of the image orientation are summarized in Tab. 5.1. The only approach that could orient all 5 images was DIM with SuperPoint+LightGlue. On the contrary, both COLMAP and Metashape oriented 4 images only, but they could not find enough tie points to orient the rightmost UAV image. However, considering the mean reprojection after the bundle adjustment, the most accurate approach was Metashape, with a reprojection error significantly smaller than 1 px, compared to DIM and COLMAP, which is around 1 px.

DIM was also used to generate a dense reconstruction of the scene using the RoMa semi-dense matching algorithm for pixel-wise correspondence estimation. Since RoMa is a detector-free approach, correspondences are limited to image pairs. Therefore, RoMa-derived corresponding points could not be reliably tracked across multiple images. While this is not ideal for image orientation, it is suitable for dense reconstruction, providing that a good geometric verification of the correspondence and some cleaning is carried out. Because of this reason, RoMa correspondences were triangulated using the camera poses estimated within the SuperPoint+SuperGlue solution. Similar to the orientation procedure, a brute-force matching strategy was applied, with images being matched at half-resolution using a tiling approach due to memory limitation constraints.

Fig. 5.5 shows the semi-dense reconstruction produced by RoMa alongside the dense reconstruction produced by Agisoft Metashape. The Metashape reconstruction shows excellent coverage and density on the streamwise left moraine (right side of the image) due to its distinct features and favorable image coverage from the three oriented images on the left. However, very few points were reconstructed on the snow-covered surface, concentrated mainly in areas with sharper edges or geometric changes (e.g., the ice cliff). This results in a skeletal representation of the glacier surface, requiring extensive interpolation for

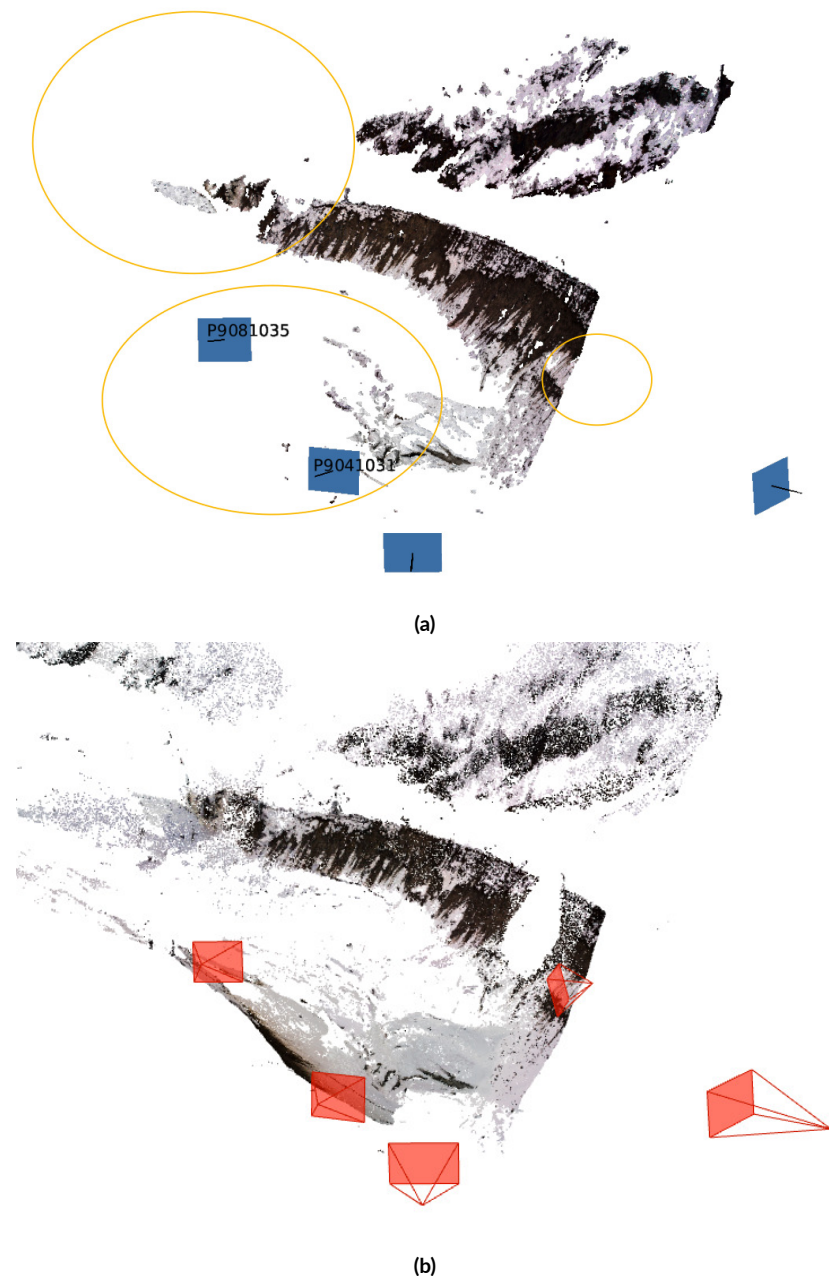


Figure 5.5: Dense reconstructions of the northwest lobe of Belvedere Glacier using (a) Agisoft Metashape and (b) RoMa. The RoMa reconstruction was computed using camera poses estimated by DIM's SuperPoint+LightGlue pipeline. Note the number of oriented images with the two different approaches, and the greater coverage of the snow-covered surface and the streamwise right moraine achieved by RoMa despite the lower overall point density (highlighted by the yellow circles).

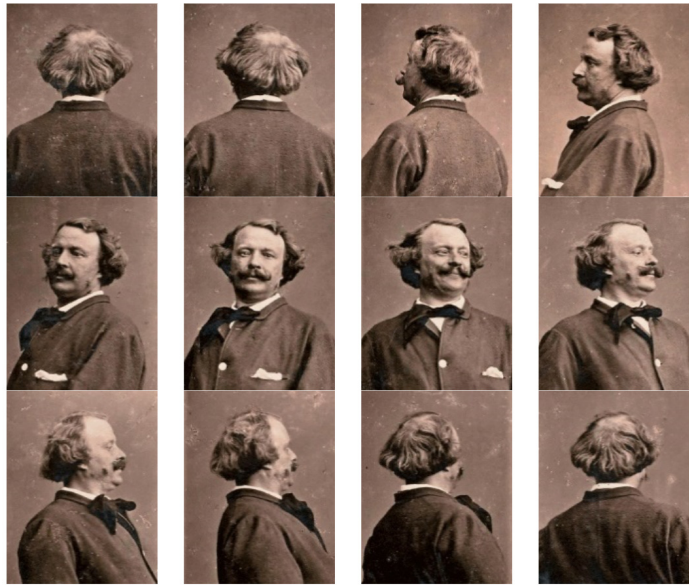


Figure 5.6: Sample images Dataset B - Nadar

DSM generation. The streamwise right moraine remains completely unreconstructed.

In contrast, the RoMa semi-dense point cloud has a lower overall density but covers a much larger area. The frontal ice cliff is almost completely reconstructed, and sparse point clusters on the upper glacier surface provide valuable data for DSM interpolation. Importantly, parts of the streamwise right moraine are captured, made possible by the successful orientation of all images within DIM. In addition, RoMa achieves some reconstruction even in background areas with difficult geometry or challenging surfaces, highlighting its potential for broader applications.

5.4.2 HISTORICAL INTERNET IMAGES

Dataset B – Nadar – is a collection of 12 self-portrait images from the opera Revolving (1865) of Gaspard-Félix Tournachon, known as Nadar⁷. The images have been downloaded from Wikipedia (resolution of 524 x 671 px), and they show significantly different viewpoints, low radiometric quality, and many time-related artifacts. In addition, the dataset is partially ill-posed for photogrammetric purposes since Nadar sometimes changed both facial expressions and the relative position between the head and shoulders. All these characteristics make the reconstruction difficult with classical approaches.

⁷Wikipedia Nadar page: <https://en.wikipedia.org/wiki/Nadar>

Table 5.2: Summary of the Nadar dataset results obtained with DIM compared to those obtained with COLMAP (with RootSIFT features) and Agisoft Metashape with its proprietary feature extractor and matches. (*) The dataset has been oriented by combining different local features: SIFT, KeyNey + HardNet, ALIKED, SuperPoint, and DISK.

Local features and matcher		Oriented/total images	Mean reprojection error [px]	Mean track length	3D tie points
B ₁	DIM (combination of LF) [*]	12/12	1.09	2.6	2791
B ₂	COLMAP (RootSIFT)	0/12	NA	NA	NA
B ₃	Metashape (proprietary)	03/12	0.36	2.0	294

For the Nadar dataset, different local features have been tested: SIFT, KeyNey + HardNet, ALIKED, SuperPoint, and DISK. SuperPoint and DISK local features were matched with LightGlue, while the others were matched with a nearest-neighbor approach. None of these approaches managed to orient more than three images, except DISK, which found significantly more tie points and oriented seven images. In Fig. 5.7, a matching pair example is reported for SIFT (a) and DISK (b). Both COLMAP and Metashape failed to orient the dataset. Metashape only managed to orient a small subset of three images, making it possible to calculate other statistics such as reprojection error. However, this cannot be considered a successful orientation of the block.

With DIM, only by combining all the tie points from the previous approaches, excluding Metashape, was it possible to orient the whole dataset (Tab. 5.2). Tie points with multiplicity equal to two were excluded because they were considered not sufficiently robust and prone to outliers. In addition, no ratio threshold has been used to retain more matches. Because of the camera network and the scarcity of tie points, images were first oriented using a rough nominal focal length, then focal length and one radial distortion parameter were updated in a final bundle adjustment with self-calibration.

Regarding 3D model reconstruction, COLMAP and Metashape dense matching failed due to the images' poor radiometry. Therefore, to obtain a point cloud dense enough to build a meshed textured 3D model, the DL semi-dense matcher RoMA available in DIM was employed and successfully reconstructed a dense point cloud of Nadar's body (Fig. 5.7e-f). Finally, using Metashape functionalities, a textureized model was created from the semi-dense point cloud (Fig. 5.7g-h).

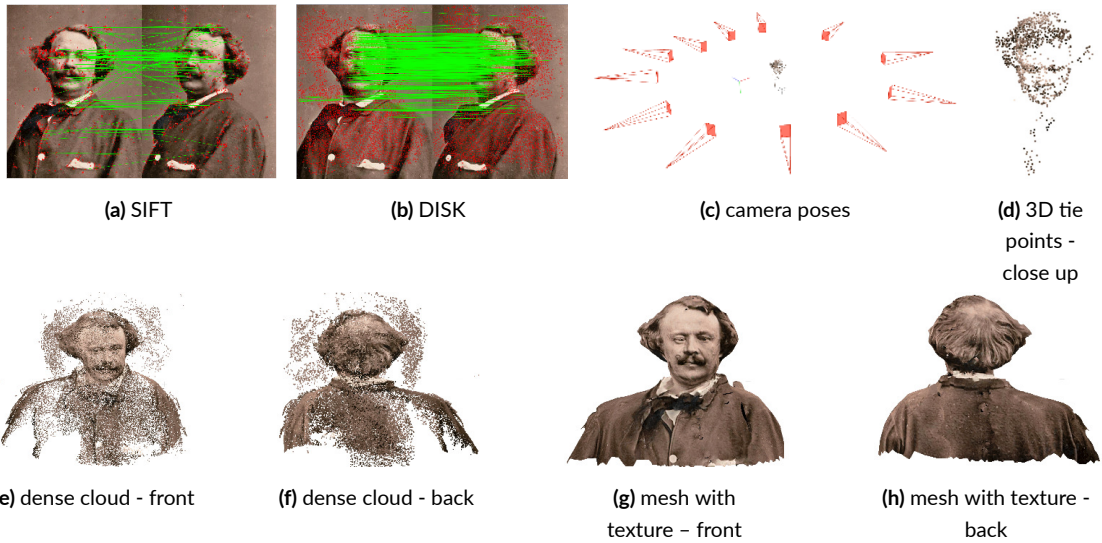


Figure 5.7: Results for Nadar dataset. (a) SIFT matches and (b) DISK matches on an image pair; (c) camera poses and (d) 3D tie points; (e-f) semi-dense point cloud generated from RoMA tie points; (g-h) textured mesh 3D model.

5.4.3 COMBINING UAV AND TERRESTRIAL IMAGES

Dataset C – Castle comprises 48 images of the half-destroyed historical Castle of Casalbagliano, Alessandria (Italy). It is a traditional photogrammetric dataset of a cultural heritage site, including 25 nadiral UAV images, 11 oblique UAV images, and 12 terrestrial images, with a camera network similar to a classical photogrammetric survey (Fig. 5.8). Dataset C is the only one with an available ground truth.

All the images of Dataset C were acquired by a single Canon Eos M with a fixed focal length of 22 mm and a size of 5184 x 3456 px. The UAV nadiral images exhibit a modest overlap, approximately 60% in the longitudinal direction and 40% in the transversal direction. The UAV oblique images consist of four convergent shots acquired at each corner of the block and five additional images positioned along the exterior perimeter. The terrestrial images are acquired along a circle all around the castle. The main challenge of this dataset is linking the nadiral UAV images with the terrestrial ones, as they have strongly different points of view. Moreover, some of the terrestrial images are underexposed and characterized by large dark areas or were acquired against the sun, and therefore, they show strong sunlight reflections.

Dataset C was extracted from a larger and more robust dataset, named Dataset C_Ground Truth (GT) (Fig. 5.9), and which was used as a ground truth reference to validate the results obtained with DIM. This dataset is composed of 172 images (83 nadiral, 61 oblique, and 28 terrestrial) with an average overlap between the images between 70% and 80% and an average GSD of approximately 9 mm ([Gagliolo et al., 2017](#),



Figure 5.8: Sample images Dataset C - Castle. Images in the first row are samples of the nadiral and oblique UAV images, and images in the second row are samples of the terrestrial images, including some of the challenging underexposed or overexposed images.

2018). The full dataset also included 19 targets deployed on the ground around the castle and measured by a total station with sub-centimetric accuracy. Dataset C_GT was processed with Metashape by using 10 targets as GCPs and performing a camera self-calibration. The quality of the photogrammetric block was evaluated on the remaining 9 targets, used as CPs, resulting in an overall RMSE of 1.9 cm in the three directions.

Similar to Dataset A, Dataset C was processed with DIM by using the SuperPoint+LightGlue pipeline. A low-resolution guided approach was used to select image pairs and reduce computational time. Images were first upscaled by a factor of two with a bicubic interpolation prior to feature extraction, which was again performed using a tile-based approach.

The results obtained with SuperPoint + LightGlue (Tab. 5.3) were significantly better only compared to those obtained with a traditional COLMAP processing pipeline (C₂), while they were similar to the outcomes obtained with Metashape (C₃). With both LightGlue and Metashape, all 48 images were oriented. On the other hand, COLMAP failed to orient all the images together, but it created two different not-linked models. The largest model comprised only 31 oriented images (Tab. 5.3). The smallest average reprojection error of 0.5 px was obtained by processing the dataset using Metashape with its proprietary local feature implementation, while a slightly higher reprojection error of 0.9 px was obtained by SuperPoint + LightGlue (Tab. 5.3), as SuperPoint do not have subpixel accuracy in keypoint detection. On the other hand, the mean track length of 3.3 obtained with SuperPoint + LightGlue was larger than the 2.5 obtained with Metashape, guaranteeing higher redundancy of the observations in the bundle adjustment.



Figure 5.9: Dataset C_GT, used as the ground truth to evaluate the results on Dataset C. The red flags are the targets used as GCPs, while the yellow ones are those used as CPs.

Table 5.3: Summary of the Castle dataset results obtained with DIM, compared to those obtained with COLMAP (with RootSIFT features) and Agisoft Metashape with its proprietary feature extractor and matches. (*) As COLMAP produced two non-linked reconstructions, the reported results refer to the reconstruction with the highest number of oriented images.

	Local features and matcher	Oriented/ total images	Mean repro- jection error [px]	Mean track length	3D tie points
C ₁	DIM: SuperPoint + LightGlue	48/48	0.9	3.3	75274
C ₂	COLMAP (RootSIFT) [*]	31/48	0.94	3.7	11367
C ₃	Metashape (proprietary)	48/48	0.5	2.5	59679



Figure 5.10: Example of matched features with the different approaches on a challenging image pair (green or blue lines are the valid matches, while the red dots are the rejected keypoints): (a) SuperPoint + LightGlue (658 valid matches); (b) COLMAP RootSIFT (49 valid matches); (c) Agisoft Metashape (1 valid match).

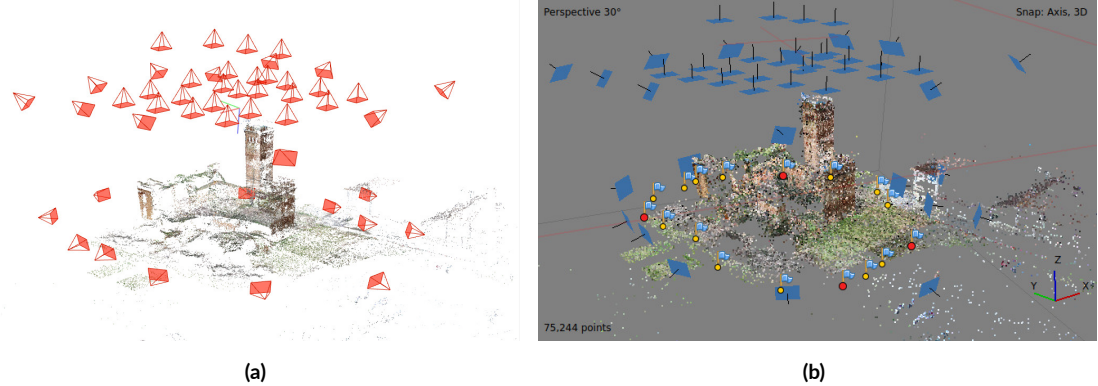


Figure 5.11: (a) Reconstructed sparse point cloud and oriented camera with SuperPoint + LightGlue after the bundle in COLMAP; (b) the same solution from Metashape, georeferenced with 4 GCPs (red flags), while all the other points are used as CPs (yellow flags)

Fig. 5.10 shows the matched keypoints for a challenging pair composed of a UAV oblique image and a terrestrial image, with a wide baseline and rather bad lighting conditions for the terrestrial image. The combination of SuperPoint + LightGlue, which works better under strong viewpoints conditions (Ioli et al., 2024), allowed for extracting more than 600 valid matches, while Metashape could find only one valid match. Surprisingly, COLMAP with RootSIFT detected more matches for this pair than Metashape, probably thanks to its ability to estimate affine descriptors (Lindeberg and Gårding, 1997). However, for other challenging pairs, the results of SuperPoint + LightGlue were comparable to those of Metashape or COLMAP without providing any relevant improvement. The matches obtained with SuperPoint + LightGlue were finally imported into COLMAP for the bundle adjustment and reconstruction (Fig. 5.11a). The two complete solutions, C₁ (SuperPoint + LightGlue) and C₃ (pure Metashape), in which all the 48 images were oriented, were validated by importing the estimated reconstructions into a new Metashape project and adding 4 GCPs at the block corner as a minimum constraint while leaving the other 15 targets as CPs (Fig. 5.11b). This made it possible to compare the solutions C₁ and C₃ with the ground truth Dataset C_GT and to evaluate the on-ground reconstruction accuracy based on the CPs and the camera pose error by comparing the camera exterior orientation parameters. Comparable results were obtained for both C₁ and C₃, with a centimetric error on the CP and an average error of less than 5 cm on the camera location (Tab. 5.4). This highlights that Dataset C was correctly oriented using both SuperPoint + LightGlue and Metashape processing without showing a clear superiority of any approach.

Table 5.4: Summary of accuracy evaluation for the solutions obtained with SuperPoint + LightGlue (C1) and Metashape (C3) with respect to the ground truth (C_GT). The RMSE on the CPs was computed as the RMS of the difference between the 3D coordinates of the targets measured on the field and those estimated in C1 and C3. The RMSE on the cameras was computed as the RMS of the differences between the estimated 3D coordinates and attitude angles of the cameras in C_GT and those estimated in C1 and C3.

	Approach	RMSE X/Y/Z on CPs [m]	RMSE X/Y/Z on camera location [m]	RMSE Yaw/Pitch/Roll on camera attitude [$^{\circ}$]
C1	SuperPoint + LightGlue	0.017/0.010/0.010	0.036/0.043/0.044	0.13/0.04/0.07
C3	Metashape	0.014/0.011/0.012	0.043/0.040/0.041	0.08/0.11/0.11

References

- Arandjelović, R., Gronat, P., Torii, A., Pajdla, T., & Sivic, J. (2016). Netvlad: Cnn architecture for weakly supervised place recognition.
- Barroso-Laguna, A., Riba, E., Ponsa, D., & Mikolajczyk, K. (2019). Key.net: Keypoint detection by handcrafted and learned cnn filters.
- Bökman, G., Edstedt, J., Felsberg, M., & Kahl, F. (2023). Steerers: A framework for rotation equivariant keypoint descriptors.
- Bökman, G. & Kahl, F. (2022). A case for using rotation invariant features in state of the art feature matchers. In *2022 IEEE/CVF Conference on Computer Vision and Pattern Recognition Workshops (CVPRW)* (pp. 5106–5115).
- Chum, O., Matas, J., & Kittler, J. (2003). Locally optimized ransac. In *Pattern Recognition* (pp. 236–243). Berlin, Heidelberg: Springer.
- Chum, O., Werner, T., & Matas, J. (2005). Two-view geometry estimation unaffected by a dominant plane. volume 1 (pp. 772–779 vol. 1).
- Cohen, T. S. & Welling, M. (2016). Steerable cnns.
- DeTone, D., Malisiewicz, T., & Rabinovich, A. (2018). Superpoint: Self-supervised interest point detection and description. In *Proceedings of the IEEE Conference on Computer Vision and Pattern Recognition (CVPR) Workshops*.
- Edstedt, J., Bökman, G., & Zhao, Z. (2024). Dedode v2: Analyzing and improving the dedode keypoint detector.
- Edstedt, J., Sun, Q., Bökman, G., Wadenbäck, M., & Felsberg, M. (2023). Roma: Robust dense feature matching.
- Gagliolo, S., et al. (2017). Use of uas for the conservation of historical buildings in case of emergencies. *The International Archives of the Photogrammetry, Remote Sensing and Spatial Information Sciences*, XLII-5/W1, 81–88, <https://doi.org/10.5194/isprs-archives-XLII-5-W1-81-2017>.
- Gagliolo, S., et al. (2018). Parameter optimization for creating reliable photogrammetric models in emergency scenarios. *Applied Geomatics*, 10(4), 501–514, <https://doi.org/10.1007/s12518-018-0224-4>.
- Ge, Y., Wang, H., Zhu, F., Zhao, R., & Li, H. (2020). Self-supervising fine-grained region similarities for large-scale image localization.
- Hong, D., Yokoya, N., Chanussot, J., & Zhu, X. X. (2019). Cospace: Common subspace learning from hyperspectral-multispectral correspondences. *IEEE Transactions on Geoscience and Remote Sensing*, 57(7), 4349–4359, <https://doi.org/10.1109/tgrs.2018.2890705>.

- Ioli, F., Dematteis, N., Giordan, D., Nex, F., & Pinto, L. (2024). Deep learning low-cost photogrammetry for 4d short-term glacier dynamics monitoring. *PFG-Journal of Photogrammetry, Remote Sensing and Geoinformation Science*, (pp. 1–22).
- Jin, Y., Mishkin, D., Mishchuk, A., Matas, J., Fua, P., Yi, K. M., & Trulls, E. (2021). Image matching across wide baselines: From paper to practice. *International Journal of Computer Vision*, 129(2), 517–547, <https://doi.org/10.1007/s11263-020-01385-0>.
- Li, Z. & Snavely, N. (2018). Megadepth: Learning single-view depth prediction from internet photos. In *Proc. CVPR IEEE* (pp. 2041–2050).
- Lindeberg, T. & Gårding, J. (1997). Shape-adapted smoothing in estimation of 3-d shape cues from affine deformations of local 2-d brightness structure. *Image and Vision Computing*, 15(6), 415–434, [https://doi.org/https://doi.org/10.1016/S0262-8856\(97\)01144-X](https://doi.org/https://doi.org/10.1016/S0262-8856(97)01144-X).
- Lindenberger, P., Sarlin, P.-E., & Pollefeys, M. (2023). Lightglue: Local feature matching at light speed.
- Lowe, D. G. (2004). Distinctive image features from scale-invariant keypoints. *International Journal of Computer Vision*, 60(2), 91–110.
- Mishkin, D., Matas, J., & Perdoch, M. (2015). Mods: Fast and robust method for two-view matching. *Computer Vision and Image Understanding*, 141, 81–93, <https://doi.org/https://doi.org/10.1016/j.cviu.2015.08.005>.
- Morelli, L., Ioli, F., Maiwald, F., Mazzacca, G., Menna, F., & Remondino, F. (2024). Deep-image-matching: A toolbox for multiview image matching of complex scenarios. *The International Archives of the Photogrammetry, Remote Sensing and Spatial Information Sciences*, XLVIII-2/W4-2024, 309–316, <https://doi.org/10.5194/isprs-archives-XLVIII-2-W4-2024-309-2024>.
- Moulon, P., Monasse, P., Perrot, R., & Marlet, R. (2016). OpenMVG: Open multiple view geometry. In *International Workshop on Reproducible Research in Pattern Recognition* (pp. 60–74). Springer.
- Napoletano, P. (2017). Visual descriptors for content-based retrieval of remote sensing images.
- Ono, Y., Trulls, E., Fua, P., & Yi, K. M. (2018). Lf-net: Learning local features from images.
- Parihar, U. S., Gujarathi, A., Mehta, K., Tourani, S., Garg, S., Milford, M., & Krishna, K. M. (2022). Rord: Rotation-robust descriptors and orthographic views for local feature matching.
- Potje, G., Cadar, F., Araujo, A., Martins, R., & Nascimento, E. R. (2024). Xfeat: Accelerated features for lightweight image matching. In *2024 IEEE/CVF Computer Vision and Pattern Recognition (CVPR)*.
- Pultar, M. (2020). Improving the hardnet descriptor.
- Remondino, F., Morelli, L., Stathopoulou, E., Elhashash, M., & Qin, R. (2022). Aerial triangulation with learning-based tie points. *Int. Arch. Photogramm.*, XLIII-B2-2022, 77–84, <https://doi.org/10.5194/isprs-archives-XLIII-B2-2022-77-2022>.
- Riba, E., Mishkin, D., Ponsa, D., Rublee, E., & Bradski, G. (2019). Kornia: an open source differentiable computer vision library for pytorch.

- Rublee, E., Rabaud, V., Konolige, K., & Bradski, G. (2011). Orb: An efficient alternative to sift or surf. In *2011 International Conference on Computer Vision* (pp. 2564–2571).
- Rupnik, E., Daakir, M., & Pierrot Deseilligny, M. (2017). Micmac—a free, open-source solution for photogrammetry. *Open Geospat. Data, Softw. Stand.*, 2(1), 1–9.
- Sarlin, P.-E., Cadena, C., Siegwart, R., & Dymczyk, M. (2019). From coarse to fine: Robust hierarchical localization at large scale. In *Proc. CVPR IEEE*.
- Sarlin, P.-E., DeTone, D., Malisiewicz, T., & Rabinovich, A. (2020). SuperGlue: Learning feature matching with graph neural networks. In *Proc. CVPR IEEE*.
- Schönberger, J. L. & Frahm, J.-M. (2016). Structure-from-motion revisited. In *Proc. CVPR IEEE*.
- Sun, J., Shen, Z., Wang, Y., Bao, H., & Zhou, X. (2021). LoFTR: Detector-free local feature matching with transformers. In *Proc. CVPR IEEE*.
- Tyszkiewicz, M. J., Fua, P., & Trulls, E. (2020). Disk: Learning local features with policy gradient.
- Vaswani, A., et al. (2023). Attention is all you need.
- Wu, T., Vallet, B., Pierrot-Deseilligny, M., & Rupnik, E. (2024). An evaluation of deep learning based stereo dense matching dataset shift from aerial images and a large scale stereo dataset. *International Journal of Applied Earth Observation and Geoinformation*, 128, 103715, <https://doi.org/https://doi.org/10.1016/j.jag.2024.103715>.
- Yang, Y. & Newsam, S. (2013). Geographic image retrieval using local invariant features. *IEEE Transactions on Geoscience and Remote Sensing*, 51(2), 818–832, <https://doi.org/10.1109/TGRS.2012.2205158>.
- Yao, G., Yilmaz, A., Meng, F., & Zhang, L. (2021). Review of Wide-Baseline Stereo Image Matching Based on Deep Learning. *Remote Sensing*, 13(16), 3247, <https://doi.org/10.3390/rs13163247>.
- Yi, K. M., Trulls, E., Lepetit, V., & Fua, P. (2016). Lift: Learned invariant feature transform.
- Zhao, X., Wu, X., Chen, W., Chen, P. C. Y., Xu, Q., & Li, Z. (2023). Aiked: A lighter keypoint and descriptor extraction network via deformable transformation.
- Zhao, X., Wu, X., Miao, J., Chen, W., Chen, P. C. Y., & Li, Z. (2022). Alike: Accurate and lightweight keypoint detection and descriptor extraction.

6

Conclusion

This chapter synthesizes the key findings presented throughout this thesis, offering a comprehensive overview of the research contributions. It highlights the main insights gained and discusses their broader implications within the field of glaciological research.

6.1 SUMMARY OF THE RESULTS

This thesis applies photogrammetric techniques to the comprehensive, long-term monitoring of the Belvedere Glacier (Italian Alps), achieving spatial resolutions from the meter to the decimeter and temporal frequencies from decades to daily.

Chapter 2 of the thesis delves into the long-term evolution of the Belvedere Glacier, employing a multi-temporal analysis of aerial imagery spanning the period from 1977 to 2009. Digitized archival analog images (1977, 1991, 2001) and a high-quality digital aerial dataset (2009) were processed using photogrammetric techniques within Agisoft Metashape. A cascade technique was employed to ensure precise georeferencing, leveraging a recent UAV dataset acquired in 2019. This involved extracting GCPs from

the UAV photogrammetric block (oriented using in-situ GNSS targets) to refine the image orientation of the digital aerial block, which had known a-priori image exterior orientation parameters thanks to an on-board GNSS-IMU system. Subsequently, GCPs strategically distributed on stable terrain surrounding the glacier were manually extracted from the 2009 block to georeference the historical datasets. These techniques enabled the generation of detailed 3D glacier reconstructions with sub-metric precision at pivotal points in its history, roughly spaced by a 10-year interval.

The analysis was able to document and quantify the peculiar evolution of the Belvedere glacier in the last half-century. The Belvedere Glacier exhibited a period of expansion from 1977 to 2001 ($+20.66 \times 10^6 \text{ m}^3$). This growth trend was disrupted by a surge event between 2002 and 2002. The expansion period was followed by a period of dramatic and continuous retreat. The comparison of historical and contemporary glacier extent reveals a net loss of $-54.28 \times 10^6 \text{ m}^3$ of ice volume between 1977 and 2023 (approximately -24 Mt of mass).

In Chapter 3, we present the results of the periodical yearly in-situ campaign carried out on the Belvedere Glacier with UAV and GNSS from 2015 to 2023. During yearly fieldwork, several flights with fixed-wing UAVs and quadcopters were executed to acquire images with GSD ranging between 5 cm and 9 cm. Moreover, targets were deployed on the glacier and along the moraines, checked, and measured yearly with topographic-grade GNSS receivers. These were used respectively for image orientation and photogrammetric block validation. Acquired data were processed using SfM-MVS techniques to obtain decimetric-accurate 3D models, orthophotos, and DSMs. Annual glacier velocity was derived by in-situ GNSS measurements of photogrammetric targets, combined with dense surface velocity fields computed by DIC on orthophotos and DSMs.

Analysis of surface velocity fields revealed distinct patterns across the glacier. The central region exhibited the highest velocities, ranging from 16 m y^{-1} to 25 m y^{-1} . In contrast, the two terminal lobes showed significantly slower movement of 2 m y^{-1} to 8 m y^{-1} . Intermediate speeds were found in the upper glacier near its steep accumulation zone and the transition zone between the fast-moving center and the terminal lobes. The gradual slowdown observed in the terminal lobes over time was particularly interesting, as it is likely due to the severe ice thinning that has been documented in recent years. Interestingly, other glacier areas do not show statistically significant speed changes. Annual volume variations, estimated by DOD, revealed a consistent loss of ice ranging from $-2 \times 10^6 \text{ m}^3$ to $-5 \times 10^6 \text{ m}^3$. Of particular concern is the dramatic increase in ice loss from 2020 to 2023, with a staggering 200% increase in the 2022-2023 period compared to the 2015-2016 baseline.

In Chapter 4, we presented a pilot study that introduced a low-cost multi-camera system for high-rate glacier monitoring. By utilizing two cameras near the snout of the Belvedere Glacier, we successfully

integrated 3D reconstruction from stereo cameras and surface velocity estimation on monoscopic cameras by DIC. This approach accurately estimated glacier dynamics, including surface movement and terminus ice volume loss and retreat. The application of DL matching techniques proved to be a significant strength of our approach, as it allowed us to overcome the challenges posed by wide camera baselines.

A total ice loss of $-63\,000\text{ m}^3$ and a retreat of the glacier snout of 17.8 m was observed from 01 May 2022 to 13 November 2022. However, the ice loss rate increased during summer and significantly reduced in autumn, particularly after mid-September. We analyzed daily surface velocity at two locations: one 10 m from the frontal ice cliff and another in the central part, approximately 120 m from the front. Both time series exhibited similar behaviors throughout the year, with comparable velocities from May to mid-June and again from late September to November. However, the point near the terminal ice cliff exhibited approximately 30% higher velocity during the warm season, with values ranging from 0.15 m d^{-1} on a few days in early August and early September to a peak of 0.23 m d^{-1} in mid-July. This finding underscores differential glacier movement in response to the exceptionally hot and dry summer of 2022.

One of the key findings derived from the stereo-camera setup was the significant correlation between air temperature and glacier surface velocity and ablation (correlation coefficient larger than 0.8 for all the signals), with negligible time lag. In the literature, the relationship between ablation and temperature is well established but rarely assessed quantitatively in the short term. On the other hand, a direct relationship between surface displacement and the temperature has not been established in the literature with the same level of detail as in our study.

Chapter 5 presents Deep-Image-Matching, a novel open-source Python toolkit that extends the DL matching algorithms implemented in Chapter 4 to tackle the stereo camera wide-baseline challenges in stereo-matching to a generic multi-view multi-view setup. DIM addresses the challenges of wide-baseline stereo matching in generic multi-view setups, facilitating the use of DL-based local features within the photogrammetric community. This tool is specifically designed to succeed in scenarios where traditional feature-matching algorithms often fail. Compared to other existing tools, DIM provides crucial advantages: it handles high-resolution images, offers robustness to rotations, and allows seamless integration with popular photogrammetric software packages like COLMAP, openMVG, MicMac, and Metashape.

DIM was designed to expand the Belvedere stereo camera setup, aiming to enhance view coverage, reduce occlusions, and improve reconstruction robustness through the installation of additional low-cost cameras along the glacier moraines. As the third camera has not yet been deployed on the glacier, the DIM software's capabilities were tested on other challenging datasets. Additionally, a multi-camera setup was simulated using UAV imagery acquired from locations that closely approximate potential camera positions.

6.2 GLOBAL CONSIDERATIONS AND FUTURE PERSPECTIVE

A LONG-TERM EXAMPLE OF PHOTOGRAHMETRIC GLACIER MONITORING

This thesis is one of the few examples of comprehensive and long-term photogrammetric monitoring of an alpine glacier. It achieves spatial resolutions from the meter to the decimeter scale and temporal frequencies spanning decades, years, and even daily intervals. Focusing on the debris-covered Belvedere Glacier in the Italian Alps, this work has provided a robust methodological framework and innovative tools that significantly advance glacier research capabilities and allow for documenting and quantifying the peculiar evolution of the Belvedere glacier in the last half-century, from 1977 to 2023.

Historical and digital aerial imagery analysis revealed a crucial long-term perspective, including decades of glacier evolution and a unique expansion period in the early 21st century. In particular, historical aerial images offer a uniquely valuable time capsule for understanding long-term alpine glacier dynamics. Vast archives of analog images documenting land surface changes for decades exist. While only a small fraction have been digitized, modern SfM software unlocks the full potential of these images for glacier reconstruction. In the case of the Belvedere Glacier, high-quality analog images from 1977, acquired and scanned by CGR S.p.A., made it possible to document the evolution of this natural heritage for half a century in the past. However, the recent release of the SwissImage archive, with its extensive collection of scanned analog images, allows it to reach even further back in time. Among the collection are a few images acquired close to the Swiss-Italian border, including the Belvedere Glacier. The oldest ones date back to 1951, and they could extend this thesis's analysis by two more decades.

The integration of UAVs in this study greatly enhanced the monitoring of Belvedere Glacier, achieving an annual survey frequency for almost 10 years, combined with periodical in-situ GNSS measurements. Low-cost UAVs and consumer-grade cameras enabled the consistent generation of photogrammetric models with decimeter accuracy. This level of spatial resolution and precision cannot be achieved with satellite or traditional aerial imagery, making UAV data uniquely valuable for detailed mass balance calculations and geomorphological process analysis.

UAVs offer flexibility compared to both archival and modern aerial platforms. Archival imagery is inherently limited by past acquisition schedules. At the same time, new aerial surveys are costly and often used only in scenarios where other options are unavailable (such as extremely high altitudes or remote locations). Similarly, high-resolution satellite imagery can be expensive, and revisit times in remote areas can be infrequent (e.g., only a few images per year are available in the Pleiades/Pleiades Neo archive). With limited time spent in the field, UAVs overcome these limitations and allow for collecting on-demand data

at a fraction of the cost and with great flexibility. In fact, despite the difficult conditions, in-situ operations on Belvedere Glacier were limited to a few days. Additionally, modern UAVs with RTK capabilities can safely and effectively survey dangerous alpine environments, significantly reducing the risk to personnel.

High-resolution orthophotos and DSMs derived from UAV photogrammetric models allowed the calculation of annual glacier surface displacements by DIC and volume variations over the entire glacier. This annual survey frequency was essential to capture the rapid evolution of a glacier acutely affected by climate change.

A NOVEL LOW-COST MULTI-CAMERAS APPROACH FOR SHORT-TERM MONITORING

Recognizing the inherently non-linear nature of glacier behavior at sub-seasonal timescales, this thesis developed a novel low-cost stereo camera system for comprehensive daily 3D motion analysis. The stereoscopic camera system, installed near the snout of the Belvedere Glacier, allowed us to integrate 3D reconstruction from stereo cameras with surface velocity estimation from monoscopic cameras using DIC. The result is a powerful tool for quantifying short-term glacier dynamics, including surface velocities, glacier retreat, and ice volume loss.

This study is one of the few examples of successfully utilizing stereo cameras for daily 3D glacier reconstruction. A key breakthrough was the implementation of DL algorithms to overcome the limitations of traditional feature matching techniques in contexts with wide baselines and extreme viewpoint changes. Such conditions are often unavoidable when deploying low-cost cameras in alpine environments.

The transferability of the camera system is a major strength. Its ease of installation allows deployment on different glaciers with minimal difficulty, making it a valuable tool for expanding glacier monitoring in diverse locations.

Currently focused on a specific portion of the glacier, this work serves as a pilot study, demonstrating the feasibility of the low-cost system in terms of both hardware and software. To expand its insights, a multi-camera setup is planned. The Deep-Image-Matching software developed in this thesis provides a crucial foundation for a multi-view 3D reconstruction pipeline.

OPEN SOURCE AND OPEN ACCESS COMMITMENT

This work demonstrates a strong commitment to open-access data sharing, fostering collaboration, and accelerating progress within glaciological research and related fields. All results from the photogrammetric campaigns, including point clouds, orthophotos, and DSMs, are publicly available in a Zenodo reposi-

tory¹. This rich dataset offers researchers a valuable base for further investigating diverse topics. Potential applications include the detailed analysis of geomorphological processes like moraine collapse in response to glacier thinning or as inputs for glacier modeling to project future glacier evolution under various climate scenarios.

To further enhance accessibility, a dedicated web app was developed, allowing even non-expert users to explore the 3D point clouds directly within a web browser². This app also integrates a GNSS measurement database collected over multiple years, enabling automated displacement and velocity calculations and generating insightful plots on glacier kinematic evolution.

Additionally, the stereo-camera dataset, including all stereo images captured between May and November 2022, the stereo processing software, and the resulting time-series of point clouds have been published on Zenodo³. A key near-future development for the web app will directly integrate these daily stereo images and automatic processing results into the platform. This will provide everyone with real-time access, minimizing the need for user intervention and specialized processing.

This thesis embraces the principle of open-source software, with all developed packages published on GitHub. This includes ICEPy4D⁴ for multi-temporal 3D reconstruction from stereo cameras and point-cloud time series analysis, and Deep-Image-Matching⁵ for multi-view image matching in complex scenarios using both traditional and DL-based local features. A collaborative effort with Niccolò Dematteis is underway to publish pyLamma⁶, an easy-to-use Python interface to LAMMA (Dematteis et al., 2022) for easily applying DIC to image series from monoscopic cameras. Future developments include the seamless integration of these three projects within ICEPy4D, leveraging DIM for matching components and pyLamma for DIC computations. This would provide a comprehensive toolkit suite for multi-temporal and multi-camera scenarios. Additionally, integrating ICEPy4D with libraries like py4dgeo (Anders et al., 2021, Winiwarter et al., 2023) would unlock powerful 4D change detection analysis on point cloud time-series.

¹Belvedere Glacier Open Data: <https://doi.org/10.5281/zenodo.7842347>

²Web app: <https://thebelvedereglacier.it/>

³Stereo-cameras data: <https://doi.org/10.5281/zenodo.8164638>

⁴ICEPy4D: <https://github.com/franioli/icepy4d>

⁵Deep-Image-Matching <https://github.com/3DOM-FBK/deep-image-matching>

⁶pyLAMMA: <https://github.com/franioli/pylamma>

References

- Anders, K., Winiwarter, L., Mara, H., Lindenbergh, R., Vos, S. E., & Höfle, B. (2021). Fully automatic spatiotemporal segmentation of 3d lidar time series for the extraction of natural surface changes. *ISPRS J. Photogramm. Remote Sens.*, 173, 297–308, <https://doi.org/10.1016/j.isprsjprs.2021.01.015>.
- Dematteis, N., Giordan, D., Crippa, B., & Monserrat, O. (2022). Fast local adaptive multiscale image matching algorithm for remote sensing image correlation. *Computers & Geosciences*, 159, 104988, <https://doi.org/10.1016/j.cageo.2021.104988>.
- Winiwarter, L., Anders, K., Czerwonka-Schröder, D., & Höfle, B. (2023). Full four-dimensional change analysis of topographic point cloud time series using kalman filtering. *Earth Surf. Dynam.*, 11(4), 593–613, <https://doi.org/10.5194/esurf-11-593-2023>.

A

Orthophotos 1977-2023



Figure A.1: [
]Historical-aerial orthophoto from 1977.



Figure A.2: Historical-aerial orthophoto from 1991.

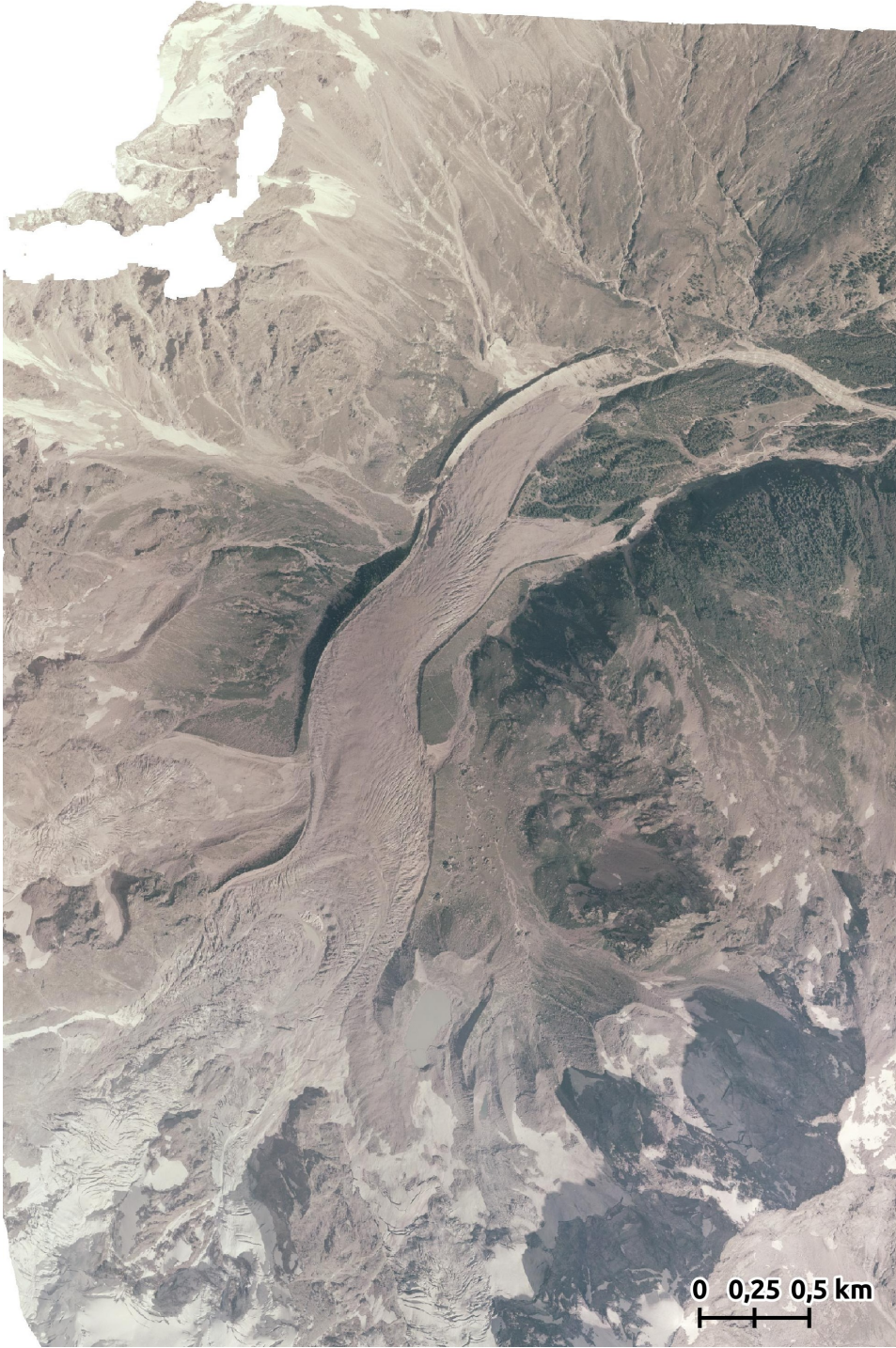


Figure A.3: Historical-aerial orthophoto from 2001.

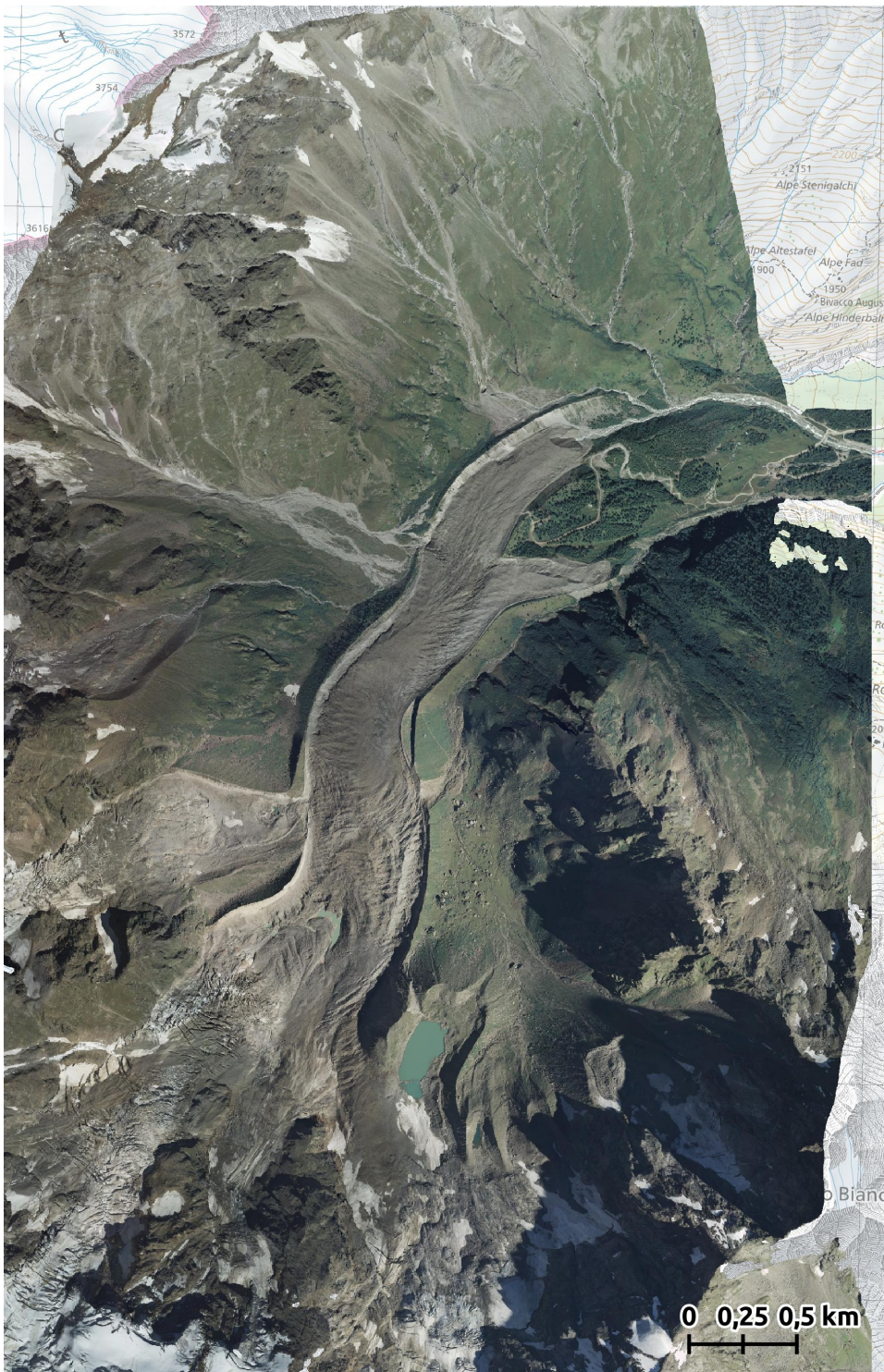


Figure A.4: Aerial orthophoto from 2009.



Figure A.5: UAV orthophoto from 2015.



Figure A.6: UAV orthophoto from 2016.

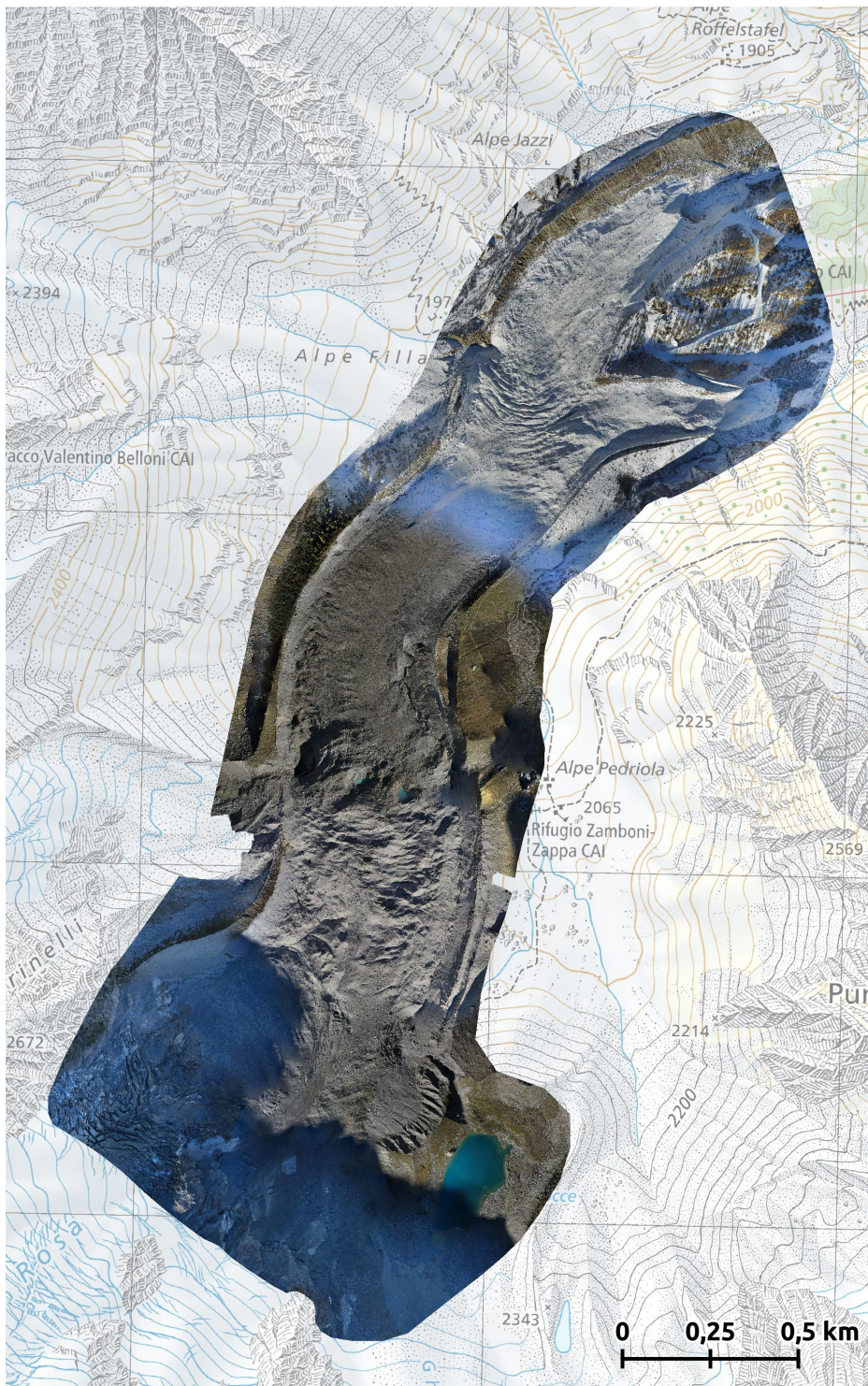


Figure A.7: UAV orthophoto from 2017.



Figure A.8: UAV orthophoto from 2018.



Figure A.9: UAV orthophoto from 2019.



Figure A.10: UAV orthophoto from 2020.



Figure A.11: UAV orthophoto from 2021.



Figure A.12: UAV orthophoto from 2022.



Figure A.13: UAV orthophoto from 2023.

B

Surface velocity fields 2015-2023

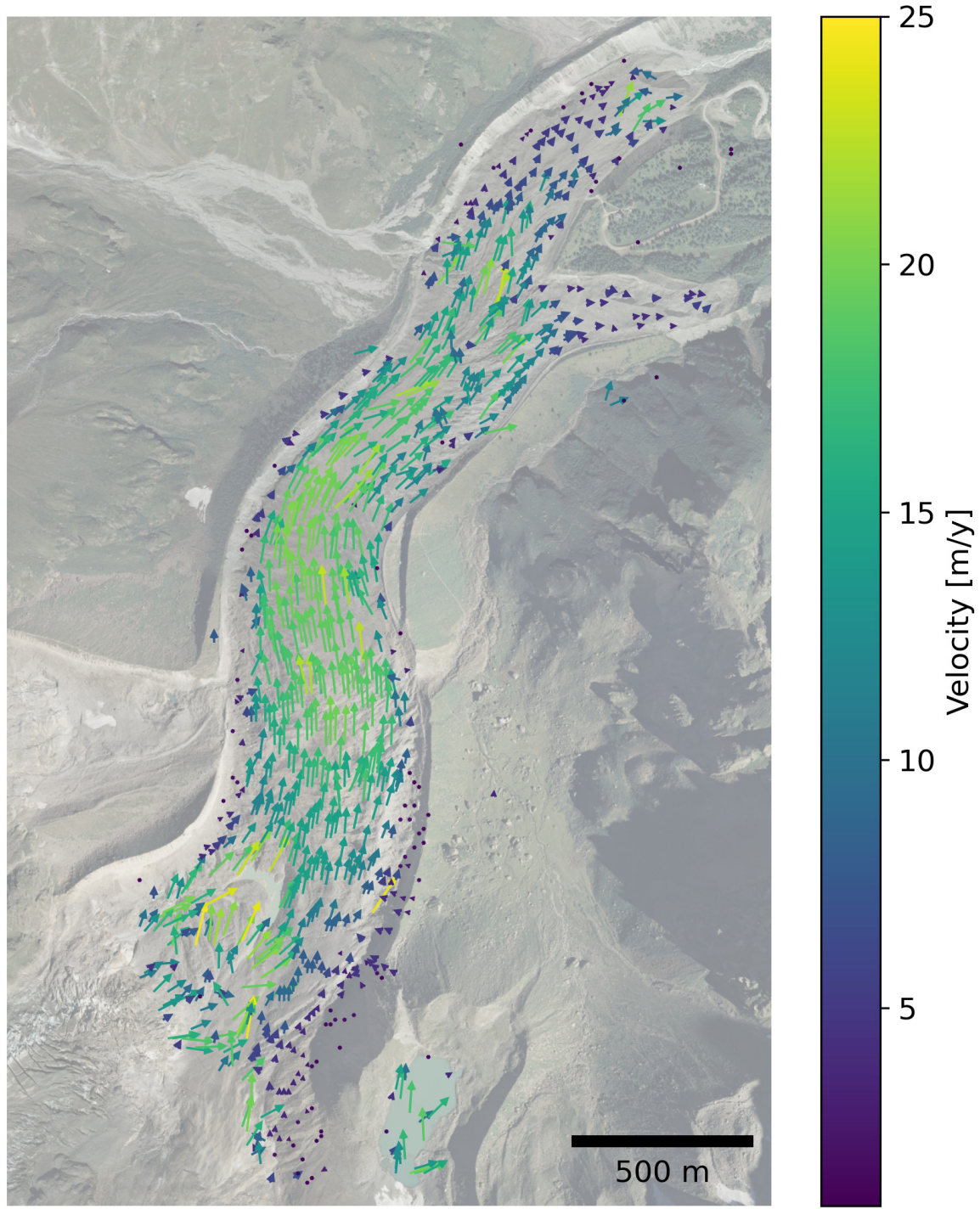


Figure B.1: Glacier surface velocity field derived by DIC on DSM 2015-2016

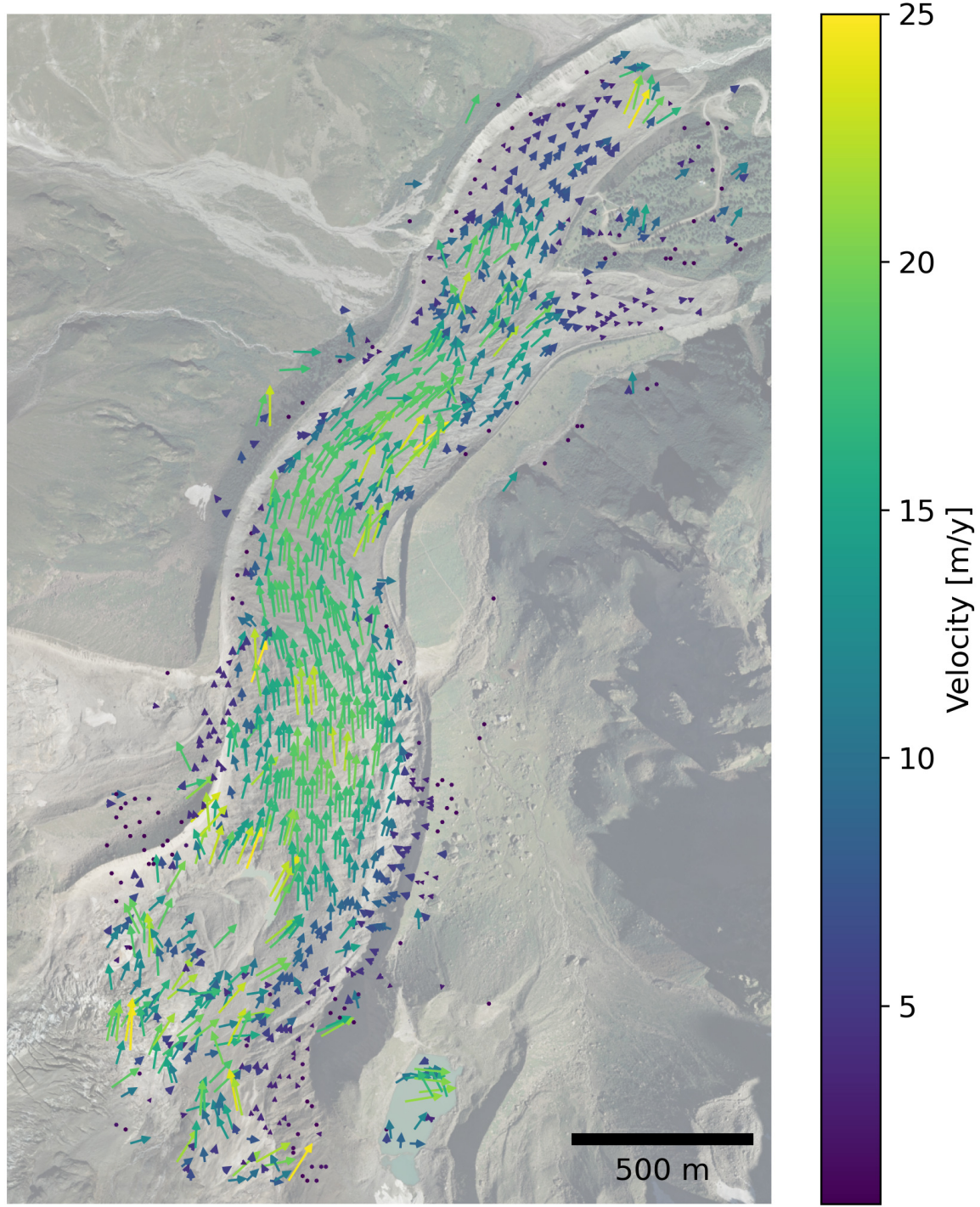


Figure B.2: Glacier surface velocity field derived by DIC on DSM 2016-2017

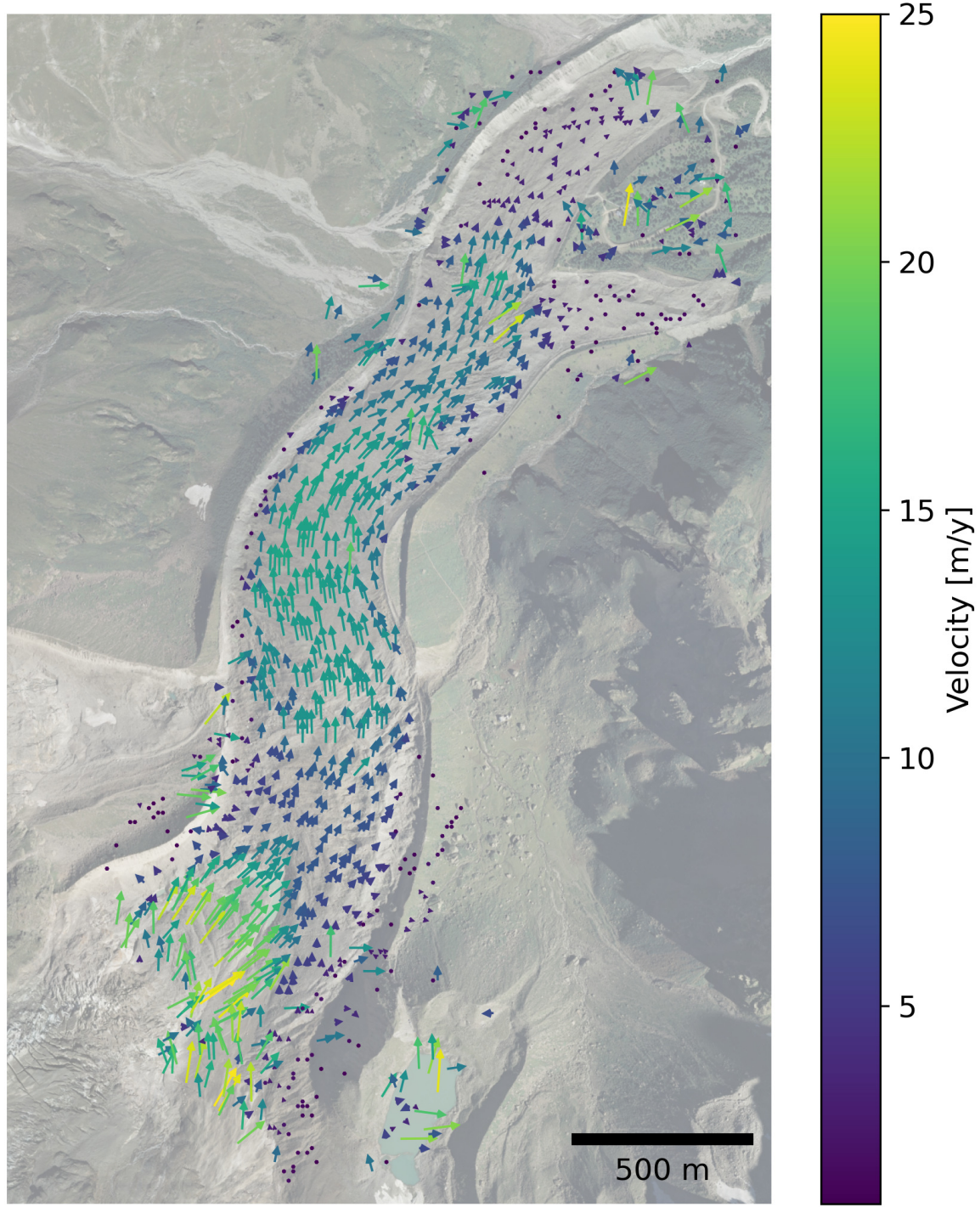


Figure B.3: Glacier surface velocity field derived by DIC on DSM 2017-2018

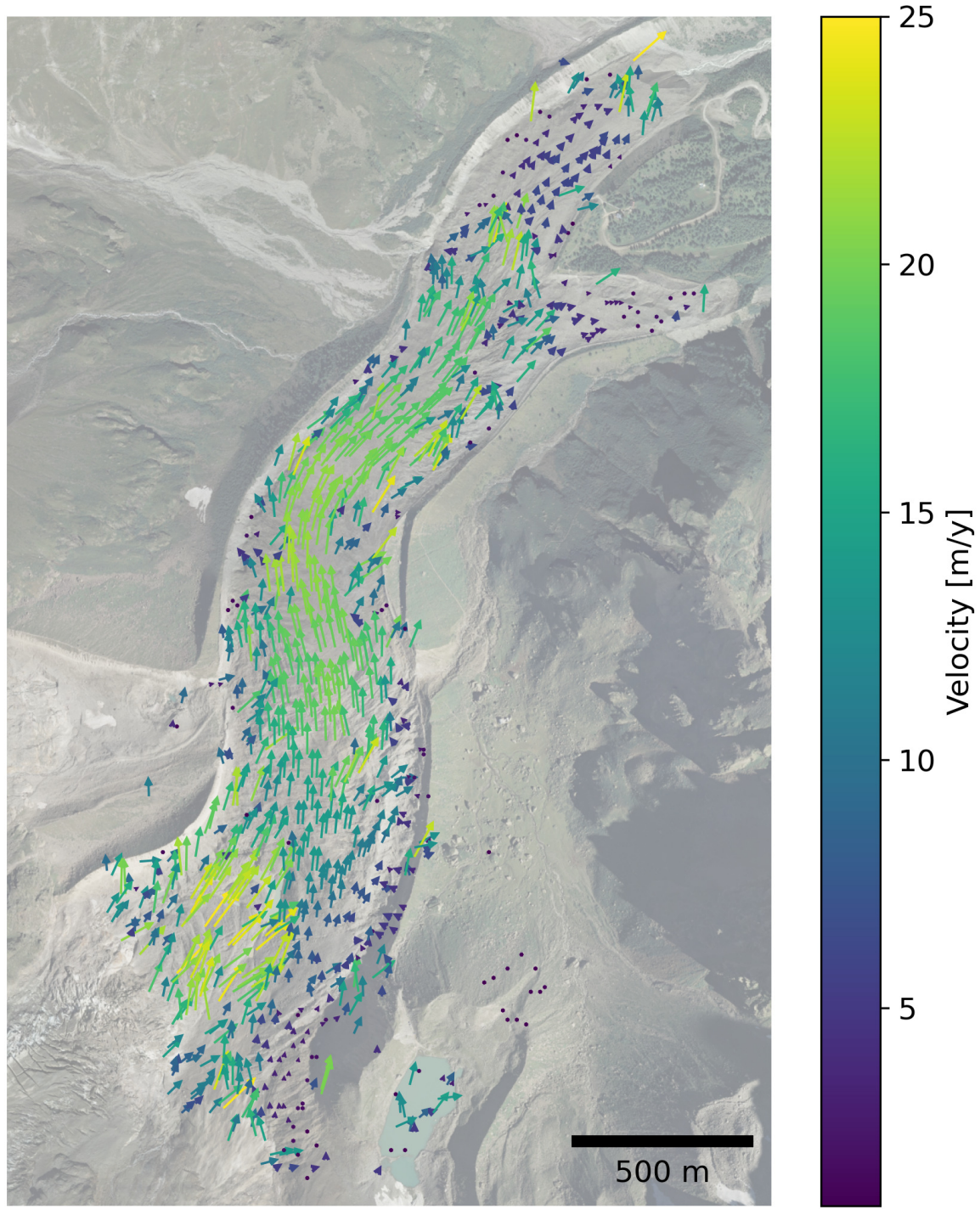


Figure B.4: Glacier surface velocity field derived by DIC on DSM 2018-2019

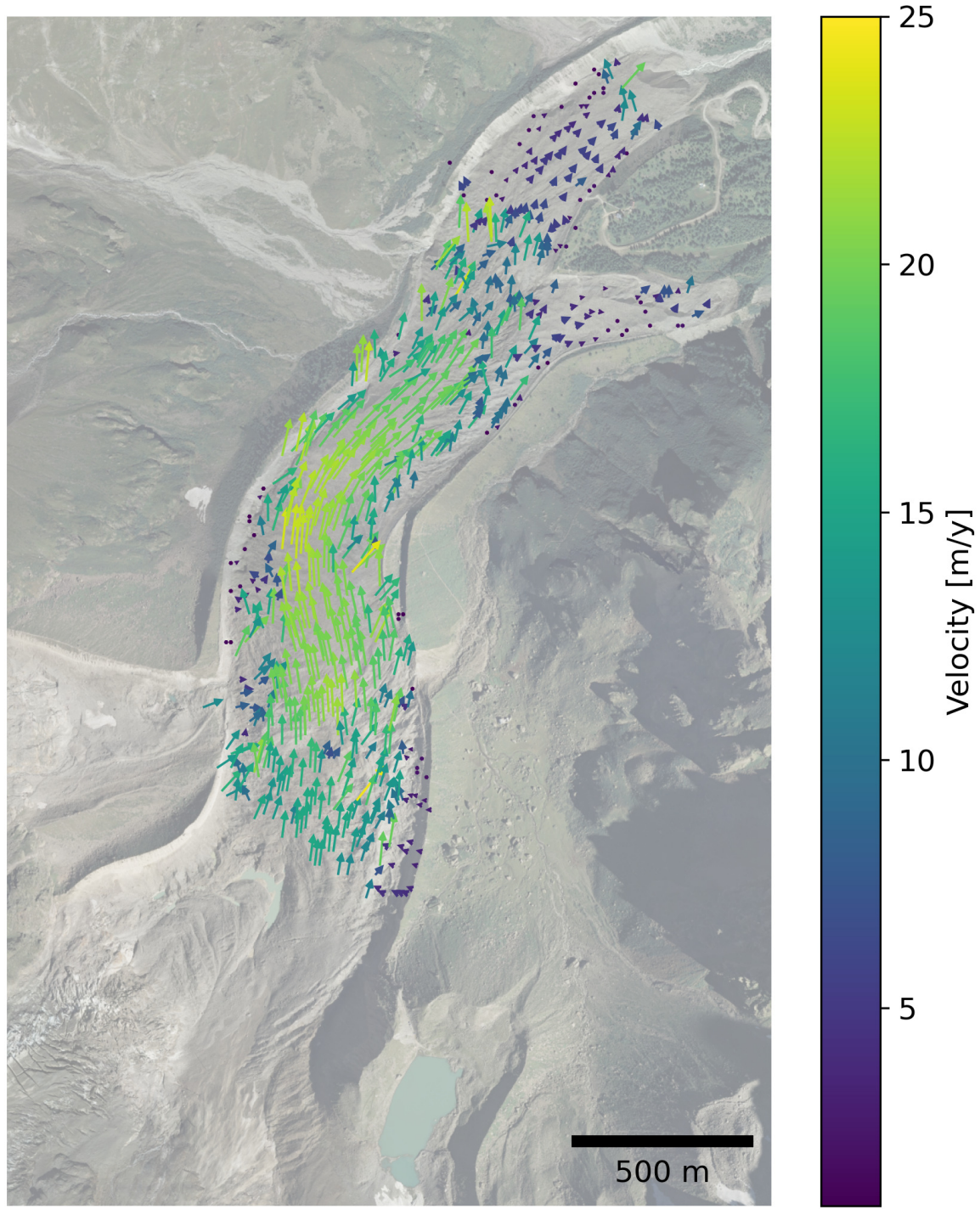


Figure B.5: Glacier surface velocity field derived by DIC on DSM 2019-2020

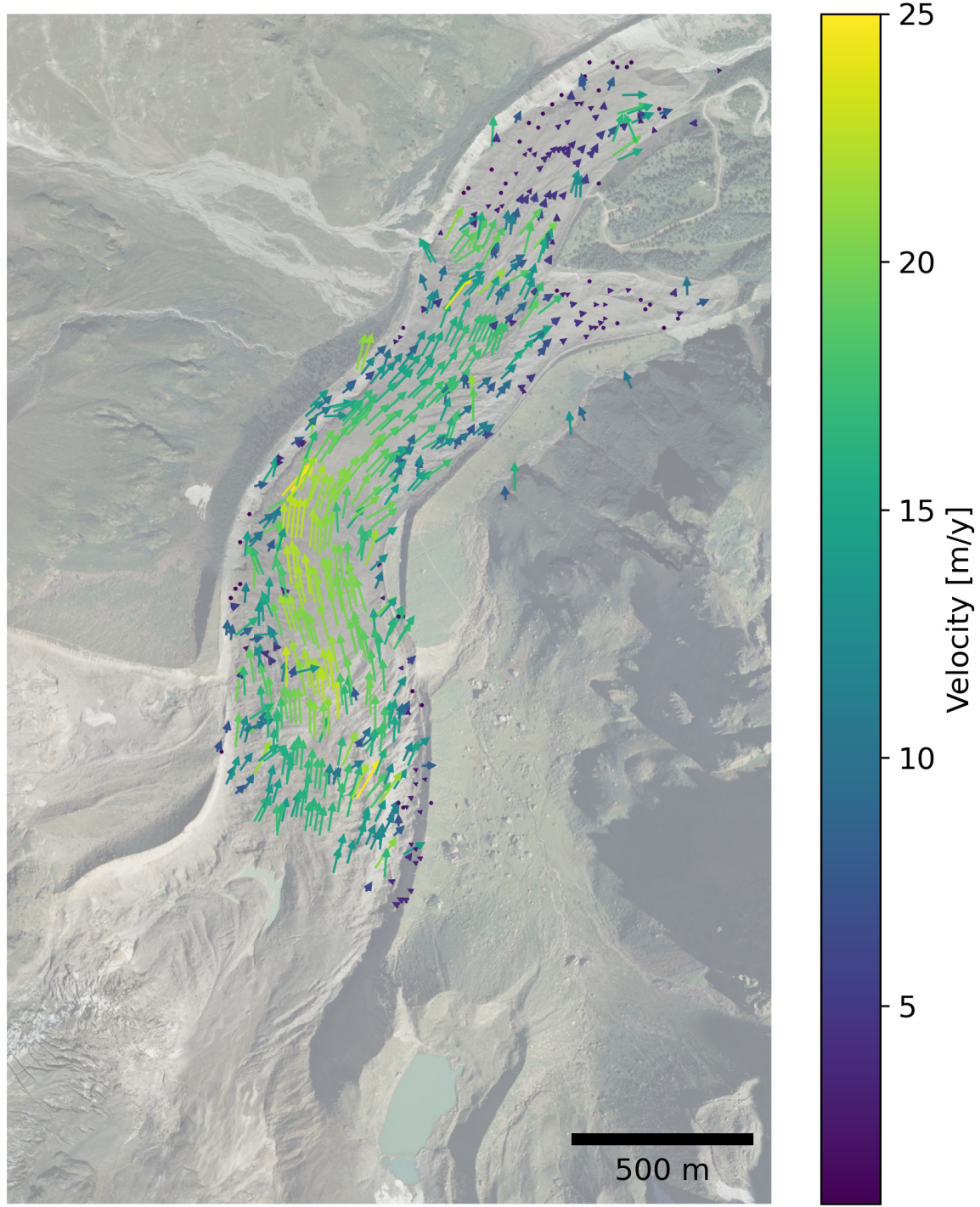


Figure B.6: Glacier surface velocity field derived by DIC on DSM 2020-2021

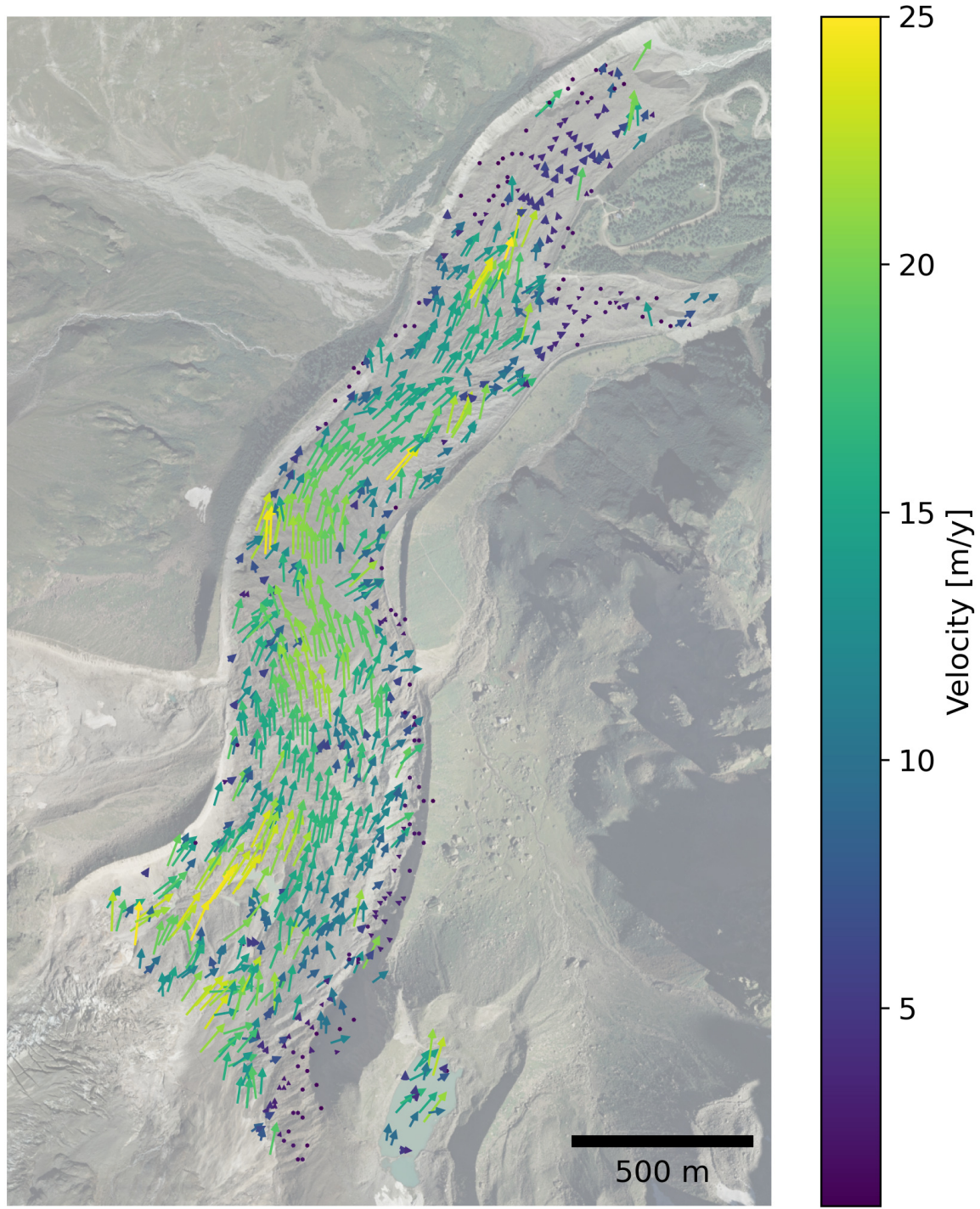


Figure B.7: Glacier surface velocity field derived by DIC on DSM 2021-2022

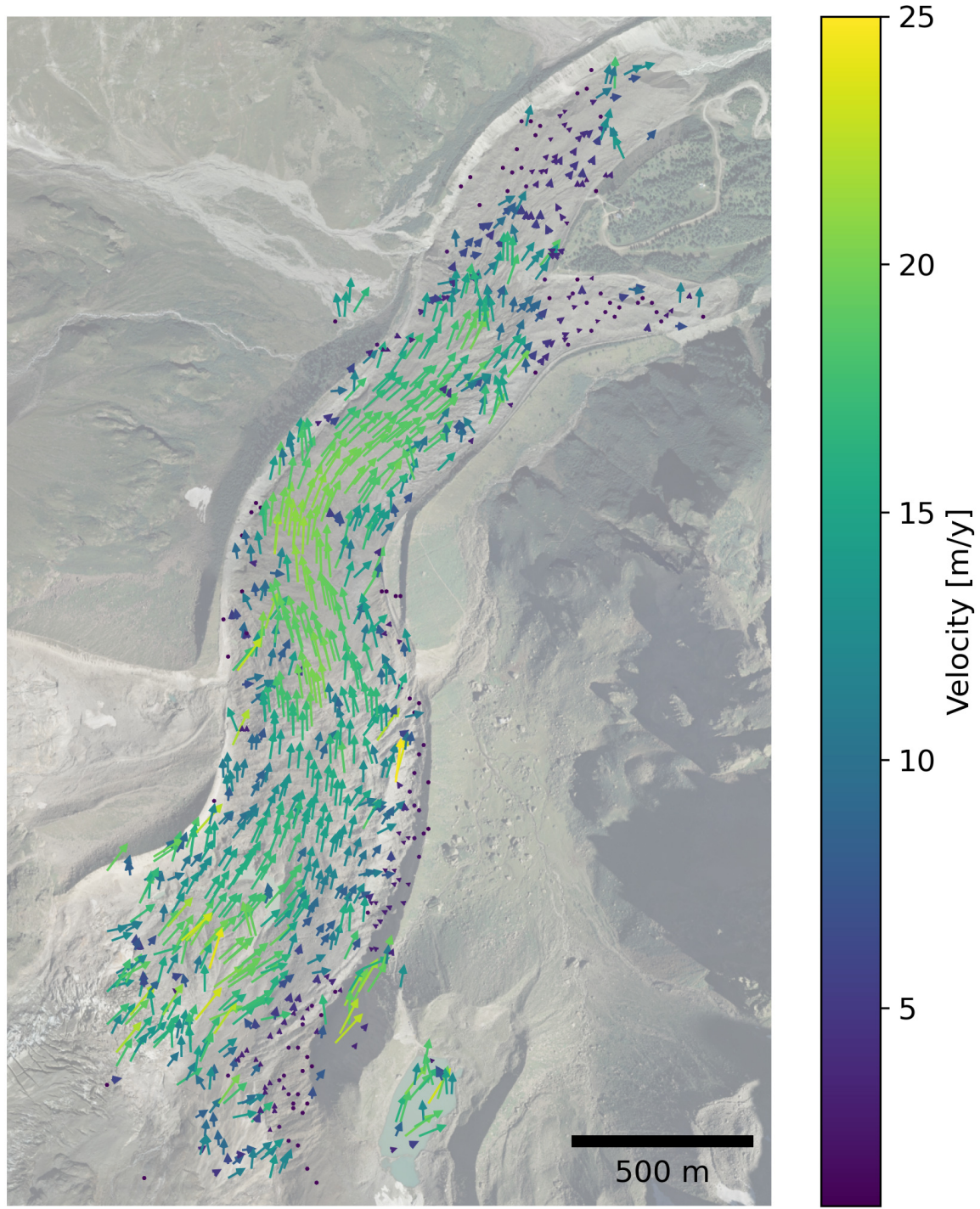


Figure B.8: Glacier surface velocity field derived by DIC on DSM 2022-2023

C

Cross-sections

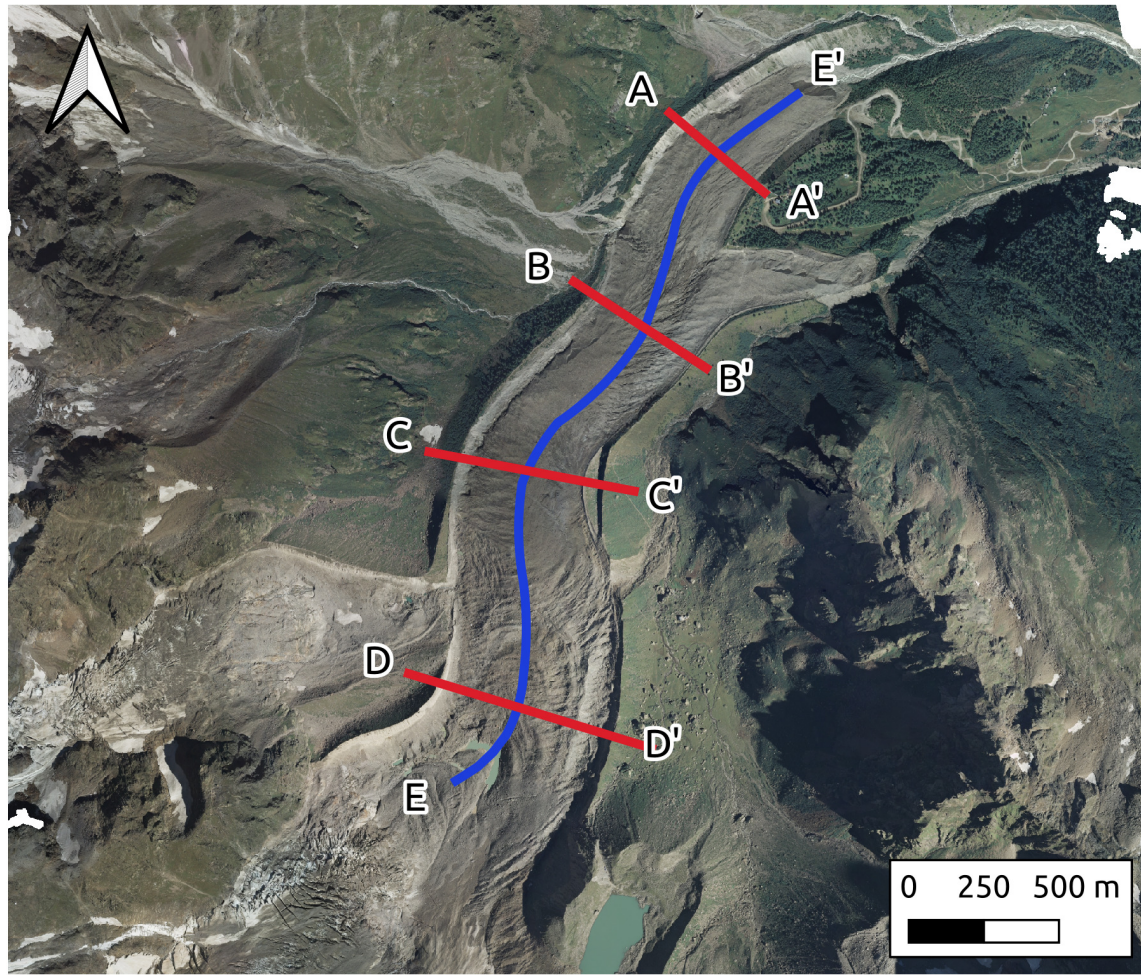


Figure C.1: Location of the cross-sections

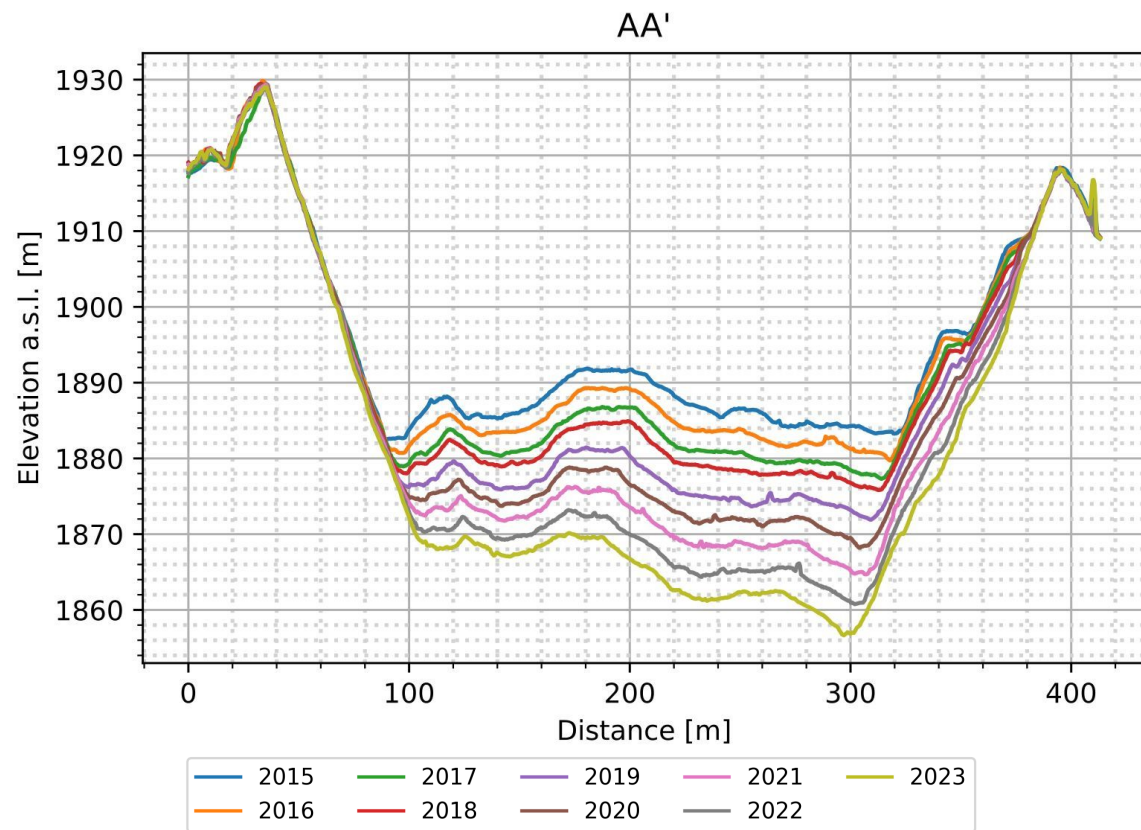


Figure C.2: Cross sections along the profile AA'

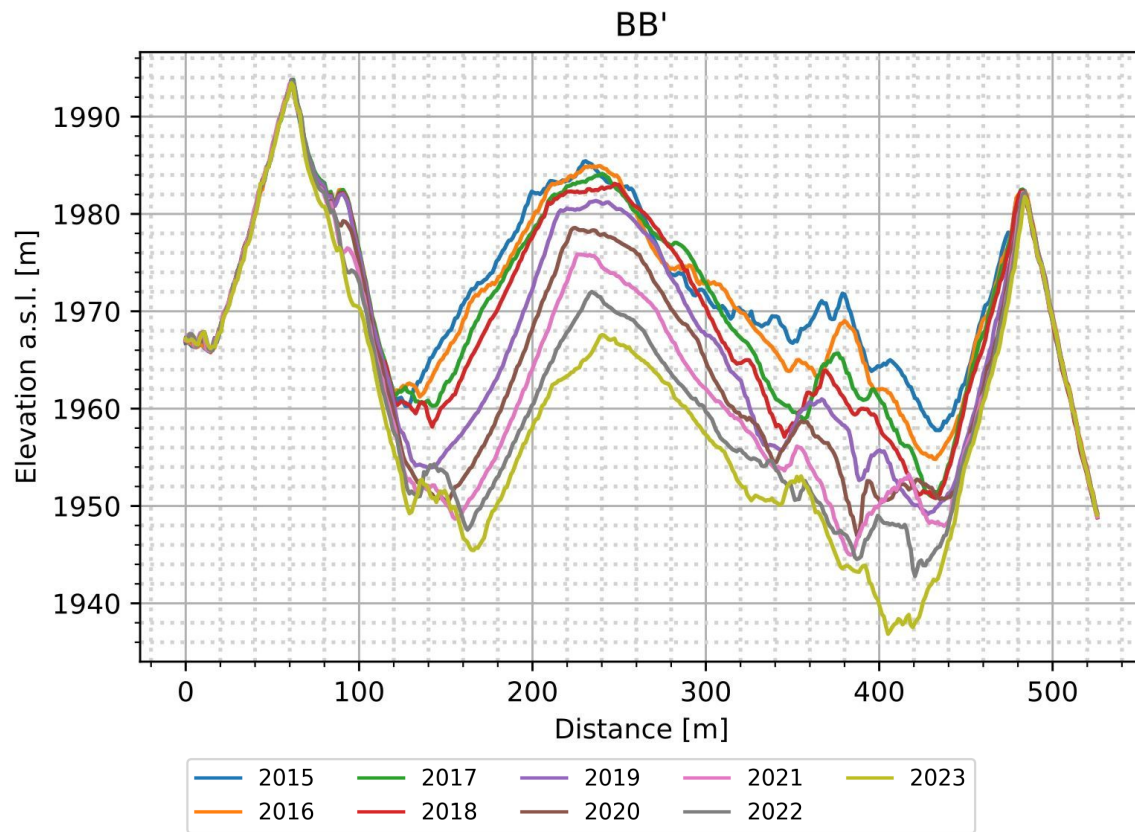


Figure C.3: Cross sections along the profile BB'

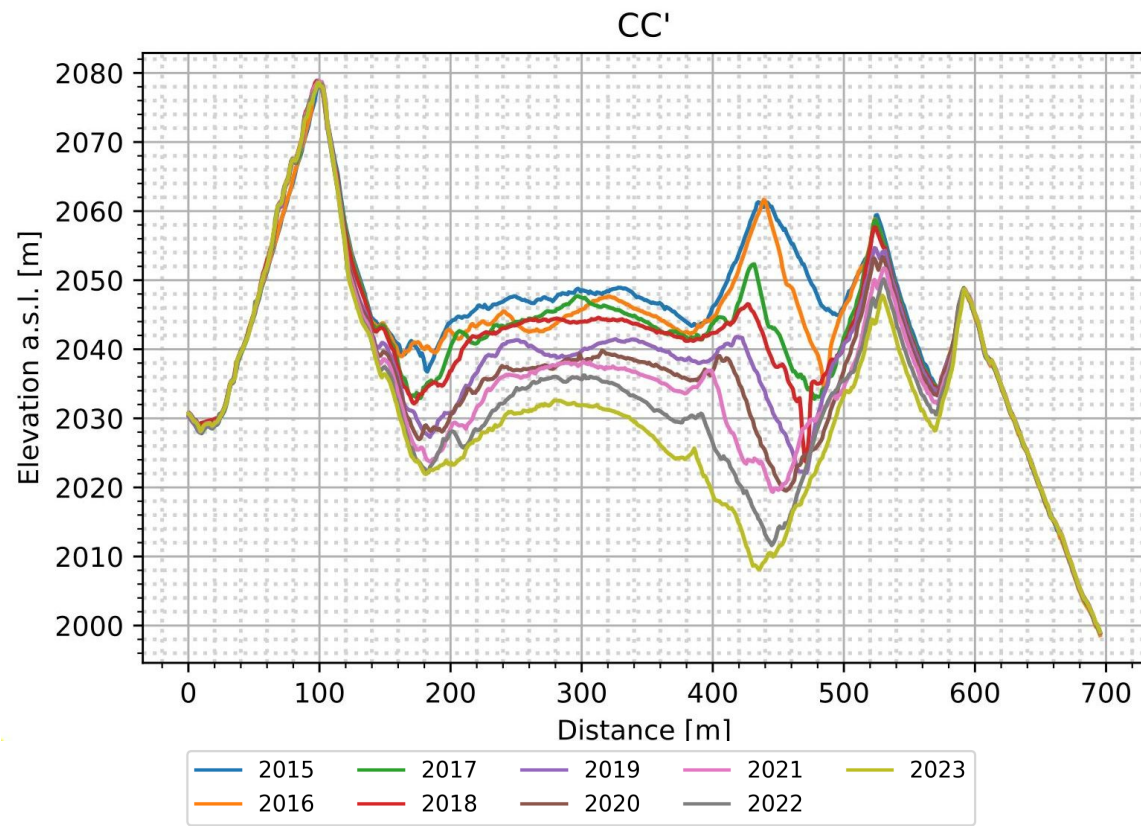


Figure C.4: Cross sections along the profile CC'

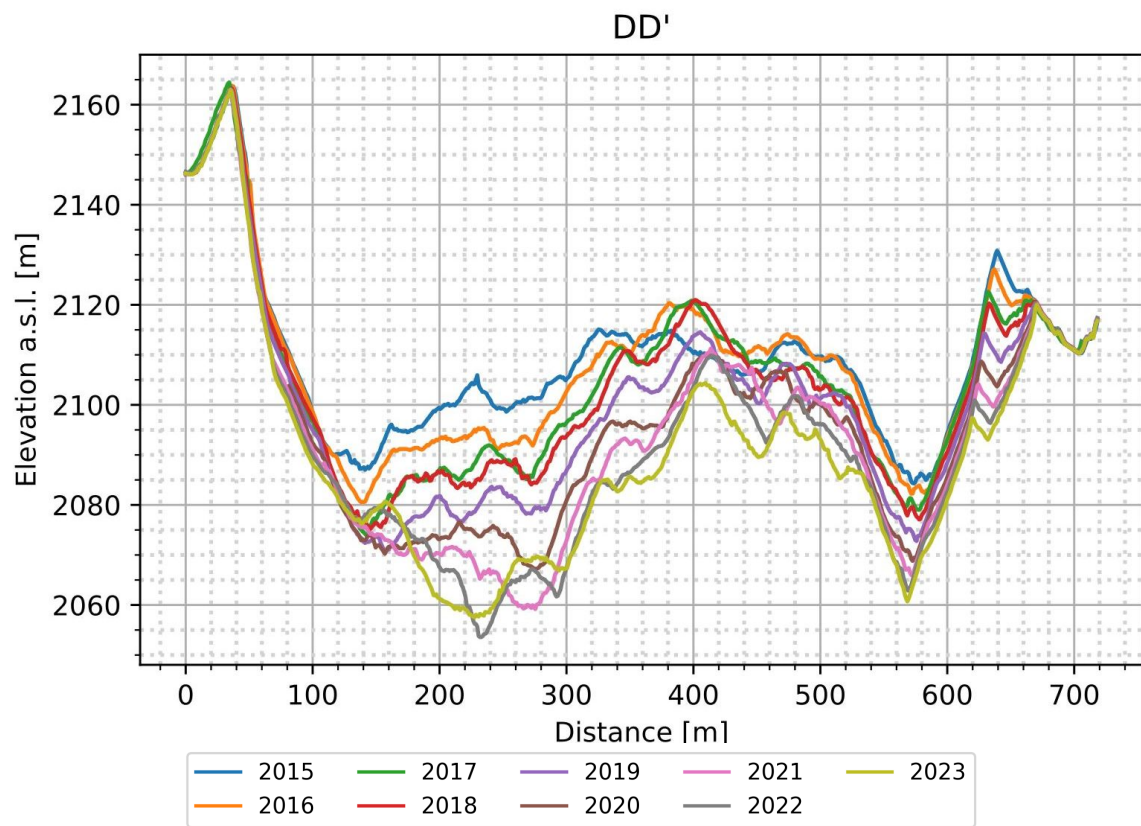


Figure C.5: Cross sections along the profile DD'

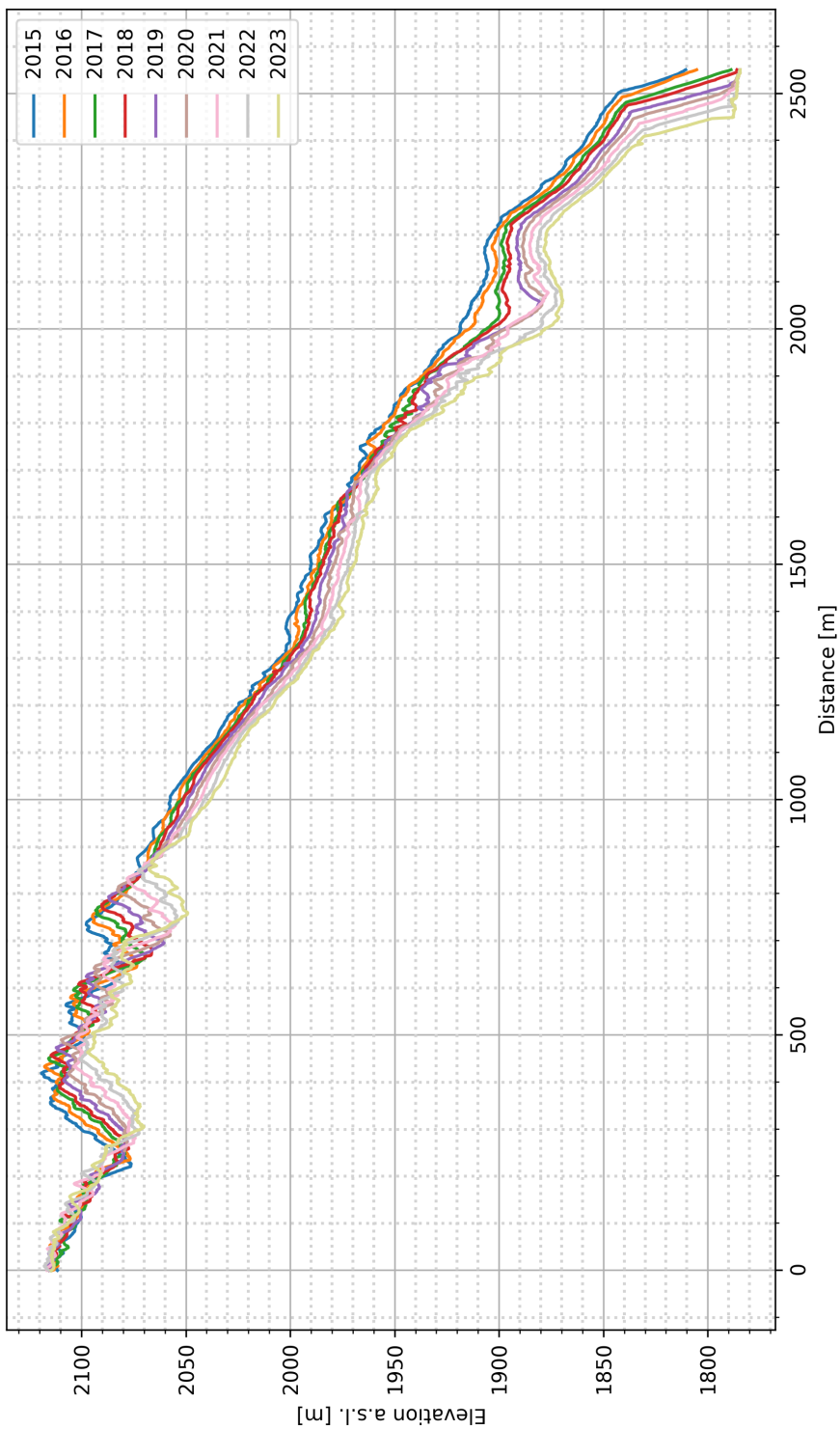


Figure C.6: Cross sections along the profile EE', extracted along the glacier flow direction.

D

Camera residuals

This appendix presents the residual images for the various cameras used in the photogrammetric blocks throughout the thesis. These residual images, as computed by Agisoft Metashape, represent the reprojection error of the tie points averaged within a regular grid in the image and averaged across all the images associated with each camera.

The reprojection errors are depicted as vectors, with colors indicating the magnitude of the error: green denotes lower error, while red indicates higher error. The scale of these vectors is provided in each plot via a scalebar located below the figure, expressed in millimeters for cameras with fiducial marks (such as the analog cameras used in Chapter 2) or pixels for digital cameras. Additionally, the RMS and the maximum reprojection errors are reported for each camera.

Some systematic errors are visible in some of the residual plots at the edges of the image, particularly with lower-quality cameras. However, the RMS values of the residuals are consistently significantly below the pixel level, with maximum residuals generally not exceeding 2 px.

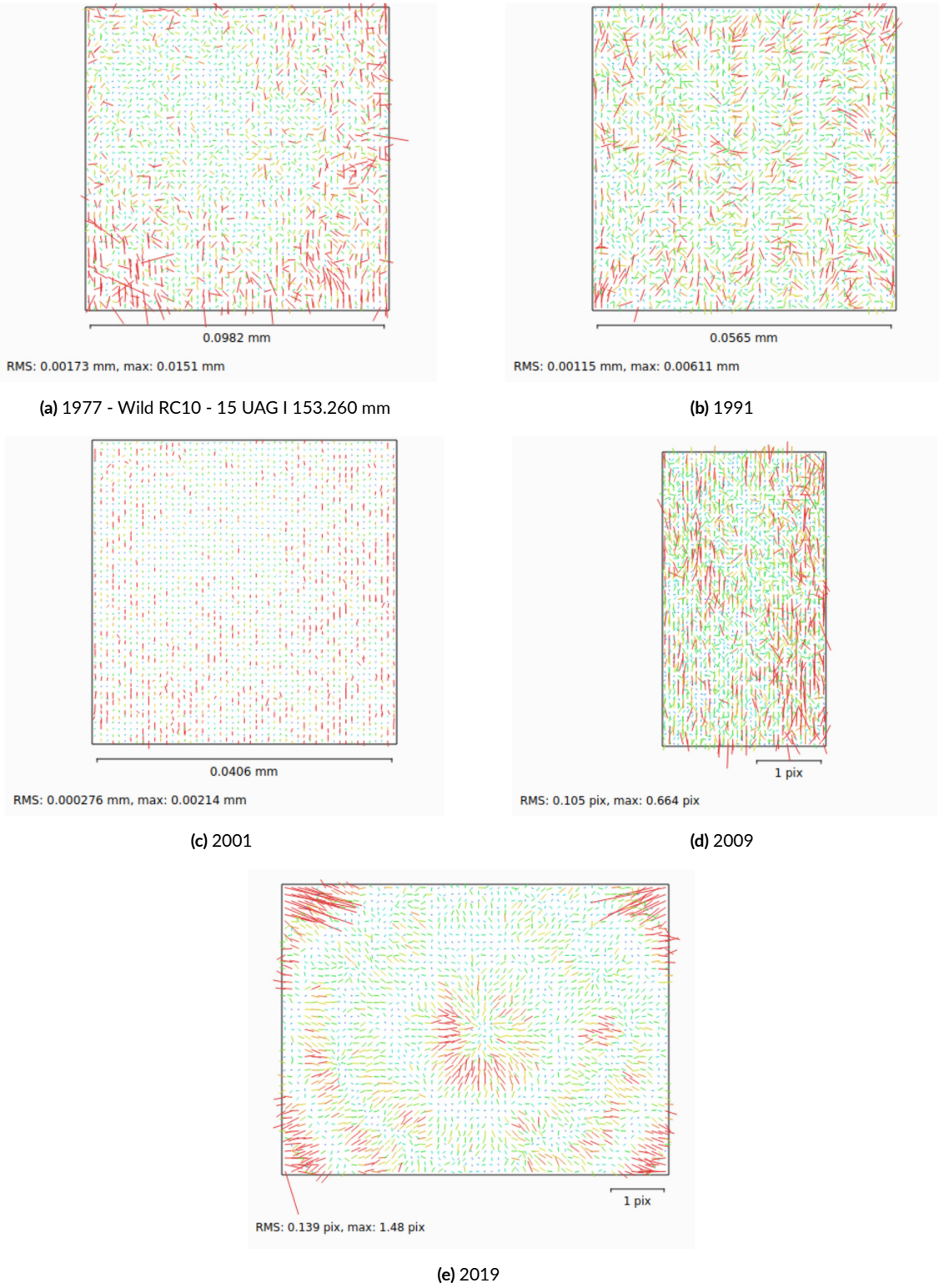


Figure D.1: Residual image for the cameras employed for reconstructing the glacier in 1977, 1991, 2001, 2009, and 2019 as described in Chapter 2.

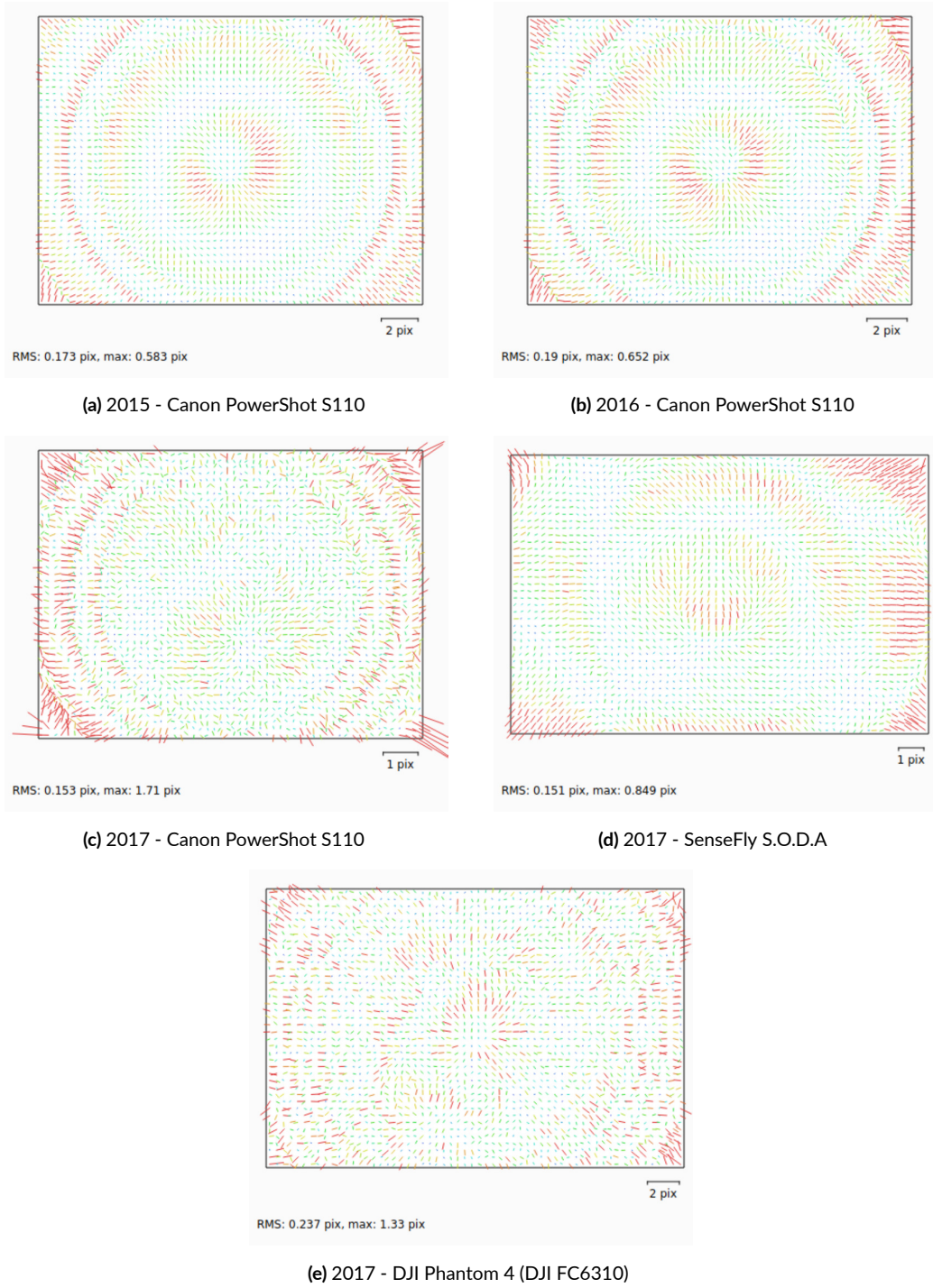


Figure D.2: Residual image for the cameras employed for the annual UAV reconstruction, described in Chapter 3.

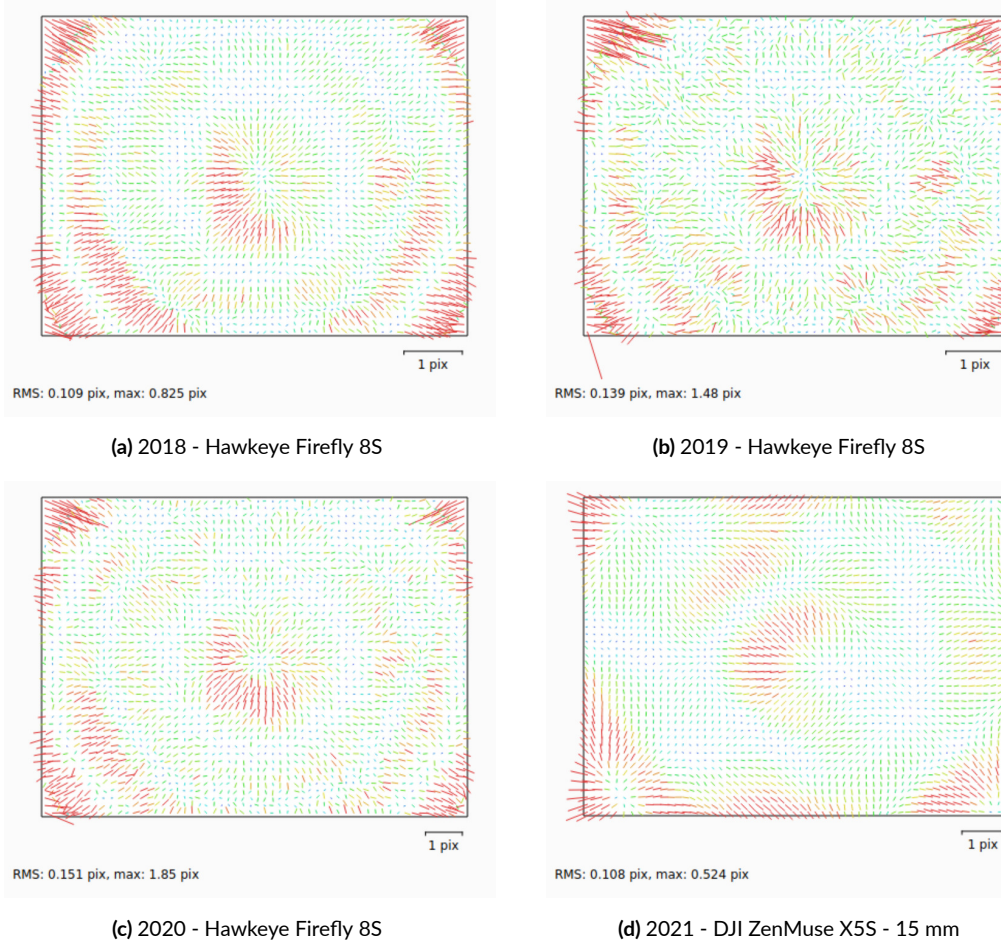


Figure D.3: Residual image for the cameras employed for the annual UAV reconstruction, described in Chapter 3.

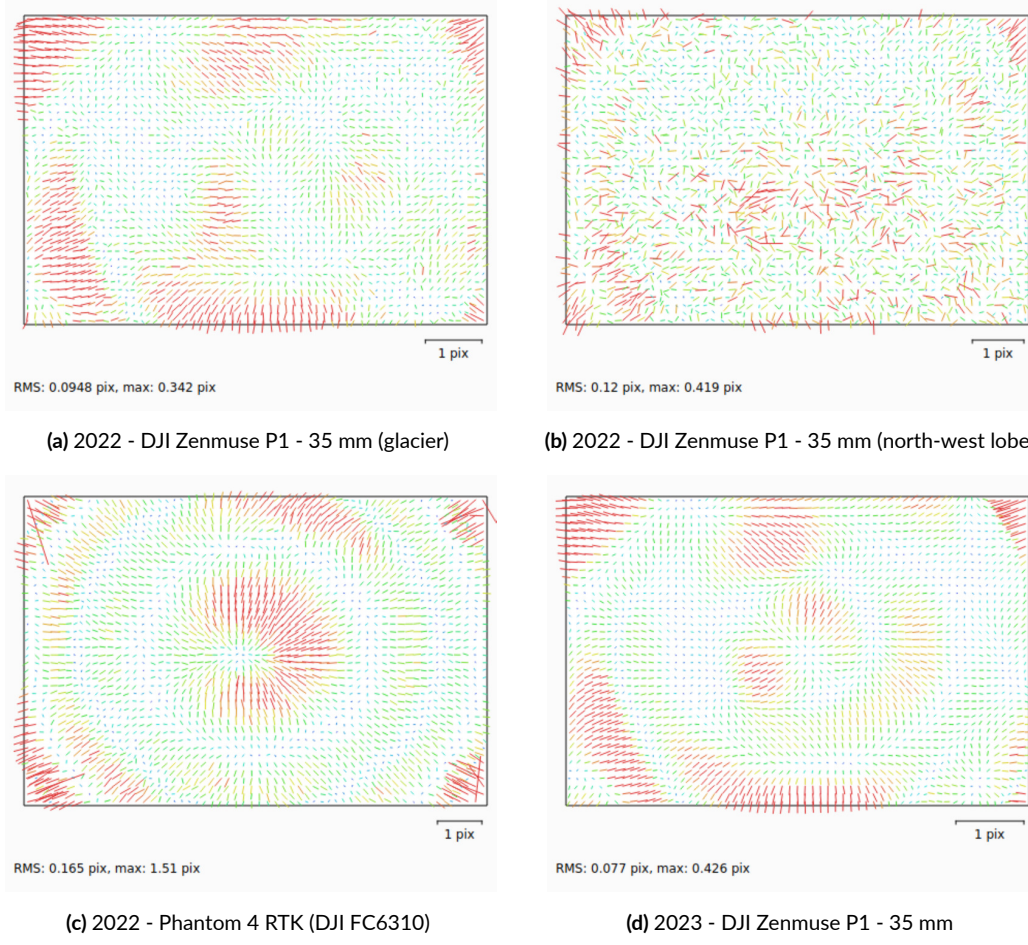


Figure D.4: Residual image for the cameras employed for the annual UAV reconstruction, described in Chapter 3.

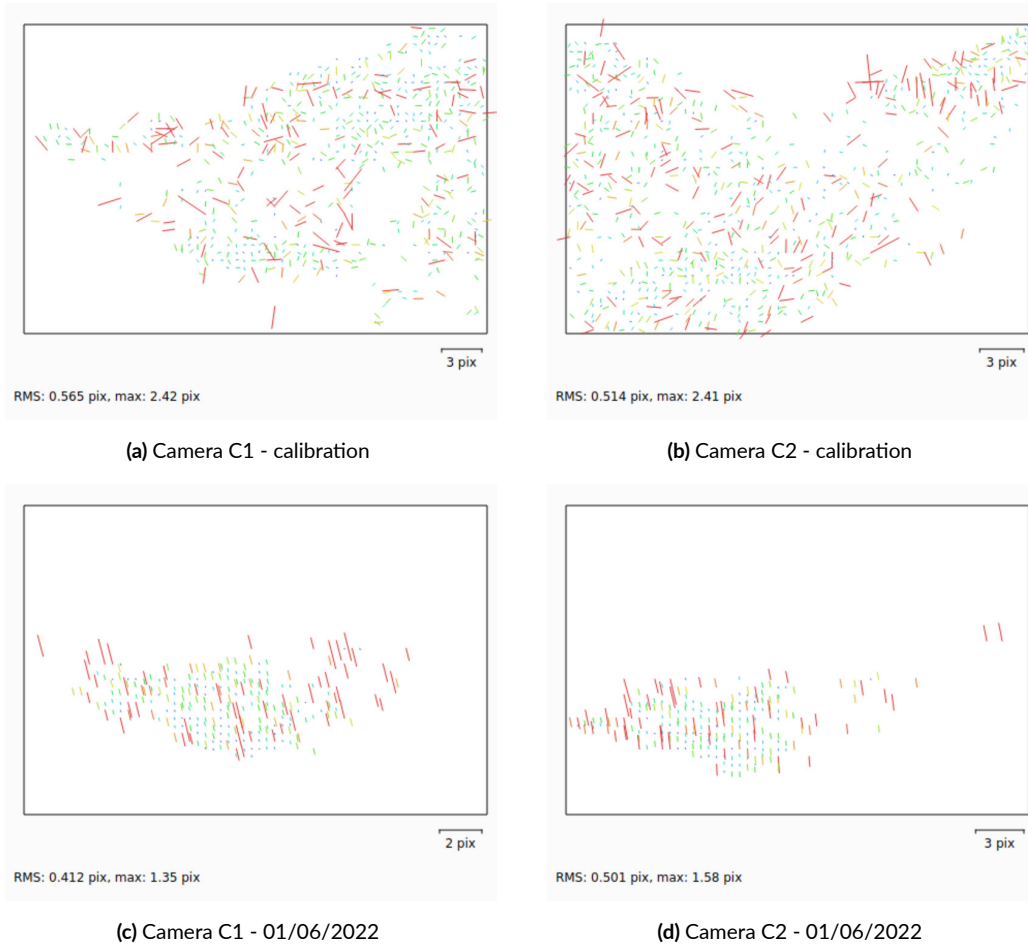


Figure D.5: Residual images for the fixed stereo cameras used for daily reconstruction of the glacier terminus, as described in Chapter 2. The top row displays the residual images during the calibration process, which was conducted by integrating the stereo images within a complete UAV block and using GCPs (see Sec. ??). The bottom row provides an example of the residual images for a single epoch (01/06/2022). In this case, the camera's interior orientation was fixed to the pre-calibrated values, except for the principal distance (focal length), which was refined through self-calibration.